SAKARYA ÜNİVERSİTESİ

FEN BİLİMLERİ ENSTİTÜSÜ DERGİSİ

Sakarya University Journal of Science (SAUJS)

SAKARYA ÜNİVERSİTESİ

e-issn: 2147-835X

SAÜ Fen Bil Der/SAUJS

Cilt/Volume: 26

Sayı/Issue: 4

Ağustos/August 2022

Sakarya Üniversitesi Fen Bilimleri Enstitüsü Dergisi
(Sakarya University Journal of Science)
Cilt/Volume: 26 No/ Issue:4 Ağustos/August 2022
Editör Kurulu/Editorial Boards

Owner

Hamza Al, Sakarya University (Turkey)

Publishing Manager

Halit Yaşar, Mechanical Engineering, Sakarya University (Turkey)

Editor-in-Chief

Davut Avcı, Pyhsics, Sakarya University (Turkey)

Associate Editors

Ihsan Hakan Selvi, Information Systems Engineering, Sakarya University (Turkey)

Ömer Tamer, Physics, Sakarya University (Turkey)

Editors

Abderrahmane Benbrik, M'Hamed Bougara University at Boumerdes (Algeria)

Abdullah Oğuz Kızılçay, Computer Engineering, Zonguldak Bülent Ecevit University (Turkey)

Ali Cemal Benim, Faculty of Mechanical and Process Engineering, Duesseldorf University of Applied Sciences (Germany)

Ali Demir, Mathematics, Kocaeli University (Turkey)

Aligholi Niaei, Chemistry, Tabriz University (İran)

Aslı Uçar, Faculty of Health Sciences, Nutrition and dietetics, Ankara University (Turkey)

Asude Ateş, Environmental Engineering, Sakarya University (Turkey)

Bahadır Saygı, Physic, Ege University (Turkey)

Barış Yüce, Engineering Management, Exeter University, UK

Belma Zengin Kurt, Chemistry, Bezmiâlem Vakıf University (Turkey)

Benjamin Durakovic, Department of Industrial Engineering, Bosnia International University of Sarajevo (Bosnia and Herzegovina)

Berrin Denizhan, Industrial Engineering, Sakarya University (Turkey)

Can Serkan Keskin, Chemistry, Sakarya University (Turkey)

Caner Erden, International Trade and Finance, Sakarya University of Applied Sciences (Turkey)

Ceren Tayran, Physic, Gazi University (Turkey)

Cansu Akbulut, Biology, Sakarya University (Turkey)

Ece Ümmü Deveci, Environmental Engineering, Niğde Ömer Halisdemir University (Turkey)

Guest Editor

English Language Editor

Editorial Assistant

SAKARYA ÜNİVERSİTESİ FEN BİLİMLERİ ENSTİTÜSÜ DERGİSİ
(SAKARYA UNIVERSITY JOURNAL OF SCIENCE)
İÇİNDEKİLER/CONTENTS
Cilt/Volume: 26 – No/Issue4: (AĞUSTOS/AUGUST-2022)

RESEARCH ARTICLES

SAKARYA ÜNİVERSİTESİ
FEN BİLİMLERİ ENSTİTÜSÜ DERGİSİ

Sakarya University Journal of Science
SAUJS

ISSN 1301-4048 | e-ISSN 2147-835X | Period Bimonthly | Founded: 1997 | Publisher Sakarya University | http://www.saujs.sakarya.edu.tr/

Title: Neutronic and Thermalhydraulic Evaluation of Annular Fuel in PWR with Three Different Nanofluids

Authors: Ali TİFTİKÇİ

Recieved: 2022-02-28 00:00:00

Accepted: 2022-05-16 00:00:00

Article Type: Research Article

Volume: 26
Issue: 4
Month: August
Year: 2022
Pages: 643-654

How to cite
Ali TİFTİKÇİ; (2022), Neutronic and Thermalhydraulic Evaluation of Annular Fuel in PWR with Three Different Nanofluids. Sakarya University Journal of Science, 26(4), 643-654, DOI: 10.16984/saufenbilder.1080287
Access link
http://www.saujs.sakarya.edu.tr/en/pub/issue/72361/1080287

Sakarya University Journal of Science 26(4), 643-654, 2022

Neutronic and Thermalhydraulic Evaluation of Annular Fuel in PWR with Three Different Nanofluids

Ali TİFTİKÇİ*[1]

Abstract

In pressurized nuclear reactors, one of the fuel design principles is the fuel centerline temperature limit. Since the thermal conductivity of UO_2 is not high, the temperature increases rapidly from the fuel surface to the fuel center. To overcome this limitation, the use of annular type fuels instead of solid fuels is one of the improvement efforts. In this study, the effects of using annular fuel in a typical PWR are investigated. At the same time, the effects of adding nanoparticles (Al_2O_3, Cu and TiO_2-with volume fractions of $0 < \varphi < 0.2$ for neutronic and $0 < \varphi < 0.03$ for thermalhydraulic calculations) and to the coolant water in the case of solid and annular fuels are also investigated. For both cases, neutronic and thermalhydraulic calculations are made and compared. In neutronic point of view, it has been shown that the use of annular fuel does not cause a significant change in the k_{eff} value but the presence of nanoparticles reduces the k_{eff}. This reduction is maximum for Cu+water and minimum for Al_2O_3+water nanofluids. In thermalhydraulic point of view, it has been shown that the annular fuel positively affects the fuel temperature limits and the addition of nanoparticles could provide an additional contribution to this, provided that it is in very small amounts ($\varphi < 0.01$). Among the three nanoparticles examined, Cu+water is found to be the least suitable both in terms of neutronics and termalhydraulic considerations. TiO_2+water and Al_2O_3+water are comparable. It has also been shown that the optimum value for the annular fuel inner radius is approximately 0.4 cm.

Keywords: Annular fuel, nanofluid, Monte Carlo method, termalhydraulics

1. INTRODUCTION

Fuel rods used in nuclear reactors generally have a solid cylindrical geometry and the heat transfer is provided to the coolant from the outermost surface of the rod. Recently, different nuclear reactor fuel and coolant combinations have been studied to strengthen nuclear reactor safety and economy. One of these studying areas is the dual-cooled annular type fuel rods. Since the use of

* Corresponding author: atiftikci@sinop.edu.tr
[1] Sinop University, Faculty of Engineering And Architecture, Department of Nuclear Energy Engineering
ORCID: https://orcid.org/0000-0002-7727-9375

such systems will allow to move away from the fuel centerline temperature limit set for solid cylindrical fuel, fuel heat generation rates can be increased and the thermal performance and burn-up time to be obtained from the fuel could be optimized. Tak et al. [1] proposed a dual-cooled annular-type fuel concept in prismatic VHTR (Very High Temperature Reactor) reactors to solve the central fuel temperature problem. They performed thermal-hydraulic performance analysis for this reactor and as a result showed that the use of annular type fuel gives better results in terms of thermal-hydraulic performance. Lee et al. [2] compared pressure drops at nominal operating conditions for 16x16 solid cylindrical and 12x12 dual-cooled annular fuel bundle configurations for the OPR1000 reactor. According to the results, it was shown that the pressure drop is 15% less for a flat type spacer grid and 7% less for a spacer grid with mixing wane. Three-dimensional coupled neutronic and thermo-hydraulic analyzes for SCWR (Supercritical Water Reactor) reactor core have been performed by Zhao et al. [3] and according to their results, it has been shown to be promising for SCWR reactors. Ghazanfari et al. used an Al_2O_3 nanofluidic water coolant in addition to a dual-cooled annular-type reactor fuel and they investigated their thermal-hydraulic performances. As a result, it was observed that the coolant temperature increased and the fuel temperature decreased with the addition of nanofluidic water coolant. Therefore, the fuel melting temperature margin has increased and it has been stated that the safety and efficiency of the nuclear power plant will increase with the addition of annular-type fuel and nanofluid particles [4]. Işık and Tugan [5] investigated the thermal performance of nanofluids used in automobile radiators experimentally and numerically. They observed that the nanofluids convective heat transfer was higher than the base fluid and increases with volumetric flow rate and air velocity. Peyghambarzadeh et al. [6] studied experimentally forced convective heat transfer in Al_2O_3 nanofluidic water compared to that of pure water in an automobile radiator. They showed that the low concentration Al_2O_3 nanofluid can enhance heat transfer efficiency up to 45% in comparison with pure water. Ebrahimian et al. [7] studied the thermo-hydraulic effects of nanofluid particles on annular type dual cooled fuel geometry for VVER-1000 reactors. According to their results, they showed that the heat transfer coefficient of the external coolant (outside of the annular fuel) can be increased with the addition of nanofluid, which decreases with the use of annular-type fuel, and at the same time, MDNBR increases. Nejad et al. [8] proposed an annular fuel design for small modular reactors and investigated the effects of fuel internal diameter on power peaking factor and natural convection. According to the results, it has been observed that the use of annular fuel increases the neutron moderation and the excessive reactivity increases for this reason. Thus, it is predicted that the fuel can burn more in the core without changing the fuel.

In this study, the effect of three different nanoparticles for solid and annular fuel and the effect of fuel inner diameter for annular type fuel are investigated in terms of neutronics and thermalhydraulics. In thermalhydraulic point of view, fluid outlet temperature, maximum fuel temperature and maximum fuel surface temperatures are compared in terms of nanoparticle volume fraction and fuel inner diameter. The results have shown that annular-type fuel improves the thermalhydraulic performance and positively affects the safety margin. Also, the addition of nanoparticles for certain nanoparticle volume ratios also positively affects reactor heat transfer performance. In neutronic point of view, the effect of nanofluid volume fraction and fuel inner diameter is investigated by comparing the change in effective multiplication factor $\delta k/k$. In terms of neutronic calculations, the addition of nanoparticles and the increase of the fuel inner diameter reduce the k_{eff} value for all nanoparticle types.

2. MODELLING and METHOD

2.1. Neutronic Calculations

Neutronic calculations of nanofluids for solid cylindrical and annular type fuel PWR unit cell are performed using Monte Carlo method via

OPENMC [9] simulations. In this study, firstly, nanoparticles with a specified volume fraction are added to water both for solid and annular type geometry. While these additions are made, it is assumed that the fuel mass/volume and the moderator-to-fuel volume ratios are to be constant. Solid fuel and annular fuel neutronic performances are compared. Then, the effect of internal diameter in annular fuel is investigated for constant nanofluid volume fraction.

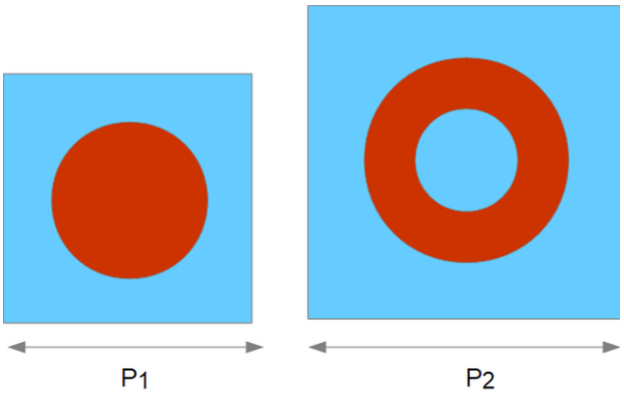

Figure 1 PWR unit cell for solid and annular fuel (not scaled)

Figure 1 shows a typical PWR unit cell for solid and annular fuel. Since the fuel mass and moderator-to-fuel volume ratios are fixed, the pitch length ($P_2 > P_1$) will increase slightly in annular type fuel. This means that the size of the annular type fueled reactor will be slightly larger than the solid cylindrical reactor.

The volume of pellet for a typical solid cylindirical fuel rod can be written as

$$V_{SF} = \pi R^2 H. \quad (1)$$

Here, R is the fuel pellet radius and H is the height of the solid fuel. Beside the fuel volume, the moderator-fuel volume ratio is also kept constant within the scope of this study. The main reason for this is to maintain the optimum moderator-fuel ratio which is specified for a typical PWR design.

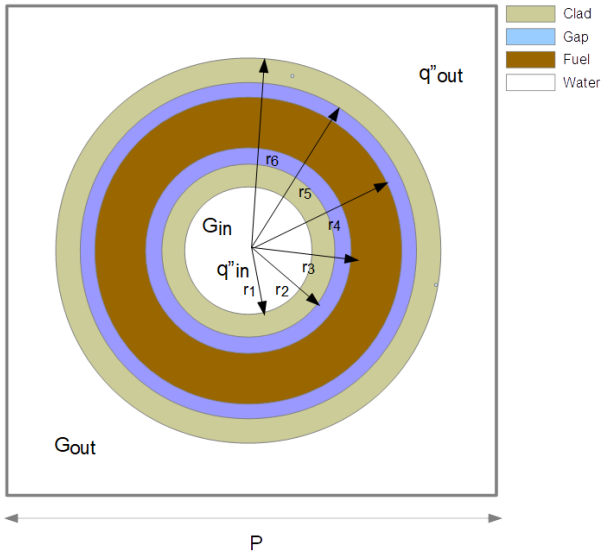

Figure 2 Schematical representation of annular fuel

As shown in Figure 2, when the thicknesses of the fuel clad (inner and outer clad for annular type fuel) and gap region are kept constant, the annular fuel pellet volume V_{AF} can be written as,

$$V_{AF} = \pi(r_4^2 - r_3^2)H \quad (2)$$

where $r_3 = r_1 + t_c + t_g$, $r_4 = r_3 + t_F$. Here, r_1: fuel rod inner radius, r_3: fuel pellet inner radius, r_4: fuel pellet outer radius, t_c: clad thickness, t_g: gap thickness, t_F: fuel thickness and r_6: fuel rod outer radius and $r_6 = r_4 + t_c + t_g$. For annular type fuel,

$$V_{AF} = \pi(r_4 - r_3)(r_4 + r_3)H \quad (3)$$

$$V_{SF} = V_{AF} = \pi(t_F)(r_3 + t_F + r_3)H \quad (4)$$

Therefore, the fuel thickness t_F can be evaluated as

$$t_F = \frac{-2r_3 \pm \sqrt{(2r_3)^2 + \frac{4V}{\pi H}}}{2}. \quad (5)$$

Thus, the moderator-fuel ratio is calculated as

$$\frac{V_M}{V_{AF}} = \frac{P^2 - \pi(r_6^2 - r_1^2)}{\pi(r_4^2 - r_3^2)}. \quad (6)$$

The unit cell parameters for annular type fuel can be obtained from Eqs. (3)-(6). The next step is to calculate the density of the mixture formed when

nanoparticles are added into water. The mixture density ρ_m [4-7] is determined by Eq.(7).

$$\rho_m = \rho_w \cdot (1-\varphi) + \rho_{np} \cdot \varphi \quad (7)$$

Here, ρ_w is the density of original water, ρ_{np} is the density of nanoparticles and φ is the volume fraction of nanoparticles in mixture. The unit cell OPENMC simulations are performed both for solid cylindrical and annular type cylindrical fuel geometries at different volume percentages ($0 < \varphi < 0.2$) of Al_2O_3, Cu and TiO_2 containing nanofluids. The fuel enrichment is selected as 3.57 w% and the periodic boundaries on lateral sides and vacuum boundaries on top and bottom sides of unit cell are implemented. ENDF/B.VIII.0 cross section data libraries are used for neutronic calculations and the k_{eff} values are obtained depending on the volumetric fractions of nanoparticles.

2.2. Thermal- Hydraulics Calculations

In this section, a typical PWR subchannel thermo-hydraulic parameters are analyzed analytically in order to evaluate the neutronic analysis together. As a reference, the results obtained for the PWR solid cylindrical fuel cell are compared with the annular type fuel cell.

If the average temperature in the direction of r, θ for each coolant point z is $T_m(z)$, one dimensional coolant temperature distribution can be obtained analytically. Also, if the heat transfer in the direction θ at any z point is neglected, the temperature distribution from the outer surface of the fuel clad to the center of the fuel can be calculated.

The heat diffusion equation at steady-state conditions can be written as

$$\nabla \cdot k(\vec{r},T)\nabla T(\vec{r},t) + q'''(\vec{r}) = 0. \quad (8)$$

Considering the thermal conductivity is constant for a cylindrical fuel rod, the diffusion equation becomes

$$\frac{d^2T}{dr^2} + \frac{1}{r}\frac{dT}{dr} + \frac{q'''}{k_f} = 0. \quad (9)$$

The solution of heat diffusion equation for a solid cylindirical fuel

$$T(r) = T_s + \frac{q'''}{4k_f}\left(R_f^2 - r^2\right) \quad (10)$$

and for an annular-fuel,

$$T(r) = T_i + \frac{q'''}{4k_f}\left(R_f^2 - r^2\right) + \left[\frac{(T_o - T_i) + \frac{q'''}{4k_f}\left(R_f^2 - r^2\right)}{ln\frac{r_4}{r_3}}\right]\left(ln\frac{r}{r_3}\right). \quad (11)$$

Here, T_i is clad outer temperature at the inner surface of the fuel and T_o is the clad outer temperature at the outer surface of the fuel. Heat fluxes for internal flow and external flow are calculated according to the point where the fuel temperature is maximum [10].

$$q''_{in} = \frac{Q_{in}}{A_{in}} = Q_{total} \times \frac{V_{in}}{V_{fuel}} \times \frac{1}{A_{in}} = Q_{total} \times \frac{1}{A_{in}} \times \frac{r_m^2 - r_3^2}{r_4^2 - r_3^2} \quad (12)$$

$$q''_{out} = \frac{Q_{out}}{A_{out}} = Q_{total} \times \frac{V_{in}}{V_{fuel}} \times \frac{1}{A_{out}} = Q_{total} \times \frac{1}{A_{out}} \times \frac{r_4^2 - r_m^2}{r_4^2 - r_3^2} \quad (13)$$

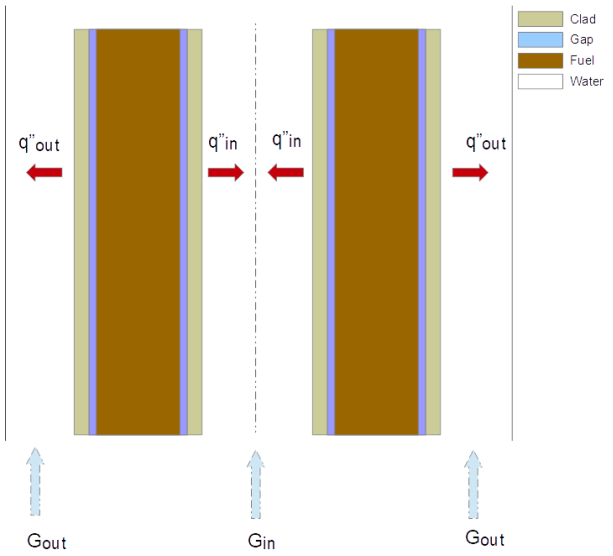

Figure 3 Axial view of annular fuel subchannel

As it is seen from Figure 3 and Eqs. (12)-(13), the heat fluxes transferred by the fuel to the inner and outer coolant may differ from each other. In order to calculate these heat fluxes, it is necessary to find the point r_m where the fuel temperature is maximum. The point r_m depends on the difference between the interior and exterior surface temperatures of annular fuel pellet. In this study, $T_o - T_i$ is assumed to be 5 ℃.

After calculating the fuel internal and external heat fluxes, the internal and external coolant temperature distributions are calculated. First of all, it is necessary to find the physical parameters (density, specific heat, viscosity and conductivity) of the relevant nanofluid. These parameters are calculated according to the volumetric fraction of nanoparticle (in this study, $0 < \varphi < 0.03$). Some of the thermophysical properties of base fluid water and three nanofluids are tabulated in Table 1. The calculation of density and specific heat of nanofluids is based on mixing theory. However, viscosity and conductivity calculations needs special attention. Viscosity is an important thermo-physical parameter especially for calculating core pressure drop and pumping power requirements. Several correlations for nanofluid viscosities are [11-14]. The thermal conductivity and the viscosity of resulting nanofluid are somewhat different from base fluid since Brownian motion effect of nanoparticles has to be taken into account. To do this, Jang and Choi model [15] for thermal conductivity of nanofluid is selected. The thermophysical properties of base fluid water and nanoparticles are given in Table 1.

Table 1
Thermophysical properties of water (at T=300 ºC) and nanoparticles (T=20 ºC)

Property	*Water*	*Al_2O_3*	*Cu*	*TiO_2*
$\boldsymbol{\rho\ (kg/m^3)}$	726.51	3970	8933	4260
$\boldsymbol{c_p(J/kgK)}$	5458.3	765	385	686.2
$\boldsymbol{k(W/mK)}$	0.5624	40	400	8.9538

Pak and Cho [12] suggested viscosity correlations for Al_2O_3+water and TiO_2+water as follows

$$\mu_{Al_2O_3} = \mu_w(533.9\varphi^2 + 39.11\varphi + 1) \qquad (14)$$

$$\mu_{TiO_2} = \mu_w(108.2\varphi^2 + 5.45\varphi + 1) \qquad (15)$$

Batchelor correlation [16] which recognizes the effect of Brownian motion is used for Cu+water nanofluid.

$$\mu_{Cu} = \mu_w(6.2\varphi^2 + 2.5\varphi + 0.1) \qquad (16)$$

Jang and Choi correlation [15] which includes Brownisn motion effect is used for all three nanofluids thermal conductivity calculation.

$$k_{nf} = k_{bf}(1-\varphi) + \beta k_p \varphi + C\frac{d_{bf}}{d_p} k_{bf} Re_p^2 Pr\varphi \qquad (17)$$

where constant related to Kapitza resistance $\beta = 0.01$, $C = 18 \times 10^6$, d_p is the diameter of nanoparticle, d_{bf} is the diameter of base fluid, Re_p is the Reynolds number of nanoparticle and defined as $Re_p = \frac{V_B d_p}{\nu}$ where $V_B = \frac{k_b T}{3\pi\mu_{bf} d_p l_{bf}}$ $k_b = 1.3807 \times 10^{-23}\ J/K$ is the Boltzmann constant, l_{bf} is the mean free path of base fuluid molecules. For water based nanofluids at $T = 27$ ℃, d_{bf} can be taken as 0.384 nm and l_{bf} can be taken as 0.738 nm.

The effective specific heat of nanofluids are calculated as [17]

$$c_{p,m} = \frac{\varphi(\rho c_p)_{np} + (1-\varphi)(\rho c_p)_w}{\rho_m} \quad (18)$$

Considering that the pressure drop due to friction will be equal for inner and outer channels,

$$\Delta P = \left(\frac{0{,}184}{Re^{0,2}}\right) \times \rho \times v^2 \times \frac{1}{2D_e}$$

Then,

$$G_{in} = \frac{\dot{m}}{\left(A_1 + A_2\left(\frac{D_{e,1}}{D_{e,2}}\right)^{0,67}\right)}$$

$$\dot{m}_1 = G_{in} \cdot A_1$$

Here, A_1 and A_2 are respectively the inner and outer flow areas, $D_{e,1}$ and $D_{e,2}$ are the equivalent diameters for the inner and outer flow. $\dot{m}$ is total subchannel coolant flow rate , $\dot{m}_1$ and $\dot{m}_2$ are the internal and external coolant flow rates respectively.

If the energy balance is written for the coolant flow in the channel,

$$q_1'(z) = q_{0,1}' \cdot \cos\left(\frac{\pi z}{L}\right)$$

$$q_2'(z) = q_{0,2}' \cdot \cos\left(\frac{\pi z}{L}\right)$$

$$\dot{m}_1 c_{p,1} \frac{dT_{m,1}}{dz} = q_1'(z)$$

$$\dot{m}_2 c_{p,2} \frac{dT_{m,2}}{dz} = q_2'(z)$$

Fuel inner and outer surface temperatures are calculated using Newton's law of cooling.

$$q_1''(z) = h_1[T_{s1}(z) - T_{m1}(z)]$$

$$q_2''(z) = h_2[T_{s2}(z) - T_{m2}(z)]$$

If thermal resistances are used for the fuel envelope and gap region, the fuel pellet inner and outer surface temperatures are calculated and the temperature distribution within the fuel pellet can be found for any axial location.

3. RESULTS and DISCUSSION

3.1. Neutronics (Solid Fuel)

Figure 4 shows the results of OPENMC simulations for solid cylindrical fuel geometry. It is seen that the k_{eff} value decreases with the increase in volumetric fraction of nanoparticles for three different nanofluids. The slope of the graph is minimum for Al_2O_3 added nanofluid, while it is maximum for Cu added nanofluid. This is because copper has a higher density than the other two nanoparticles and therefore absorbs more neutrons, since its macroscopic neutron absorption cross section is higher.

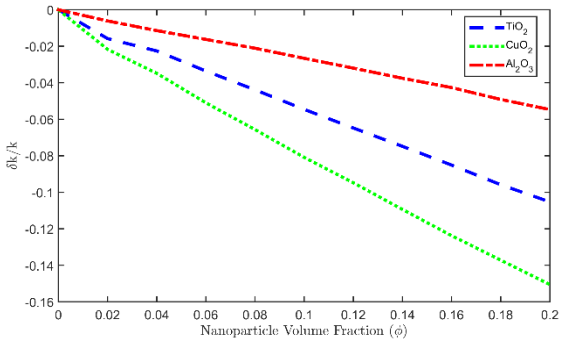

Figure 4 Solid fuel k_{eff} values for different nanoparticle fractions

3.2. Neutronics (Annular Fuel)

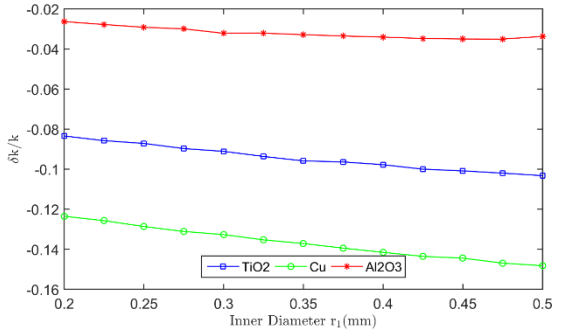

Figure 5 Change in effective multiplication factor $\delta k/k$ values of annular fuel for different inner diameters

Figure 5 shows the results of OPENMC simulations for annular-type cylindrical fuel geometry. Here, the effect of the change in fuel inner diameter on the k_{eff} value has been

investigated. For these simulations, the volumetric fraction φ is fixed at 0.1. For all three fluids, the increase in the inner diameter of the fuel causes a decrease in the k_{eff} value. For Al_2O_3 added nanofluid, the change in the fuel inner diameter has a minimum effect, while the maximum effect is seen for the Cu added nanofluid. This is because the fuel gets thinner as the inner radius increases, and the neutrons interact more within the nanofluid moderator until fission occurs. This can cause extra neutron absorption, and this is particularly evident for the copper-containing nanofluid.

3.3. Thermal-Hydraulics (Solid)

While all other parameters are constant, the effect of nanoparticle fraction for a solid fuel in a typical PWR subchannel is investigated. The nominal average linear heat rate of 17.86 kW/m is used. At the nominal PWR pressure, the addition of nanoparticles above a certain ratio causes boiling. Therefore, the volumetric percentage of nanoparticles is limited to 0.03.

Figure 6 shows fluid outlet temperature as a function of nanoparticle volume fraction ($0 < \varphi < 0.03$) for a typical PWR and for three different nanoparticle types. The fluid outlet temperatures increase with nanoparticle fraction since possible specific heat (c_p) reduction from the base water (has higher c_p than nanoparticles). Cu+water nanofluid has maximum slope, Al_2O_3+water and TiO_2+water shows similar behavior.

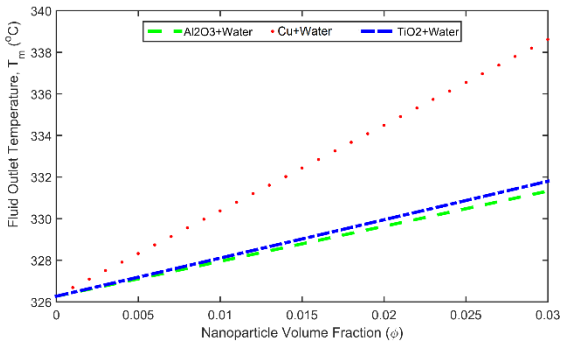

Figure 6 Fluid outlet temperature of subchannel for different nanoparticle fractions

Figure 7 shows fuel centerline temperature as a function of nanoparticle fraction for a typical PWR and for three different nanoparticle types. It is observed that the fuel centerline temperature decreases as the nanoparticle ratio increases up to $\varphi = 0.01 - 0.015$. A significant increase is observed after this range in Cu+water, while the decrease continues for Al_2O_3+water and TiO_2+water. Figures 6, 7 and 8 should be considered together for the discussion of Figure 7. In Figure 8, the heat transfer coefficients increase with the increase of nanoparticles, but the lowest increase is seen in Al_2O_3+water. At the same time, as mentioned earlier, the coolant temperature also increases as a result of nanoparticle increase in Figure 6. According to Newton's law of cooling, for the same heat flux and fuel conductivity values, the fuel surface temperature T_s and also fuel centerline temperature depends on the coolant temperature and heat transfer coefficient h. While the increase in the heat transfer coefficient is effective up to the $\varphi \cong 0.01$ point, the increase in the coolant temperature after this point causes the fuel surface temperature and thus the fuel centerline temperature to increase for Cu+water nanofluid. When TiO_2+water and Al_2O_3+water are compared, it can be said that the nanofluid with the best performance is TiO_2+water, since the improvement in the heat transfer coefficient of Al_2O_3+water is the least one.

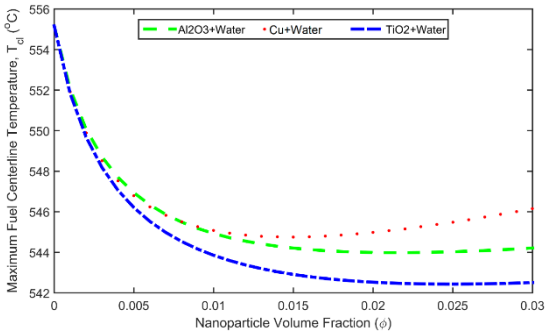

Figure 7 Fuel centerline temperature of solid fuel in PWR hot channel for different nanoparticle fractions

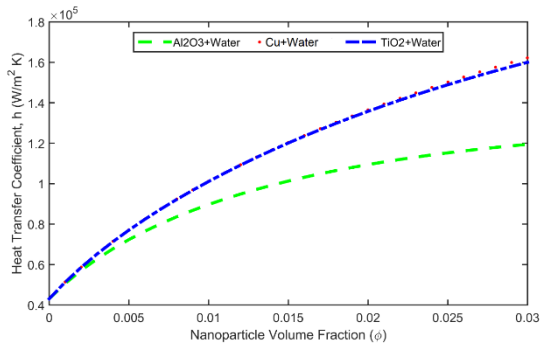

Figure 8 Heat transfer coefficient of subchannel

3.4. Thermal-Hydraulics (Annular)

3.4.1. Effect of Inner Diameter

The effect of inner diameter in case of an annular type fuel is investigated. Firstly, temperature dependencies of inner and outer fluid and inner and outer surface of fuel are evaluated in the absence of nanoparticles. The inner and outer fluid temperatures, inner and outer clad maximum temperatures, fuel maximum temperature and heat transfer coefficient of inner and outer fluid as a function of inner diameter are shown in Figs. 9-12.

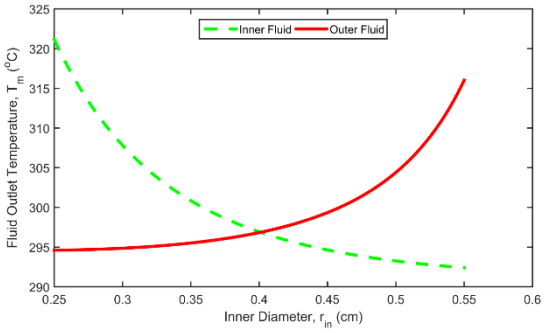

Figure 9 Fluid outlet temperature of inner and outer coolant as a function of inner diameter

As seen in Figure 9, as the fuel internal diameter increases, the internal flow temperature decreases while the external flow temperature increases. They become equal to each other approximately $r_{in} = 0.4$ cm.

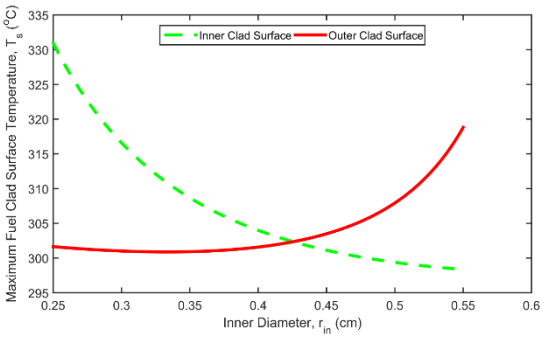

Figure 10 Maximum fuel clad temperature of inner and outer surface as a function of inner diameter

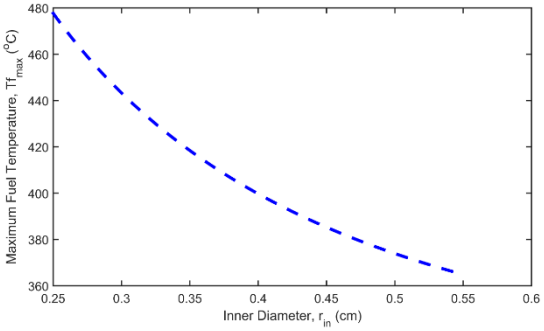

Figure 11 Maximum fuel temperature as a function of inner diameter

As demonstrated in Figure 11, as the inner radius increases, the fuel centerline temperature decreases, but the fuel outer clad temperature (Figure 10) increases rapidly after $r_{in} \cong 0.4 - 0.45\ cm$ range. This is due to the deterioration in the heat transfer coefficient is shown in Figure 12. Considering Figs. 9-12 together, $r_{in} \cong 0.4\ cm$ might be considered as an optimum option.

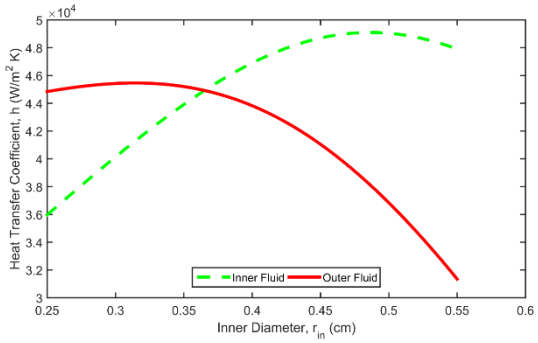

Figure 12 Heat transfer coefficient of inner and outer coolant as a function of inner diameter

3.4.2. Effect of Nanoparticle Fraction

In this part, the effect of nanoparticle volume fraction is investigated. The inner radius of fuel is fixed as $r_{in} = 0.4$ cm. The inner fluid outlet, outer fluid outlet, maximum inner and outer clad and maximum fuel tempertaures as a function of nanoparticle volume fraction are shown in Figs. 13-17.

The effect of nanoparticle volume fraction on selected fuel parameters are similar that of solid fuel case except the temperature values are lowered. Here, when all nanofluids are compared TiO_2+water can be considered as the best option in terms of safety.

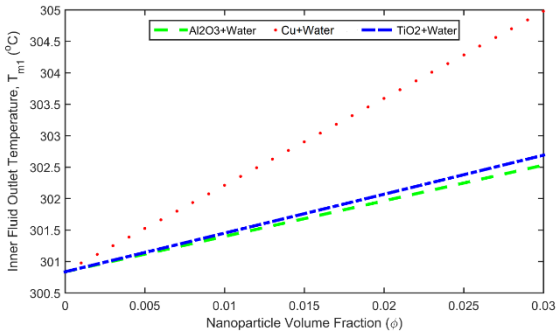

Figure 13 Fluid outlet temperature of inner coolant as a function of nanoparticle volume fraction

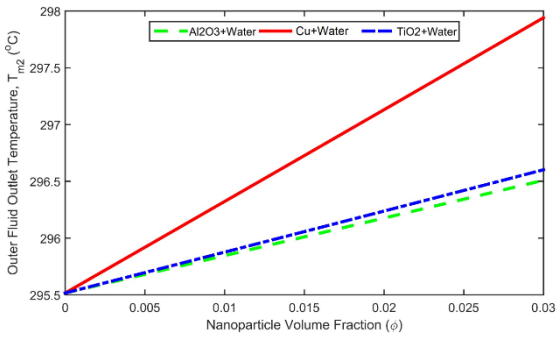

Figure 14 Fluid outlet temperature of outer coolant as a function of nanoparticle volume fraction

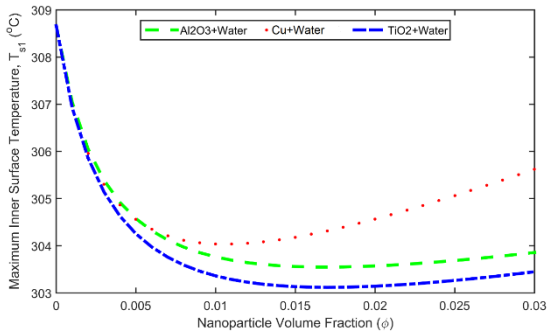

Figure 15 Maximum inner fuel clad temperature as a function of nanoparticle volume fraction

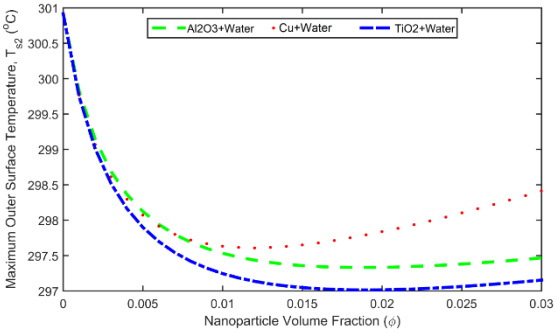

Figure 16 Maximum outer fuel clad temperature as a function of nanoparticle volume fraction

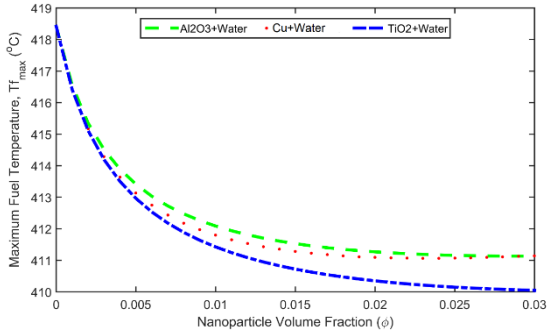

Figure 17 Maximum fuel temperature as a function of nanoparticle volume fraction

4. CONCLUSIONS

In pressurized nuclear reactors, one of the fuel design principles is the fuel centerline temperature limit. Since the thermal conductivity of UO_2 is not high, the temperature increases rapidly from the fuel surface to the fuel center. In order to overcome this, there have been studies such as the use of some metal alloys in new generation fuels. In addition to these studies, it is thought that this problem can be prevented with

annular fuels. In addition, it is envisaged to increase the thermal performance by adding nanoparticles to the coolant. The data obtained in this study show that, the addition of nanoparticles causes a decrease in the k_{eff} value. The minimum amount of decrease occurs in Al_2O_3+water and the maximum decrease occurs in Cu+water for solid fuel case. Therewithal, the effect of inner diameter on k_{eff} value of annular fuel is investigated for a fixed volume fraction of $\varphi = 0.1$. The results showed that the increase in inner fuel diameter causes decrease in k_{eff} value. The minimum decrease is seen in Al_2O_3+water nanofluid and the maximum is in Cu+water since the fuel gets thinner when the inner diameter increases and neutrons make more interactions while slowing down to thermal energies. This causes extra neutron absorptions within the copper containing nanofluid. It has also been observed that the addition of excess nanoparticles for PWR reactors leads to boiling. Additionally, the fuel centerline temperature begins to increase for $\varphi > 0.01$. In case of the change in inner diameter of annular fuel, the k_{eff} values are not significantly affected except Cu+water nanofluid. $r_{in} \cong 0.4$ cm could be considered as an optimum choice when the inner and outer coolant temperatures and the inner and outer clad temperatures are examined together. Finally, it has been shown that the annular fuel positively affects the fuel temperature limits and the addition of nanoparticles could provide an additional contribution to this, provided that it is in very small amounts ($\varphi < 0.01$). Among the three nanoparticles examined, Cu+water is found to be the least suitable both in terms of neutronics and termal considerations. TiO_2+water and Al_2O_3+water are comparable. It can be said that Al_2O_3 from the neutronic calculations and TiO_2 from the thermal point of view show the relatively best performance. This study could be improved in the future with fuel burnup and detailed computational fluid dynamics calculations. In addition, fuel material behavior analyzes should be performed for the fuel configuration that is found to be neutronically and thermally suitable.

Nomenclature and List of Abbreviations

φ	Volume fraction of nanofluid
k_{eff}	Effective multiplication factor
OPR1000	Optimized Power Reactor (1000 MWe)
VVER1000	Water-Water Energetic Reactor (1000 MWe)
MDNBR	Minimum Departure From Nucleate Boiling Ratio
PWR	Pressurized Water Reactor
$k(\vec{r},T)$	Space and temperature dependent thermal conductivity ($W/m \cdot K$)
$q'''(\vec{r})$	Space dependent volumetric heat generation rate (W/m^3)
μ_w	Dynamic viscosity of water
k_{bf}	Conductivity of base fluid ($W/m \cdot K$)
h_1	Heat transfer coefficient of inner nanofluid ($W/m^2 \cdot K$)
h_2	Heat transfer coefficient of outer nanofluid ($W/m^2 \cdot K$)

Funding

The author (s) has no received any financial support for the research, authorship or publication of this study.

The Declaration of Conflict of Interest/ Common Interest

No conflict of interest or common interest has been declared by the authors.

The Declaration of Ethics Committee Approval

This study does not require ethics committee permission or any special permission.

The Declaration of Research and Publication Ethics

The author of the paper declare that he complies with the scientific, ethical and quotation rules of SAUJS in all processes of the paper and that he does not make any falsification on the data collected. In addition, he declares that Sakarya University Journal of Science and its editorial board have no responsibility for any ethical violations that may be encountered, and that this study has not been evaluated in any academic publication environment other than Sakarya University Journal of Science.

REFERENCES

[1] N. Tak, Y. Kim, J. Choi, W. J. Lee "Thermo-fluid investigation on a double-side-cooled annular fuel for the prismatic very high temperature gas-cooled reactor," Nuclear Engineering and Design, vol. 238, pp. 2821–2827, 2008.

[2] C. Y. Lee, C. H. Shin, W. K. In "Pressure drop in dual-cooled annular and cylindrical solid fuel assemblies for pressurized water reactor," Nuclear Engineering and Design, vol. 250, pp. 287–293, 2012.

[3] C. Zhao, L. Cao, H. Wu, Y. Zheng, "Pre-conceptual core design of SCWR with annular fuel rods," Nuclear Engineering and Design, vol. 267, pp. 23–33, 2014.

[4] V. Ghazanfari, M. Talebi, J. Khorsandi, R. Abdolahi, "Thermal-hydraulic modeling of water/Al2O3 nanofluid as the coolant in annular fuels for a typical VVER-1000 core," Progress in Nuclear Energy, vol. 87, pp. 67–73, 2016.

[5] E. Isik, V. Tugan, "Experimental and numerical analysis of the thermal performance of nanofluids used in automobile radiators," Fresenius Environmental Bulletin, vol. 30, no. 9, pp. 10492-10504, 2021.

[6] S. M. Peyghambarzadeh, S. H. Hashemabadi, M. S. Jamnani, S. M. Hoseini, "Improving the cooling performance of automobile radiator with Al2O3/water nanofluid," Applied Thermal Engineering, vol. 31, pp. 1833-1838, 2011.

[7] M. Ebrahimian, G. R. Ansarifar, "Investigation of the nano fluid effects on heat transfer characteristics in nuclear reactors with dual cooled annular fuel using CFD (Computational Fluid Dynamics) modeling," Energy, vol. 98, pp. 1–14, 2016.

[8] M. Z. Nejad, G.R. Ansarifar, "Design of a Small Modular Nuclear Reactor with dual cooled annular fuel and investigation of the fuel inner radius effect on the power peaking factor and natural circulation parameters," Annals of Nuclear Energy, vol. 138, pp. 107185, 2020.

[9] P. K. Romano, N. E. Horelik, B. R. Herman, A. G. Nelson, B. Forget, K. Smith, "OpenMC: A State-of-the-Art Monte Carlo Code for Research and Development," Annals of Nuclear Energy, vol. 82, pp. 90–97, 2015.

[10] Y. S. Yang, C. H. Shin, T. H. Chun, K. W. Song, "Evaluation of a Dual-Cooled Annular Fuel Heat Split and Temperature Distribution," Journal of Nuclear Science and Technology, vol. 46, no. 8, pp. 836–845, 2009.

[11] X. Wang, X. Xu, S. U. S. Choi, "Thermal Conductivity of Nanoparticles Fluid Mixture," Journal of ThermoPhysic Heat Transfer, vol. 13, no. 4, pp. 474-80, 1999.

[12] B. C. Pak, Y. I. Cho, "Hydrodynamic and Heat Transfer Study of Dispersed Fluids with Submicron Metallic Oxide Particle," Experimental Heat Transfer, vol. 11, no. 2, pp. 151–170, 1998.

[13] H. Chen, Y. Ding, Y. He, C. Tan "Rheological Behaviour of Ethylene Glycol Based Titania Nanofluids," Chemical

Physics Letters, vol. 444, no. 4, pp. 333–337, 2007.

[14] P. D. Kukarni, K. D. Das, A. G. Chukwu, "Temperature Dependent Rheological Property of Copper Oxide Nanoparticle Suspension (Nanofluid)," Journal of Nanoscience and Nanotechnology, vol. 6, no. 4, pp. 1150–1154, 2006.

[15] S. P. Jang, S. U. S. Choi, "Effects of various parameters on nanofluid thermal conductivity," Journal of Heat Transfer, vol. 129, pp. 617-623, 2007.

[16] G. Batchelor, "The effect of Brownian motion on the bulk stress in a suspension of spherical particles," Journal of Fluid Mechanics, vol. 83, pp. 97–117, 1977.

[17] K. Khanafer, K. Vafai, "A critical synthesis of thermophysical characteristics of nanofluids," International Journal of Heat and Mass Transfer, vol. 54, pp. 4410–4428, 2011.

SAKARYA ÜNİVERSİTESİ
FEN BİLİMLERİ ENSTİTÜSÜ DERGİSİ

Sakarya University Journal of Science
SAUJS

ISSN 1301-4048 | e-ISSN 2147-835X | Period Bimonthly | Founded: 1997 | Publisher Sakarya University | http://www.saujs.sakarya.edu.tr/

Title: Energy Levels and Radiative Lifetimes for Four Times Ionized Xenon (Xe V)

Authors: Selda ESER

Recieved: 2022-01-12 00:00:00

Accepted: 2022-05-19 00:00:00

Article Type: Research Article

Volume: 26
Issue: 4
Month: August
Year: 2022
Pages: 655-665

How to cite
Selda ESER; (2022), Energy Levels and Radiative Lifetimes for Four Times Ionized Xenon (Xe V). Sakarya University Journal of Science, 26(4), 655-665, DOI: 10.16984/saufenbilder.1056924
Access link
http://www.saujs.sakarya.edu.tr/en/pub/issue/72361/1056924

Sakarya University Journal of Science 26(4), 655-665, 2022

Energy Levels and Radiative Lifetimes for Four Times Ionized Xenon (Xe V)

Selda ESER*[1]

Abstract

By employing the general-purpose relativistic atomic structure package (GRASP) based on fully relativistic multiconfiguration Dirac-Fock (MCDF) method, energies and radiative lifetimes of levels have been reported for four times ionized xenon (Xe V). In calculations, the Breit interactions for relativistic effects, quantum electrodynamical (QED) contributions have been included as a perturbation, as well as electron correlation effects (VV, CV and CC). We have compared the results obtained in this work with experimental and theoretical values in available literature for Xe V. We have obtained good agreement with previous works.

Keywords: Energy levels, correlation effects, relativistic effects, radiative lifetimes

1. INTRODUCTION

There is quite a lot of interest in rare gases because of their applications in collision physics, fusion diagnostics, photo-elect^{2}ron spectroscopy, astrophysics, and laser physics [1]. Especially for the understanding of the mechanisms involved in the multi-ionic xenon laser action, obtained spectroscopic data from xenon ions are needed in these areas [2]. Four times ionized xenon (Z=54), which belongs to the Sn I isoelectronic sequence, has $5s^25p^2$ electron ground configuration. The ground level of this ion is $5p^2\ ^3P_0$, and this level is followed by $^3P_1$, $^3P_2$, $^1D_2$ and $^1S_0$ in the same configuration. Saloman compiled the energy levels and observed spectral lines of the xenon atom, in all stages of ionization [3]. Reyna Almandos et al. presented an overview of studies concerning the spectral analysis of several ions for noble gases [4]. Calculated lifetimes for 12 new energy levels belonging to the $5s^25p6d$ and $5s^25p7s$ configurations and weighted oscillator strengths and transition probabilities for 81 new classified lines were presented by Raineri et al. [2]. Dzuba and Flambaum calculated the energy levels and Landé *g* factors for neutral xenon and all its positive ions from Xe II to Xe VIII [5]. The energies, lifetimes and transition probabilities were calculated with the pseudorelativistic Hartree-Fock (HFR) approach for Xe V by Biémont et al. [6]. Sobral et al. reported laser gain analyses for several lines by using level parameters (lifetimes and radiative transition rates) obtained from HFR method [7]. Tauheed et al. analyzed some energy levels and $5s^25p^2$-$(5s5p^3+5s^25p5d+5s^25p6s)$ transitions of four-times ionized xenon [8]. Using MCHF method Pinnington and co-workers calculated energy levels, lifetimes and some transition parameters for Xe V [9]. Larsson et al. obtained the

* Corresponding author: skabakci@sakarya.edu.tr
[1] Sakarya University
ORCID: https://orcid.org/0000-0002-1863-2976

wavelengths and energy levels of Xe V and Xe VI by collision-based spectroscopy [10]. For zirconium and xenon and their some ion lines in the ultraviolet (UV) spectra, oscillator strengths were reported by Rauch et al [11]. The spectrum of four times ionized xenon, were observed in the 500-6800 Å range and 84 new lines were identified as transitions between levels of $5s5p^3$, $5s^25p5d$, $5s^25p6s$, $5s^25p^2$, and $5s^25p6p$ configurations by Gallardo et al [12, 13].

The aim of this work is to calculate the level energies and lifetimes in four times ionized xenon, using the general-purpose relativistic atomic structure package (GRASP) [14] based on a fully relativistic multiconfiguration Dirac-Fock (MCDF) method [15]. This code includes Breit interactions (magnetic interaction between the electrons and retardation effects of the electron-electron interaction) for relativistic effects and quantum electrodynamical (QED) contributions (self-energy and vacuum polarization) beside the electron correlation effects (valence-valence (VV), core-valence (CV) and core-core (CC)). These contributions are important in investigations include electronic structure and spectroscopic properties of many electron systems. We have performed a series of calculations according to configuration sets including excitations from valence and core (valence, core-valence and core-core correlation) for considering correlation effects. We have reported the configuration sets, which have been here taken into account, in Table 1 below.

Table 1
Configuration sets taken in calculations for Xe V

VV	$5s^25p^2$, $5s^25p5d$, $5s^25p6s$, $5s^25p4f$, $5s^25p6p$
CV	VV+($5s5p^3$, $5s5p7s^2$, $5s5p6d^2$, $5s5p7p^2$, $5s^25p7s$, $5s^25p6d$, $5s^25p7p$)
CC	$5s^25p^2$, $5p^4$, $5s^25p4f$, $5p^25d^2$, $5s^25p6p$, $5s^25p7p$, $5s5p^3$, $5s^25p5d$, $5s^25p6s$, $5s5p7s^2$, $5s5p6d^2$, $5s^25p6d$, $5s5p7p^2$, $5s^25p7s$

The spectral analysis of rare -gas atoms have been carried out in our groups for many years. More detailed information is available on the ref. [16].

2. CALCULATION PROCEDURE

The calculations were performed by using the general-purpose relativistic atomic structure package, GRASP code [14], which is based on a multiconfiguration Dirac-Fock (MCDF) method, although we used MCHF code in our previous studies. The both method includes correlation effects. But fully relativistic MCDF method is based on the Dirac-Coulomb Hamiltonian and MCHF method is based on the non-relativistic Hamiltonian. So, obtained results are better in MCDF method than the MCHF method. MCDF code considers the Thomas-Fermi and Coulomb potential for calculate wavefunctions according to JJ and LS couplings. In the MCDF method [15], an atomic state can be expanded as a linear combination of configuration state functions and is optimized usually on the basis of the many-electron Dirac-Coulomb Hamiltonian

$$\Psi_a(PJM) = \sum_{r=1}^{n_c} C_r(\alpha)\left|\gamma_r(PJM)\right\rangle \qquad (1)$$

where n_c is the number of CSFs included in the evaluation of atomic state functions and C_r is the mixing coefficient, optimized usually on the basis of the many-electron Dirac-Coulomb Hamiltonian. The CSFs are the sum of products of single-electron Dirac spinors,

$$\phi(r,\theta,\varphi,\sigma) = \frac{1}{r}\begin{pmatrix} P(r)\chi_{\kappa m}(\theta,\varphi,\sigma) \\ iQ(r)\chi_{-\kappa m}(\theta,\varphi,\sigma) \end{pmatrix} \qquad (2)$$

where κ is a quantum number and $\chi_{\kappa m}$ is the spinor spherical harmonic in the LSJ coupling scheme. The *P(r)* and *Q(r)* are large and small radial components of one-electron wavefunctions represented on a logarithmic grid. The energy functional is based on the Dirac-Coulomb Hamiltonian,[3]

$$H_{DC} = \sum_{j=1}^{N}[C\boldsymbol{\alpha_j}.\boldsymbol{p_j}) + (\beta_j - 1)c^2 + V(r_j)] + \sum_{j<k}^{N}\frac{1}{r_{jk}} \qquad (3)$$

where $V\left(r_j\right)$ is the electron-nucleon interaction. Once initial and final state functions have been

calculated, the radiative matrix element for radiative properties computation can be obtained from

$$O_{if} = \langle \psi(i) | \boldsymbol{O}_q^{\pi(k)} | \psi(f) \rangle \quad (4)$$

where $\boldsymbol{O}_q^{\pi(k)}$ is a spherical operator of rank k and parity π, and $\pi(k)$ is $\pi = (-1)^k$, for an electric multipole transition or $\pi = (-1)^{k+1}$, for a magnetic multipole transition. The largest transition probability is for electric dipole (E1) radiation, dominated by the least factor $1/\alpha^2$ over other types of transitions (E2, M1, M2, etc.).

The lifetime, $\tau_{\gamma' J'}$, of upper level $\gamma' J'$ is

$$\tau_{\gamma' J'} = \frac{1}{\sum_{\pi k, \gamma J} A^{\pi k}(\gamma' J', \gamma J)}. \quad (5)$$

In calculations we have used the option *extended average level* (EAL) averaging of the expression energy. It is extended to configuration states with not only different total angular momentum but also with different parity. Also, Breit corrections (magnetic interaction between the electrons and retardation effects of the electron-electron interaction), and QED (self-energy and vacuum polarization), and various correlation contributions have been considered. Due to the Coulomb interaction between the electrons, the electron correlation effects are also important, in particular, for fine structure and transitions. Therefore, the configurations including excitations from valence and core have been taken into account in calculations. QED contributions are self-energy and vacuum polarization, which are also included in the computations of the transition energy. The finite-nucleus effect is taken into account by assuming an extended Fermi distribution for the nucleus. Both the Breit and QED contributions are treated as perturbation and are not included directly in the SCF procedure. The mixing coefficients are calculated by diagonalizing the modified Hamiltonian.

The used package program had been written by the other authors and we have compiled this code in our computations.

3. RESULTS

In this work, we have determined the excitation energies and radiative lifetimes for Xe V by employing the MCDF method [15]. Breit interactions for relativistic effects and QED contributions have been included in this method. Due to the Coulomb interaction between the electrons, the electron correlation effects are also important. Therefore, we have considered the various correlation effects and configuration sets including electron excitations from the valence 5p to other high sub-shell (VV) and electron excitation(s) from 5s subshell to other high subshells (CV and CC). We have taken into account three configuration sets, which have been given in Table 1 in details, represented by VV, CV and CC. When the excitation is made from the core, the number of configuration state functions (CSF) is increased. We have obtained 43, 215 and 331 energy levels for VV, CV and CC computation, respectively. In Table 2, only 65 energy levels and their radiative lifetimes have been sorted, for Xe V. In generally, VV and CV calculation results are close to each other. But the results have improved when calculations have been made with the CC configuration set. We think that these levels can be improved by considering more the configurations excited from the core. For this reason, the effects of Breit effects and QED contributions have been examined for the levels obtained from CC calculations. Breit and QED contributions have been shown to have an effect in reducing to MCDF energies in generally. We have compared our energy level results both theoretical values and experimental values [2-6, 9-13, 16] in Table 2. When the differences (%) in percent between our results and other results are investigated, the differences are generally in range of 0.01- 15.75. In addition, the obtained results from this work have been compared with other previous works in Fig. 1. Linear correlation coefficient R^2 is 0.9995 for MCDF results. It is seen that both differences in percent and Fig.1, there is good agreement between our results and others. The excellent agreement between obtained data in this work and the other works is a strong evidence for reliability of MCDF calculations. Also, the radiative lifetimes have good agreement with comparison values in generally. The results obtained from this

work using MCDF method can be useful for describing the spectra of four times ionized xenon.

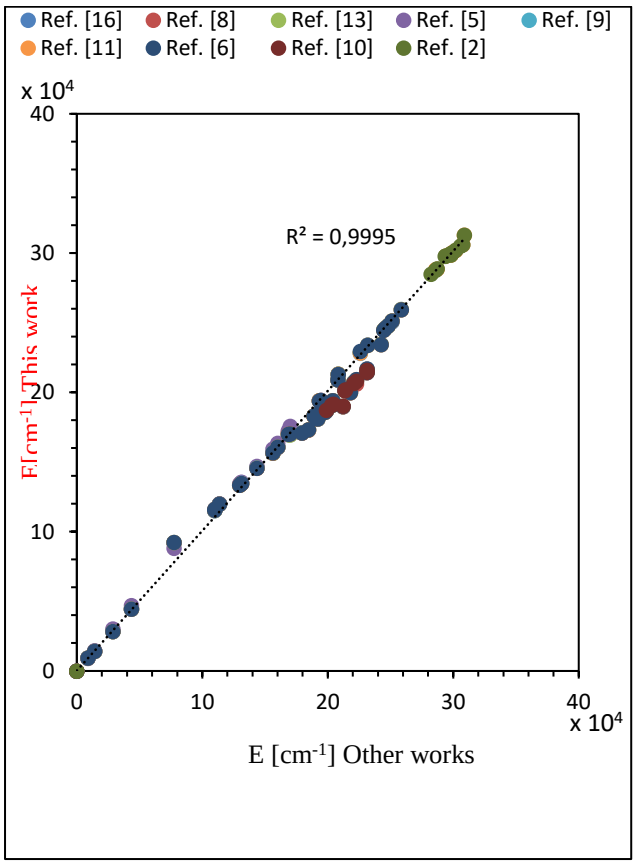

Figure 1 A comparison of energy levels obtained from MCDF calculation with other works.

Table 2
Excitation energies, E [cm^{-1}], and radiative lifetimes, τ [ns], for Xe V. $E^T = E^0 + E^1 + E^2$ (E^T: Total energies, E^0: MCDF energies, E^1: Breit contributions, E^2: QED contributions).

Level	Term	E^0			E_{CC}^1	E_{CC}^2	E_{CC}^T	Eow	τ	τow
		VV	CV	CC						
$5s^25p^2$	$^3P_0$	0.0	0.0	0.0	0.0	0.0	0.0	0.0	-	-
$5s^25p^2$	$^3P_1$	8727.2	8614.4	9028.4	-169.0	7.49	8866.5	9291.8[a] 9286.3[b] 9300.8[c] 8969.0[d] 9320.0[e] 9290.0[f] 9289[g]	-	-
$5s^25p^2$	$^3P_2$	14203.5	14041.4	14387.3	-211.0	8.76	14184.9	14126.7[a] 14102.5[b] 14150.2[c] 14643.0[d] 14150.0[e] 14142.0[f] 14146[g]	-	-
$5s^25p^2$	$^1D_2$	29416.2	29100.7	29130.6	-355.0	13.9	28789.4	28411.2[a] 28398.6[b] 28387.8[c] 30169.0[d] 28440.0[e] 28402.0[f] 28401[g]	-	-
$5s^25p^2$	$^1S_0$	50556.3	50103.3	44104.9	-372.0	8.8	43741.6	44470.4[a] 44470.7[b] 44476.1[c] 47061.0[d] 44580.0[e] 44471.0[f] 44471[g]	-	-
$5s5p^3$	$^5S°_2$	-	75851.0	77955.5	-181.0	-110.0	77664.8	92182.8[a] 92158.7[b] 92202.7[c] 88033.0[d] 92210.0[e] 92194.0[f] 92194[g]	89.023	34.7[e] 19.3[e] 37.16[g] 39.19[g] 45.55[g] 54.31[g]
$5s5p^3$	$^3D°_1$	-	108629.4	110186.0	-181.0	-94.7	109909.9	115286.3[a] 115298.5[b] 115276.0[c] 115554.0[d] 115300.0[e] 115441.0[f] 115434[g]	3.293	1.87[e] 0.97[e] 1.81[g] 1.97[g] 2.00[g] 2.57[g]
$5s5p^3$	$^3D°_2$	-	109006.8	110569.8	-197.0	-94.6	110278.6	116097.0[a] 116172.7[b] 116021.0[c] 116202.0[d] 116140.0[e] 116138.0[f] 116130[g]	4.473	4.53[e] 1.47[e] 3.01[g] 2.99[g] 3.23[g] 3.91[g]
$5s5p^3$	$^3D°_3$	-	112670.4	114238.6	-282.0	-91.9	113864.7	119919.0[a] 119902.5[b] 119931.7[c] 120152.0[d] 119940.0[e] 119913.0[f] 119906[g]	8.091	6.56[e] 1.82[e] 3.49[g] 3.80[g] 3.77[g] 5.02[g]

Table 2 Continue

$5s5p^3$	$^3P°_0$	-	128907.0	130281.9	-270.0	-93.0	129919.0	133408.1[a]	0.717	1.38[g]
								133417.1[b]		1.03[g]
								133406.5[c]		1.46[g]
								134320.0[d]		1.31[g]
								133488.0[f]		
								133481[g]		
$5s5p^3$	$^3P°_1$	-	130086.7	131486.7	-307.0	-90.7	131088.8	134575.2[a]	0.726	0.94[g]
								134616.9[b]		0.81[g]
								134536.5[c]		1.02[g]
								135493.0[d]		1.01[g]
								134507.0[f]		
								134506[g]		
$5s5p^3$	$^3P°_2$	-	130215.4	131696.6	-330.0	-79.4	131286.8	134702.7[a]	1.331	1.55[e]
								134654.7[b]		0.65[e]
								134737.0[c]		1.29[g]
								135579.0[d]		1.28[g]
								134710.0[e]		1.41[g]
								134496.0[f]		1.69[g]
								134525[g]		
$5s5p^3$	$^1D°_2$	-	196070.2	144204.9	-454.0	-40.4	143710.3	145807.0[a]	0.033	1.83[e]
								145633.8[b]		0.86[e]
								145976.2[c]		2.03[g]
								147030.0[d]		1.71[g]
								145820.0[e]		2.10[g]
								145525.0[f]		2.28[g]
								145577[g]		
$5s5p^3$	$^3S°_1$	-	182893.2	179014.4	-378.0	-34.5	178601.7	155518.1[a]	0.037	0.115[e]
								155498.4[b]		0.049[e]
								155545.3[c]		0.080[g]
								160672.0[d]		0.078[g]
								155545.0[e]		0.092[g]
								155393.0[f]		
								155402[g]		
$5s^25p(^2P°)5d$	$^3F°_2$	152500.1	154600.1	156947.7	-456.0	1.5	156493.0	156506.8[a]	1.823	1.28[e]
								156550.7[b]		0.68[e]
								156462.7[c]		0.78[h]
								159419.0[d]		1.12[g]
								156540.0[e]		1.04[g]
								156303.0[f]		1.16[g]
								156525[g]		1.21[g]
$5s^25p(^2P°)5d$	$^3F°_3$	159084.5	158297.9	160783.7	-511.0	8.3	160280.8	160630.4[a]	1.202	1.14±0.1[e]
								160642.4[b]		0.69[e]
								160663.5[c]		0.71[h]
								163534.0[d]		0.95[g]
								160660.0[e]		0.96[g]
								160677.0[f]		1.03[g]
								160679[g]		
$5s^25p(^2P°)5d$	$^3F°_4$	168248.5	166921.4	169311.4	-671.0	14.5	168655.3	169799.4[a]	0.000	-
								171311.0[b]		
								169759.2[c]		
								172418.0[d]		
								170055.0[f]		
								170013[g]		
$5s5p^3$	$^1P°_1$	-	169041.8	170435.7	-226.0	-88.4	170120.8	169672.6[a]	0.063	0.07[h]
								169918.3[b]		0.082[g]
								169435.1[c]		0.089[g]
								175704.0[d]		0.104[g]
								170261.0[f]		0.099[g]
								170155[g]		
$5s^25p(^2P°)5d$	$^3P°_2$	174693.5	176915.5	180078.1	-420.0	-13.9	179643.7	170987.6[a]	0.039	0.080[e]
								170941.6[b]		0.043[e]
								171018.9[c]		0.04[h]
								171010.0[e]		0.066[g]
								170919.0[f]		0.065[g]
								170938[g]		0.072[g]
										0.073[g]

Table 2 Continue

$5s^25p(^2P°)5d$	$^3P°_0$	181390.5	186326.4	189568.2	-582.0	2.1	188988.4	183025.2[a] 182986.5[b] 183059.3[c] 182962.0[f] 182980[g]	0.033	0.04[h] 0.062[g] 0.059[g] 0.066[g] 0.064[g]
$5s^25p(^2P°)5d$	$^3P°_1$	182059.8	176150.1	191829.8	-583.0	0.2	191247.1	184147.6[a] 184148.9[b] 184139.3[c] 184255.0[e] 184100.0[f] 184111[g]	0.032	0.087[e] 0.042[e] 0.04[h] 0. 057[g] 0.063[g]
$5s^25p(^2P°)5d$	$^3D°_1$	170959.0	-	185109.7	-437.0	-51.0	184621.3	173071.7[a] 172879.3[b] 173220.1[c] 173063.0[f] 173086[g]	0.036	0.06[h] 0.050[g] 0.053[g] 0.060[g]
$5s^25p(^2P°)5d$	$^3D°_2$	182807.2	189325.4	192640.4	-575.0	-7.9	192057.2	181004.3[a] 180967.9[b] 181050.6[c] 181000.0[e] 181097.0[f] 181084[g]	0.030	0.072[e] 0.034[e] 0.05[h] 0.045[g] 0.051[g] 0.054[g] 0.057[g]
$5s^25p(^2P°)5d$	$^3D°_3$	181680.4	188146.4	191716.9	-587.0	-1.0	191129.1	182167.2[a] 182385.9[b] 181959.0[c] 182165.0[e] 182145.0[f] 182142[g]	3.066	0.071[e] 0.035[e] 0.04[h] 0.048[g] 0.050[g] 0.055[g]
$5s^25p(^2P°)5d$	$^1D°_2$	163261.1	142494.1	198633.1	-500.0	-43.7	198089.3	185795.0[a] 185821.4[b] 185803.9[c] 185800.0[e] 185780.0[f] 185766[g]	2.588	0.083[e] 0.046[e] 0.05[h] 0.059[g] 0.063[g] 0.068[g] 0.070[g]
$5s^25p(^2P°)4f$	$^3G_3$	194244.0	196911.5	199563.8	-452.0	6.2	199117.8	186746.7[a] 186745[b] 186752.3[c] 187089.0[i] 186635.0[f] 186647[g]	2.812	9.9[h]
$5s^25p(^2P°)4f$	$^3G_4$	198414.1	201086.8	203730.0	-524.0	7.0	203213.4	190644.7[a] 190643.0[b] 190712.6[c] 190955.0[i] 190745.0[f] 190719[g]	3.275	-
$5s^25p(^2P°)4f$	$^3G_5$	209909.8	212488.5	215048.1	-722.0	14.5	214340.3	202281.8[a] 203796.0[b] 202517.7[c] 201913.0[i] 202341.0[f] 202311[g]	3.410	-
$5s^25p(^2P°)4f$	$^3F_3$	197438.4	200120.8	212911.5	-660.0	14.1	212265.8	189663.8[a] 189662.0[b] 189876.0[c] 190154.0[i] 189859.0[f] 189841[g]	2.791	9.7[h]
$5s^25p(^2P°)4f$	$^3F_4$	209262.9	211901.6	214490.9	-699.0	14.4	213805.9	201545.2[a] 201554.0[b] 201559.1[c] 201176.0[i] 201629.0[f] 201628[g]	2.975	12.0[h]

Table 2 Continue

$5s^25p(^2P°)4f$	$^3F_2$	199724.8	202448.3	205104.0	-483.0	7.6	204628.3	191603.5[a] 191604.0[b] 191268.2[c] 191545.0[i] 191400.0[f] 191436[g]	2.680	8.8[h]
$5s^25p(^2P°)6s$	$^3P°_0$	193572.3	191186.1	193847.7	-470.0	22.4	193399.7	194033.1[a] 194060.1[b] 194065.0[c] 194105.0[f] 193957[g]	0.620	0.170[g] 0.179[g] 0.158[g]
$5s^25p(^2P°)6s$	$^3P°_1$	193840.3	192410.0	195099.5	-487.0	16.3	194628.8	194232.9[a] 194208.2[b] 194182.5[c] 194190.0[f] 194349	0.152	0.103[g] 0.106[g] 0.101[g]
$5s^25p(^2P°)6s$	$^3P°_2$	208907.7	206010.9	208816.5	-686.0	32.9	208163.9	209068.9[a] 209067.7[b] 209045.5[c] 209100.0[e] 209078.0[f] 209120[g]	0.164	0.163[e] 0.123[e] 0.124[g] 0.121[g] 0.122[g] 0.114[g]
$5s^25p(^2P°)5d$	$^1F°_3$	204496.4	200732.4	204739.8	-662.0	12.2	204090.1	194138.0[a] 194091.8[b] 194190.1[c] 194170.0[e] 194159.0[f] 194156[g]	0.030	0.068[e] 0.033[e] 0.04[h] 0.047[g] 0.046[g] 0.051[g] 0.050[g]
$5s^25p(^2P°)5d$	$^1P°_1$	201407.9	215665.3	218760.4	-607.0	-5.6	218148.1	199959.0[a] 199893.4[b] 200018.4[c] 199730.0[f] 199765[g]	0.036	0.07[h] 0.064[g] 0.075[g] 0.076[g] 0.081[g]
$5s^25p(^2P°)4f$	$^3D_3$	214383.3	217097.4	219662.4	-683.0	13.4	218993.3	205758.8[a] 205762.0[b] 205913.2[c] 205185.0[i] 205942.0[f] 246023[g]	2.645	9.2[h]
$5s^25p(^2P°)4f$	$^3D_2$	216327.2	219045.8	221604.4	-648.0	13.7	220969.6	207366.7[a] 207204.4[c] 206391.0[i] 207261.0[f] 207283[g]	2.498	8.6[h]
$5s^25p(^2P°)4f$	$^3D_1$	218362.7	221018.2	223594.2	-651.0	14.2	222957.5	209310.7[a] 206145.0[b] 209139.1[c] 208139.0[i] 209194.0[f] 209213[g]	2.254	8.3[h]
$5s^25p(^2P°)6s$	$^1P°_1$	214446.1	206113.9	209163.7	-647.0	11.9	208528.4	213040.2[a] 213045.9[b] 213058.2[c] 213135.0[e] 213053.0[f] 213000[g]	0.051	0.097[e] 0.062[e] 0.052[g] 0.057[g] 0.053[g] 0.055[g]
$5s^25p(^2P°)4f$	$^1G_4$	226507.9	229549.8	232078.3	-658.0	13.3	231433.4	214317.7[a] 214323.0[b] 214683.1[c] 214505.0[i] 214380.0[f] 214336[g]	11.831	38.3[h]

Table 2 Continue

$5s^25p(^2P°)4f$	$^1D_2$	227951.6	232327.5	231960.6	-596.0	9.8	231374.3	216745.6[a] 216483.3[c] 215850.0[i] 216701.0[f] 216737[g]	1.047	8.2[h]
$5s^25p(^2P°)6p$	$^3D_1$	226803.1	223517.1	226572.4	-457.0	5.2	226120.6	228064.9[a] 228484.3[c] 228416.0[f] 229428[g]	0.536	-
$5s^25p(^2P°)6p$	$^3D_3$	247274.5	243652.5	246739.3	-722.0	15.0	246032.1	246208.0[a] 246101.9[c] 245966.0[f] 246023[g]	0.445	-
$5s^25p(^2P°)6p$	$^3P_0$	232900.3	229532.7	232308.3	-430.0	4.9	231883.3	233999.3[a] 233755.0[c] 233744.0[f] 233773[g]	0.591	-
$5s^25p(^2P°)6p$	$^3P_1$	233369.5	240312.2	243234.0	-665.0	13.4	242582.4	234455.6[a] 234452.7[c] 234336[f] 234337[g]	0.549	-
$5s^25p(^2P°)6p$	$^3P_2$	245975.3	242575.9	245374.3	-651.0	12.3	244735.1	244821.3[a] 244805.1[c] 244637[f] 244676[g]	0.563	-
$5s^25p(^2P°)6p$	$^3S_1$	249437.6	245749.5	248823.4	-704.0	14.3	248133.8	247810.4[a] 247814.9[c] 247929[f] 247857[g]	0.516	-
$5s^25p(^2P°)6p$	$^1D_2$	252906.1	249435.5	251903.2	-655.0	-0.0	251248.1	250557.2[a] 251227.1[c] 251379[f] 251293[g]	0.546	-
$5s^25p(^2P°)6p$	$^1S_0$	261612.8	256768.9	259320.7	-683.0	9.2	258647.3	259642.3[a] 259642.3[c] 259444[f] 259452[g]	0.628	-
$5s^25p(^2P°)6d$	$^3F°_2$	-	280367.9	282984.7	-514.0	5.4	282476.3	284871[j]	0.364	0.48[j] 0.41[j*]
$5s^25p(^2P°)6d$	$^3P°_2$	-	283811.1	286205.6	-526.0	5.0	285684.8	287391[j] 287420[f]	0.177	0.29[j] 0.23[j*]
$5s^25p(^2P°)6d$	$^3F°_3$	-	283951.0	286516.5	-543.0	6.0	285979.6	287696[j] 288003[f]	0.230	0.53[j] 0.27[j*]
$5s^25p(^2P°)6d$	$^3D°_1$	-	285489.0	287838.8	-501.0	5.3	287343.5	288830[j] 288586[f]	0.118	0.28[j] 0.16[j*]
$5s^25p(^2P°)7s$	$^3P°_0$	-	291068.3	294086.3	-519.0	9.8	293577.5	297673[j]	0.137	0.16[j] 0.19[j*]
$5s^25p(^2P°)7s$	$^3P°_1$	-	291649.6	294668.6	-518.0	9.9	294160.1	298053[j] 298054[f]	0.117	0.15[j] 0.18[j*]
$5s^25p(^2P°)6d$	$^3F°_4$	-	296411.1	299093.3	-764.0	14.3	298343.4	298739[j] 298717[f]	0.542	0.65[j] 0.55[j*]
$5s^25p(^2P°)6d$	$^1D°_2$	-	296386.4	298794.1	-733.0	13.3	298074.9	299596[j] 299417[f]	0.184	0.34[j] 0.21[j*]
$5s^25p(^2P°)6d$	$^3D°_3$	-	297797.4	300183.8	-735.0	13.6	299462.1	300327[j] 300484[f]	0.160	0.28[j] 0.21[j*]
$5s^25p(^2P°)6d$	$^3P°_1$	-	299854.5	302231.6	-723.0	13.6	301522.5	301555[j] 301796[f]	0.161	0.31[j] 0.21[j*]
$5s^25p(^2P°)6d$	$^3P°_0$	-	300325.5	302744.4	-724.0	13.8	302034.3	301998[j] 301794[f]	0.187	0.38[j] 0.25[j*]
$5s^25p(^2P°)6d$	$^1P°_1$	-	305939.1	308411.4	-717.0	13.5	307707.8	306065[j] 306081[f]	0.152	0.35[j] 0.21[j*]
$5s^25p(^2P°)7s$	$^3P°_2$	-	306634.2	309629.5	-744.0	18.4	308904.1	312956[j] 312959[f]	0.161	0.18[j] 0.23[j*]
$5s^25p(^2P°)7s$	$^1P°_1$	-	308382.8	311354.8	-733.0	17.6	310.639	313883[j] 313880[f]	0.086	0.14[j] 0.15[j*]

[a]: Ref. [17], [b]: Ref. [8], [c]: Ref. [13], [d]: Ref. [5], [e]: Ref. [9], [f]: Ref. [11], [g]: Ref. [6], [h]: Ref. [4], [i]: Ref. [10], [j, j*]: Ref. [2]

4. CONCLUSION

The main purpose of this paper is to obtain energy levels and radiative lifetimes for four times ionized xenon (Xe V). I have compared my results in available literature. In this work, the values reported for energy levels and radiative lifetimes can be useful to investigations for these parameters. We hope that these results will be useful for theoretical and experimental works on Xe V spectra in the future.

Funding

The authors have no received any financial support for the research, authorship or publication of this study.

The Declaration of Ethics Committee Approval

This study does not require ethics committee permission or any special permission.

The Declaration of Research and Publication Ethics

During the writing process of our study, the information of which is given above, international scientific, ethical and citation rules have been followed, no falsification has been made on the data collected, and Sakarya University Journal of Science and its editorial board have no responsibility for any ethical violations that may be encountered. I undertake that I have full responsibility and that this study has not been evaluated in any academic environment other than Sakarya University Journal of Science.

REFERENCES

[1] J. Reyna Almandos, M. Raineri, "Spectral analysis of moderately charged rare-gas atoms,'' Atoms, vol. 5, no. 1, pp. 5010012, 2017.

[2] M. Raineri, M. Gallardo, S. Padilla, J. Reyna Almandos, "New energy levels, lifetimes and transition probabilities in four times ionized xenon (Xe V),'' Journal of Physics B Atomic Molecular and Optical Physics, vol. 42, no. 20, pp. 205004, 2009.

[3] E.B. Saloman "Energy Levels and Observed Spectral Lines of Xenon, XeI through Xe LIV," Journal of Physical and Chemical Reference Data, vol. 33, no. 3, pp. 765-921, 2004.

[4] J. Reyna Almandos, F. Bredice, M. Raineri, M. Gallardo, "Spectral analysis of ionized noble gases and implications for astronomy and laser studies,'' Physica Scripta, vol. 2009, no. T134, pp. 014018, 2009.

[5] V. A. Dzuba, V. V. Flambaum, "Core-valence correlations for atoms with open shells,'' Physical Review A, vol. 75, pp. 052504, 2007.

[6] E. Biémont, P. Quinet, C. J. Zeippen, "Transition probabilities in Xe V,'' Physica Scripta, vol. 71, pp. 163-169, 2005.

[7] H. Sobral, M. Raineri, D. Schinca, M. Gallardo, R. Duchowicz, "Excitation mechanisms and characterization of a multi-ionic xenon laser,'' IEEE Journal of Quantum Electronics, vol. 35, no. 9, pp. 1308-1313, 1999.

[8] A. Tauheed, Y. N. Joshi, V. Kaufman, J. Sugar, E. H. Pinnington, "Analysis of the $5s^25p^2$–($5s5p^3$ + $5s^25p5d$ + $5s^25p6s$) transitions of four-times ionized xenon (Xe V),'' Journal of the Optical Society of America B, vol. 10, no. 4, pp. 561-565, 1993.

[9] E. H. Pinnington, R. N. Gosselin, Q. Ji, J. A. Kernahan, B. Guo, A. Tauheed, "A study of the beam-foil spectrum of Xe V,'' Physica Scripta, vol. 46, pp. 40-44, 1992.

[10] M. O. Larsson, A. M. Gonzalez, R. Hallin, F. Heijkenskjöld, B. Nyström,G. O'Sullivan, C. Weber, A. Wännström, "Wavelengths and energy levels of Xe V and Xe VI obtained by collision-based spectroscopy,'' Physica Scripta, vol. 53, no. 3, pp. 317-324, 1996.

[11] T. Rauch, S. Gamrath, P. Quinet, L. Löbling, D. Hoyer, K. Werner, J. W. Kruk, M. Demleitner, "New Zr IV–VII, Xe IV–V, and Xe VII oscillator strengths and the Al, Zr, and Xe abundances in the hot white dwarfs G191-B2B and RE 0503-289,'' Astronomy and Astrophysics, vol. 599, pp. A142, 2017.

[12] M. Gallardo, M. Raineri, J. G. Reyna Almandos, "Analysis of the 5p6p configuration of Xe V,'' Zeitschrift für Physik D Atoms, Molecules and Clusters, vol. 30, pp. 261-264, 1994.

[13] M. Gallardo, M. Raineri, J. G. Reyna Almandos, H. Sobral, F. Callegari, "Revısed and extended analysıs ın four tımes ıonızed xenon Xe V,'' Journal of Quantitative Spectroscopy and Radiative Transfer, vol. 61, no. 3, pp. 319-327, 1999.

[14] K. G. Dyall, I. P. Grant, C. T. Johnson, F. A. Parpia, E. P. Plummer, "GRASP: A general-purpose relativistic atomic structure program,'' Computer. Physics Communications, vol. 55, no. 3, pp. 425-456, 1989.

[15] I. P. Grant, Relativistic Quantum Theory of Atoms and Molecules, first edition, Springer, Verlag New York, 2007.

[16] S. Eser, L. Özdemir, "Energies and Lifetimes of Levels for Doubly Ionized Xenon and Radon,'' Acta Physica Polonica A, vol. 133(5), pp. 1324- 1332, 2018.

[17] A. Kramida, Yu Ralchenko, J. Reader, NIST ASD Team (2018). *NIST Atomic Spectra Database* (ver. 5.6.1), [Online]. Available: https://physics.nist.gov/asd [2018, November 22]. National Institute of Standards and Technology, Gaithersburg, MD.

SAKARYA ÜNİVERSİTESİ
FEN BİLİMLERİ ENSTİTÜSÜ DERGİSİ

Sakarya University Journal of Science
SAUJS

ISSN 1301-4048 | e-ISSN 2147-835X | Period Bimonthly | Founded: 1997 | Publisher Sakarya University | http://www.saujs.sakarya.edu.tr/

Title: Modeling and Analysis of Battery Thermal Control in a Geostationary Satellite

Authors: Murat BULUT, Nedim SÖZBİR

Recieved: 2021-02-07 00:00:00

Accepted: 2022-05-26 00:00:00

Article Type: Research Article

Volume: 26
Issue: 4
Month: August
Year: 2022
Pages: 666-676

How to cite
Murat BULUT, Nedim SÖZBİR; (2022), Modeling and Analysis of Battery Thermal Control in a Geostationary Satellite. Sakarya University Journal of Science, 26(4), 666-676, DOI: 10.16984/saufenbilder.1069404
Access link
http://www.saujs.sakarya.edu.tr/en/pub/issue/72361/1069404

Sakarya University Journal of Science 26(4), 666-676, 2022

Modeling and Analysis of Battery Thermal Control in a Geostationary Satellite

Murat BULUT*[1], Nedim SÖZBİR[2]

Abstract

Battery technology has been used for satellites since the first satellite sputnik-1 was launched in 1957. The majority of larger satellite's (geostationary or communication satellites) lives range from 7 to 15 years. During the lifetime of satellites, the batteries used must complete 1000 to 33000 cycles without any problems or likelihood of maintenance. There are three battery technologies, Li-ion, Ni-H_2 and Ni-Cd, that are well proven for Geostationary satellite applications. Energy density, lifetime, weight, ampere-hour capacity, depth of discharge, ruggedness and recharge-ability, battery management, thermal management, and self-discharge are main parameters that should be considered when comparing electrical and thermal performance of these three battery technologies. The purpose of this study is to compare the thermal control system for these three batteries for three-axis stabilized geostationary satellites. In particular, the thermal dissipation was compared, which is the temperature range required for battery operation. Thermal analysis was performed for Li-ion batteries using ThermXL software, and showed a temperature results variation ranging between 10.9 ^{o}C and 32.7 ^{o}C. The temperature during the battery module was not greater that its qualification temperature results.

Keywords: Battery, geostationary satellite, thermal control, Li-ion, Ni-H_2, Ni-Cd

1. INTRODUCTION

For the majority of satellites, whether for military, observation, scientific, communication or other purposes, in low Earth Orbit (LEO), Medium Earth Orbit (MEO), or Geostationary Orbit (GEO), continuous power and its supply is a matter of careful consideration [1].

GEO satellites are made up of several subsystems including the payload subsystem, telemetre and command subsystem, the propulsion subsystem, the structure and mechanical subsystem, the thermal control subsystem, the altitude orbit control subsystem (AOCS), and the power subsystem (EPS).

* Corresponding author: bulut44@gmail.com
[1] Türksat A.Ş.
ORCID: https://orcid.org/0000-0002-9024-7722
[2] Düzce University, Merkez, Düzce, 81620, Türkiye
E-mail: nedimsozbir@duzce.edu.tr
ORCID: https://orcid.org/0000-0003-4633-2521

The power subsystem comprises all components that deliver power. Energy is essential for supplying satellite load demand at all phases of each operation. Solar arrays and batteries are two devices that provide energy to satellites. When there is sunlight, solar arrays provide power as a primary power source. On the other hand, during an eclipse period, power is provided by batteries as a secondary power source. Normally a satellite in GEO orbit experiences two 45-day cycles per year of eclipses that last more than 72 min per day, resulting in 90 sequences of charging and discharging annually. For satellites in orbit for 15 years, this amounts to 90 eclipses per year and 1350 eclipses for 15 years.

The electrical power system (EPS) has the biggest mass ratio for spacecraft dry mass, approximately 30%, and the mass of batteries is the main contributor having about a 40% ratio of EPS mass [2, 3]. Therefore, it is critical to select an appropriate battery type and configuration.

Batteries convert chemical energy within its active material directly into electric energy via an electrochemical oxidation-reduction (redox) reaction [4], which is then stored energy in electrochemical form. Primary and rechargeable are the two main types of batteries. For primary batteries, the electrochemical reaction is irreversible; therefore, it cannot be used again after being fully discharged, and is therefore thrown away after use. Primary batteries are used for small periods of time during operations as the principal power source. For rechargeable batteries, the electrochemical reaction is reversible, meaning recharging can occur with direct current from an external location. Rechargeable batteries are utilized in longer operations in which a secondary source of power is accessible for recharging the battery. Rechargeable batteries have been used for satellite applications since early in the space age. Nickel cadmium (Ni-Cd), nickel hydrogen (Ni-H_2), and lithium-ion (Li-ion) are commonly used secondary batteries for spacecraft.

Although battery technology is a widely studied subject with a large corpus of published work [1, 3-30], there is a persistent lack of established literature on thermal control systems for batteries. In their paper [3-30], a study on batteries technologies from nanosatellite to deep-space exploration missions was presented. Bulut et al. [31] studied thermal design and thermal analysis of a Turkish satellite. Thermal analysis was performed using ESATAN software. The satellite performed within a temperature range between 0 and 40 ^{o}C. Bulut et al. [32] discussed electrical and thermal properties and performance comparison of li-Ion, NiH_2 and NiCD batteries for geostationary satellite applications. They presented a thermal analysis of Li-ion batteries, and they found that the temperatures varied within the qualification temperatures. Sundu and Döner [33] studied the detailed thermal design and control of an observation satellite in low earth orbit and included a battery thermal analysis. They concluded that the design temperature of the battery was achieved by utilizing a thermistor to control the heaters automatically [34]. Boushan [35] studied thermal modeling of Li-ion battery boxes using Thermal Desktop 6.0, with SINDA/FLUINT 5.8 for MR SAT, and included five model revisions. Both steady state and transient analyses were performed. For steady state analysis of model revision D, the temperatures were 4.32 ^{o}C for the hot case and -21.47 ^{o}C for the cold case. For transient analysis of model revision D, the temperatures were 7.35 ^{o}C for the hot case and -24.58 ^{o}C for the cold case. For transient analysis of model revision E, the temperatures were 42.87 ^{o}C for the hot case and 5.42 ^{o}C for the cold case. The modeling and design of the passive thermal control system for the European Student Orbiter (ESEO) satellite was also studied [36, 37]. Thermal analysis was performed using Thermal Desktop (TD) software. Temperature results obtained from the simulation were presented and compared with ESEO published results using ESATAN software. The battery temperatures were between 5.3 ^{o}C and 10.3 ^{o}C for the operative phase. Bailing et al. [38] studied influence analysis of Li-ion battery configuration outside the east/west panel on GEO satellite platform. Thermal analysis results showed that the new configuration of Li-ion battery has more advantages compared to its configuration inside the north/south panel. The heating power and heat rejection area was decreased by 70%. Ya et al. [39] studied thermal

behavior of Li-ion battery for the large power synthetic aperture radar (SAR) satellites. The charge and discharge process were tested. The temperature rise during 2C, 3C and 5C discharge process under the adiabatic state increased to 18 ^{o}C, 21.7 ^{o}C and 33 ^{o}C, respectively.

Batteries are designed and qualified to withstand extreme temperature ranges, high vibration/shock levels, high specific energy, very high reliability, etc. Because the cost often limits satellite and space programs, it is essential to decrease the weight and size of rechargeable batteries to gain the largest return on investment.

Batteries need to be designed to support all equipment power loads from beginning of life (BOL) to end of life (EOL). This paper provides a summary of the thermal control system (TCS) for batteries in three-axis stabilized GEO satellites. This paper also discusses the thermal design and the results of a thermal analysis for the batteries using ThermXL software.

2. SATELLITE BATTERY TECHNOLOGY EVALUATION

There is a wide range of battery systems available for spacecraft applications. Ni-Cd was the first satellite battery that was produced in the 1960s. It was the most common battery until the mid-1980s. Unfortunately, series problems such as degradation of the electrodes and hydrolysis of the separator limited the lifetime and performance of Ni-Cd batteries [5]. The Ni-Cd battery consists of a cadmium negative electrode, a nickel positive electrode, an aqueous 35 % potassium hydroxide (KOH) electrolyte, and a nylon cloth separator [6]. During discharge, the cadmium negative electrode provides electrons to the external circuit during the oxidizing phase [31], after which these electrons are accepted by the nickel positive electrode. The 35 percent potassium hydroxide (KOH) electrolyte completes the circuit internally [32], which is held in place by a nylon cloth that separates the positive and negative plates [32].

Ni-H_2 technology batteries, a successor to Ni-Cd, came into use in the 1980s. These batteries are hybrid battery-fuel cell devices. The battery has a positive electrode like a standard battery and a fuel cell negative electrode [37]. Ni-H_2 batteries have a rechargeable electrochemical power source formed from nickel and hydrogen. Even though hydrogen exits as either a liquid or gas, nickel is considered a ferrite [37]. Hydrogen gas is diffused onto a catalyst, usually platinum, at the negative electrode where the reaction occurs [37]. High pressure vessels are required to contain the gas [37]. For an electrolyte, Ni-H_2 cells use 26% potassium hydroxide (KOH). Ni-H_2 rechargeable batteries have notable electrical attributes making them a good candidate for storing electrical energy in satellites.

The earliest on-orbit use of Li-ion battery technology was by the European Space Agency (ESA) funded PROBA-1 LEO technology development satellite launched in October, 2001 [7]. Li-ion batteries provide high energy density and are therefore very attractive candidates as secondary energy sources for telecommunication satellites. After seeing the success of the Li-ion battery technology, many are hopeful that it has potential to accept a large number of cycles with future and further development of rechargeable Li-ion technology using it on future missions [6].

Li-ion batteries have exclusive properties that markedly affect charge/discharge cycles. Over charging or discharging Li-ion cells will cause irreversible damage, which is different from Ni-Cd and Ni-H_2 cells [40]. Therefore, Li-ion batteries are sensitive to overcharge and over-discharge conditions. Figure 1 shows mass and volume comparison of Li-ion against heritage battery technologies [8]. Values given are for a 10 kWh battery with a maximum DoD of 75% and shows that a Li-ion battery would cause a noteworthy decrease in mass and volume versus Ni-Cd and Ni-H_2 technologies [41].

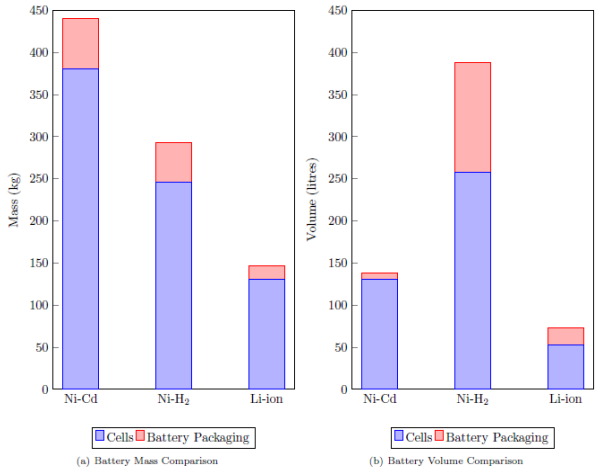

Figure 1 Mass and volume comparison of battery technologies [8].

Li-ion batteries will likely become more commonly used within the satellite structure because they have both a high energy density and working voltage as compared to Ni-Cd and Ni-H2 batteries. In addition, Li-ion energy densities are approximately 125 Wh/kg, about two times the densities of Ni-Cd and Ni-H2 batteries. As the weight and low heat dissipation become a key driving parameter for satellites, Li-ion is the likely technology of choice to meet this criterion.

3. ELECTRICAL PERFORMANCE COMPARISON OF BATTERIES

Comparison of Li-ion, Ni-H_2, and Ni-Cd is shown in Table 1. Useful energy density, battery management complexity, thermal management, self-discharge, and flight heritage are chosen in order to compare the batteries. Table 1 shows that the Li-ion battery has less hazardous problems and higher energy density versus the Ni-Cd or Ni-H_2 technology batteries. In addition, a greater amount of available energy can be used by Li-ion batteries, because they can accept deep discharge [6]. Li-ion provides considerable wider operating temperature ranges than either Ni-Cd or Ni-H_2 batteries.

The high specific energy contained in the Li-ion battery system gives it an advantage over the other batteries because of the added weight reduction. In fact, the specific energy of Li-ion is greater than 125 Wh/kg, much higher that of the Ni-H_2, which can achieve no higher than 60 Wh/kg. The higher specific energy achieved by the Li-ion results in at least a 40 percent battery weight reduction, and more than 350 kg weight reduction (a factor of 2) on a 20 kW satellite is anticipated.

The Li-ion battery can discharge itself at a rate of 0.03% of capacity loss per day, which is quite low compared with the Ni-H2 system, which is 10%. Managing the state of charge (SOC) for a Li-ion battery on a satellite during the integration, launch pad and solstice phases is not as difficult compared with Ni-H2 because recharge is given to the battery until the final countdown.

Table 2 Comparison of batteries [1, 13].

	Ni-Cd	**Ni-H_2**	**Li-ion**
Energy Density (Wh/kg)	25	60	125
Battery Management	Is tolerant to overcharge mechanism	Is tolerant to overcharge mechanism	No overcharge allowed: rigid constraints on charge management, dedicated balancing electronics, bypass and protection are required
	Reconditioning needed	Reconditioning needed	No reconditioning
Thermal Management (oC)	0 to 25	0 to 20 . Need to be cold charged for food charge efficiency	0 to 40. Optimum condition 20
	at lower temperatures and at high temperatures degraded	High heat generation in discharge	Between 3 and 4 times less dissipations in discharge
Self discharge	High self discharge according to nominal capacity	High self discharge	Low discharge
			AIT operations simplified
Flight Heritage	Many tests/in flight data available	Many tests/in flight data available	Many tests/in flight data available

Furthermore, Li-ion does not have a memory effect which influences battery cycling performance. On the other hand, Ni-Cd and Ni-H_2 systems do have a memory affect. If the battery has been repeatedly discharges slightly (10-20%) and then recharged again, it will gradually

developed a memory effect and lose some of its capacity after a period of time [9].

The Li-ion system is also advantageous because there is a direct relationship between SOC and the open-circuit voltage (OCV). The SOC of Li-ion batteries is always known during missions because the voltage can indicate an absolute energy gauge. On the other hand, for Ni-H_2 batteries, strain gauges on the pressure vessel are employed, and show just a rough estimate of SOC.

4. THERMAL PERFORMANCE COMPARISON OF BATTERIES

Studying battery performance based on experimental work is costly and not available for designers during preliminary design phases [9]. Mathematical modelling and simulation help the designer to study and analyze the performance of the battery stack during the design phases [35].

Three different types of batteries, Ni-Cd, Ni-H_2, and Li-ion, are normally used on satellites. There is a slight difference between thermal control requirements and thermal design [42-44].

Battery thermal control is critical because it the largest sources of heat dissipation and the smallest allowable temperature range of the operation. Temperature significantly impacts the performance of batteries and also limits the application of batteries. The capacity and voltage characteristics of a battery is largely controlled by the temperature at which the battery is charged and discharged [10], because chemical activity decreases and internal resistance increases at lower temperatures. The ideal temperature depends on the specific chemistry and design of every battery and can be custom designed [10].

Ni-Cd batteries are utilized in older spacecraft power systems. The life of these batteries is maximized when the temperature of the batteries is maintained between 0 and 10 ^oC. The maximum beneficial life decreases markedly as the battery temperature rises above this range, and also, when the temperature falls below this range, because the electrolyte can freeze, damaging the battery [11]. One of the important thermal control requirements is to keep all the batteries on the spacecraft and cells within the same temperature range, above or below a specific value (for example, +/- 5 ^oC), ensuring that all cells charge and discharge simultaneously [11].

Li-ion batteries are best operated at room temperature around, 20-25 ^oC, and suffers degradation at low temperature. Battery thermal control would be more manageable if the temperature range of operation for Li-ion batteries was wider than for Ni-Cd and Ni-H_2 (typically -5 to +25 ^oC) [11]. An example photograph of a Li-ion battery assembly is shown in Fig. 2.

Figure 2 Photography of battery assembly [40]

Compared with the Ni-H_2 battery, the Li-ion is at an advantage because there is 5-10 % weight savings with its lower thermal dissipation and higher Faradic efficiency. These features impact the solar panel and radiator sizes. The Li-ion also needs less radiator area according to thermal dissipation which is shown in Fig. 3.

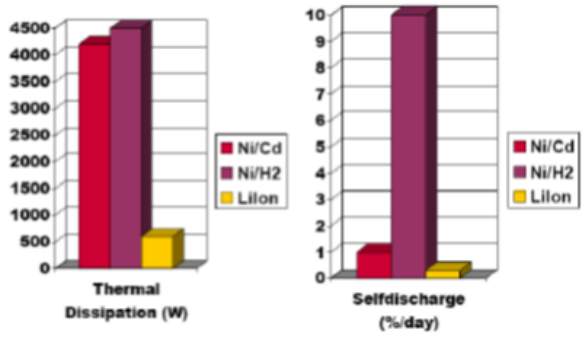

Figure 3 Thermal dissipation and self-discharge comparison of batteries (for 8kW satellite) [12, 13].

5. BATTERY THERMAL DESIGN CONCEPT

The overall cost, the thermal behavior including heat dissipation and optimal temperature ranges, and the weight and dimensions of a satellite, are the main drivers which are considered at the beginning of a satellite project.

The key part of battery design is ensuring that all cells are at similar temperatures. Consequently, designing thermal control of batteries is critical on spacecraft because of the narrow working temperature ranges of batteries. Therefore, most spacecraft manufacturers design thermal control of batteries individually. Figure 4 shows the location of the batteries on a three-axis stabilized GEO satellite. The location of the batteries is on the North and South service. Figure 5 shows the battery location on a GEO satellite.

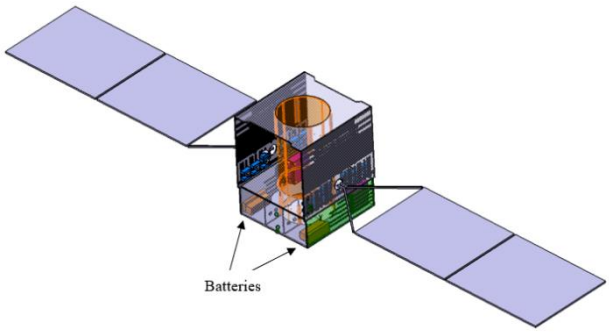

Figure 4 Location of the batteries at three-axis stabilized GEO satellite

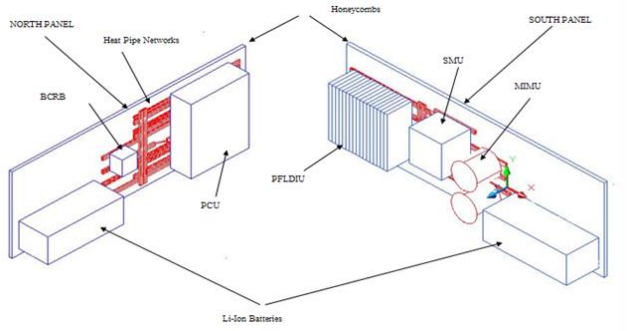

Figure 5 Schematic of the battery location [13].

Figure 6 shows the thermal design concept in which batteries' thermal status is self-contained because they are thermally insulated from the interior of the satellite. For thermal design, there is a multi-layer insulation (MLI) blanket cover, that keeps the batteries from being exposed to the interior of the satellite, and optical solar reflector (OSR) radiators located on a honeycomb panel containing heat pipes that radiate heat away from the batteries [45]. Heat dissipation also affects radiative areas. The size of the radiator is constructed to ensure the battery temperature is no more than the maximum allowable temperature for worst hot-case scenarios while controlled heaters are utilized to sustain lowest allowable temperatures for cold-case scenarios.

A thermal inter-filler provides good and removable thermal contact for the radiator. RTV 566 and CV-2942 are widely used between the batteries and honeycomb panel. MLI is used to decouple batteries from the internal thermal environment of the satellite. To control the temperature range, OSR radiators are installed under batteries [31]. To maintain batteries at lowest possible temperatures, nominal and redundant heaters are used [46].

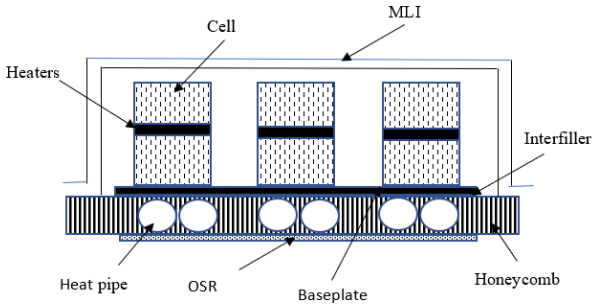

Figure 6 Battery thermal design concept

6. THERMAL MODELLING AND ANALYSIS

To extend the cycle and life of batteries and ensure safe use, heat dissipation during charge, discharge and self-discharge of batteries is an important part of the satellite system [14]. Many components of a satellite will only work within a specific temperature range. The thermal satellite design has three components: identifying the heat sources, designing appropriate heat transfer among all satellite components, and emitting heat to ensure all constituents operate within operating temperature ranges [47, 48].

Each component of the satellite is affected by external heat fluxes which are influenced by the position of the satellite in orbit, satellite attitude in its current position, relative positions of the sun and earth (equinox (EQ), winter solstice (WS), summer solstice (SS)), eclipse time, and satellite geometry [11].

By knowing the external heat fluxes and the dissipation of the elements, the temperature distribution variations can be calculated as a function of thermal couplings, area, solar absorptivity, and emissivity. These parameters can then be controlled, and various groups of parameters can be used to create the optimum temperature for a given dissipation.

The energy equation is used for calculating temperature distribution and is made up of transient, conduction, and radiation terms and a source term that defines the boundary conditions (solar, albedo, earth radiation), and is given as [49-52]

$$M_i C_{pi} \frac{dT_i}{dt} = Q_{in} - Q_{out} \quad (1)$$

where M_i is mass, C_{pi} is specific heat, dT_i/d_t is the temperature derivative with respect to time, and Q_{in} is the sum of all heat flows into the element. Electronic equipment is represented by the node i and the heat generated in the equipment after it is switched on is represented by the thermal load Q_i. The thermal radiation absorbed by an external panel from an external source is also Q_i and is the sum of the following: $Q_{Sun} + Q_{albedo} + Q_{EarthIR}$. Q_{out} is the sum of all heat flows leaving the component and the subscript i is used as an index of the element number.

$$\left(MC_{pi}\right)\frac{dT_i}{dt} = Q_i + \sum_{j=1}^{N} C_{ji}\left(T_j - T_i\right) + \sum_{j=1}^{N} R_{ji}(T_j^4 - T_i^4)\,, \quad i = 1 \ldots . N \quad (2)$$

The conductive couplings C_{ji} are calculated with knowledge of the unidirectional fluxes, while T_i and T_j are the temperatures of nodes i and j, respectively. The radiative couplings R_{ji} are determined using the Gebhart method [53].

The battery is investigated by running a mathematical model that determines radiator area and heater use. The battery thermal analyses are performed based on the most extreme condition which is obtained by a combination of cell dissipation (cell failure, discharge/charge, and shunt), solar illumination (seasons and solar array heat fluxes), thermo-optical properties (BOL and EOL), and external environment (webs/reflectors).

Table 2 shows an example of optical properties and thermophysical properties of the material, [32].

Table 2 Thermophysical and optical properties of several components [32].

Components	Solar absorptivity (BOL)	Solar absorptivity (EOL)	Emissivity	Thermal Conductance (W/m^2K)	Conductivity (W/mK)
Baseplate-honeycomb				3200	
Lateral					3.5
Transversal					1.35
External MLI	0.35	0.5	0.61		
External Black MLI	0.93	0.93	0.84		
Internal MLI	N/A	N/A	0.05		
OSR	0.11	0.27	0.84		

7. THERMAL ANALYSIS RESULTS

Thermal analysis of predicts the temperature of batteries in a given or expected heating realm, and is required to test and improve thermal design [51]. In this study, a thermal analysis was performed using ThermXL software. ThermxL provides an environment for constructing a lumped-parameter thermal analysis network, as well as built-in routines for solving the analysis in both transient and steady state (using the well-known finite difference method) [54]. Temperature results are indicated in Table 3. The qualification temperatures range of the batteries was from 0°C to 54 °C. As expected, the highest temperature was 32. 7 °C during EQ EOL with 2 stacks failing at the north panel. The lowest temperature was 10.9 °C during SS EOL at the north panel. As indicated in Table 3, there was a large variation in the calculated temperatures because of the parameters, shown in Table 2.

Table 3 also illustrates that all the temperatures were within the range of the allowable maximum values.

Table 3 The calculated cell temperatures of the batteries

		North Panel		South Panel	
		Cell		Cell	
Cases	Condition	Min	Max	Min	Max
WS BOL		18.8	25.4	18.3	24.3
SS BOL		17.1	21.7	18.8	25.8
WS EOL		18.5	26.1	15.1	21.2
SS EOL		11.2	19.3	19.6	24.7
WS EOL	shunt	18.1	25.9	14.8	21.8
SS EOL	shunt	10.9	18.8	19.1	26.1
EQ EOL		18.8	30.3	18.8	29.5
EQ EOL	1 stack failed	18.4	31.2	18.9	29.5
EQ EOL	2 stacks failed	18.9	32.7	18.9	31.4

8. CONCLUSION

An overview of TCS for batteries in three-axis stabilized GEO satellite were briefly reviewed and detailed information of electrical performance, thermal performance, thermal design, thermal modelling and analysis were presented for Ni-Cd, Ni-H_2 and Li-ion batteries.

In addition, the thermal model is developed and thermal analysis of Li-ion batteries was performed using ThermXL software. The thermal analysis results showed that the passive thermal control system is designed to withstand the hot and cold cases within the required operational temperature range. It has been seen that the analysis results are in line with the recommendations of the battery manufacturer and in the desired temperature range. The temperature of batteries did not exceed its qualification temperature results.

Acknowledgments

The author thanks to Dr. Sheila Christopher for revising the whole manuscript.

Funding

The authors received no financial support for the research, authorship, and/or publication of this study.

The Declaration of Conflict of Interest/ Common Interest

The authors declare that they have no known competing financial interests or personal relationships that could have appeared to influence the work reported in this paper.

Authors' Contribution

The authors contributed equally to the study.

The Declaration of Ethics Committee Approval

The authors declare that this document does not require ethics committee approval or any special permission.

The Declaration of Research and Publication Ethics

The authors of the paper declare that they comply with the scientific, ethical and quotation rules of SAUJS in all processes of the paper and that they do not make any falsification on the data collected. In addition, they declare that Sakarya University Journal of Science and its editorial board have no responsibility for any ethical violations that may be encountered, and that this study has not been evaluated in any academic publication environment other than Sakarya University Journal of Science."

REFERENCES

[1] T. Ormston, V.D.Tran, M. Denis, N. Mardle and B. Khoshnevis, "Lithium ion battery

management strategies for european space operations centre missions," in SpaceOps Conferences, 5-9 May 2014, Pasadena, CA, A.I.of Aeronautics and Astronautics, eds., European Space Operations Center, may 2014.

[2] M. R. Patel, "Spacecraft power systems," Florida, CRC, 2005.

[3] L. Honglin, L. Sanchez, W. Qiang, X. Jie, Y. Wentao, H. Zhi, Z. Xuan, "Lithium-Ion battery flight experience return on China large GEO communication satellite," 2019 European Space Power Conference (ESPC), Juan-les-Pins, France, 30 September- 4 October 2019.

[4] D. Linden, T. B. Reddy, "Handbook of batteries," 3rd ed., McGraw-Hill, 2002.

[5] M.J. Milden, B. Khoshnevis, "State of the art: Aerospace batteries," AIAA paper 96-0125, January 1996.

[6] A.N. Nelson, "Spacecraft battery technology," Via Satellite, February, 1999.

[7] T. P. Barrera, M. L. Wasz, "Spacecraft li-Iion battery power system state-of-practice: A critical review," AIAA Propulsion and Energy Forum July 9-11, 2018, Cincinnati, Ohio 2018 International Energy Conversion Engineering Conference.

[8] G. Dudley, J. Verniolle, "Secondary lithium batteries for spacecraft," ESA Bulletin, No. 9, pp. 50–54, May 1997.

[9] "Proper care of NiCd battery back," RAE Systems [online database], URL: http://www.raesystem.com, TN-145.

[10] B. McKissock, P. Loyselle, E. Vogel, "Guidelines on lithium-ion battery use in space applications," Technical Report NASA/TM-2009-215751 NESC-RP-08-75/06-069-I; NASA, Glenn Research Center: Cleveland, OH, USA, May 2009.

[11] G.J. Dudley, "Lithium-ion batteries for space," Proceedings of the Fifth European Space Power Conference, Tarragona, Spain, 21-25 September 1998.

[12] Y.Borthomieu, "Satellite Li-ion batteries," Advances and Applications, pp. 311-344, 2014.

[13] S. Demirel, E. Sanli, M. Gokten, A.F.Yagli, S. Gulgonul, "Properties and performance comparison of electrical power sub-system on TUSAT communication satellite," In: 2012 IEEE first AESS European conference on satellite communications (ESTEL 2012), Rome, Italy, 2-5 October 2012.

[14] H. Vaidyanathan, G. Rao, "Electrical and thermal characteristics of lithium-ion cells," 14th Annual Battery Conference on Applications and Advances, pp. 79-84, 1999.

[15] M.C. Smart, B.V. Ratnakumar, R.C. Ewell, S. Surampudi, F.J. Puglia, R. Gitzendanner, "The use of lithium-ion batteries for JPL's Mars Missions," Electrochimica Acta, vol.268, pp. 27-40, 2018.

[16] S. Yayathi, W. Walker, D. Doughty, H. Ardebili, "Energy distributions exhibited during thermal runaway of commercial lithium ion batteries used for human spaceflight applications," Journal of Power Sources, vol.329, pp. 197-206, 2016.

[17] C. Tatard, "Li-ion battery for Geo satellites," Proceedings of the 21th International Communications Satellite Systems Conference and Exhibit, 2003.

[18] M.M. Kim, K.S. Ma, Y.C. Lim, J.D. Lee, "Development of Lithium-Ion based onboard battery for space launch vehicle," Journal of the Korean Society for Aeronautical & Space Sciences, vol.35, no. 4, pp. 363-368, 2007.

[20] M.J. Isaacson, M.E. Daman, "Li-ion batteries for space applications," Proceedings of the 32th Intersociety Energy Conversion Engineering Conference, 1997.

[21] J. Miao, Q. Zhong, Q. Zhao, X. Zhao, "Spacecraft thermal control technologies,"

Springer Nature Singapore Pte Ltd, Beijing, China, 2021.

[22] S. Demirel, "Modelling and analyses of electrical power system of communication satellites," Sakarya University, Institute of Natural Sciences, PhD dissertation, 2017.

[23] C.A. Hill, "Satellite battery technology- A tutorial and overview," 1998 IEEE Aerospace Conference Proceedings, Snowmass, Co, USA, 28 March 1998.

[24] S.V. Martinez, E.M. Filho, L.O. Seman, E.A. Bezarra, V.D.P.Nicolau, R.G. Overjero, V.R.Q.Leithardt, "An integrated thermal-electrical model for simulations of battery behavir in cubesats," Applied Sciences, vol.11, no. 4, 1554, 2021.

[25] S. Wang, Y. Li, Y.Z Li, Y. Mao, Y. Zhang, M. Zhong, "A forced gas cooling circle packaging with liquid cooling plate for the thermal management of Li-ion batteries under space environment," Applied Thermal Engineering, vol.123, pp. 929-939, 2017.

[26] A. Megahed, A. El-Dib, "Thermal design and analysis for battery module for a remote sensing satellite," Journal of Spacecraft and Rockets, vol.44, no.4, pp. 920-926, July-August 2007.

[27] E.W. Grob, D.R. Chalmers, C.W. Bennett "Thermal design and verification of the EOS-AM1 nickel hydrogen batteries," Proceedings of the 32nd Intersociety Energy Conversion Engineering Conference (IECEC-97), Honolulu, HI, July 27- August 02, 1997.

[28] A. Boudjemai, R. Hocine, M.N. Sweeting, "Thermal analysis of the Alsat-1 satellite battery pack sub assembly into the honeycomb," Proceedings of the 3rd International Conference on Control, Engineering&Information Technology (CEIT), Tlemcen, Algeria, 25-27 May 2015.

[29] C. Lurie, "Evaluation of lithium ion cells for space appications," Proceedings of the 32nd Intersociety Energy Conversion Engineering Conference (IECEC-97), Honolulu, HI, July 27- August 02, 1997.

[30] J. C. Koo, S. K. Lee, S. W. Ra, "Lithium-ion battery design for the hybrid satellite in the geostationary orbit," In Proceedings of the INTELEC 2009- 31st International Telecommunications Energy Conference, Incheon, Korea, 18-22 October 2009.

[31] M. Bulut, S. Demirel, N. Sozbir, S. Gulgonul, "Battery thermal design conception of Turkish satellite," 6th International Energy Conversion Engineering Conference (IECEC), Cleveland, Ohio, 28-30 July 2008.

[32] M. Bulut, S. Demirel, N. Sozbir, S. Gulgonul, "Electrical and thermal properties and performance comparison of li-Ion, NiH_2 and NiCD batteries for geostationary satellite's applications," 8. Ankara International Aerospace Conference, Ankara, 10-12 September 2015.

[33] H. Sundu, N. Döner, "Detailed thermal design and control of an observation satellite in Low Earth Orbit," European Mechanical Science, vol. 4, no.4, pp. 171-178, 2020.

[34] K. E. Boushon, "Thermal analysis and control of small satellites in Low Earth Orbit," Masters Theses, Missouri University of Science and Technology, 2018.

[35] A. Elweteedy, A. Elmaihy and A. Elhefnawy, "Small satellite operational phase thermal analysis and design: a comparative study," INCAS Bulletin, vol. 13, no. 4, pp. 59–74, 2021.

[36] A. Elhefnawy, A. Elweteedy, "Thermal anlaysis of a small satellite in post-mission phase," Journal of Multidisciplinary Engineering Science and Technology (JMET), vol. 6, no.2, pp. 9495-9504, 2019.

[37] "Spacecraft design structure and operation," Air University Space Primer [online database], URL:

http://space.au.af.mil/primer/spacecraft_design_structure_ops.pdf [cited August 2003].

[38] L. Bailin, L. Xiufeng, Z. Zuokin, "Influence analysis of lithium-ion battery configuration outside the east/west panel on GEO satellite platform," Chine Space Science and Technology, vol. 37, no. 6, pp. 75–81, Dec.25, 2017.

[39] M. Ya, W. Bingxin, M. Shangde, G. Rui, X. Jingying, W. Ke, "Thermal behavior of Lithium Ion battery for SAR satellites," 2021 2nd China International SAR Symposium (CISS), Shanghai, China, 3-5 November 2021.

[40] J.C. Hal, Space Systems/Loral, Inc., Palo Alto, CA, U.S. Patent Application for a "Lithium ion satellite battery charge control circuit," Patent Number. 6,034,506, filed 16 Jan. 1998.

[41] J.H. Saleh, D. E. Hastings, D. J. Newman, "Spacecraft design lifetime," Journal of Spacecraft and Rockets, vol. 39, no. 2, March-April 2002.

[42] M. Zahran, A. Atef, "Electrical and thermal properties of NiCd battery for low earth orbit satellite's applications," Proceedings of the 6th International Conference on Power Systems, Lisbon, Portugal, pp. 122-130, 2006.

[43] D.G. Gilmore, "Spacecraft thermal control handbook volume I: Fundamental technologies," 2nd ed., The Aerospace Press, California, 2002.

[44] Saft Space & Defense Division https:// www.saftbatteries.com(accessed 9/11/2021).

[45] S. Suresha, G.S. Gupta, R.A. Katti, "Thermal sensitivity analysis of spacecraft battery," Journal of Spacecraft and Rockets, vol. 34, no. 3, pp. 384–390, 1997.

[46] N. Sozbir, M. Bulut, "Thermal control of CM and SM panels for Turkish satellite," 6th SAE 39th International Conference on Environmental Systems, Savannah, Georgia, USA, July 12-16, 2009.

[47] J. Wertz, W. Larson, "Space mission analysis and design," 3rd ed., Microcosm Press, Torrence, CA, and Kluwer Academic, Dordrecht, The Netherlands, pp. 428-458, 1999.

[48] M. Bulut, A. Kahriman, N. Sozbir, "Design and analysis for thermal control system of nanosatellite," ASME 2010 International Mechanical Engineering Congress and Exposition (IMECE2010), Vancouver, British Columbia, Canada, 12-18 November 2010.

[49] B. A. Moffitt, "Predictive thermal analysis of the combat sentinel satellite test article," Utah State University, MSc. 2003.

[50] M. Bulut, "Thermal design, analysis, and testing of the first Turkish 3U communication CubeSat in low earth orbit," Journal of Thermal Analysis and Calorimetry, vol. 143, pp. 4341–4353, 2021.

[51] M. Bulut, N. Sözbir, "Thermal design, analysis, and test validation of TURKSAT-3USAT satellite," Journal of Thermal Engineering, vol. 7, no. 3, pp. 468–482, March 2021.

[52] A. Magehed, A. El-Dib, "Thermal design and analysis for battery module for a remote sensing satellite," Journal of Spacecraft and Rockets, vol. 44, no. 4, pp. 920–926, 2007.

[53] B. Gebhart, "Surface temperature calculations in radiant surroundings of arbitrary complexity - for gray, diffuse radiation," International Journal of Heat and Mass Transfer, vol. 3, no.4, pp. 341-346, 1961.

[54] M. Bulut, "Thermal simulation software based on excel for spacecraft application," Selcuk University Journal of Engineering, Science & Technology, vol. 6, no. 4, pp. 592–600, 2018.

SAKARYA ÜNİVERSİTESİ
FEN BİLİMLERİ ENSTİTÜSÜ DERGİSİ

Sakarya University Journal of Science
SAUJS

ISSN 1301-4048 | e-ISSN 2147-835X | Period Bimonthly | Founded: 1997 | Publisher Sakarya University | http://www.saujs.sakarya.edu.tr/

Title: Investigation of Matrices Q^(n._L), M^(n._L) and R^(n._L) and Some Related Identities

Authors: İbrahim GÖKCAN, Ali Hikmet DEĞER

Recieved: 2021-12-08 00:00:00

Accepted: 2022-05-30 00:00:00

Article Type: Research Article

Volume: 26
Issue: 4
Month: August
Year: 2022
Pages: 677-686

How to cite
İbrahim GÖKCAN, Ali Hikmet DEĞER; (2022), Investigation of Matrices Q^(n._L), M^(n._L) and R^(n._L) and Some Related Identities. Sakarya University Journal of Science, 26(4), 677-686, DOI: 10.16984/saufenbilder.1034057
Access link
http://www.saujs.sakarya.edu.tr/en/pub/issue/72361/1034057

Sakarya University Journal of Science 26(4), 677-686, 2022

Investigation of Matrices $Q^{n\cdot L}$, $M^{n\cdot L}$ and $R^{n\cdot L}$ and Some Related Identities

İbrahim GÖKCAN*[1], Ali Hikmet DEĞER[2]

Abstract

In this study, it is aimed to use the Lorenz matrix multiplication to find the n^{th} powers of some special matrices and to reach the quadratic equations and characteristic roots of the matrices obtained in this way. In addition, it is aimed to contribute literature to the studies in the field by reaching some identities.

Keywords: Characteristic Roots, Fibonacci and Lucas Numbers, Lorentz Matrix Multiplication, Identity, Quadratic Equations

1. INTRODUCTION

Fibonacci and Lucas numbers are studied extensively in the literature and are associated with many scientific facts. The Fibonacci number sequence is $0,1,1,2,3,\cdots$ known by the recurrence relation $F_n = F_{n-1} + F_{n-2}$. Similarly, the Lucas number sequence is $2,1,3,4,\cdots$ known by the recurrence relation $L_n = L_{n-1} + L_{n-2}$. [1, 2] can be examined about Fibonacci and Lucas numbers. In [3], Ruggles obtained some findings related with Fibonacci and Lucas numbers. In recent years, studies realised on the generalization of the Fibonacci and Lucas numbers. In [4], Tasci and Kilic achieved generalization of Lucas numbers by the help of matrices and a relation between generalized order-k Lucas and Fibonacci numbers. In [5], Kilic and Tasci studied on the generalized order-k Fibonacci and Lucas numbers. They generalized Binet's formula for these numbers and obtained some data that also included these numbers. In [6], Kızılateş and Tuglu examined extented concolved (p,q)-Fibonacci and Lucas polynomials and obtained some recurrence relations about these polynomials. In [7], Qi, Kızılateş, and Du achieved a closed formula for Horadam polynomials by using tridiagonal determinat and from here they reproduced closed formulas for other poylnomial sequences. In [8], Kızılateş worked finite operators on Horadam sequences and defined Horadam finite operator sequences. In addition, in [8], Kızılateş investigated recurrence relation, Binet-like formula, summation formula and generating function by using this sequences. Moreover, in [8], Kızılateş obtained a closed formula that given number of

* Corresponding author: gokcan4385@gmail.com
[1] Artvin Çoruh Universıty
ORCID: https://orcid.org/ 0000-0002-6933-8494
[2] Karadeniz Technical University
E-mail: ahikmetd@ktu.edu.tr
ORCID: https://orcid.org/ 0000-0003-0764-715X

this sequences by using tridiagonal determinant. In [9], Kızılateş, Du and Qi made a few explicit formulas for (p,q,r)-tribonacci polynomials and generalized tribonacci sequences by using Hessenberg determinants and from here they reproduced explicit formulas for some other sequences. One of the studies in this field is to obtain identities related to Fibonacci, Lucas and other number sequences with the help of n^{th} powers of the matrices consisting of the elements of Fibonacci and Lucas number sequences, to reach the quadratic equations and characteristic roots of the matrices with the help of the determinants of the n^{th} powers of the matrices. Matrices $\mathcal{Q}=\begin{pmatrix}1 & 1\\ 1 & 0\end{pmatrix}, M=\begin{pmatrix}1 & 1\\ 1 & 2\end{pmatrix}$ and $R=\begin{pmatrix}1 & 2\\ 2 & -1\end{pmatrix}$ were used specially.

In this section, some historical information were given about the matrices $\mathcal{Q}$, M and R in order to make sense of our work. In this regard, [10] was our main reference source. The subject of examining Fibonacci sequences with the method matrix $\mathcal{Q}$ and discovering the relations between their elements has been discussed by mathematicians for many years. With initial conditions $F_0=0$ and $F_1=1$, the Fibonacci sequence is obtained with the recurrence relation $F_n=F_{n-1}+F_{n-2}$. The n^{th} power of the matrix $\mathcal{Q}$ formed by the elements of the Fibonacci sequence becomes $\mathcal{Q}^n=\begin{pmatrix}F_{n+1} & F_n\\ F_n & F_{n-1}\end{pmatrix}$. The determinant of this matrix satisfies the equation $F_{n+1}F_{n-1}-F_n^2=(-1)^n$ given by Robert Simson in 1753. This equation is the basis of Lewis Carroll's famous geometric paradox. Basin and Hoggatt [11] refer to Charles King's [12] master's thesis for the first definition of the matrix $\mathcal{Q}$. Earlier, work on using the matrix $\mathcal{Q}$ to construct Fibonacci sequences was published by Brenner [13]. J. Sutherland Frame [14] used matrix $\begin{pmatrix}\alpha & 1\\ 1 & 0\end{pmatrix}$ for studying continued fractions [10]. Note that this matrix becomes the matrix $\mathcal{Q}$ for $\alpha=1$ and the matrix which produces the Pell sequences for $\alpha=2$. Schwerdtfeger [15] studied Jacobsthal [16]'s Fibonacci polynomial matrix methods and defined the Fibonacci polynomial with the elements of $\mathcal{Q}^n$. White [17] used the matrices $\begin{pmatrix}1 & 1\\ 1 & 0\end{pmatrix}$ and $\begin{pmatrix}1 & 1\\ 0 & 1\end{pmatrix}$ to generate $GL(2,\mathbb{Z})$. Bicknell [18] found the square root of the matrix $\mathcal{Q}$ and used it in fractional powers [10].

1.1. Examining the Matrix $\mathcal{Q}$

Determinant of matrix $\mathcal{Q}$ is -1. Under classical matrix multiplication, the powers of the matrix $\mathcal{Q}$ are found as $\mathcal{Q}^2=\begin{pmatrix}2 & 1\\ 1 & 1\end{pmatrix}$, $\mathcal{Q}^3=\begin{pmatrix}3 & 2\\ 2 & 1\end{pmatrix}$, $\mathcal{Q}^4=\begin{pmatrix}5 & 3\\ 3 & 2\end{pmatrix},\cdots$. From here, n^{th} power of matrix $\mathcal{Q}$ is found as $\mathcal{Q}^n=\begin{pmatrix}F_{n+1} & F_n\\ F_n & F_{n-1}\end{pmatrix}$.

Theorem 1. [19] Let $n\geq 1$. Then $\mathcal{Q}^n=\begin{pmatrix}F_{n+1} & F_n\\ F_n & F_{n-1}\end{pmatrix}$.

Proposition 1. [19] Let $n\geq 1$. Then $F_{n+1}F_{n-1}-F_n^2=(-1)^n$.

Proposition 2. [19] Let $m,n\in\mathbb{N}$. Then,

i) $F_{m+n+1}=F_{m+1}F_{n+1}+F_mF_n$

ii) $F_{m+n}=F_{m+1}F_n+F_mF_{n-1}$

iii) $F_{m+n}=F_mF_{n+1}+F_{m-1}F_n$

iv) $F_{m+n-1}=F_mF_n+F_{m-1}F_{n-1}$

1.2. Examining the Matrix M

Determinant of matrix M is 1. Under classical matrix multiplication, the powers of the matrix M are found as $M^2=\begin{pmatrix}2 & 3\\ 3 & 5\end{pmatrix}$, $M^3=\begin{pmatrix}5 & 8\\ 8 & 13\end{pmatrix}$, $M^4=\begin{pmatrix}13 & 21\\ 21 & 34\end{pmatrix},\cdots$. From here, n^{th} power of matrix M is found as $M^n=\begin{pmatrix}F_{2n-1} & F_{2n}\\ F_{2n} & F_{2n+1}\end{pmatrix}$.

Proposition 3. [19] Let $n\geq 1$. Then $M^n=\begin{pmatrix}F_{2n-1} & F_{2n}\\ F_{2n} & F_{2n+1}\end{pmatrix}$.

Conclusion1. Let $n\geq 1$. Then $F_{2n-1}F_{2n+1}-F_{2n}^2=1$.

Conclusion 2. Let $m,n \in \mathbb{N}$.Then,

i) $F_{2m+2n-1} = F_{2m-1}F_{2n-1} + F_{2m}F_{2n}$

ii) $F_{2(m+n)} = F_{2m-1}F_{2n} + F_{2m}F_{2n+1}$

iii) $F_{2(m+n)} = F_{2m}F_{2n-1} + F_{2m+1}F_{2n}$

iv) $F_{2m+2n+1} = F_{2m}F_{2n} + F_{2m+1}F_{2n+1}$

1.3. Examining the Matrix *R*

Determinant of matrix R is -5. Under classical matrix multiplication, the powers of the matrix R are found as $R^2 = 5I$, $R^3 = 5R$, $R^4 = 5^2I$, $R^5 = 5^2R$, $R^6 = 5^3I$, $R^7 = 5^3R$, ⋯. Powers of $(2n)^{th}$ and $(2n+1)^{th}$ of matrix R are obtained as $R^{2n} = 5^nI$ and $R^{2n+1} = 5^nR$, respectively.

Conclusion 3. Let $n \geq 1$. Then $R^{2n} = 5^nI$.

Conclusion 4. Let $n \geq 0$. Then $R^{2n+1} = 5^nR$.

1.4. Quadratic Equations and Characteristic Roots of Matrices Q^n, M^n and R^n

The characteristic equation of Q is $|Q - xI| = 0$, where Q is a 2×2 matrix and I is a 2×2 unit matrix. The roots of the characteristic equation are the characteristic roots of Q. With the help of the equation given above, the characteristic roots of Q^n are found as follows:

$$|Q^n - xI| = \left|\begin{pmatrix} F_{n+1} & F_n \\ F_n & F_{n-1} \end{pmatrix} - x\begin{pmatrix} 1 & 0 \\ 0 & 1 \end{pmatrix}\right|$$

$$= \left|\begin{pmatrix} F_{n+1} & F_n \\ F_n & F_{n-1} \end{pmatrix} - \begin{pmatrix} x & 0 \\ 0 & x \end{pmatrix}\right|$$

$$= \left|\begin{pmatrix} F_{n+1}-x & F_n \\ F_n & F_{n-1}-x \end{pmatrix}\right|$$

$$= (F_{n+1} - x)(F_{n-1} - x) - F_n^2$$

$$= x^2 + F_{n+1}F_{n-1} - x(F_{n+1} + F_{n-1}) - F_n^2$$

$$= x^2 - x(F_{n+1} + F_{n-1}) + F_{n+1}F_{n-1} - F_n^2$$

$$= x^2 - xL_n + (-1)^n = 0. \quad (1)$$

Using the quadratic equation, we can obtain the following characteristic roots. From the method $\Delta = b^2 - 4ac$,

$$x_{1,2} = \frac{L_n \pm \sqrt{L_n^2 - 4(-1)^n}}{2} \quad (2)$$

are found. Substituting the identity $L_n^2 - 4(-1)^n = 5F_n^2$ at (2),

$$x_{1,2} = \frac{L_n \pm \sqrt{5F_n^2}}{2} = \frac{L_n \pm \sqrt{5}F_n}{2} \quad (3)$$

roots are found [19].
Let's examine the quadratic equation and characteristic roots of the matrix M^n with a similar method. M^n is a 2×2 matrix and I is a 2×2 unit matrix. The characteristic equation of M^n is $|M^n - xI| = 0$. From here,

$$|M^n - xI| = \left|\begin{pmatrix} F_{2n-1} & F_{2n} \\ F_{2n} & F_{2n+1} \end{pmatrix} - x\begin{pmatrix} 1 & 0 \\ 0 & 1 \end{pmatrix}\right|$$

$$= \left|\begin{pmatrix} F_{2n-1} & F_{2n} \\ F_{2n} & F_{2n+1} \end{pmatrix} - \begin{pmatrix} x & 0 \\ 0 & x \end{pmatrix}\right|$$

$$= \left|\begin{pmatrix} F_{2n-1}-x & F_{2n} \\ F_{2n} & F_{2n+1}-x \end{pmatrix}\right|$$

$$= (F_{2n-1} - x)(F_{2n+1} - x) - F_{2n}^2$$

$$= x^2 + F_{2n+1}F_{2n-1} - x(F_{2n+1} + F_{2n-1}) - F_{2n}^2$$

$$= x^2 - x(F_{2n+1} + F_{2n-1}) + F_{2n+1}F_{2n-1} - F_{2n}^2$$

$$= x^2 - xL_{2n} + 1 = 0. \quad (4)$$

From the Δ method,

$$x_{1,2} = \frac{L_{2n} \pm \sqrt{L_{2n}^2 - 4}}{2} \quad (5)$$

roots are found. $L_{2n}^2 - 4 = 5F_{2n}^2$is obtained from $L_n^2 - 4(-1)^n = 5F_n^2$ (please see [19]) for $n \to 2n$. From here, $L_{2n}^2 - 4 = 5F_{2n}^2$ is substituting at (5),

$$x_{1,2} = \frac{L_{2n} \pm \sqrt{5F_{2n}^2}}{2} = \frac{L_{2n} \pm \sqrt{5}F_{2n}}{2} \quad (6)$$

roots are obtained.

Now let's examine the quadratic equation of the matrix R^n and its characteristic roots. R^n is a 2×2 matrix and I is a 2×2 unit matrix. R^n's characteristic equation is $|R^n - xI| = 0$. Since the matrix R^n is found differently for powers $(2n)^{th}$ and $(2n+1)^{th}$, there are different quadratic equations and characteristic roots for both values. Quadratic equation for matrix R^{2n},

$$|R^{2n} - xI| = \left|\begin{pmatrix} 5^n & 0 \\ 0 & 5^n \end{pmatrix} - x\begin{pmatrix} 1 & 0 \\ 0 & 1 \end{pmatrix}\right|$$

$$= \left|\begin{pmatrix} 5^n & 0 \\ 0 & 5^n \end{pmatrix} - \begin{pmatrix} x & 0 \\ 0 & x \end{pmatrix}\right|$$

$$= \left|\begin{pmatrix} 5^n - x & 0 \\ 0 & 5^n - x \end{pmatrix}\right|$$

$$= (5^n - x)(5^n - x)$$

$$= 5^{2n} - 2x5^n + x^2$$

$$= x^2 - 2.5^n x + 5^{2n} = 0. \quad (7)$$

From the Δ method,

$$x_{1,2} = \frac{2.5^n \pm \sqrt{4.5^{2n} - 4.5^{2n}}}{2} = \frac{2.5^n}{2} = 5^n \quad (8)$$

roots are obtained. Quadratic equation for matrix R^{2n+1},

$$|R^{2n+1} - xI| = \left|\begin{pmatrix} 5^n & 2.5^n \\ 2.5^n & -5^n \end{pmatrix} - x\begin{pmatrix} 1 & 0 \\ 0 & 1 \end{pmatrix}\right|$$

$$= \left|\begin{pmatrix} 5^n & 2.5^n \\ 2.5^n & -5^n \end{pmatrix} - \begin{pmatrix} x & 0 \\ 0 & x \end{pmatrix}\right|$$

$$= \left|\begin{pmatrix} 5^n - x & 2.5^n \\ 2.5^n & -5^n - x \end{pmatrix}\right|$$

$$= (5^n - x)(-5^n - x) - 4.5^{2n}$$

$$= (5^n - x)(5^n + x) + 4.5^{2n}$$

$$= -x^2 + 5^{2n+1} = 0. \quad (9)$$

From the Δ method,

$$x_{1,2} = \frac{\pm\sqrt{-4.(-1)5^{2n+1}}}{2} = \pm 5^n\sqrt{5} \quad (10)$$

roots are obtained.

1.5. Lorentz Matrix Multiplication

In [20], the authors defined Lorentz matrix multiplication between two matrices unlike the classical matrix multiplication. Let's R_n^m denote matrices of type $m \times n$ and R_p^n denote matrices of type $n \times p$. Lorentz matrix multiplication

$$\langle a, b\rangle_{\cdot_L} = -a_{i1}b_{1k} + \sum_{j=2}^{n} a_{ij}b_{jk} \quad (11)$$

by "$\cdot_L$" is defined between lines of matrices $A = (a_{ij}) \in R_n^m$ and columns of matrices $B = (b_{jk}) \in R_p^n$. $A._L B$ is a matrix of type $m \times p$. $(i,j)^{th}$ inner product of $A._L B$ is $\langle A_i, B^j\rangle_L$ when A_i is i^{th} line of matrix A and B^j is j^{th} column of matrix B. $A._L B$ is defined as follows:

$$A._L B = \begin{pmatrix} \langle A_1, B^1\rangle_L & \cdots & \langle A_1, B^j\rangle_L \\ \vdots & \ddots & \vdots \\ \langle A_i, B^1\rangle_L & \cdots & \langle A_i, B^j\rangle_L \end{pmatrix} \quad (12)$$

Determinant of $A._L B$ is defined as

$$\det(A._L B) = -detA.detB. \quad (13)$$

[20-22] can be examined for Lorentz matrix multiplication and its related properties.

2. OBTAINING IDENTITIES WITH HELP OF MATRICES $Q^{n._L}$, $M^{n._L}$ AND $R^{n._L}$

n^{th} power under Lorentz matrix multiplication of matrices Q, M and R is denoted with $Q^{n._L}$, $M^{n._L}$ and $R^{n._L}$,respectively.

2.1. Matrix $Q^{n._L}$ and Related Identity

n^{th} power of matrix Q is obtained under Lorentz matrix multiplication as follows for $k \in \mathbb{N}$:

$$Q^{2._L} = \begin{pmatrix} 1 & 1 \\ 1 & 0 \end{pmatrix} \cdot_L \begin{pmatrix} 1 & 1 \\ 1 & 0 \end{pmatrix} = \begin{pmatrix} F_0 & -F_1 \\ -F_1 & -F_1 \end{pmatrix},$$

$$Q^{3._L} = \begin{pmatrix} 1 & 1 \\ 1 & 0 \end{pmatrix} \cdot_L \begin{pmatrix} 0 & -1 \\ -1 & -1 \end{pmatrix} = \begin{pmatrix} -F_1 & F_0 \\ F_0 & F_1 \end{pmatrix},$$

$$Q^{4.L}=\begin{pmatrix}1&1\\1&0\end{pmatrix}\cdot_L\begin{pmatrix}-1&0\\0&1\end{pmatrix}=\begin{pmatrix}F_1&F_1\\F_1&F_0\end{pmatrix},$$
$$Q^{5.L}=\begin{pmatrix}1&1\\1&0\end{pmatrix}\cdot_L\begin{pmatrix}1&1\\1&0\end{pmatrix}=\begin{pmatrix}F_0&-F_1\\-F_1&-F_1\end{pmatrix},$$
$$Q^{6.L}=\begin{pmatrix}1&1\\1&0\end{pmatrix}\cdot_L\begin{pmatrix}0&-1\\-1&-1\end{pmatrix}=\begin{pmatrix}-F_1&F_0\\F_0&F_1\end{pmatrix},\cdots$$

$$Q^{n.L}=\begin{cases}\begin{pmatrix}F_1&F_1\\F_1&F_0\end{pmatrix}, & n=3k+1\\ \begin{pmatrix}F_0&-F_1\\-F_1&-F_1\end{pmatrix}, & n=3k+2\\ \begin{pmatrix}-F_1&F_0\\F_0&F_1\end{pmatrix}, & n=3k+3\end{cases} \quad (14)$$

Let us prove identity (14) by using induction.
It is provided $Q^{1.L}, Q^{2.L}$ and $Q^{3.L}$ for $n=1, n=2$ and $n=3$,respectively. Then,

$$Q^{n.L}=\begin{cases}\begin{pmatrix}F_1&F_1\\F_1&F_0\end{pmatrix}, & n=1\\ \begin{pmatrix}F_0&-F_1\\-F_1&-F_1\end{pmatrix}, & n=2\\ \begin{pmatrix}-F_1&F_0\\F_0&F_1\end{pmatrix}, & n=3\end{cases}$$

Let assume that $Q^{3k+1.L}, Q^{3k+2.L}$ and $Q^{3k+3.L}$ is provided for $n=3k+1, n=3k+2$ and $n=3k+3$,respectively. Then,

$$Q^{n.L}=\begin{cases}\begin{pmatrix}F_1&F_1\\F_1&F_0\end{pmatrix}, & n=3k+1\\ \begin{pmatrix}F_0&-F_1\\-F_1&-F_1\end{pmatrix}, & n=3k+2\\ \begin{pmatrix}-F_1&F_0\\F_0&F_1\end{pmatrix}, & n=3k+3\end{cases}$$

Let demonstrate that $Q^{3k+4.L}, Q^{3k+5.L}$ and $Q^{3k+6.L}$ is provided for $n=3k+4, n=3k+5$ and $n=3k+6$, respectively.

$$Q^{n.L}=\begin{cases}\begin{pmatrix}F_1&F_1\\F_1&F_0\end{pmatrix}, & n=3k+4\\ \begin{pmatrix}F_0&-F_1\\-F_1&-F_1\end{pmatrix}, & n=3k+5\\ \begin{pmatrix}-F_1&F_0\\F_0&F_1\end{pmatrix}, & n=3k+6\end{cases}$$

For $Q^{3k+4.L}=Q._L Q^{3k+3.L}$,
$$Q^{3k+4.L}=\begin{pmatrix}1&1\\1&0\end{pmatrix}\cdot_L\begin{pmatrix}-1&0\\0&1\end{pmatrix}=\begin{pmatrix}F_1&F_1\\F_1&F_0\end{pmatrix}.$$
For $Q^{3k+5.L}=Q._L Q^{3k+4.L}$,
$$Q^{3k+5.L}=\begin{pmatrix}1&1\\1&0\end{pmatrix}\cdot_L\begin{pmatrix}1&1\\1&0\end{pmatrix}=\begin{pmatrix}F_0&-F_1\\-F_1&-F_1\end{pmatrix}.$$
For $Q^{3k+6.L}=Q._L Q^{3k+5.L}$,
$$Q^{3k+6.L}=\begin{pmatrix}1&1\\1&0\end{pmatrix}\cdot_L\begin{pmatrix}0&-1\\-1&-1\end{pmatrix}=\begin{pmatrix}-F_1&F_0\\F_0&F_1\end{pmatrix}.$$
Determinants of matrices are obtained as follows from (13).
$$detQ^{2.L}=-det\begin{pmatrix}1&1\\1&0\end{pmatrix}.det\begin{pmatrix}1&1\\1&0\end{pmatrix}=-1$$
$$detQ^{3.L}=-det\begin{pmatrix}1&1\\1&0\end{pmatrix}.det\begin{pmatrix}0&-1\\-1&-1\end{pmatrix}=-1$$
$$detQ^{4.L}=-det\begin{pmatrix}1&1\\1&0\end{pmatrix}.det\begin{pmatrix}-1&0\\0&1\end{pmatrix}=-1$$
$$detQ^{5.L}=-det\begin{pmatrix}1&1\\1&0\end{pmatrix}.det\begin{pmatrix}1&1\\1&0\end{pmatrix}=-1,\cdots$$
Determinants of matrices are $detQ^{n.L}=-1$ for $n\geqslant 1$.

2.2. Matrix $M^{n.L}$ and Related Identities

n^{th} power of matrix M is obtained under Lorentz matrix multiplication as follows:
$$M^{2.L}=\begin{pmatrix}1&1\\1&2\end{pmatrix}\cdot_L\begin{pmatrix}1&1\\1&2\end{pmatrix}=\begin{pmatrix}F_0&F_2\\F_2&F_4\end{pmatrix},$$
$$M^{3.L}=\begin{pmatrix}0&1\\1&3\end{pmatrix}\cdot_L\begin{pmatrix}1&1\\1&2\end{pmatrix}=\begin{pmatrix}F_1&F_3\\F_3&F_5\end{pmatrix},$$
$$M^{4.L}=\begin{pmatrix}1&2\\2&5\end{pmatrix}\cdot_L\begin{pmatrix}1&1\\1&2\end{pmatrix}=\begin{pmatrix}F_2&F_4\\F_4&F_6\end{pmatrix},$$
$$M^{5.L}=\begin{pmatrix}1&3\\3&8\end{pmatrix}\cdot_L\begin{pmatrix}1&1\\1&2\end{pmatrix}=\begin{pmatrix}F_3&F_5\\F_5&F_7\end{pmatrix},\cdots$$

$$M^{n.L}=\begin{pmatrix}F_{n-2}&F_n\\F_n&F_{n+2}\end{pmatrix} \quad (15)$$

Let us prove identity (15) by using induction.
It is provided $M^{2.L}$ for $n=2$. Then,
$$M^{2.L}=\begin{pmatrix}F_0&F_2\\F_2&F_4\end{pmatrix}.$$
Let assume that $M^{k.L}$ is provided for $n=k$. Then,
$$M^{k.L}=\begin{pmatrix}F_{k-2}&F_k\\F_k&F_{k+2}\end{pmatrix}.$$
Let demonstrate that $M^{k+1.L}$ is provided for $n=k+1$.
For $M^{k+1.L}=M._L M^{k.L}$,
$$M^{k+1.L}=\begin{pmatrix}1&1\\1&2\end{pmatrix}\cdot_L\begin{pmatrix}F_{k-2}&F_k\\F_k&F_{k+2}\end{pmatrix}$$
$$=\begin{pmatrix}-F_{k-2}+F_k&-F_{k-2}+2F_k\\-F_k+F_{k+2}&-F_k+2F_{k+2}\end{pmatrix}$$
$$=\begin{pmatrix}F_{k-1}&F_{k+1}\\F_{k+1}&F_{k+3}\end{pmatrix}.$$
Determinants of matrices are obtained as follows from (13).
$$detM^{2.L}=-det\begin{pmatrix}1&1\\1&2\end{pmatrix}.det\begin{pmatrix}1&1\\1&2\end{pmatrix}=-1$$

$detM^{3.L} = -det\begin{pmatrix}0 & 1\\ 1 & 3\end{pmatrix}.det\begin{pmatrix}1 & 1\\ 1 & 2\end{pmatrix} = 1$
$detM^{4.L} = -det\begin{pmatrix}1 & 2\\ 2 & 5\end{pmatrix}.det\begin{pmatrix}1 & 1\\ 1 & 2\end{pmatrix} = -1$
$detM^{5.L} = -det\begin{pmatrix}1 & 3\\ 3 & 8\end{pmatrix}.det\begin{pmatrix}1 & 1\\ 1 & 2\end{pmatrix} = 1, \cdots$
If we continue like this, we obtained
$detM^{2.L} = detM^{4.L} = \cdots = detM^{2n.L} = -1$ and
$detM^{3.L} = detM^{5.L} = \cdots = detM^{2n+1.L} = 1.$
From here, the determinant for the generalized matrix is $F_{n-2}F_{n+2} - F_n^2 = (-1)^{n+1}$ for $n \geq 2$. This identity can be proved by inductive method. Among the matrices obtained by Lorentz matrix multiplication, the following operations are provided by Lorentz matrix operations.
$M^{2.L}._L M^{3.L} = \begin{pmatrix}2 & 5\\ 5 & 13\end{pmatrix} = M^{5.L}$,
$M^{1.L}._L M^{5.L} = \begin{pmatrix}3 & 8\\ 8 & 21\end{pmatrix} = M^{6.L}$,
$M^{2.L}._L M^{4.L} = \begin{pmatrix}3 & 8\\ 8 & 21\end{pmatrix} = M^{6.L}$
If the situation is generalized for different m and n numbers, the equation $M^{m.L}._L M^{n.L} = M^{m+n.L}$ is obtained. Using this equation, identities can be obtained. The identities in the following theorem are reached by both Lorentz and classical matrix multiplication.

Theorem 2.

i) $F_{m+n-2} = -F_{m-2}F_{n-2} + F_mF_n$

ii) $F_{m+n} = -F_{m-2}F_n + F_mF_{n+2}$

iii) $F_{m+n} = -F_mF_{n-2} + F_{m+2}F_n$

iv) $F_{m+n+2} = -F_mF_n + F_{m+2}F_{n+2}$

v) $\frac{F_m}{F_n} = \frac{F_{m+2}+F_{m-2}}{F_{n+2}+F_{n-2}}$

vi) $F_{2n} = L_nF_n$

Proof. Following equation is provided with Lorentz matrix multiplication when m and n are natural numbers for $M^{m.L} = \begin{pmatrix}F_{m-2} & F_m\\ F_m & F_{m+2}\end{pmatrix}$ and $M^{n.L} = \begin{pmatrix}F_{n-2} & F_n\\ F_n & F_{n+2}\end{pmatrix}$.
$M^{m.L}._L M^{n.L} = \begin{pmatrix}F_{m-2} & F_m\\ F_m & F_{m+2}\end{pmatrix}._L \begin{pmatrix}F_{n-2} & F_n\\ F_n & F_{n+2}\end{pmatrix}$
$=$
$\begin{pmatrix}-F_{m-2}F_{n-2} + F_mF_n & -F_{m-2}F_n + F_mF_{n+2}\\ -F_mF_{n-2} + F_{m+2}F_n & -F_mF_n + F_{m+2}F_{n+2}\end{pmatrix}$

$= \begin{pmatrix}F_{m+n-2} & F_{m+n}\\ F_{m+n} & F_{m+n+2}\end{pmatrix}$
$= M^{m+n.L}$

i) If taken as $r = 2$, $m = n-2$ and $n = m$ in $F_rF_{m+n} = F_{m+r}F_n - (-1)^rF_mF_{n-r}$ (please see [23]), $F_2F_{n-2+m} = F_{n-2+2}F_m - (-1)^2F_{n-2}F_{m-2}$ is obtained. So, $F_{n+m-2} = -F_{n-2}F_{m-2} + F_nF_m$.

ii) If taken as $r = 2, m = n$ and $n = m$ in $F_rF_{m+n} = F_{m+r}F_n - (-1)^rF_mF_{n-r}$ (please see [23]),
$F_2F_{n+m} = F_{n+2}F_m - (-1)^2F_nF_{m-2}$
is obtained.So, $F_{m+n} = -F_nF_{m-2} + F_{n+2}F_m$.

iii) If taken as $r = 2$ in $F_rF_{m+n} = F_{m+r}F_n - (-1)^rF_mF_{n-r}$ (please see [23]),
$F_2F_{m+n} = F_{m+2}F_n - (-1)^2F_mF_{n-2}$ is obtained.
So, $F_{m+n} = F_{m+2}F_n - F_mF_{n-2}$.

iv) If taken as $r = 2, n = m+2$ and $m = n$ in $F_rF_{m+n} = F_{m+r}F_n - (-1)^rF_mF_{n-r}$ (please see [23]),
$F_{n+m+2} = -F_nF_m + F_{n+2}F_{m+2}$ is obtained.

v) From (ii) and (iii) identities,
$F_{m+n} = -F_{m-2}F_n + F_mF_{n+2}$ and
$F_{m+n} = -F_mF_{n-2} + F_{m+2}F_n$
are found. From the equality of two identities,
$-F_{m-2}F_n + F_mF_{n+2} = -F_mF_{n-2} + F_{m+2}F_n$
is obtained. So,
$F_mF_{n+2} + F_mF_{n-2} = F_{m+2}F_n + F_{m-2}F_n$.
$\frac{F_m}{F_n} = \frac{F_{m+2}+F_{m-2}}{F_{n+2}+F_{n-2}}$
identity is obtained from
$F_m(F_{n+2} + F_{n-2}) = (F_{m+2}+F_{m-2})F_n$.

vi) If taken as $m = n$ in (ii),
$F_{2n} = -F_{n-2}F_n + F_nF_{n+2} = (F_{n+2}-F_{n-2})F_n$
$= L_nF_n$
is obtained.

Now let's give the theorem about newly obtained identities according to Lorentz matrix multiplication.

Theorem 3.

i) $3F_{m+n} = F_{m+2}F_{n+2} - F_{m-2}F_{n-2}$

ii) $L_{m+n-1} = -L_{m-1}F_{n-2} + L_{m+1}F_n$

iii) $L_{m+n+1} = -L_{m-1}F_n + L_{m+1}F_{n+2}$

iv) $F_{2n-2} = -F_{n-2}^2 + F_n^2$

v) $F_{2n+2} = -F_n^2 + F_{n+2}^2$

vi) $3F_{2n} = F_{n+2}^2 - F_{n-2}^2$

vii) $L_{2n-1} = -L_{n-1}F_{n-2} + L_{n+1}F_n$

viii) $L_{2n+1} = -L_{n-1}F_n + L_{n+1}F_{n+2}$

ix) $L_{2n-1} + L_{2n+1} = -L_{n-1}^2 + L_{n+1}^2$

x) $L_{2n-1} = -F_{n-2}^2 + F_n^2 + L_nF_n$

Proof.
i) From Theorem 2 (i) and Theorem 2 (iv), we get $F_{m+n-2} + F_{m-2}F_{n-2} = F_mF_n$ and $F_mF_n = F_{m+2}F_{n+2} - F_{m+n+2}$. From the equality of two identities,
$F_{m+n-2} + F_{m-2}F_{n-2} = F_{m+2}F_{n+2} - F_{m+n+2}$
is obtained. So,
$3F_{m+n} = F_{m+2}F_{n+2} - F_{m-2}F_{n-2}$ is obtained from
$F_{m+n-2} + F_{m+n+2} = F_{m+2}F_{n+2} - F_{m-2}F_{n-2}$.

ii) From Theorem 2 (i) and Theorem 2 (iii) , we obtain $F_{m+n-2} = -F_{m-2}F_{n-2} + F_mF_n$ and $F_{m+n} = -F_mF_{n-2} + F_{m+2}F_n$. From the sum of two identities,
$F_{m+n-2} + F_{m+n} =$
$= -F_{m-2}F_{n-2} + F_mF_n - F_mF_{n-2} + F_{m+2}F_n$
$= -(F_{m-2}+F_m)F_{n-2} + (F_m + F_{m+2})F_n$
$= -L_{m-1}F_{n-2} + L_{m+1}F_n$
$F_{m+n-2} + F_{m+n} = -L_{m-1}F_{n-2} + L_{m+1}F_n$
So, $L_{m+n-1} = -L_{m-1}F_{n-2} + L_{m+1}F_n$.

iii) From Theorem 2 (ii) and Theorem 2 (iv), we find that $F_{m+n} = -F_{m-2}F_n + F_mF_{n+2}$ and $F_{m+n+2} = -F_mF_n + F_{m+2}F_{n+2}$. From the sum of two identities,
$F_{m+n} + F_{m+n+2} =$
$= -F_{m-2}F_n + F_mF_{n+2} - F_mF_n + F_{m+2}F_{n+2}$
$= -(F_{m-2} + F_m)F_n + (F_m + F_{m+2})F_{n+2}$
$= -L_{m-1}F_n + L_{m+1}F_{n+2}$
So, $L_{m+n+1} = -L_{m-1}F_n + L_{m+1}F_{n+2}$.

iv) If taken as $m = n$ in Theorem 2 (i),
$F_{2n-2} = -F_{n-2}F_{n-2} + F_nF_n = -F_{n-2}^2 + F_n^2$ is obtained.

v) If taken as $m = n$ in Theorem 2 (iv),
$F_{2n+2} = -F_nF_n + F_{n+2}F_{n+2} = -F_n^2 + F_{n+2}^2$ is obtained.

vi) If taken as $m = n$ in (i),
$3F_{2n} = F_{n+2}F_{n+2} - F_{n-2}F_{n-2} = F_{n+2}^2 - F_{n-2}^2$ is obtained.

vii)If taken as $m = n$ in (ii),
$L_{2n-1} = -L_{n-1}F_{n-2} + L_{n+1}F_n$ is obtained.

viii)If taken as $m = n$ in (iii),
$L_{2n+1} = -L_{n-1}F_n + L_{n+1}F_{n+2}$ is obtained.

ix) From the sum of (vii) and (viii) identities,
$L_{2n-1} + L_{2n+1} =$
$= -L_{n-1}F_{n-2} + L_{n+1}F_n - L_{n-1}F_n + L_{n+1}F_{n+2}$
$= -(F_{n-2} + F_n)L_{n-1} + (F_n + F_{n+2})L_{n+1}$
$= -L_{n-1}L_{n-1} + L_{n+1}L_{n+1}$
$= -L_{n-1}^2 + L_{n+1}^2$
$L_{2n-1} + L_{2n+1} = -L_{n-1}^2 + L_{n+1}^2$ is obtained.

x) From the sum of (iv) and Theorem 2 (vi), $F_{2n-2} + F_{2n} = -F_{n-2}^2 + F_n^2 + L_nF_n$. So,

$L_{2n-1} = -F_{n-2}^2 + F_n^2 + L_nF_n$ is obtained.

2.3. Examining of Matrix $R^{n._L}$

n^{th} power of matrix R is obtained under Lorentz matrix multiplication as follows:

$$R^{2._L} = \begin{pmatrix}1 & 2\\ 2 & -1\end{pmatrix}._L\begin{pmatrix}1 & 2\\ 2 & -1\end{pmatrix} = \begin{pmatrix}L_2 & -L_3\\ -L_3 & -L_2\end{pmatrix},$$
$$R^{3._L} = \begin{pmatrix}1 & 2\\ 2 & -1\end{pmatrix}._L\begin{pmatrix}3 & -4\\ -4 & -3\end{pmatrix} = \begin{pmatrix}-L_5 & -F_3\\ -F_3 & L_5\end{pmatrix},$$
$$R^{4._L} = \begin{pmatrix}1 & 2\\ 2 & -1\end{pmatrix}._L\begin{pmatrix}-11 & -2\\ -2 & 11\end{pmatrix} = \begin{pmatrix}L_4 & 24\\ 24 & -L_4\end{pmatrix},$$
$$R^{5._L} = \begin{pmatrix}1 & 2\\ 2 & -1\end{pmatrix}._L\begin{pmatrix}7 & 24\\ 24 & -7\end{pmatrix} = \begin{pmatrix}41 & 38\\ -38 & -41\end{pmatrix},$$

…

Determinants of matrices are $detR^{2\cdot L} = -25$, $detR^{3\cdot L} = -125$, $detR^{4\cdot L} = -625$ and $detR^{5\cdot L} = -1325$.
Identities could not be found because matrix $R^{n\cdot L}$ could not be written in terms of the elements of the Fibonacci and Lucas Number sequences.

3. QUADRATIC EQUATIONS AND CHARACTERISTIC ROOTS OF $Q^{n\cdot L}$, $M^{n\cdot L}$ AND $R^{n\cdot L}$

3.1. Quadratic Equations and Characteristic Roots of $Q^{n\cdot L}$

Matrix $Q^{n\cdot L}$ could not be written in terms of the elements of the Fibonacci and Lucas Number sequences. Then, quadratic equation and characteristic roots could not be reached.

3.2. Quadratic Equations and Characteristic Roots of $M^{n\cdot L}$

The determinant of the matrix $M^{n\cdot L}$ found as $F_{n-2}F_{n+2} - F_n^2 = (-1)^{n+1}$. The quadratic equation of the matrix $M^{n\cdot L}$ is obtained as follows where $I^{2\cdot L} = \begin{pmatrix} -1 & 0 \\ 0 & 1 \end{pmatrix}$ is unit matrix.

$$|M^{n\cdot L} - xI^{2\cdot L}| = \left|\begin{pmatrix} F_{n-2} & F_n \\ F_n & F_{n+2} \end{pmatrix} - x\begin{pmatrix} -1 & 0 \\ 0 & 1 \end{pmatrix}\right|$$

$$= \left|\begin{pmatrix} F_{n-2} & F_n \\ F_n & F_{n+2} \end{pmatrix} - \begin{pmatrix} -x & 0 \\ 0 & x \end{pmatrix}\right|$$

$$= \left|\begin{pmatrix} F_{n-2} + x & F_n \\ F_n & F_{n+2} - x \end{pmatrix}\right|$$

$$= (F_{n-2} + x)(F_{n+2} - x) - F_n^2$$

$$= -x^2 + F_{n-2}F_{n+2} - x(F_{n-2} - F_{n+2}) - F_n^2$$

$F_{n+2} - F_{n-2} = L_n$ (please see [19]),
here, $F_{n-2} - F_{n+2} = -L_n$. If the obtained value is substituted in the quadratic equation of the matrix $M^{n\cdot L}$,

$$|M^{n\cdot L} - xI^{2\cdot L}| = -x^2 + xL_n + (-1)^{n+1} \quad (16)$$

is obtained. From the method Δ,

$$x_{1,2} = \frac{-L_n \pm \sqrt{L_n^2 - 4(-1)^n}}{-2} \quad (17)$$

roots are obtained.

3.3. Quadratic Equations and Characteristic Roots of $R^{n\cdot L}$

Matrix $R^{n\cdot L}$ could not be written in terms of the elements of the Fibonacci and Lucas Number sequences. Then, quadratic equation and characteristic roots could not be reached.

4. CONCLUSION

In this study, Lorentz matrix multiplication was used, unlike classical matrix multiplication, to find the n^{th} power of a matrix. Under classical matrix multiplication, previously known identities [Theorem 2] were obtained. However, new identities [Theorem 3] were obtained. In this article, matrices that type of 2×2 are used. In [5], matrices that type of $k \times k$ are worked to obtain generalized order-k Fibonacci and Lucas matrices under classical matrix multiplication. Unlike these matrices, different generalized matrices can be reached under Lorentz multiplication. At the same time, in this study, identities are obtained with classic Fibonacci and Lucas numbers. Differently from this article, in [5], identities are achieved with generalized order-k Fibonacci and Lucas numbers. These identities are generalized of identities obtained with classic Fibonacci and Lucas numbers for different k value. The quadratic equation and characteristic roots of the matrix M, which can be generalized by both classical matrix multiplication and Lorentz matrix multiplication, are obtained.

Funding

The author (s) has no received any financial support for the research, authorship or publication of this study.

Competing Interests

No conflict of interest or common interest has been declared by the authors.

Author's Contributions

All authors contributed equally to the writing of this paper. All authors read and approved the final manuscript.

Acknowledgment

This study was produced from the doctoral thesis I. Gökcan,"Some relations between special vertex values of suborbital graphs and special number sequences", PhD. Thesis, Karadeniz Technical University, Trabzon, 2021. prepared by the first author under the supervision of the second author. This study was presented orally at the "1st International Symposium on Recent Advances in Fundamental and Applied Sciences" held between 10-12.09.2021.

The Declaration of Ethics Committee Approval

This study does not require ethics committee permission or any special permission

The Declaration of Research and Publication Ethics

The authors of the paper declare that they comply with the scientific, ethical and quotation rules of SAUJS in all processes of the paper and that they do not make any falsification on the data collected. In addition, they declare that Sakarya University Journal of Science and its editorial board have no responsibility for any ethical violations that may be encountered, and that this study has not been evaluated in any academic publication environment other than Sakarya University Journal of Science.

REFERENCES

[1] B.U. Alfred, "An Introduction to Fibonacci Discovery",The Fibonacci Association, California, 1965.

[2] M. Bicknell, V.E. Hoggatt, "A Primer for the Fibonacci Numbers", The Fibonacci Quarterly, 1973.

[3] I.D. Ruggles,"Some Fibonacci results using Fibonacci-type sequences",The Fibonacci Quarterly, vol.1, pp.75-80, 1963.

[4] D. Tasci, E. Kilic,"On the order-k generalized Lucas numbers",Applied Mathematics and Computation, vol.155, pp.637-641,2004.

[5] E. Kilic, D. Tasci, "On the generalized order-k Fibonacci and Lucas numbers", Rocky Mountain Journal of Mathematics, vol.36, pp.1915-1926, 2006.

[6] C. Kızılateş, N. Tuglu, "A New generalization of convolved (p,q) −Fibonacci and (p,q) −Lucas polinomials", Journal of Mathematical and Computational Science, vol.7, pp.995-1005, 2017.

[7] F. Qi, C. Kızılateş, W.S. Du, "A closed formula for the Horadam polynomials in terms of a tridiagonal determinant", Symettery, vol. 11, pp. 782, 2019.

[8] C. Kızılateş, "New families of Horadam numbers associated with finite operators and their applications", Mathematical Methods in the Applied Sciences, vol. 44, pp. 14371-14381, 2021.

[9] C. Kızılateş, W.S. Du, F. Qi "Several determinantal expressions of generalized tribonacci polynomials and sequences, Tamkang Journal of Mathematics, vol. 53, pp. 277-291, 2022.

[10] H.W. Gould, "A history of the Fibonacci Q-matrix and a higher-dimensional problem", Fibonacci Quarterly, vol.9, pp.7-250, 1981.

[11] S. L. Basin, V. E. Hoggatt, "A primer on the Fibonacci sequence",Part II, Fibonacci Quarterly, vol.2, pp.61-68, 1963.

[12] C.H. King, "Some properties of the Fibonacci numbers", Master Thesis, San Jose State College, 1960.

[13] J.L. Brenner,"Lucas' matrix",The American Mathematical Monthly, vol.58, pp.220-221, 1951.

[14] J.S. Frame, "Continued fractions and matrices", The American Mathematical Monthly,vol.56,pp.98-103,1949.

[15] H. Schwerdtfeger, "Geometry of complex numbers, mathematical expositions", University of Totonto Press,1962.

[16] E.Jacobsthal, "Fibonaccische polynome und kreistheilungsgleichungen",Sitzungsberisc hte der Berliner Math. Gesellschaft, vol.17 pp. 43-47, 1919-20.

[17] G.K. White, "On generators and defining relations for the unimodular group M2",The American Mathematical Monthly, vol.71, pp.743-748, 1964.

[18] M.Bicknell, "Fibonacci fantasy:The square root of the Q matrix",Fibonacci Quarterly, vol.3,pp.67-71, 1965.

[19] T.Koshy, "Fibonacci and Lucas numbers with applications", Wiley-Interscience Publication, New York, 2001.

[20] H. Gündoğan, O. Keçilioğlu, "Lorentzian matrix multiplication and the motions on Lorentzian plane",Glasnık Matematic ki, vol.41, pp.329-334, 2006.

[21] J.G. Ratcliffe, "Foundations of Hyperbolic manifolds",Springer-Verlag, New York, 1994.

[22] O. Keçilioğlu, H. Gündoğan, "Pseudo matrix multiplication",Communications Faculty of Science University of Ankara Series A1 Mathematics and Statistics, vol.66, pp.37-43, 2017.

[23] J.H. Halton, "On a general Fibonacci identity",The Fibonacci Quarterly, vol.3, pp.31-43, 1965.

SAKARYA ÜNİVERSİTESİ
FEN BİLİMLERİ ENSTİTÜSÜ DERGİSİ

Sakarya University Journal of Science
SAUJS

ISSN 1301-4048 | e-ISSN 2147-835X | Period Bimonthly | Founded: 1997 | Publisher Sakarya University | http://www.saujs.sakarya.edu.tr/

Title: An Investigation of the Influence of Various Shaped Cutouts on the Free Vibration Behavior of Sandwich Structures

Authors: Ufuk DEMİRCİOĞLU, Mutlu Tarık ÇAKIR

Recieved: 2022-01-26 00:00:00

Accepted: 2022-05-30 00:00:00

Article Type: Research Article

Volume: 26
Issue: 4
Month: August
Year: 2022
Pages: 687-694

How to cite
Ufuk DEMİRCİOĞLU, Mutlu Tarık ÇAKIR; (2022), An Investigation of the Influence of Various Shaped Cutouts on the Free Vibration Behavior of Sandwich Structures. Sakarya University Journal of Science, 26(4), 687-694, DOI: 10.16984/saufenbilder.1063422
Access link
http://www.saujs.sakarya.edu.tr/en/pub/issue/72361/1063422

Sakarya University Journal of Science 26(4), 687-694, 2022

An Investigation of the Influence of Various Shaped Cutouts on the Free Vibration Behavior of Sandwich Structures

Ufuk DEMİRCİOĞLU*[1], Mutlu Tarık ÇAKIR[1]

Abstract

The current study deals with free vibration analysis of a sandwich beam in presence of different cutouts. PVC foam and glass fiber were used for the core and surface layers of the sandwich structures, respectively. First 6 frequencies of the sandwich structures were determined for different cutout shapes to see the effect of cutout shapes on the free vibration behavior of sandwich structures. For this, sandwich beams with different cutout shapes but with the same area were modeled. To see the effect of cutouts-shape only the shape of cutouts was changed and all other parameters were kept unchanged. Analyses were performed by using ANSYS apdl commercially available software. The analysis gives information about the influence of the cutout shape on the first six natural frequencies of the sandwich structures. From the results, it was observed that the changes of cutout shapes caused a significant decrease or increase in natural frequencies of sandwich structures beam depending on the cutout shape.

Keywords: Finite element method, free vibration, sandwich structure, various shaped cutouts

1. INTRODUCTION

These days, development in the industry is paramount. This advancing and ever-developing technology require advanced materials. As a result, researchers are in search of advanced materials. Sandwich structures are the one of the biggest candidate considered as one that can replace conventional materials, when high damping properties, fabrication diversity, good resitance to fatigue, good strength and good stiffness to weight ratio is desired. Sandwich structures can be determined as heterogeneous composite structures in which they are made up of two or more individual materials [1]. Sandwich structures consist of two thin face sheet materials and low-density core materials [2]. In this configuration, face sheet materials bear bending loads while the core carries the transfer shear force and increases stiffness by separating face sheet materials [3, 4].

The cutouts are inevitable because they are used as access locations for electrical and mechanical components. Therefore, the effects of the cutout on the free vibration characteristic of sandwich structure has been studied by several researchers extensively. N. Mishra et al. investigated the influence of the rectangular central cutout on the vibration characteristic of sandwich beam by using the finite element method. From analys the effect of cutout size on the free vibration caharacteristic of sandwich beam is determined [5]. H. K. Bhardwaj et al. studied the influence of triangular cutout on the vibration behavior of composite plates by using ANSYS APDL code.

* Corresponding author: udemircioglu@sivas.edu.tr
[1] Sivas University of Science and Technology
E-mail: tcakir@sivas.edu.tr
ORCID: https://orcid.org/0000-0002-9707-8271, https://orcid.org/0000-0002-0107-594X

The effect of parameters on the free vibration behavior of the sandwich structure was investigated [6]. S. Ramakrishna et al. studied the free vibration of composite plate with circular cutout at the center utilizing the finite element method. The orientation effect of fiber, different ratios (thickness, size), and hole size on the vibration behavior of the sandwich structure is evaluated [7]. S. Chikkol Venkateshappa et al. studied vibration analysis of composite plates with different shaped cutouts experimentally and numerically. The natural frequencies were got by using MSC/NASTRAN. Experimental results was compared to that of finite element results. The influence of ratio of aspect, size of cutout, and cut-out shape on the natural frequencies of sandwich plates were investigated [8]. H. K. Bhardwaj et al. studied the influence of cutouts at a different position on the vibration characteristic of sandwich composite plate experimentally and numerically. The effect of ratios of aspect, ratios of thickness, different material properties, cutouts, number of layers, and boundary conditions, for a cross-ply composite laminate with a skew hole, were evaluated [9]. J. Vimal et al. studied the influence of the circular hole on the vibration behavior of functionally graded composite plates by using the finite element method utilizing ANSYS. The influence of cutout, size of the cutout, index of volume fraction, boundary conditions, and ratio of thickness on the natural frequencies of sandwich structure is evaluated [10]. J. Vimal et al. studied the free vibration of sandwich structure with different cutouts by using the finite element method. Trapezoidal and circular plates that have cutouts are studied and the influence of volume

fraction, thickness ratio, and different boundary conditions on the natural frequencies of plates are studied [11]. They presented the influence of cutouts on the vibration behavior of composite plates. Maharudra, B. Arya, and T. Rajanna investigate the effect of central circular cutouts, plyorientation and boundary conditions on the vibration behavior of trapezoidal composite panels using finite element method. Edge conditions, trapezoidal shape ratio, cutout ratio and aspect ratio of the trapezoidal laminated panel are parametrized to investigate the effect of them. From study it was observed that different ply-orientations and boundary condition are more important parameters [12]. S. Dey, T. Mukhopadhyay, S. K. Sahu, and S. Adhikari investigated on stochastic natural frequency analyses of laminated composite curved panels with cetral rectangular cutout using support vector regression model. Vector regression model based on uncertainty quantification algorithm in along with latin hypercube sampling is developed for the study. The developed algorithm is validated by using finite element method. The effect of twist angle and variation in geometry (like cylindrical, spherical, hyperpolic paraboloid and plate) are investigated. From result it was observed that computational time is reduced by using above mentioned algorithm [13]. V. N. Van Do and C. H. Lee investigated free vibration analaysis of fuctionally graded material plate that has complex cutout. Isogeometric analysis method and quasi-3D higher-order shear deformation theory is employed for the vibration analysis. The ingredient fraction, plate geometric parameter and boundary condition are studied to see their effects on free vibration behavior of the plate. From results it was obtained that after a certain length-to-thickness ratio natural frequencies of perforated plate does not increase any more [14].

From the literature review above one can see there are lots of studies about the influence of cutouts on the free vibration characteristic of sandwich beam. Yet, there are no studies that investigate the effect of cutouts shape. The purpose of this study is to investigate the effect of the cutout shape on the free vibration behavior of the sandwich beam.

2. MATERIALS and METHODS

Different shaped cutouts located at the center of sandwich beams were considered to investigate the effect of the shape of cutouts on the first six natural frequency of the sandwich beam. Therefore, six different sandwich structures without cutout and with different cutouts but with the same area (1.1309x10^-4 m2) were modeled by using ANSYS apdl as illustrated in figure 1. The upper and lower skins of sandwich beam are composed of unidirectional glass fiber, while the core is assumed to be Polyvinyl Chloride (PVC)

foam. Properties of materials are given in table 1. The length and width of the sandwich beam are 250 mm and 20 mm, respectively. Each layer of the face sheet is 0.2 mm in thickness, whereas the thickness of PCV foam is 10 mm. The sandwich structure has a lay-up sequence (90^0/0^0/core/0^0/90^0).

Figure 1 A schematic model of a sandwich structure. 1) no cutout, 2) circular cutout, 3) triangular cutout, 4) rectangular cutout, 5) pentagonal cutout, 6) hexagonal cutout.

To perform the study of free vibration analysis of the sandwich beam with cutouts, the sandwich structure is designed using ANSYS 20.0 apdl software. Shell 281 element is considered to model the sandwich structure since Shell 281 is suitable for analyzing thin to moderately-thick shell structures. Shell 281 may be used for layered applications for modeling composite shells or sandwich construction. Block Lanczos method is used to get the mode shapes and natural frequency of the sandwich structure under a cantilevered boundary condition. Mesh size is 1 mm as global element size and quadratic mesh is used.

Table 1
Properties of materials considered for analysis

Property	Glass Fiber	PVC Foam
Density (Kg/m^3)	2000	60
Young's Modulus E_x (pa)	4.5e+10	7e+07
Young's Modulus E_y (pa)	1e+10	-
Young's Modulus E_z (pa)	1e+10	-
Poisson's Ratios v_{xy}	0.3	0.3
Poisson's Ratios v_{yz}	0.4	0.3
Poisson's Ratios v_{zx}	0.3	0.3
Modulus of Rigidity G_{xy} (pa)	5e+09	2.6923e+07
Modulus of Rigidity G_{xz} (pa)	3.8462e+09	2.6923e+07
Modulus of Rigidity G_{yz} (pa)	5e+09	2.6923e+07

3. RESULTS and DISCUSSIONS

The influence of different cutouts shape on the free vibration characteristic of sandwich structure has been investigated by using Ansys apdl. Different cutouts circular, triangular, rectangular, pentagonal, and hexagonal-shaped holes were considered in this study. To verify the accuracy of the presented finite element method, validation is made by comparing the results with those presented by [15]. The results of the validation study are given in table 2.

Table 2
Comparison of present model with those of a similar model for a laminated plate [15].

Mode	Reference [15]	Present
1.	35.055	35.054
2.	126.4	126.39
3.	218.46	218.45
4.	420.57	420.54
5	606.05	606.00

In this study, the influence of different shaped cutouts on the free vibration characteristic of the sandwich structure is investigated by using ANSYS apdl. Different cutouts but the same area are subtracted from the center of the sandwich plate and the effects of cutout shape on vibration were evaluated. To evaluate the effects of cutouts shape on the free vibration, only the shape of the cutout is changed but the cutout area is held constant regardless of cutouts shape.

Table 3 represents the natural frequency and figure 2 shows the change of natural frequency with cutout shapes of each model. The results indicate that changes in the cutout shapes give a significant influence on the stiffness of the sandwich beam, which leads to decreasing or increasing the natural frequencies of the perforated sandwich beam. Along with stiffness, mass of beam has also effect on the natural frequencis of sandwich structures. However in this study we subtracted the same area from sandwich beams. Same area means the same mass. So, there is no mass effect on the free vibration behavior of sandwich strucres in this study. Through the results, we found out that the cutout shape leads to a change in the natural frequencies of the sandwich beam when compared to the sandwich plate with no cutout. Naturel frequencies increase for all cutout shape except for triangular cutout in mode one, mode two, and mode five. Cutouts cause a decrease in natural frequencies in mode three and mode six, whereas it gives rise an increase in natural frequencies in mode four. To conclude, different cutout shapes changed the natural frequencies of sandwich beam significantly. This situation coincides with experimental and numerical results in the literature. For example, N. Mishra et al. investigated the influence of the rectangular central cutout on the vibration behavior of sandwich structure by using the finite element method. They reported that up to a certain cutout percentage natural frequencies decrease but thereafter they increase [5]. A similar study was verified by researchers using the finite element method [16]. Some studies performed with different cutouts with similar results can be found in ref [17, 18].

Table 3
The natural frequency of sandwich structures with different cutouts.

The shape of the cutouts	Mode 1. Frequency	Mode 2. Frequency	Mode 3. Frequency	Mode 4. Frequency	Mode 5. Frequency	Mode 6. Frequency
No cutouts	571.24	979.99	1200.05	1237.24	1922.18	2483.96
Circular cutouts	580.66	998.25	1188.07	1281.06	1947.58	2423.62
Triangular cutouts	571.12	976.96	1169.18	1279.37	1918.73	2404.57
Rectangular cutouts	581.39	998.05	1185.83	1280.21	1951.30	2372.53
Pentagonal cutouts	577.09	993.16	1184.11	1282.86	1938.51	2423.38
Hexagonal cutouts	577.52	995.20	1183.23	1285.28	1940.74	2422.60

Figure 2 Changes of the natural frequency with cutout shapes

4. CONCLUSION

In this study, free vibration study of the perforated sandwich structure is studied. The finite element method is employed by using the ANSYS apdl to study the free vibration characteristics of a sandwich beam when there are cutouts. The study focus on to reveal the influence of various shaped cutouts on the free vibration behavior of the sandwich structure. Sandwich beams consist of glass fiber face sheet and PVC foam is considered for evaluation of numerical results. The analysis shows the influence of various cutout shapes on the natural frequency of the sandwich beam. From the results, it was observed that the vibration

characteristic of sandwich beams changes with cutout shapes without showing any trend. Therefore, it can be concluded that the natural frequencies of the laminated composite sandwich beam are significantly influenced by the cutout shapes.

Acknowledgments

We thank to reviewers and editors for their valuable time they spent evaluating our article.

The Declaration of Conflict of Interest/ Common Interest

"No conflict of interest or common interest has been declared by the authors".

Authors' Contribution

The authors contributed equally to the study.

The Declaration of Ethics Committee Approval

This study does not require ethics committee permission or any special permission.

The Declaration of Research and Publication Ethics

"The authors of the paper declare that they comply with the scientific, ethical, and quotation rules of SAUJS in all processes of the paper and that they do not make any falsification on the data collected. In addition, they declare that Sakarya University Journal of Science and its editorial board have no responsibility for any ethical violations that may be encountered, and that this study has not been evaluated in any academic publication environment other than Sakarya University Journal of Science."

REFERENCES

[1] C. Wick, Tool and Manufacturing Engineers Handbook: Materials, Finishing, and Coating, vol. 3. 1985.

[2] K. N. Shivakumar, Argade, S. D., Sadler, R. L., Sharpe, M. M., Dunn, L., Swaminathan, G., & Sorathia, U. "Processing and properties of a lightweight fire resistant core material for sandwich structures," Journal of Advanced Materials vol. 38, no. 1, pp. 32–38, 2006.

[3] C. Chen, A. M. Harte, N. A. Fleck, "Plastic collapse of sandwich beams with a metallic foam core," International Journal of Mechanical Sciences, vol. 43, no. 6, pp. 1483–1506, 2001.

[4] A. Shahdin, L. Mezeix, C. Bouvet, J. Morlier, Y. Gourinat, "Fabrication and mechanical testing of glass fiber entangled sandwich beams: A comparison with honeycomb and foam sandwich beams," Composite. Structures., vol. 90, no. 4, pp. 404–412, 2009.

[5] N. Mishra, B. Basa, S. K. Sarangi, "Free vibration Analysis of Sandwich Plates with cutout," IOP Conference Series: Materials Science and Engineering, vol. 149, no. 1, 2016.

[6] H. K. Bhardwaj, J. Vimal, A. K. Sharma, "Study of Free Vibration Analysis of Laminated Composite Plates with Skew Cut-outs based on FSD," Journal of Civil Engineering and Environmental Technology, vol. 1, no. 1, pp. 71–75, 2014.

[7] S. Ramakrishna, K. M. Rao, and N. S. Rao, "Free vibration analysis of laminates with circular cutout by hybrid-stress finite element," Composite. Structure., vol. 21, no. 3, pp. 177–185, 1992.

[8] S. Chikkol Venkateshappa, P. Kumar, T. Ekbote, "Free vibration studies on plates with central cut-out," CEAS Aeronaut. Journal., vol. 10, no. 2, pp. 623–632, 2019.

[9] H. K. Bhardwaj, J. Vimal, A. K. Sharma, "Study of Free Vibration Analysis of Laminated Composite Plates with Skew Cut-outs based on FSDT," Journal of Civil Engineering and Environmental Technology., vol. 1, no. 1, pp. 71–75, 2014.

[10] J. Vimal, R. K. Srivastava, A. D. Bhatt, A. K. Sharma, "Free vibration analysis of

functionally graded skew plates with circular cutouts," International Journal of Engineering, Science and Technology., vol. 6, no. 3, 2014.

[11] J. Vimal, R. K. Srivastava, A. D. Bhatt, A. K. Sharma, "Free vibration analysis of moderately thick functionally graded plates with multiple circular and square cutouts using finite element method," Journal of Solid Mechanics, vol. 7, no. 1, pp. 83–95, 2015.

[12] Maharudra, B. Arya, T. Rajanna, "Effect of trapezoidal shaped laminated composite plate with and without cutout on vibration characteristics," Materials Today: Proceedings, vol. 45, pp. 34–40, 2020.

[13] S. Dey, T. Mukhopadhyay, S. K. Sahu, S. Adhikari, "Effect of cutout on stochastic natural frequency of composite curved panels," Composites Part B: Engineering., vol. 105, pp. 188–202, 2016.

[14] V. N. Van Do, C. H. Lee, "Free vibration analysis of FGM plates with complex cutouts by using quasi-3D isogeometric approach," International Journal of Mechanical Sciences., vol. 159, pp. 213–233, 2019.

[15] P. Pushparaj, B. Suresha, "Free vibration analysis of laminated composite plates using finite element method," Polymers and Polymer Composites, vol. 24, no. 7, pp. 529–538, 2016.

[16] D. Bhatt, Y. Mishra, D. P. K. Sharma, "Model Analysis of Centre Circular Cutout of Laminated Composite Plate and Square Skew Plate by using FEM," vol. 3, no. 11, pp. 8–16, 2014.

[17] S. Mondal, A. K. Patra, S. Chakraborty, N. Mitra, "Dynamic performance of sandwich composite plates with circular hole/cut-out: A mixed experimental-numerical study," Composite. Structures., vol. 131, no. April 2016, pp. 479–489, 2015.

[18] M. S. H. Al-araji, A. S. Gafer, R. S. Saed, "Vibration Analysis of Perforated Composite Sandwich Plate," Journal of University of Babylon for Engineering Sciences., vol. 26, no. 26, pp. 166–178, 2018.

SAKARYA ÜNİVERSİTESİ
FEN BİLİMLERİ ENSTİTÜSÜ DERGİSİ

Sakarya University Journal of Science
SAUJS

ISSN 1301-4048 | e-ISSN 2147-835X | Period Bimonthly | Founded: 1997 | Publisher Sakarya University | http://www.saujs.sakarya.edu.tr/

Title: Global Existence and Uniqueness of The Inviscid Velocity-Vorticity Model of the g-Navier-Stokes Equations

Authors: Özge KAZAR, Meryem KAYA

Recieved: 2021-04-01 00:00:00

Accepted: 2022-05-30 00:00:00

Article Type: Research Article

Volume: 26
Issue: 4
Month: August
Year: 2022
Pages: 695-702

How to cite
Özge KAZAR, Meryem KAYA; (2022), Global Existence and Uniqueness of The Inviscid Velocity-Vorticity Model of the g-Navier-Stokes Equations. Sakarya University Journal of Science, 26(4), 695-702, DOI: 10.16984/saufenbilder.1097179
Access link
http://www.saujs.sakarya.edu.tr/en/pub/issue/72361/1097179

Sakarya University Journal of Science 26(4), 695-702, 2022

Global Existence and Uniqueness of The Inviscid Velocity-Vorticity Model of the g-Navier-Stokes Equations

Özge KAZAR*[1], Meryem KAYA[2]

Abstract

In this paper, we prove the global existence and uniqueness of the weak solutions to the inviscid velocity-vorticity model of the g-Navier-Stokes equations. The system is performed by entegrating the velocity-pressure system which is involved by using the rotational formulation of the nonlinearity and the vorticity equation for the g-Navier-Stokes equations without viscosity term. In this study we particularly interest the inviscid velocity-vorticity system of the g-Navier-Stokes equations over the two dimensional periodic box $\Omega = (0,1)^2 \subset R^2$.

Keywords: Existence and uniqueness, g-Navier-Stokes equations, inviscid velocity-vorticity model

1. INTRODUCTION

Velocity-vorticity formulation have been considered extensively by many scientists for example [1-4]. In [2] Gardner et al. studied continuous data assimilation to a velocity-vorticity formulation of the 2D Navier-Stokes equations. In [1, 3, 4] researchers studied in velocity-vorticity formulation of the Navier-Stokes equations by numerically. In recent years, the velocity-vorticity formulation and Voigt regularization combined for some fluid dynamical models. In [5] Larios et al. suggested the velocity-vorticity model for the Navier-Stokes-Voigt equations and they studied the global well-posedness of this system. Pei [6] studied velocity-vorticity-Voigt model for 3D Boussinesq equations and he considered global well-posedness and also higher order regularity. Inviscid form of the models in computational fluid dynamics have been attracted and extensively studied by many researchers [7-9]. Using classical Picard iteration method Cao, Lunasin and Titi prove global existence and uniqueness of inviscid Bardina model [7]. Larios and Titi have studied the inviscid Navier-Stokes-Voigt equations. They proved the global existence and uniqueness of weak solutions and higher order regularity of the solutions of this system [8]. In this study we are particularly interest the following velocity-vorticity system of the g-Navier-Stokes (gNS) equations over the two dimensional periodic box $\Omega = (0,1)^2 \subset R^2$:

* Corresponding author: ozgekazar@gmail.com
[1] Hitit Universıty, Vocatıonal School of Technical Sciences
ORCID: https://orcid.org/0000-0003-4876-3077
[2] Gazi University
E-mail: meryemk@gazi.edu.tr
ORCID: https://orcid.org/0000-0002-5932-9105

$$\frac{\partial u}{\partial t} - \nu\Delta_g u + \nu\frac{1}{g}(\nabla g.\nabla)u + w \times u + \nabla \mathrm{P} = \mathrm{f}, \quad (1)$$

$$\frac{\partial w}{\partial t} - \nu\Delta_g w + \nu\frac{1}{g}(\nabla g.\nabla)w + (u.\nabla)\mathrm{w} = \nabla \times \mathrm{f} + \mathrm{w}\left(\frac{\nabla g}{g}.u\right). \quad (2)$$

In this system $P = p + \frac{1}{2}|u^2|$, u represent velocity, w which play the role of vorticity, f is an external forcing term. We consider this problem under the periodic boundary conditions. We assume u, p and w and the first derivative of u, w to be spatially periodic. The existence and uniqueness of the weak and strong solutions of this system with the viscosity term is proved in [10]. Now we consider the following inviscid form. The inviscid velocity-vorticity model of the g-Navier-Stokes is equivalent to the functional differential equations

$$\frac{du}{dt} + P_g(w \times u) = P_g f, \quad (3)$$

$$\frac{dw}{dt} + B_g(u, w) = P_g(\nabla \times \mathrm{f}) + P_g\left(\mathrm{w}\left(\frac{\nabla g}{g}.u\right)\right), \quad (4)$$

$$\nabla.(gu) = 0, \qquad \nabla.(gw) = 0, \quad (5)$$

$$u(x, 0) = u_0, \qquad w(x, 0) = w_0, \quad (6)$$

where, for simplicity, we assume f to be time independent. We rewrite $B_g = P_g\big((u.\nabla)w\big)$ and $P_g: L^2(\Omega, g) \longrightarrow H_g$ is Helmholtz-Leray orthogonal projection. The function $g = g(x_1, x_2)$ is positive real-valued smooth function. We assume that g satisfies the following conditions,

i. $g(x_1, x_2) \in C^\infty(\Omega)$.

ii. $0 < m_o \leq g(x_1, x_2) \leq \mathrm{M}_o$ where m_o and M_o are positive constants for all $(x_1, x_2) \in \Omega$.

iii. $\|\nabla g\|_\infty = \sup_{(x_1,x_2)\in\Omega} |\nabla g(x_1, x_2)| < \infty$.

Throughout in this study c will denote a generic positive constant. It can be different from line to line. This study is organized as follows. In section 2 we give some notations and present the mathematical spaces. We also give some preliminary results [11, 12]. In section 3, we investigate global existence and uniqueness of the inviscid velocity-vorticity model of the gNS equations using the classical Picard iteration method.

2. PRELIMINARIES AND FUNCTIONAL SETTING

In this section we introduce the usual notation used in the context [11, 12]. $L^2(\Omega, g)$ denotes the Hilbert space with the inner product and norm

$(u, v)_g = \int_\Omega (u, v) g dx$ and

$\|u\|^2_{L^2(\Omega,g)} = (u, u)_g,$

respectively. The inner product and norm in H_g are the same of $L^2(\Omega, g)$. The norm in $H^1(\Omega, g)$

$\|u\|^2_{H^1(\Omega,g)} = \left[(u, u)_g + \sum_{\mathrm{I}=1}^{2}(D_i u, D_i u)_g\right]^{\frac{1}{2}},$

where $D_i = \frac{\partial}{\partial x_i}$. The norm in V_g are the same of $H^1(\Omega, g)$. The two spaces $L^2(\Omega)$ and $L^2(\Omega, g)$ have equivalent norms in the following inequalities

$m_0\|u\|^2_{L^2(\Omega)} \leq \|u\|^2_{L^2(\Omega,\mathrm{g})} \leq M_0\|u\|^2_{L^2(\Omega)},$

where m_0 and M_0 positive constants. We define spaces in the periodic setting for the gNS equations are

$$\mathcal{V}_1 = \left\{u \in \left(C^{\infty}_{per}(\Omega)\right)^2 : \nabla(gu) = 0,\ \int_\Omega udx = 0\right\},$$

$\boldsymbol{H_g}$ = the closure of $\mathcal{V}_1$ in $L^2(\Omega, g)$,

$\boldsymbol{V_g}$ = the closure of $\mathcal{V}_1$ in $H^1(\Omega, g)$,

in two dimensions. Vorticity is considered as a scalar, we define vorticity space as

$$\mathcal{V}_2 = \left\{u \in C^{\infty}_{per}(\Omega): \nabla(gu) = 0, \int_\Omega udx = 0\right\},$$

H_g = the closure of $\mathcal{V}_2$ in $L^2(\Omega, g)$,

V_g = the closure of $\mathcal{V}_2$ in $H^1(\Omega, g)$,

$$H_{gcurl} = \{f \in H_g:\ \nabla \times f \in L^2(\Omega, g)\ \}.$$

Now we rewrite g-Laplacian operator and g-Stokes operator and some notations in the following

$$-\Delta_g u := -\frac{1}{g}(\nabla. g\nabla u) = -\Delta u - \frac{1}{g}(\nabla \mathrm{g}. \nabla)u,$$

$$A_g u = P_g\left[-\tfrac{1}{g}(\nabla. g\nabla \mathrm{u})\right],$$

respectively. A_g have countable eigenvalues which are satisfying as in the below;

$$0 < \lambda_g \le \lambda_1 \le \lambda_2 \le \lambda_3 \le \cdots$$

where $\lambda_g = \frac{4\pi^2 m_0}{M_0}$. The Poincare inequality

$$\sqrt{\lambda_g}\|\phi\|_{L^2} \le \|\nabla\phi\|_{L^2},$$

satisfy for all $\phi \in V_g$. Since the operators A_g and P_g are self adjoint, using integration by parts we have

$$\langle A_g u, u\rangle_g = \int_\Omega (\nabla u, \nabla u) g dx = \langle \nabla u, \nabla u\rangle_g = \|\nabla u\|_g.$$

The bilinear operator $B_g: V_g \times V_g \to V_g'$

$$B_g(u, v) = P_g(u.\nabla)v$$

and for this term the inner product of $w \in V_g$, we get

$$\langle B_g(u, v), w\rangle_{V_g'} = b_g(u, v, w).$$

The trilinear form b_g defined as

$$b_g(u, v, w) = \sum_{i,j=1}^{n} \int_\Omega u_i\,(D_i v_j) w_j g dx = (P_g(u.\nabla)v, w)_g.$$

We have the following properties

i. $b_g(u, v, w) = -b_g(u, w, v)$,
ii. $b_g(u, v, v) = 0$.

The function Cu defined by

$$Cu = P_g\left[\tfrac{1}{g}(\nabla g. \nabla)u\right]$$

and the inner product of $v \in V_g$ we write

$$\langle Cu, v\rangle_g = \langle \frac{1}{g}(\nabla g. \nabla)u, v\rangle_g = b_g\left(\frac{\nabla g}{g}, u, v\right).$$

It is easy to show this term belong to $L^2(0, T; H_g)$ and hence belong to $L^2\left(0, T; V_g'\right)$.

2.1. Lemma

The bilinear operator B_g satisfies the following inequality;

$$\left|\langle B_g(u,v),w\rangle_{V_g'}\right|$$

$$\leq c\|u\|_{L^2}^{1/2}\|\nabla u\|_{L^2}^{1/2}\|\nabla v\|_{L^2}\|w\|_{L^2}^{1/2}\|\nabla w\|_{L^2}^{1/2},$$

$for\ all$ u, v, w $\in V_g$ [11,12]. (7)

3. GLOBAL EXISTENCE AND UNIQUENESS OF THE INVISCID VELOCITY-VORTICITY MODEL OF THE g-NAVIER-STOKES EQUATIONS

In this section, we will established the global existence and uniqueness of the inviscid velocity-vorticity model of the gNS equations using the classical Picard iteration method. Note that the $(3)-(4)$ equality is understood to hold in the sense of $\boldsymbol{V_g'}\times V_g'$.

3.1. Theorem

Let $u_0\in \boldsymbol{V_g}$, $w_o\in V_g$ and $f\in \boldsymbol{V_g'}$, $\nabla\times f\in V_g'$. There exist a short time $T^*\left(\|u_0\|_{\boldsymbol{V_g}},\|w_0\|_{V_g}\right)$ such that the equations $(3)-(6)$ has a unique solution $u,w\in C^1([-T^*,T^*],\boldsymbol{V_g}\times V_g)$.

Proof

We will use the classical Picard iteration principle to prove the short time existence and uniqueness theorem. Namely, it is enough to show that the vector field $N(u)=f-w\times u$ and $N(w)=\nabla\times f+\mathrm{w}\left(\frac{\nabla g}{g}.u\right)-B_g(u,w)$ is locally Lipschitz in the Hilbert Space $\boldsymbol{V_g}$ to $\boldsymbol{V_g'}$ and V_g to V_g' respectively. From the classical theory of ordinary differential equations we consider the equivalent equation for $(3)-(4)$ respectively.

$$u(t)=u_0-\int_0^t w(s)\times u(s)ds+ft, \quad (8)$$

$$w(t)=w_0-\int_0^t B_g\big(u(s),w(s)\big)ds+\int_0^t\left(\mathrm{w(s)}\left(\frac{\nabla g}{g}.u(s)\right)\right)ds+(\nabla\times f)t\,. \quad (9)$$

Let $u_1,u_2\in \boldsymbol{V_g}$ and $w_1,w_2\in V_g$, $\boldsymbol{\phi}\in \boldsymbol{V_g}$ and $\phi\in V_g$

$$\|N(u_1)-N(u_2)\|_{\boldsymbol{V_g'}}=\|w_1\times u_1-w_2\times u_2\|_{\boldsymbol{V_g'}}=\|w_1\times(u_1-u_2)+(w_1-w_2)\times u_2\|_{\boldsymbol{V_g'}}=\sup_{\substack{\phi\in \boldsymbol{V_g}\\ \|\boldsymbol{\phi}\|_{\boldsymbol{V_g}}=1}}\left|\langle w_1\times(u_1-u_2)+(w_1-w_2)\times u_2,\boldsymbol{\phi}\rangle_{\boldsymbol{V_g'}}\right|, \quad (10)$$

Applying Poincare inequality and (7) for (10) we write

$$\|N(u_1)-N(u_2)\|_{\boldsymbol{V_g'}}\leq c\|w_1\|_{L^2}^{1/2}\|\nabla w_1\|_{L^2}^{1/2}\|u_1-u_2\|_{L^2}^{1/2}\|\nabla(u_1-u_2)\|_{L^2}^{1/2}+c\|u_2\|_{L^2}^{1/2}\|\nabla u_2\|_{L^2}^{1/2}\|w_1-\mathrm{w}_2\|_{L^2}^{1/2}\|\nabla(w_1-\mathrm{w}_2)\|_{L^2}^{1/2}\leq c\frac{1}{\lambda_g^{1/2}}\|\nabla w_1\|_{L^2}\|\nabla(u_1-u_2)\|_{L^2}+c\frac{1}{\lambda_g^{1/2}}\|\nabla u_2\|_{L^2}\|\nabla(w_1-w_2)\|_{L^2}. \quad (11)$$

Similar estimates can be obtained for $N(w)$ as in the following

$$\|N(w_1)-N(w_2)\|_{V_g'}=\left\|\mathrm{w}_1\left(\frac{\nabla g}{g}.u_1\right)-B_g(u_1,w_1)-\mathrm{w}_2\left(\frac{\nabla g}{g}.u_2\right)+B_g(u_2,w_2)\right\|_{V_g'}\leq\left\|\mathrm{w}_1\left(\frac{\nabla g}{g}.(u_1-u_2)\right)+(\mathrm{w}_1-\mathrm{w}_2)\left(\frac{\nabla g}{g}.u_2\right)\right\|_{V_g'}+\left\|B_g(u_1,w_1-\mathrm{w}_2)+B_g(u_1-u_2,w_2)\right\|_{V_g'}\leq\sup_{\substack{\phi\in V_g\\ \|\phi\|_{V_g}=1}}\left|\langle\mathrm{w}_1\left(\frac{\nabla g}{g}.(u_1-u_2)\right)+(\mathrm{w}_1-\mathrm{w}_2)\left(\frac{\nabla g}{g}.u_2\right),\phi\rangle_{V_g'}\right|+\sup_{\substack{\phi\in V_g\\ \|\phi\|_{V_g}=1}}\left|\langle B_g(u_1,w_1-\mathrm{w}_2)+B_g(u_1-u_2,w_2),\phi\rangle_{V_g'}\right|. \quad (12)$$

Again using Poincare inequality and (7) for (12) we obtained

$$\|N(w_1)-N(w_2)\|_{V_g'}\leq c\|\nabla g\|_\infty\|w_1\|_{L^2}^{1/2}\|\nabla w_1\|_{L^2}^{1/2}\|u_1-u_2\|_{L^2}^{1/2}\|\nabla(u_1-u_2)\|_{L^2}^{1/2}+c\|\nabla g\|_\infty\|w_1-\mathrm{w}_2\|_{L^2}^{1/2}\|\nabla(w_1-\mathrm{w}_2)\|_{L^2}^{1/2}\|u_2\|_{L^2}^{1/2}\|\nabla u_2\|_{L^2}^{1/2}+c\|u_1\|_{L^2}^{1/2}\|\nabla u_1\|_{L^2}^{1/2}\|w_1-\mathrm{w}_2\|_{L^2}^{1/2}\|\nabla(w_1-$$

$w_2)\|_{L^2}^{1/2} + c\|u_1 - u_2\|_{L^2}^{1/2}\|\nabla(u_1 - u_2)\|_{L^2}^{1/2}\|w_2\|_{L^2}^{1/2}\|\nabla w_2\|_{L^2}^{1/2} \leq$
$c\|\nabla g\|_\infty \frac{1}{\lambda_g^{1/2}}\|\nabla w_1\|_{L^2}\|\nabla(u_1 - u_2)\|_{L^2} +$
$c\|\nabla g\|_\infty \frac{1}{\lambda_g^{1/2}} \|\nabla(w_1 - w_2)\|_{L^2}\|\nabla u_2\|_{L^2} +$
$c\frac{1}{\lambda_g^{1/2}}\|\nabla u_1\|_{L^2}\|\nabla(w_1 - w_2)\|_{L^2} + c\frac{1}{\lambda_g^{1/2}}\|\nabla(u_1 - u_2)\|_{L^2}\|\nabla w_2\|_{L^2}.$ (13)

Now adding the inequalities (11) and (13), we have

$\|N(u_1) - N(u_2)\|_{\boldsymbol{V}_g'} + \|N(w_1) - N(w_2)\|_{V_g'} \leq$
$c\frac{1}{\lambda_g^{1/2}}\|\nabla w_1\|_{L^2}\|\nabla(u_1 - u_2)\|_{L^2} +$
$c\frac{1}{\lambda_g^{1/2}}\|\nabla u_2\|_{L^2}\|\nabla(w_1 - w_2)\|_{L^2} +$
$c\|\nabla g\|_\infty \frac{1}{\lambda_g^{1/2}}\|\nabla w_1\|_{L^2}\|\nabla(u_1 - u_2)\|_{L^2} +$
$c\|\nabla g\|_\infty \frac{1}{\lambda_g^{1/2}} \|\nabla(w_1 - w_2)\|_{L^2}\|\nabla u_2\|_{L^2} +$
$c\frac{1}{\lambda_g^{1/2}}\|\nabla u_1\|_{L^2}\|\nabla(w_1 - w_2)\|_{L^2} + c\frac{1}{\lambda_g^{1/2}}\|\nabla(u_1 - u_2)\|_{L^2}\|\nabla w_2\|_{L^2}$.

Then, after rearranging the right hand side of the above inequality, it follows that

$\|N(u_1) - N(u_2)\|_{\boldsymbol{V}_g'} + \|N(w_1) - N(w_2)\|_{V_g'} \leq$
$\left(c\frac{1}{\lambda_g^{1/2}}\|\nabla w_1\|_{L^2} + c\|\nabla g\|_\infty \frac{1}{\lambda_g^{1/2}}\|\nabla w_1\|_{L^2} + c\frac{1}{\lambda_g^{1/2}}\|\nabla w_2\|_{L^2}\right)\|\nabla(u_1 - u_2)\|_{L^2} +$
$\left(c\frac{1}{\lambda_g^{1/2}}\|\nabla u_2\|_{L^2} + c\|\nabla g\|_\infty \frac{1}{\lambda_g^{1/2}} \|\nabla u_2\|_{L^2} + c\frac{1}{\lambda_g^{1/2}}\|\nabla u_1\|_{L^2}\right)\|\nabla(w_1 - w_2)\|_{L^2}.$

We have

$\|N(u_1) - N(u_2)\|_{\boldsymbol{V}_g'} + \|N(w_1) - N(w_2)\|_{V_g'} \leq$
$\leq \frac{2c}{\lambda_g^{1/2}} \|u_1 - u_2\|_{\boldsymbol{V_g}}\left(\|w_1\|_{V_g} + \|w_2\|_{V_g}\right) +$
$\frac{2c}{\lambda_g^{1/2}} \|w_1 - w_2\|_{V_g}\left(\|u_1\|_{\boldsymbol{V_g}} + \|u_2\|_{\boldsymbol{V_g}}\right).$ (14)

For any large enough R such that $\|u_1\|_{\boldsymbol{V_g}}$, $\|u_2\|_{\boldsymbol{V_g}}$, $\|w_1\|_{V_g}$, $\|w_2\|_{V_g} \leq R$, we have

$\|N(u_1) - N(u_2)\|_{\boldsymbol{V}_g'} + \|N(w_1) - N(w_2)\|_{V_g'} \leq$
$\frac{4cR}{\lambda_g^{1/2}} \|u_1 - u_2\|_{\boldsymbol{V_g}} + \frac{4cR}{\lambda_g^{1/2}}\|w_1 - w_2\|_{V_g} \leq$
$\frac{4cR}{\lambda_g^{1/2}}\left(\|u_1 - u_2\|_{\boldsymbol{V_g}} + \|w_1 - w_2\|_{V_g}\right)$ (15)

From the inequality (15) we say that $N(u)$ and $N(w)$ is locally Lipschitz continuous function from the Hilbert Space $\boldsymbol{V_g}$ to $\boldsymbol{V_g'}$ and V_g to V_g' respectively. Therefore by the classical theory of ordinary differential equation $(8) - (9)$ has a unique fixed point in a small interval $[-T^*, T^*]$ and $u \in C\left([-T^*, T^*]; \boldsymbol{V_g}\right)$, $w \in C\left([-T^*, T^*]; V_g\right)$ (see, e.g., [13]). In particular, the forcing term f assume to be time independent and since the terms under the integral sign to the right of (8) and (9) are continuous functions with valued in $\boldsymbol{V_g'}$ and V_g' so left hand side $u(t)$ and $w(t)$ are differentiable and (3) and (4) satisfied with $u(0) = u_0$ and $w(0) = w_0$. From these results give us the local-in-time existence and uniqueness of solutions.

3.2. Theorem

Let $f \in \boldsymbol{V_g}$, $\nabla \times f \in V_g$ and $u_0 \in \boldsymbol{V_g}$, $w_o \in V_g$. Then the system in $(3) - (6)$ has a unique solution $u, w \in C^1((-\infty, \infty), \boldsymbol{V_g} \times V_g)$.

Proof

Let's show that global existence for the equations $(3) - (6)$. To do this we need to show that on the maximal interval of existence, $\|u(t)\|_{\boldsymbol{V_g}}$ ve $\|w(t)\|_{V_g}$ remain finite. Let $[0, T_{max}]$ be the maximal interval of existence. If $T_{max} = \infty$ in this case nothing need to prove. Let's admit

$T_{max} < \infty.$ (16)

This implies that

$\limsup_{t \to T_{max}^-} \|u(t)\|_{\boldsymbol{V_g}} = \infty \; and \; \limsup_{t \to T_{max}^-} \|w(t)\|_{V_g} = \infty.$ (17)

However we will provide a contradiction to the result in (17) We take inner product (3) with the $A_g u(t)$. We get

$$\frac{d}{dt}\|\nabla u\|_{L^2}^2 \le 2\left|\left(P_g(w\times u), A_g u\right)_g\right| + 2\left|\left(P_g f, A_g u\right)_g\right|. \quad (18)$$

Cauchy-Schwarz and Young inequalities are applied for each term on the right hand side for (18), we write

$$\frac{d}{dt}\|\nabla u\|_{L^2}^2 \le \frac{1}{2}\left\|A_g u\right\|_{L^2}^2 + \frac{27}{4}c\|\mathrm{w}\|_{L^2}^2\|\nabla w\|_{L^2}^2\|\nabla u\|_{L^2}^2 + 4\|\mathrm{f}\|_{L^2}^2. \quad (19)$$

We take inner product (4) with the $A_g w(t)$, we get

$$\frac{1}{2}\frac{d}{dt}\|\nabla w\|_{L^2}^2 + b_g(u,w,A_g w) \le \left(P_g\left(w\left(\frac{\nabla g}{g}.u\right)\right), A_g w\right)_g + \left(\nabla\times P_g f, A_g w\right)_g.$$

And then we write

$$\frac{d}{dt}\|\nabla w\|_{L^2}^2 \le 2\left|b_g(u,w,A_g w)\right| + 2\left|\left(P_g\left(w\left(\frac{\nabla g}{g}.u\right)\right), A_g w\right)_g\right| + 2\left|\left(\nabla\times P_g f, A_g w\right)_g\right|. \quad (20)$$

Cauchy-Schwarz and Young inequalities are applied for each term on the right hand side for (20), we have

$$\frac{d}{dt}\|\nabla w\|_{L^2}^2 \le \frac{3}{4}\left\|A_g w\right\|_{L^2}^2 + \frac{27}{4}c\|\mathrm{u}\|_{L^2}^2\|\nabla u\|_{L^2}^2\|\nabla w\|_{L^2}^2 + \frac{4c\|\nabla g\|_\infty^2}{m_0^2\lambda_g}\|\nabla w\|_{L^2}^2\|\nabla u\|_{L^2}^2 + 4\|\nabla\times\mathrm{f}\|_{L^2}^2. \quad (21)$$

Adding the inequalities (19) and (21), we obtain

$$\frac{d}{dt}\left(\|\nabla u\|_{L^2}^2 + \|\nabla w\|_{L^2}^2\right) \le \frac{1}{2}\left\|A_g u\right\|_{L^2}^2 + \frac{3}{4}\left\|A_g w\right\|_{L^2}^2 + \frac{27}{4}c\|\mathrm{w}\|_{L^2}^2\|\nabla w\|_{L^2}^2\|\nabla u\|_{L^2}^2 + \frac{27}{4}c\|\mathrm{u}\|_{L^2}^2\|\nabla u\|_{L^2}^2\|\nabla w\|_{L^2}^2 + \frac{4c\|\nabla g\|_\infty^2}{m_0^2\lambda_g}\|\nabla w\|_{L^2}^2\|\nabla u\|_{L^2}^2 + 4\|\mathrm{f}\|_{L^2}^2 + 4\|\nabla\times\mathrm{f}\|_{L^2}^2. \quad (22)$$

In [10] we proved that $u\in L^\infty(0,T;\boldsymbol{H_g})$, $w\in L^\infty(0,T;H_g)$ and $u\in L^\infty(0,T;\boldsymbol{V_g})$, $w\in L^\infty(0,T;V_g)$ because of u and w weak and strong solution of the velocity-vorticity model of gNS equations. So we have

$$\underset{s\in[0,T]}{Sup}\|u(s)\|_{\boldsymbol{H_g}}^2 \le K_1,\ \underset{s\in[0,T]}{Sup}\|w(s)\|_{H_g}^2 \le K_2$$

and

$$\underset{s\in[0,T]}{Sup}\|\nabla u(s)\|_{\boldsymbol{H_g}}^2 \le K_8,\ \underset{s\in[0,T]}{Sup}\|\nabla w(s)\|_{H_g}^2 \le K_9,$$

where K_1, K_8 depend on u_0, f, ν, T and K_2, K_9 depend on w_0, f, ν, T. Using the above results in (22) we get

$$\frac{d}{dt}\left(\|\nabla u\|_{L^2}^2 + \|\nabla w\|_{L^2}^2\right) \le \frac{1}{2}\left\|A_g u\right\|_{L^2}^2 + \frac{3}{4}\left\|A_g w\right\|_{L^2}^2 + \left(\frac{27}{4}cK_2K_9 + \frac{27}{4}cK_1K_9\right)\|\nabla u\|_{L^2}^2 + \frac{4c\|\nabla g\|_\infty^2}{m_0^2\lambda_g}K_8\|\nabla w\|_{L^2}^2 + 4\|\mathrm{f}\|_{L^2}^2 + 4\|\nabla\times\mathrm{f}\|_{L^2}^2. \quad (23)$$

After some arrangement right hand side of the (23) we have the following inequality.

$$\frac{d}{dt}\left(\|\nabla u\|_{L^2}^2 + \|\nabla w\|_{L^2}^2\right) - \alpha\left(\|\nabla u\|_{L^2}^2 + \|\nabla w\|_{L^2}^2\right) \le \frac{1}{2}\left\|A_g u\right\|_{L^2}^2 + \frac{3}{4}\left\|A_g w\right\|_{L^2}^2 + 4\|\mathrm{f}\|_{L^2}^2 + 4\|\nabla\times\mathrm{f}\|_{L^2}^2, \quad (24)$$

where

$$\alpha = max\left\{\frac{27}{4}cK_2K_9 + \frac{27}{4}cK_1K_9, \frac{4c\|\nabla g\|_\infty^2}{m_0^2\lambda_g}K_8\right\}.$$

Using Gronwall inequality for (24), we get

$$\|\nabla u(t)\|_{L^2}^2 + \|\nabla w(t)\|_{L^2}^2 \le e^{\alpha t}\left[\|\nabla u(0)\|_{L^2}^2 + \|\nabla w(0)\|_{L^2}^2\right] + e^{\alpha t}\left[\frac{1}{2}\int_0^t\left\|A_g u\right\|_{L^2}^2 ds + \frac{3}{4}\int_0^t\left\|A_g w\right\|_{L^2}^2 ds\right] + 4te^{\alpha t}\|\mathrm{f}\|_{L^2}^2 + 4te^{\alpha t}\|\nabla\times\mathrm{f}\|_{L^2}^2.$$

Since u and w are strong solutions of the velocity-vorticity model of gNS equations in [10], we have $u \in L^2(0,T;D(\boldsymbol{A_g})),\ w \in L^2(0,T;D(A_g))$. Thus

$$\int_0^T \|A_g u\|_{L^2}^2 dt \le K_{10}, \int_0^T \|A_g u\|_{L^2}^2 dt \le K_{11}.$$

Using these results, we get

$$\begin{aligned}\|\nabla u(t)\|_{L^2}^2 + \|\nabla w(t)\|_{L^2}^2 &\le e^{\alpha t}\left[\|\nabla u(0)\|_{L^2}^2 + \|\nabla w(0)\|_{L^2}^2\right] \\ &+ e^{\alpha t}\left[\frac{1}{2}K_{10} + \frac{3}{4}K_{11} + 4t\|\mathrm{f}\|_{L^2}^2 \right. \\ &\left. + 4t\|\nabla \times \mathrm{f}\|_{L^2}^2\right].\end{aligned}$$

For all $t < T_{max}$. Hence we obtain

$$\begin{aligned}\|\nabla u(t)\|_{L^2}^2 + \|\nabla w(t)\|_{L^2}^2 &\le e^{\alpha T_{max}}\left[\|\nabla u(0)\|_{L^2}^2 \right. \\ &\left. + \|\nabla w(0)\|_{L^2}^2\right] \\ &+ e^{\alpha T_{max}}\left[\frac{1}{2}K_{10} + \frac{3}{4}K_{11} \right. \\ &+ 4T_{max}\|\mathrm{f}\|_{L^2}^2 \\ &\left. + 4T_{max}\|\nabla \times \mathrm{f}\|_{L^2}^2\right].\end{aligned}$$

This gives us

$$\limsup_{t \to T_{max}^-} \|u(t)\|_{V_g}^2 + \|w(t)\|_{V_g}^2 \le K$$

This is a contradiction to conclusion (17) The proof is completed.

Acknowledgments

We would like to thank the editor referees for their valuable comments and remarks that led to a great improvement of the article.

Funding

The authors has no received any financial support for the research, authorship or publication of this study.

The Declaration of Conflict of Interest/ Common Interest

No conflict of interest or common interest has been declared by the authors.

Authors' Contribution

The authors contributed equally to the study.

The Declaration of Ethics Committee Approval

This study does not require ethics committee permission or any special permission.

The Declaration of Research and Publication Ethics

In the writing process of this study, international scientific, ethical and citation rules were followed, and no falsification was made on the collected data. Sakarya University Journal of Science and its editorial board have no responsibility for all ethical violations. All responsibility belongs to the responsible author and this study has not been evaluated in any academic publication environment other than Sakarya University Journal of Science.

REFERENCES

A sample references list is given below;

[1] M. Akbas, L. G. Rebholz, C. Zerfas, "Optimal vorticity accuracy in an efficient velocity-vorticity method for the 2D Navier-Stokes equations," Calcolo, Vol. 55, no. 1, pp.1-29, 2018.

[2] M. Gardner, A. Larios, L. G. Rebholz, D. Vargun, C. Zerfas, "Continuous data assimilation applied to a velocity-vorticity formulation of the 2D Navier-Stokes equations," Electronic Research Archive, Vol. 29, no. 3, pp. 2223-2247, 2021.

[3] T. B. Gatski, "Review of incompressible fluid flow computations using the vorticity-velocity formulation," Applied Numerical Mathematics, Vol. 7, no. 3, pp. 227-239, 1991.

[4] T. Heister, M. A. Olshanskii, L. G. Rebholz, "Unconditional long-time stability of a velocity- vorticity method for the 2D Navier-Stokes equations," Numerische Mathematik, Vol. 135, no. 1, pp. 143-167, 2017.

[5] A. Larios, Y. Pei, L. Rebholz, "Global well-posedness of the velocity-vorticity-Voigt model of the 3D Navier-Stokes equations," Journal of Differential Equations, Vol. 266, no. 5, pp. 2435-2465, 2019.

[6] Y. Pei, "Regularity and Convergence Results of the Velocity-Vorticity-Voigt Model of the 3D Boussinesq Equations," Acta Applicandae Mathematicae, Vol. 176, no. 1, pp. 1-25, 2021.

[7] Y. Cao, E. M. Lunasin, E. S. Titi, "Global well-posedness of the three-dimensional viscous and inviscid simplified Bardina turbulence models," Communications in Mathematical Sciences, Vol. 4, no. 4, pp. 823-848, 2006.

[8] A. Larios, E. S. Titi, "Higher-order global regularity of an inviscid Voigt-regularization of the three-dimensional inviscid resistive magnetohydrodynamic equations," Journal of Mathematical Fluid Mechanics, Vol. 16 no.1, pp. 59-76, 2014.

[9] J. Wu, "Viscous and inviscid magneto-hydrodynamics equations," Journal d'analyse Mathematique, Vol. 73 no. 1, pp. 251-265, 1997.

[10] Ö. Kazar, M. Kaya, "On the weak and strong solutions of the velocity-vorticity model of the g-Navier-Stokes equations," (to appear).

[11] J. Roh, "g-Navier-Stokes equations," PhD, University of Minnesota, Minneapolis, MN, USA, 2001.

[12] R. Temam, "Navier-Stokes equations, theory and numerical analysis," American Mathematical Society, Chelsea Publication, Vol.343, pp. 161-163, pp. 252-290, 2001.

[13] M. Schechter, "An Introduction to Nonlinear Analysis," Cambridge University Press, 2004.

SAKARYA ÜNİVERSİTESİ
FEN BİLİMLERİ ENSTİTÜSÜ DERGİSİ

Sakarya University Journal of Science
SAUJS

ISSN 1301-4048 | e-ISSN 2147-835X | Period Bimonthly | Founded: 1997 | Publisher Sakarya University | http://www.saujs.sakarya.edu.tr/

Title: Notes On A Rare Species From Turkey: Opopanax chironius

Authors: Mehmet SAĞIROĞLU

Recieved: 2022-02-10 00:00:00

Accepted: 2022-05-31 00:00:00

Article Type: Research Article

Volume: 26
Issue: 4
Month: August
Year: 2022
Pages: 703-709

How to cite
Mehmet SAĞIROĞLU; (2022), Notes On A Rare Species From Turkey: Opopanax chironius. Sakarya University Journal of Science, 26(4), 703-709, DOI: 10.16984/saufenbilder.1071214
Access link
http://www.saujs.sakarya.edu.tr/en/pub/issue/72361/1071214

Sakarya University Journal of Science 26(4), 703-709, 2022

Notes On A Rare Species From Turkey: *Opopanax chironius*

Mehmet SAĞIROĞLU*[1]

Abstract

The first Turkish record of *Opopanax chironius* (L.) W.D.J. Koch was firstly collected from Tekirdağ province in 1969. The morphological description of the species in "Flora of Turkey and the East Aegean Islands" was written based on these specimens. The species has not been collected for along time untilday. This species was re-collected by us during a flora study in 2014 at Malkara district, Karaiğdemir Dam road in Tekirdağ. The name of this species was mispelled. This situation has been corrected here. Its correct use is *Opopanax chironius*. Also, in this study, expanded description of the species, pictures, disdictive morphological characters from other species, ecology, fruit photographs and ethnobotanical usage were given.

Keywords: *Opopanax*, Apiaceae, Ethnobotanical use, Tekirdağ, Turkey

1. INTRODUCTION

Turkey shows a rich floristic structure with nearly 12 thousand seed plant species. Floristic research are studies that reveal the existence and diversity of plants in a region. Flora studies in Türkey have not been completed yet. In many floristic studies, interesting findings emerge for Turkey [1-8]. One of these studies was carried out by us in the Tekirdağ-Malkara region. In this study, *O.chironius* species belonging to the genus Opopanax were investigated.

Opopanax chironius (L.)W.D.J. Koch, was first defined by Linnaues as *Laserpitium chironium* L. Later, in 1824 Wilhelm Daniel Joseph Koch conveyed it to *Opopanax* [9, 10]. *Opopanax chironius* has been added to Turkish flora by Asuman Baytop in the years 1969 and 1971, depending upon the samples collected in Tekirdağ (Turkey). The species was listed as the number 1 species of the genus Opopanax in the Flora of Turkey and East Aegean Islands [11]. According to Güner et al. it has four species [12]. Asuman Baytop claimed that she collected the plant on the road of Tekirdağ-İnecik motorway. We have not found any of this species within this locality. However, we have collected it on the dam way between Tekirdağ city and Malkara province in 2014. *O.chironius* stays at the sideways of the road and its population is very rare and under human pressure. Its collection has been recorded only by Asuman Baytop and there is no record that could be encountered in any herbaria. Apart from the Asuman Baytop collections, there is no collection for the Flora of Turkey record. No record has been detected for the species in the herbaria searched. Furthermore, there is no any

[1] * Corresponding author: msagiroglu@sakarya.edu.tr
[1] Sakarya University
ORCID: https://orcid.org/ 0000-0001-8654-3361

record related to *Opopanax chironius* amongst the plants collected by the herbalist researchers in the book of Turkish Botanic Investigations by Baytop [13]. There is no record related to that O. chironius in Edinburgh herbarium and other herbaria related to Turkish flora, except the collection of Baytop. In this case, this plant may have come to Turkey from Europe by trade caravans. The collection area of A. Baytop is a main route for the trade to Europe. Thus, it is likely that *O.chironius* has come from those caravans to Turkey and has been gone natural in those regions.

While the genus *Opopanax* is represented by 3 species in Turkish Flora, the amount of species number has been increased to 4 in the book of Turkish Plant List. Here *Crenasciadium siifolium* Boiss. & Heldr.species of the genus *Crenasciadium* has been transfered to *Opopanax* [12]. This species is an endemic one. There exists no any other endemic species in the genus *Opopanax*. Even though the *O. chironius* is not an endemic one, it is known as rare species in single locality. In this study, the expanded definition of *O.chironius*, its pictures, morphological properties which are discrete from other Opopanax, ecological features, the pictures of fruits with rosin channels, distribution map and, the plant's ethnobotanical usage are given.

2. MATERIALS AND METHOD

This work is carried out on the collected plant materials of *Opopanax chironius* (Figure 1). The collected samples have been arranged to be the herbarium material and then are being kept at the SAKU herbarium for further purposes. For the description of *O.chironius*, measurement number of 20 has been selected for every character of different specimen. We have also investigated the samples *O.chironius* collected by Asuman Baytop and kept at E herbarium. Samples of *O.chironius* have been collected only from one place, that was on Tekirdağ, Hayrabolu, Karaiğdemir dam way. That plant has not been found in the locality from where Baytop claimed to collect it. The flowery and fruity samples of the species have been collected from the collection area, the population status has been determined and all investigations have performed on those collected samples. Turkish naming has been determined using the book "*Türkiye Bitkileri Listesi (Damarlı Bitkiler)* (Turkish Plant List (Vascular Plants)" [12].

In addition, no new collection records from Turkey were found in ANK, GAZI, HUB, KNYA, AEF, ISTE, NGBB, SAKU, AIBU, VANF, DUOF, E, G, K, WU herbariums.

3. RESULTS AND DISCUSSION

Opopanax chironius has not been collected since 1969. It has been collected in the years 2014 and 2020 during a research in a place near the first collection locality. With this study it is aimed to complete some lack of information such as the policarpicity, stem leaves' properties and the fruit rosin channel numbers as well as the plant distribution map. *O.chironius* is a plant generally distributed in Europe and Balkans. The eastern most border in Turkey for this plant is known to be Thrace region. *O. chironius* has not been observed and recorded in any other region except Thrace in Turkey. *O.chironius* differs with its habitus, base leaves and fruits from the other *Opopanax* species (*O.hispidus (Friv.)Gris., O. persicus Boiss., O. siifolius (Boiss. &Heldr.) Menemen* in Turkey.

3.1. Description

Opopanax chironius (L.) W.D.J. Koch, Nova Acta Acad. Leop.-Carol. 12{1):96 (1824) (Figure 1).

Perennial, stout, erect, fibrous collar present to 10 cm. Rootstock oblong, 5-10 cm diameter. Stem terete, 3-4 m tall, weakly sulcate, weakly glaucescent, glabrous, 2-5 cm diameter at the base. Basal leaves triangular-ovate in outline, upto 140 cm long, 2 pinnate, petiole 15-20 cm long; ultimate segments broadly oblong-elliptic, (4-)6-30 cm long, subsessile, with crenate-serrate margins, stellate hairy, upper leaves sheated, Sheaths semiamplexicaul, weakly inflated, papery, glabrous, lamina reduced. Inflorescence long branches paniculate-corymbose. Central

umbel peduncled, 1.5- 4 cm long; lateral umbels 2-6 cm long, usually fertile, rays 2-3.5 cm, (9-) 14-22 (-28), umbellules (12-) 14-18 (-22) flowered. Bracts linear-lanceolate, 4-6, 6-10 mm long, setaceous, usually deciduousus. Bracteoles linear-lanceolate,1-2, 3-7 mm long, setaceous, deciducous. Sepal absent. Petal yellow, obovate-lanceolate,1.5-2 x 0.5-1 mm, glabrous, deflexed. Pedicel 5-8 mm long, glabrous. Mericarps 5-8 x 3-4 mm, elliptic, glabrous, brown when ripe, dorsal ridges filiform, margins thickened, 1 mm wide; style 1-2 mm, persıstent, stigma capitate; dorsal vittae 1-2, commussural 6-10. Fl. 6.

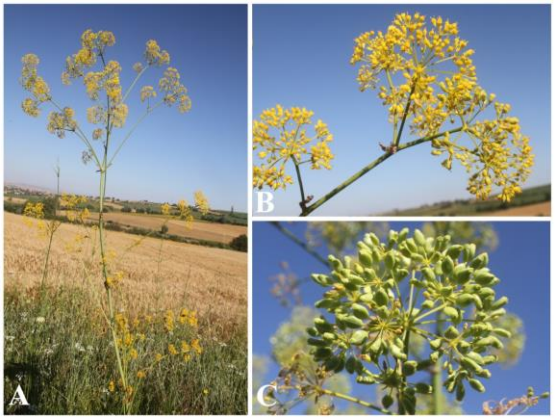

Figure 1 *Opopanax chironius*: A- habitus; B- Flower; C-Fruit (Photo M.Sağıroğlu 6787).

Opopanax chironius shows distribution in Thrace region. *O. hispidus* (Friv.) Gris. and *O. persicus* Boiss are observed througout Anatolia (Figure 2).

When the species of the genus opopanax are examined, it is seen that *O. chironius* is distinctly different from other species of Opopanax. The base leaves and lobes of *O.chironius* are bigger and oblong- elliptic. Bracts and bracteoles are not persistent and deciduous when the plant goes for fructify. *O.chironius*' commissural rosin channels are big in number when compared with other species (Table 3). Similar differences are valid for other characteristics as well (Table 1).

There exists a misusage for the name of *Opopanax chironius*. This species is named as *O.chironium* in Europe, Turkey and Iranian flora. Furthermore, it named as *O.chironium* the species *O.chironius* in various publications. According to "International Code of Nomenclature for algae, fungi, and plants", it is not true to name it *O.chironium* [14]. This is because the Latin names are not spelled correctly. The gender of the genus Opopanax is masculine. Species epithet has to be in accordance with it, and the species masculine form has to be ended with letters 'us'. Hence the epithet should take 'us' letters at the end. This situation has been corrected in "The plantlist a working list of all plant species"[15] the true usage will be as follows: *Opopanax chironius* (L.). W.koch

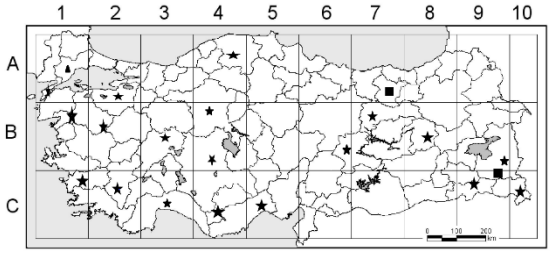

Figure 2 Distribution of the species *Opopanax chironius*(▲), *O. hispudus* (✶), *O. persicus* (■).

3.2. Ecology and habitat

Opopanax chironius has been only collected from the Tekirdağ, Malkara, Karaiğdemir dam way. This species is grown in the altitude of 250-300 m. It is grown in brown forest soil at the pathways (Figure1 a,b.c), sideways of the streams and rocky hilsides together with *Eryngium creticum* Lam.,*Eryngium campestre* L. var. *campestre*, *Oenanthe fistulosa* L.), *Daucus guttatus* Sibth. and Sm., *Conium maculatum* L.,*Caucalis platycarpos* L., *Scandix pecten-veneris* L., *Torilis arvensis* Huds. and Link, *Turgenia latifolia* (L.) Hoffm., *Fraxinus angustifolia* Vahl, *Prunus spinosa* L., *Clinopodium vulgare* L. *Briza maxima* L., *Carduus nutans* L. subsp. *leiophyllus* (Petrovič) Stoj. and Stef., *Cirsium vulgare* (Savi.) Ten., *Centaurea solstitialis* L.subsp. *solstitialis*, *Raphanus raphanistrum* L. subsp. *raphanustrum*, *Carpinus betulus* L., *Quercus robur* L.subsp. *robur*, *Quercus frainetto* Ten., *Quercus petraea* Liebl.subsp. *petraea*, *Quercus cerris* L. subsp. *cerris*, *Ulmus glabra* Huds., *Rosa canina* L., *Salvia sclarea* L., *Chenopodium album* L.subsp. *album* var. *album*, *Rubus sanctus* Schreb., *Papaver dubium* subsp. Lecoqii Lamotte, *Poa*

bulbosa L., *Avena barbata subsp. Barbata* pottex Link, *Epilobium hirsutum* L., *Lolium rigidum var. rigidum* Gaudin, *Dactylis glomerata subsp. hispanica* (Roth) Nyman, *Datura stramomium* L., *Ecballium elaterium* (L.) A. Rich., *Xanthium spinosum* L., *Sambucus nigra* L.

3.2. Distribution

Opopanax chironius is a limited species in Thrace region in Turkey. It is known from two localities. In the researches carried out in the locality specified in the flora of Turkey, no any population encountered due to the lack of habitat and destroying the area to create cultivated area. However, it was collected from the observation area of the Karaiğdemir dam road, which is close to this first area (Figure 1). In that area the plant grows in the sideways of the road, in the rocky areas and hill sides in an altitude of 280 m. It could be collected solely from one location and has been represented by 25 individuals. Since it stays close to the cultivated area its generation is under imperilement.

The definition of the species *O. chironius* at European, Italian and Turkey Floras is very short and insufficient [11, 16, 17]. In this study we have given a wide definition by increasing the information related to the characters of the species. Being polycarpic, presence of fibrous collars, properties of stem leaves, inflorescense state, status of petals and the number of the mericarp vittae are given for the first time with the current study. Furthermore, properties of the stem, base leaves measures, ray number and similar other characteristics are widely discussed in that work

Both species related to genus *Opopanax* (*O. hispidus*, *O. persicus*) and the other plant species are well known by Anatolian indigenes. So, a condensed ethnobothanical cultural heritage is naturaly created [18-29]. Even though there exists limited usage of the species *Opopanax chironius* in that region by local indigenes, some special applications have been detected during our survey. The reason for that limited usage may be attributed to the limited area at which the plant is grown.

In our survey it has been found that the indigenes use the plant (*Opopanax chironius*) for headache and arthralgia. In the villages Kınıklar and Evciler it used to apply widely than today. The villagers uproot the plant, cut it when it is fresh, boil it and drink it, it was good for headaches and arthralgia.

Opopanax chirionus has widespread ethnobotanic usage in the world. The extracts obtained from the water, coming from the cut stem of the plant, dried under the sun light is used in falk medicine. Charming and persistent odour rosin has antispasmodic activity. In addition to those it can be used in the healing processes of menstruel disorders, asthma and cronic visceral illnesses.

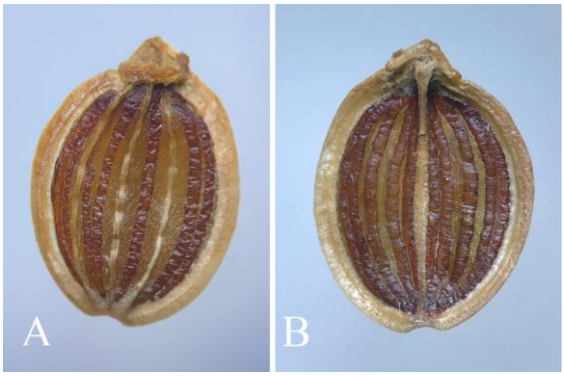

Figure 3 *Opopanax chironius*:A- fruit dorsal vittae; B- Commissural vittae

Table 1 Discrete properties of the species *Opopanax chironius*, *O.hispidus* and *O. persicus*.

Characters	*O. chironius*	*O. hispidus*	*O.persicus*
Ultimate segments	Stellate hairs, oblong-elliptic	Stellate hairs, elliptic	glabrous, elliptic

Inflorescence	Long branches panicula te-corymb ose	panicula te-corymb ose	panicul ate-corymb ose
Bırakte ve bırakteoller	Undistinct deciduous	distinct, persistent	distinct , persistent
Mericarps	elliptic, 5–8 × 3–4 mm	obovate, oblong-elliptic, 7–12 × 6–9 mm	elliptic, 8–10 × 6–8 mm
Lateral wings	1 mm wide, thick	2–3 mm wide, thin	1–1.5 wide, thin
Dorsal vittae	1–2	1	1
Commissural vittae	6–10	2–6	2–4

3.3. Searched samples

Opapanax chironius. A1Tekirdağ: The way from Tekirdağ to Hayrabolu, riverside, 24.vii.1969, *A. Baytop* 15790 E!;between Tekirdağ and Hayrabolu, 19 km from Tekirdağ, riverside, 15. vii. 1971, *A. Baytop* 20676 E!; ibid; 21.v.1971, *A. Baytop* 19813 E!; between Tekirdağ and İnecik, 20 from Tekirdağ, under *Fraxinus* trees, 31.vii. 1971, *A. Baytop* 20716 E!.Tekirdağ, Malkara Karaiğdemir baraj yolu, 3. km, 280 m, 27.05.2014. *M. Sağıroğlu* 4439; ibid; 02.10.2014, *M. Sağıroğlu* 4883; ibid; 03.07.2020, *M. Sağıroğlu* 6787, *A.B. Semerci* and *D. Karaduman*.

Opopanax hispidus. A7 Gümüşhane: Kızılcık köyü, Kuşakkaya mevkii, *P. sylvetsris* ormanı, 2050 m, 11.07.1989, *Z. Aytaç* 2812 GAZI!.

B4 Ankara: Kayaş, vadi içi, 6.7.1947,Davis 13150, E!.B4 Ankara, Tuz Gölü kenarı, 905 m, 25. july. 1969, *J. Darrah* 180, E!.

B4 Ankara: Çankaya, Dikmen, korunmuş step,1000 m, 26.06.1985, *A.Koçak*, V.3393 GAZI!.

B4 Kırıkkale, Keskin, Böbrek dağı, Tılkıllı köyü, step, 650 m, 19.07.1992, *U. Güler* 1981 GAZI!.

C1 Muğla: Köyceğiz, Sultaniye, taşlık alanlar,100-300 m, 16.06.1991, *A. Güner* 9417 GAZI!.

C3 Antalya: Akseki Gidefi dağı, Evlek boğazı güneyi, kayalıklar, 1780 m, 5.7.1994, *A. Duran* 1883 GAZI!.

C3 Antalya: Akseki, Çukurköy yaylası, Toptaş mevkii, 1950-2050 m, 19.07.1995, *A.Duran* 2933 GAZI!.

C3 Antalya : Manavgat to Akseki 40. miles, 800 m, 14.June. 1962, *Davis* 35790, E!Malatya: Malatya- Maraş 40. km, 1400 m, 9.June. 1960, *Stainto* and *Henderson* 5464, E!.

C4 Konya: Hadim, Gevne vadiisi, Beyrekli köyü, 1600 m, 22.07.2021, *M. Sağıroğlu* 7051 SAKU C4 Konya: Hadim, Geyne vadiisi, Tasmur yaylası-Beyreli arası, 1800 m, 10.06.1999, *H.Duman* 6976 GAZI!.

C10 Van: distr. Hoşap, Başkale, 2400 m, 30.july. 1954, *Davis* 23341 and *O. Polunin*, E!.

C9 Van: Çatak, Atlıhan köyü çevresi, meşe açıklığı, 1350 m, 30.06.2003, *B. Bani* 1980 GAZI!.

Van:Gürpınar, Sarıyaprak-Güleçler köyü arası, step, 18.07.2001, 2300 m, *M. Ünal* 6111 VANF!.

Bitlis: Adilcevaz, Süte yaylası, alpin çayır, kayalık yamaçlar, 2000 m, 11.08.1993, *Y. Altan* 5509 GAZI!.

Opopanax persicus. örnek No: K 00109718 [Photo!]. Van:Gürpınar, Giyimli- Güleçler köyü arası, step, 01.08.2002, 2400 m, *M. Ünal* 7893 VANF!.

Acknowledgements

The author would like to thank for latin rules Prof. Dr.Hayri Duman, Alican Bahadır Semerci

and Didem Karaduman for their assistance in fieldwork, and grateful to the curators ANK, GAZI, HUB, KNYA, AEF, ISTE, NGBB, SAKU, AIBU, VANF, DUOF, E, G, K, WU.

Funding

The author has no received any financial support for the research, authorship or publication of this study.

REFERENCES

[1] D. Karaduman, M. Sağıroğlu, Flora of Acarlar Longoz (Floodplaın) (Sakarya) and its Surroundings, Sakarya University Journal of Science, 25(1), 215-237, 2021.

[2] İ. Eker, A. Çelik, A. Kaya, A. Aydın, Bolu'nun Endemik ve Nadir Bitkileri, Ankara, Durnat Ofset Matbaacılık San. VeTic. Lim. Şti., 2019. ISBN 978-605-80817-0-3.

[3] İ. Eker, A. Kaya, A. Çelik, N. Eker, Bolu Abant İzzet Baysal Üniversitesi Kampüs Florası, Bolu, Kemal Matb. San. Ve Tic. Ltd.Şti., 2018. ISBN 978-605-245-222-6.

[4] C.S. Demir, İ. Eker, PetaloId Monocotyledonous Flora of Bolu ProvInce, IncludIng Anatolions on CrItIcal PetaloId Geophytes of Turkey. Pegem Akademi May Ankara, 2015. ISBN 978-605-318-145-3.

[5] M. Sağıroğlu, The Geophytes of Sakarya City, Sakarya University Journal of Science, 24/5, 991-1007, 2020.

[6] O. Aslan, M. Sağıroğlu, Flora of Arslanbey (İzmit, Turkey) and Cultivated Plants in İzmit City Center, Biological Diversity and Conservation, 4(2), 172-184, 2011.

[7] M.S. Yılancı, M. Sağıroğlu, Kocaeli-Karamürsel-Yalakdere Beldesi ve Çevresinin Florası, SAU Fen Bil. Der., 17(3), 405-423, 2013.

[8] M. Turna, M. Sağıroğlu, Flora of Ikramiye Valley (Sapanca) Sakarya. Journal of Bartin Faculty of Forestry, 22 (3): 963-978, 2020.

[9] C. Linnaeus, Species Plantarum, vol. 1. Laurentii Salvii, Holmiae, 249 pp 1753.

[10] Leop.-Carol. O. chironium, Nova Acta Acad, 12 (1):96, 1824.

[11] D.F. Chamberlain. Opopanax W.Koch, In: Davis, P.H. (ed.), Flora of Turke yandthe East Aegean Islands 4: 471-473, Edinburgh Univ. Press. Edinburgh, 1972.

[12] A. Güner, S. Aslan, T. Ekim, M. Vural, M.T. Babaç, Türkiye Bitkileri Listesi (Damarlı Bitkiler), Nezahat Gökyiğit Botanik Bahçesi ve Flora Araştırmaları Derneği Yayını. İstanbul, 2012.

[13] A. Baytop, Türkiye'de Botanik Tarihi Araştırmaları, Çetin Matbaacılık, İstanbul, 2003.

[14] International Code of Nomenclature for algae, fungi, and plants: https://www.iapt-taxon.org/nomen/main.php, (date of access:08.02.2022).

[15] The plant list: https//www.theplantlist.org, (date of access:08.02.2022).

[16] T.G. Tutin,V.H. Heywood, N.A. Burges, D.M. Moore, S.M. Valentine, D.A.Webb, Flora Europae, volume 2, 360, Cambridge, 2001.

[17] B. Anzalone, A. Becherer, F. Ehrendorfer, F. Merxmüller, H. Metlesics, G. Montelucci, F., Rasetti, T., Re,ichstein, T. and I. Segelberg, Flora D'Italia, Volume secondo 509, 1982 Bologna.

[18] E. Tuzlacı, P:E: Aymaz, Turkish folk Medicinal Plants Part IV: Gönen(Balıkesir),Fitoterapia, 72, 323-343, 2001.

[19] Ş. Yıldırımlı, Etnobotanik ve Türk Etnobotaniği, Kebikeç-İnsan Bilimleri İçin Kaynak Araştırmaları Dergisi 17: 175-193, 2004.

[20] G. Genç, N. Özhatay, An ethnobotanical study in Çatalca (European part o Istanbul) II, Turkish Journal of Pharmaceutical Sciences 3, 73–89., 2006

[21] Ş. Kültür, An ethnobotanical study of Kırklareli (Turkey), Phytologia Balcanica 14 (2): 279 –289, Sofia, 2008.

[22] G. Yaldız, T. Yüksek, N. Şekeroğlu, Rize ili Florasında bulunan tıbbi ve aromatik bitkiler ve kullanım alanları, 3.Ulusal Karadeniz Ormancılık Kongresi,.cilt:3,1100-1114, 2010.

[23] U. Çakılcıoğlu, S. Khatun, İ. Türkoğlu, İ, Ş. Hayta, Ethnopharmacological survey of medical plants in Maden (Elazığ)-Turkey). J.of Ethnopharmacology, 137, 469-486, 2011.

[24] F. Güneş, N. Özhatay, An ethnobotanical study from Kars (Eastern) Turkey, Biological Diversity and Conservation, 4/1.30-41, 2011.

[25] R. Polat, F. Satıl, U. Çakılcıoğlu, Medical Plants and their propeties of sold in herbal market in Bingöl (Turkey) district. *Biodicon*, 4/3, 25-35, 2911.

[26] M. Sağıroğlu, E. Olgaç, B. Ertürk, M. Turna, An Ethnobotanical Survey from Şile (İstanbul) and Karasu (Sakarya). Ot Sistematik Dergisi, 19,2 (93-104), 2012.

[27] M. Sağıroğlu, A. Arslantürk, Z.K. Akdemir, M. Turna, An ethnobotanical survey from Hayrat (Trabzon) and Kalkandere (Rize/Turkey).Biological Diversity and Conservation, 5/1, 31-43, 2012.

[28] M. Sağıroğlu, S.T. Köseoğlu, M. Turna, Medicinal Plants in Flora of İkramiye Sapanca-Sakarya-Türkiye).Sakarya Üniv. Fen Bil. Enst. Der.vol.21, no:3, 527-539, 2016.

[29] Ş. Türkan, H. Malyer, S.Z. Aydın, G. Tümen, Ordu ili ve çevresinde yetişen bazı bitkilerin etnobotanik özellikleri, Süleyman Demirel Üniversitesi, Fen Bilimleri Enstitüsü Dergisi.10-02,162-166, 2006.

SAKARYA ÜNİVERSİTESİ
FEN BİLİMLERİ ENSTİTÜSÜ DERGİSİ

Sakarya University Journal of Science
SAUJS

ISSN 1301-4048 | e-ISSN 2147-835X | Period Bimonthly | Founded: 1997 | Publisher Sakarya University | http://www.saujs.sakarya.edu.tr/

Title: Temporal Analysis based Driver Drowsiness Detection System using Deep Learning Approaches

Authors: Furkan KUMRAL, Ayhan KÜÇÜKMANİSA

Recieved: 2022-02-15 00:00:00

Accepted: 2022-05-31 00:00:00

Article Type: Research Article

Volume: 26
Issue: 4
Month: August
Year: 2022
Pages: 710-719

How to cite
Furkan KUMRAL, Ayhan KÜÇÜKMANİSA; (2022), Temporal Analysis based Driver Drowsiness Detection System using Deep Learning Approaches. Sakarya University Journal of Science, 26(4), 710-719, DOI: 10.16984/saufenbilder.1071863
Access link
http://www.saujs.sakarya.edu.tr/en/pub/issue/72361/1071863

Sakarya University Journal of Science 26(4), 710-719, 2022

Temporal Analysis Based Driver Drowsiness Detection System Using Deep Learning Approaches

Furkan KUMRAL[1], Ayhan KÜÇÜKMANİSA*[1]

Abstract

With the development of technology, artificial intelligence comes into our lives more and also comes up as a solution to many problems. Recently, deep learning approaches have been bringing fast and highly accurate solutions to problems. In this work, within the scope of Advanced Driver Assistance Systems (ADAS), deep learning based driver drowsiness detection system is proposed. First, face regions of drivers are detected using SSD MobileNet object detection method. The aim is to detect the eye, mouth and head positions of the drivers from this face region and to make a situation estimation with the combinations of these detected objects which are “normal”, “drowsy” and “danger”. The proposed approach examines the driver's behaviour over a certain period of time for making a decision, rather than a one-time eye closure or yawning decision. The detected eye, mouth and head positions are monitored and recorded over a period of time. Finally, these merged patterns are classified with Convolutional Neural Networks (CNN). Experimental results show that the performance of proposed novel CNN approach outperforms existing approaches in literature.

Keywords: Driver drowsiness, deep learning, ADAS.

1. INTRODUCTION

According to the statistics of the Traffic Directorate of the General Directorate of Security [1], there were a total of 108,171 traffic accidents until April 2021 in Turkey, and it was determined that 88.16% of these traffic accidents were caused by drivers. Drivers who make mistakes such as not following the lane, not adapting the vehicle speed to the conditions required by the road, weather and traffic, and hitting the vehicle in front with an uncontrolled speed from the rear constitute the reason for the high percentage of these accident statistics. In 2019, there were a total of 1168144 traffic accidents and 174896 of them included 5473 deaths and 283234 injuries, in Turkey [2]. Another statistic is that, there were 33,244 fatal motor vehicle crashes in the United States in 2019 in which 36,096 deaths occurred. This resulted in 11.0 deaths per 100,000 people and 1.11 deaths per 100 million miles traveled. The fatality rate per 100,000 people ranged from 3.3 in the District of Columbia to 25.4 in

* Corresponding ayhan.kucukmanisa@gmail.com
[1] Kocaeli University
E-mail: kumralf@hotmail.com
ORCID: https://orcid.org/0000-0002-1886-1250, https://orcid.org/0000-0001-6762-713X

Wyoming. The death rate per 100 million miles traveled ranged from 0.51 in Massachusetts to 1.73 in South Carolina [3].

The excessive tiredness of the drivers increases the causes of the above-mentioned accidents. Drowsiness and inattention cause the drivers to not be able to control the vehicle, weaken his reflexes during maneuvering, and not be able to perceive the distance between him and the vehicle in front of him. For this reason, the development of a system that monitors the driver's attention and drowsiness, and helps the driver to concentrate in dangerous situations, is of great importance in order to prevent the driver from causing an accident due to drowsiness during long-distance and/or night trips. Systems that warn drivers and try to prevent accidents are called Advanced Driver Support System (ADAS).

Although the driver drowsiness systems which is one of the ADAS are still subject of research, there are systems used by well-known companies today [4]. In Ford's Driver Alert system, whether the driver stays in the lane is monitored by a camera, if the driver turns the steering wheel out of the lane, a vibration occurs in the steering wheel and the vehicle moves the steering wheel to automatically return to the lane.

Mercedes' Attention Assist fatigue monitoring system uses a steering wheel mounted sensor. This sensor can detect speed and movements of wheel and learn the behavior of the driver. This system is available in all Mercedes top segment vehicles. The company has determined that the steering wheel provides the best fatigue detection system, as tired drivers make very rapid and very small movements while steering. When the system detects an unusual steering wheel movement, it evaluates 70 other parameters such as how long the driver has been behind the wheel, the hours of travel and so on. If it is detected that the driver is drowsy, the warning "fatigue detected" appears on the instrument panel. There is also a dashboard in the car that displays the time elapsed since the driver's last stop and the driver's level of attention. When fatigue is detected, drivers receive a warning with an alarm and a search for rest areas is initiated.

Nissan's Driver Fatigue System, like BMW's Attention Assist System in the 6 and 7 series, monitors the driver's behavior during the journey via the steering wheel and alerts a drowsy drive. BMW also allows drivers to customize fatigue system related alerts; When set to "sensitive", the driver assistance system is activated one hour after the start of the journey, and 90 minutes after starting to drive when set to "normal".

It is difficult to create a detection system that could only identify vehicle behaviors associated with sleep-deprived drivers and fatigue. Drivers can relinquish control of the steering wheel to take care of their baby or pick up a fallen item. Also, winds hitting the car can trick the system into thinking the driver is drowsy. When a system's sensors give too many false warnings, most drivers choose to turn them off.

Today, artificial intelligence-based approaches are used in driver drowsiness systems. In this preference, the effect of the performance increase provided by deep learning which is an artificial intelligence method is important.

The main contributions of this paper are summarized as follows:

- Temporal analysis based driver drowsiness detection approach that is different compared to most methods in the literature.
- Comparing the performance of the proposed method with image processing and deep learning based methods in comprehensive analysis.
- Suitable for low complexity embedded platforms with its low computational load.

2. RELATED WORK

When the studies in the literature are examined, it has been seen that the methods used in Advanced Driver Support Systems are considered as two separate approaches, in-vehicle and out-of-vehicle.

Systems using the out-of-vehicle monitoring approach control the factors outside the vehicle,

such as whether the vehicle leaves the lane, how much it deviates, and whether the driver can keep forward vehicle distance. In-vehicle monitoring systems generally control the driver's driving status using computer vision methods. These methods are also diversified within themselves. EAR (Eye Aspect Ratio) and PERCLOS (PERcentage of eye CLOSure) are the most basic known fatigue detection methods [5]. In EAR, 6 points are determined around the eye image and these points follow the eye's circumference in the positions when the eye is closed and opened. When the eye is open and closed, the values of the mathematical operation performed with these 6 points are different from each other. In this way, it is detected whether the eye is open or closed. In these algorithms, a counter starts counting during the time the eyes are closed and when it exceeds a certain threshold value, the alarm system is activated. When the eye is opened, the number in the counter decreases and the alarm system is disabled because it falls below the threshold value.

In [6], which is basically use similar approach to the proposed method, eye and face detection are considered as an object detection approach. Eyes are labeled and trained as open and closed. Fatigue decision is determined by determining a threshold value, as mentioned in previous studies, and depending on whether the duration of eye closure exceeds this threshold value. This threshold value is determined as 40% of the frame rate of the image captured from the camera. For example, if camera is 30 FPS (Frame Per Second), the threshold value is 12. If blindfold is detected in at least 12 of the 30 frames, the alarm is activated.

Apart from these methods, there are also systems in which in-vehicle and out-of-vehicle approaches are used together. Systems have been proposed to detect signs of fatigue such as closing eyes, tilting the head, and yawning, and also checking whether there is any deviation from the lane by road observation [7]. In these systems, if there is a lane violation and there is a fatigue detection in the facial expressions of the driver simultaneously, the system gives a warning.

Recent study [8] presents an improved drowsiness detection system based on CNN-based approach. The main objective of this method is to render a system that is lightweight to be implemented in embedded systems while maintaining and achieving high performance. The system is able to detect facial landmarks from images captured on a mobile device and inference it with a deep CNN model to detect drowsy driving behavior. Another study [9] benefits from image processing methods to detect driver drowsiness. These methods are calculating the percentage of white in eyes, detection of skin surrounding the eye and Hough transform to detect the iris. Calculation of distance between the eyelids yields the best result as a final step. In [10], a system is proposed based on monitoring the driver's face of using a camera and using image processing methods to obtain some physical indicators, such as closing the eyes, blinking speed and PERCLOS, and detection of yawning, gaze direction. The driver's drowsiness is manifested as a result of features of fatigue on the driver's face. [11] propose a condition-adaptive representation learning method for efficient driver drowsiness detection which is invariant to various driving conditions containing a driving time such as day and night and a driver's appearance. The spatio-temporal representation is extracted and merged with the vectors that represent the scene understanding results using the feature fusion method based on the tensor product approach. These problems are effectively modelled using 3D-DCNN (3 Dimensional-Deep Convolutional Neural Network) and fully connected neural network.

3. PROPOSED METHOD

In this work, a deep learning based in-vehicle drowsiness detection approach is proposed. Detection of driver drowsiness is considered as an object detection problem. The eye, mouth and head positions on the image which captured from a camera towards to the driver, are determined by object detection algorithm.

The states of the detected eye, mouth and head position are recorded as a series. For example, closed eyes and yawning indicate drowsiness, open eyes and closed mouths indicate normal

conditions, and tilting the head forward indicates danger. However, these decisions are not made after one-time determinations. For example, it does not mean that a driver sleeps every time he closes his eyes and yawns every time he opens his mouth. In addition, trying to understand that a person is tired simply by closing the eyes or yawning can lead to making wrong decisions. In order to prevent this, a novel approach is developed in this work. First, frame-by-frame object detections are made on the incoming frames. These objects are detected as open eyes, closed eyes, sunglasses, closed mouth, talking, yawning, and tilting the head. The driver is monitored for 50 frames (approximately 2 seconds) in the videos with approximately 25 FPS and the detected driver movements are recorded as an image. Then, an image classification approach is applied on these images with convolutional neural network. By this way, considering detected eye, mouth and head situations normal, drowsy or dangerous situation are detected. Flowchart of the proposed method is given in Figure 1.

3.1. Dataset

In this work YawDD [12], NTHU-DDD [13] and custom dataset are used in training and test stages. YawDD is a dataset of videos of drivers (men and women of different ethnicities, with and without glasses) in a real car, talking, singing, silent and yawning, recorded by a dash camera. Algorithms for yawn detection are used to develop and test models, as well as to recognize and track face and mouth. Videos shot in natural and variable lighting conditions come in two sets: In the first set, the camera is placed under the car's front mirror. This set contains 322 videos, each for a different situation: there are 3 or 4 videos of each topic: normal driving, talking or singing while driving, and yawning while driving. In the second set, the camera is installed on the driver control panel. This set includes 29 videos, one for each topic, featuring quiet driving, talking driving and driving while yawning. Certain frames are selected from these 29 videos and labeled. The number of images annotated in the YawDD dataset is 1675. Example labeling of an image from this dataset is shown in Figure 2. In this figure, it is seen that the labels 'open eye' and 'talking' are given. (The act of laughing is included in the 'talking' class).

Since YawDD is not enough with 7 different classes (open eye, closed eye, sunglasses, closed mouth, speech, yawning, head tilt) to be used in this work, another custom data set is created. In this custom data set, various videos are collected from 21 different people in their normal and

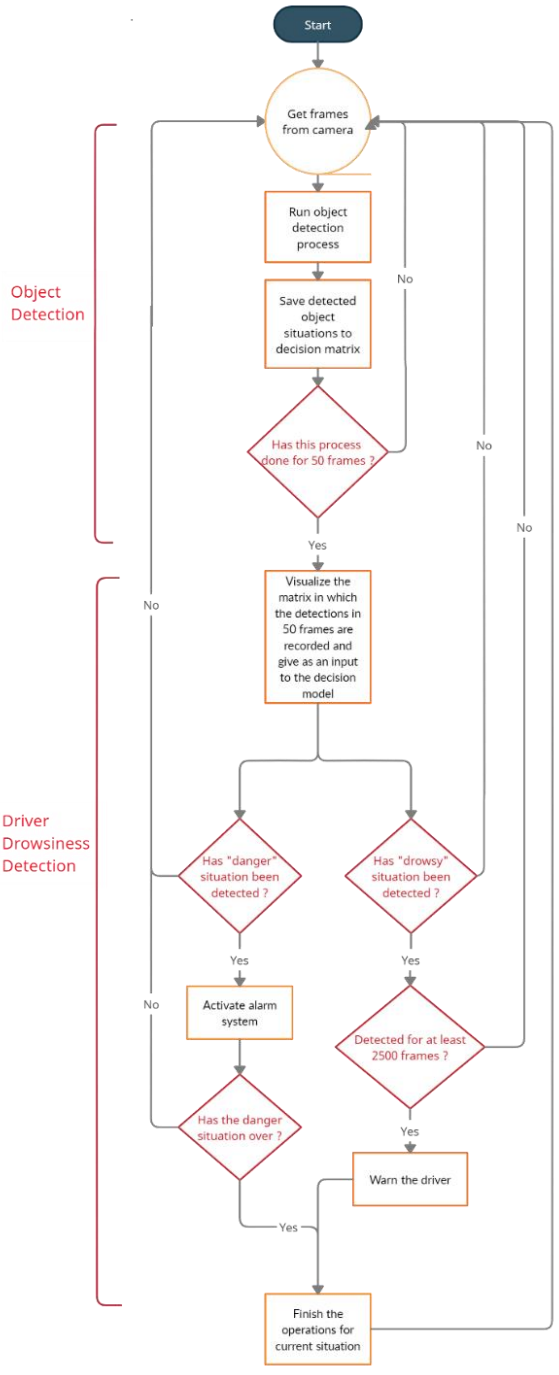

Figure 1 Flowchart of the proposed algorithm

sunglasses state. There are 45 videos in total. Certain frames are selected from these videos and labeled. An example labeling is given in Figure 2. In this figure, it is seen that the labels 'lean forward' and 'sunglasses' are given. The number of photos annotated in this custom dataset is 4504. There are 6179 annotated images for object detection model training.

3.2. Deep Learning based Object Detection

Object detection approach is used to detect the instant status of the driver in the images taken from the camera. In recent years, deep learning-based approaches have been used for the object detection function, which has achieved significant performance. Since real-time operation is an important criterion of the proposed method, the SSD MobileNet approach is preferred considering the balance of speed and performance. In addition, since this model does not have a complex neural network architecture and is a lightweight model, it is very convenient to integrate it into embedded systems. SSD MobileNet V2 FPNLite 640×640 is used as pre-trained model. There are 7 object class as “open_eye”, “close_eye”, “talking”, “closed_mouth”, “yawning”, “sunglasses” and “head_down”. Example annotations from YawDD and custom dataset are shown in Figure 2.

3.3. Driver Drowsiness Detection

After the object detection step, a novel driver drowsiness detection method is started. Flowchart of the driver drowsiness detection method is given in Figure 1 (mentioned with Driver Drowsiness Detection part).

In this this work, it is aimed not to make the decision of the driver's drowsiness status based on a single action, but to make it from the driver's general state and movements, and also to carry out this process on an ongoing basis. Thus, it is prevented to detect a drowsiness state every time the driver yawns or closes his/her eyes. The basis of this algorithm is a matrix registration system. Detected eye, mouth and head state results are recorded in a matrix. Number values between “0-6” comes as output from the object detection model.

0 : Open eye

1 : Closed eye

2 : Talking

3: Closed mouth

4 : Yawn

5 : Sunglasses

6 : Head tilt

This detected label used as a matrix index. If one of these states detected, index of these state value is become “1”. For example, if “Open eye” and “Closed mouth” states are detected for a driver, these detections are recorded in a list as [1,0,0,1,0,0,0]. Table 1 gives the instantaneous information about the driver drowsiness by these frame-based situations.

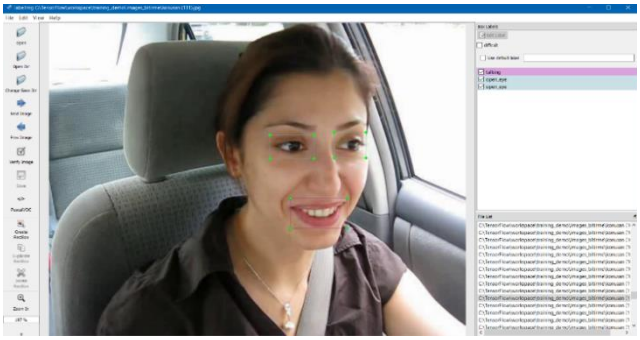

(a)

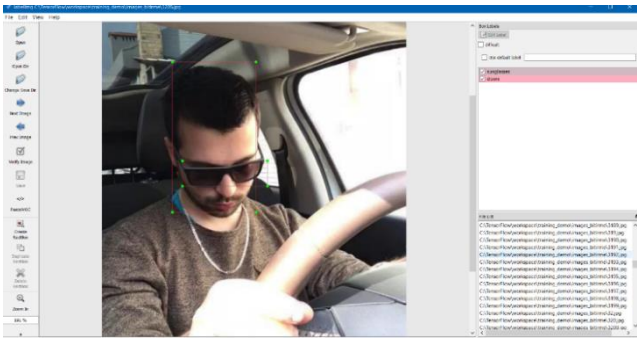

(b)

Figure 2 Annotations examples from datasets (a) YawDD dataset (b) Custom dataset

Table 1 Training parameters

OE	CE	T	CM	Y	S	HT	DS
1	0	1	0	0	0	0	Normal
1	0	0	1	0	0	0	Normal
0	0	1	0	0	1	0	Normal
0	0	0	1	0	1	0	Normal
1	0	0	0	1	0	0	Drowsy
0	0	0	0	1	1	0	Drowsy
0	1	0	0	1	0	0	Danger
0	1	0	1	0	0	0	Danger
0	0	0	0	0	1	1	Danger

OE: Open Eye, CE: Closed Eye, T: Talking, CM: Closed Mouth, Y: Yawning, S: Sunglasess, HT: Head Tilt, DS: Drowsiness State

(a) (b) (c)

Figure 3 Decision matrix visualization (a) Drowsy (b) Normal (c) Danger

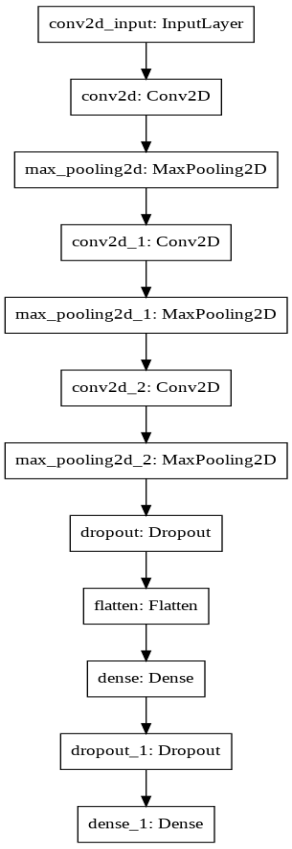

Figure 4 Driver drowsiness detection network

However, these values should be monitored for a certain period of time, as these instantaneous detections may lead to erroneous decisions. Therefore, this process is done for 50 frames. Then, these 50 lists are combined, and a decision matrix with 50×7 size is created. Finally, this decision matrix is resized to 50×50 for convolutional operations efficiency. Visualization of this decision matrix is shown in Figure 3.

The decision matrix is inferenced with a simple Convolutional Neural Network (CNN) as an image input. Proposed CNN is given in Figure 4. As shown in Figure 5, driver drowsiness detection is performed by processing every 50 overlapping frames from the start time. “Normal”, “Drowsy” and “Danger” classification decisions are obtained as a result of this approach.

4. EXPERIMENTAL RESULTS

The proposed method is trained with YawDD, NTHU and custom dataset. The object detection training loss curves are obtained for every 100 steps of the model and all training process is completed at 110000 steps (107 epoch). Training parameters used in the object detection method are given in Table 2. While training stage classification loss, localization loss and total loss are examined separately. These training loss curves are given in Figure 6.

The trained model is evaluated using COCO Object Detection Metrics. The mAP (mean Average Precision) is obtained as 0.949 which is calculated at 0.5 IoU (Intersection over Union). The comparison of the mAP values in this work with another method [10] which deals with the Driver Drowsiness Detection problem as an object detection is given in Table 3.

In driver drowsiness detection step, for training dataset, 202748 images of the normal class, 10226 of the drowsy class and 12160 of the danger class are collected from 383 videos. Training parameters used in the drowsiness detection method are given in Table 4. Test and training loss and accuracy curves are given in Figure 7. The hyperparameters in Table 2 and Table 4 are

obtained using manual tuning approach. A small set of possible values of hyperparameters are determined. Then, these different sets of hyperparameters are manually performed and the set with best performance is chosen as final parameter set.

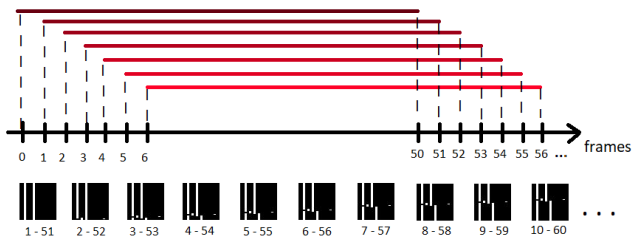

Figure 5 Flowchart of drowsiness detection processing

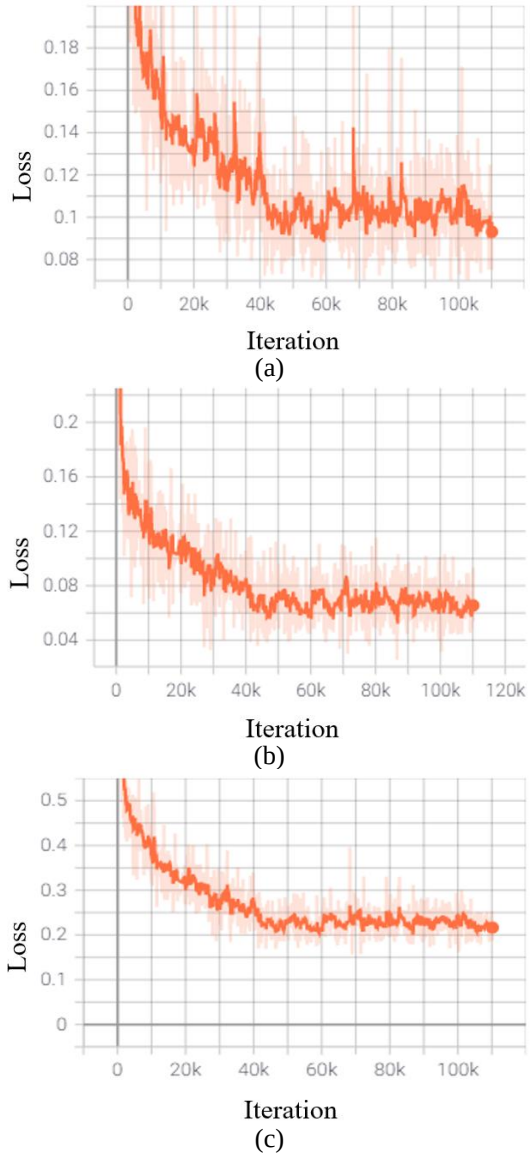

Figure 6 Training loss curves (a) Classification loss (b) Localization loss (c) Total loss

Table 2 Object detection network training parameters

Parameter	Value
Learning rate	0.08
Epoch size	107
Batch size	6
Optimization algorithm	SGDM

Table3
Object detection evaluation on YawDD dataset

Method	mAP
[6]	0.837
Proposed Method	0.949

Proposed method is tested on custom dataset and NTHU-DDD dataset. Visual detection results on custom dataset are given in Figure 8. As seen from this figure, the proposed method is able to provide reliable detection results. Detailed quantitative evaluation on the NTHU-DDD dataset is given in Table 5.

Table 6 show objective evaluation in terms of accuracy of recent methods and proposed method on NTHU-DDD dataset. Jabbar et al. [8], Ramachandran et al. [9], Gaidar and Yakimov [10], Mehta et al. [5] and Jongmin Yu et al. [11] detect drowsiness situtation in the test conditions (with glasses, without glasses at night, with glasses at night, without glasses, with sunglasses) in NTHU-DDD dataset as same as proposed method. Accuracy results of these methods are directly taken from papers. As seen from Table 6, proposed method gives best result among the compared methods.

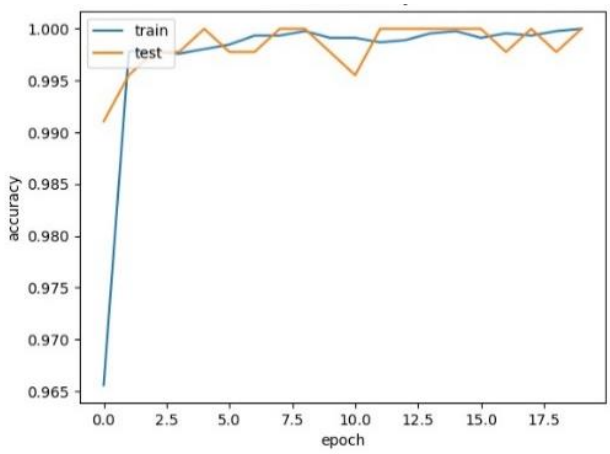

(a)

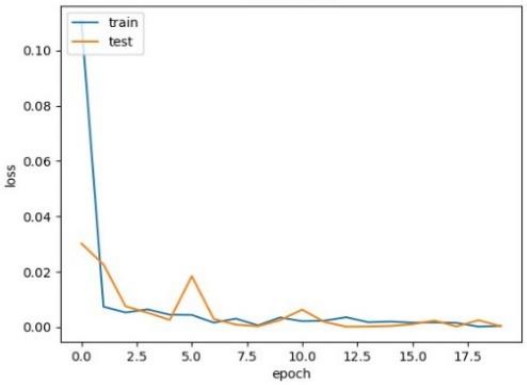

(b)

Figure 7 Training loss and accuracy curves (a) Accuracy curve (b) Loss curve

(a)

(b)

(c)

Figure 8 Visual driver drowsiness detection results (a) Normal (b) Drowsy (c) Danger

Table 4 Drowsiness detection network training parameters

Parameter	Value
Learning rate	0.01
Epoch size	20
Batch size	32
Optimization algorithm	SGDM

Table 5 Performance evaluation of proposed method on NTHU-DDD dataset

Category	Total frame number	Detected "drowsy" instead of "normal"	Detected "normal" instead of "drowsy"	Accuracy (%)
With glasses	38467	4518	275	87.19
Night time without glasses	39785	6637	480	82.39
Night with glasses	31141	5400	544	86.14
Without glasses	12450	741	320	92.12
With sunglasses	20319	4134	149	78.92
Total	142162	21430	1768	**85.35**

Table 6 Performance evaluation of proposed method and recent methods on NTHU-DDD dataset

Method	Accuracy (%)
Jongmin Yu et al. [11]	76.2
Ramachandran et al. [9]	79
Gaidar and Yakimov [10]	81
Jabbar et al. [8]	83.33
Mehta et al. [5]	84
Proposed Method	**85.35**

5. CONCLUSION

Most of the traffic accidents are caused by the carelessness of the drivers. An important part of these carelessness comes from drowsy driving. The aim of this work is to accurately determine the situations where the driver is normal, drowsy and in danger.

Mainly, driver drowsiness detection is handled as an object detection problem and drowsiness decision is provided by a simple Convolutional Neural Networks. In the proposed method, the fatigue decision is made as a result of an observation within a certain period of time, rather than instantaneous determinations. With this approach, erroneous detections are prevented by ensuring that every driver's eye closing or every opening his mouth is not perceived as drowsiness. In addition, one of the biggest problems of driver drowsiness detection, the inability to understand whether drivers with sunglasses are sleepy or tired, is solved by using the head position as an additional decision parameter. The experimental results show that the proposed drowsiness detection method is able to detect drowsy drivers in the challenging conditions with low computational complexity models which makes it suitable for real-time applications.

Funding

This work is supported by Kocaeli University Scientific Research Projects Coordination Unit under grant number 2019/021.

The Declaration of Conflict of Interest/ Common Interest

No conflict of interest or common interest has been declared by the authors.

Authors' Contribution

The first author contributed 40% and the second author 60% contributed to the study.

REFERENCES

[1] General Directorate of Police. URL http://trafik.gov.tr/kurumlar/trafik.gov.tr/04-Istatistik/Aylik/nisan21.pdf (accessed 5.22.21).

[2] Turkish Statistical Institute, URL https://data.tuik.gov.tr/Bulten/Index?p=Karayolu-Trafik-Kaza-Istatistikleri-2019-33628, (accessed 22.05.21).

[3] IIHSHLDI, URL https://www.iihs.org/topics/fatality-statistics/detail/state-by-state#fatal-crash-totals, (accessed 16.6.21).

[4] Cars, URL https://www.cars.com/articles/drowsy-driver-detection-systems-sense-when-you-need-a-break-1420684409199/#:~:text=BMW%20also%20allows%20you%20to,set%20it%20to%20%E2%80%9Cnormal.%E2%80%9D, (accessed 22.05.21)

[5] S. Mehta, S. Dadhich, S. Gumber, A. J. Bhatt, "Real-Time Driver Drowsiness Detection System Using Eye Aspect Ratio and Eye Closure Ratio", Proceedings of International Conference on Sustainable Computing in Science, Technology and Management (SUSCOM), Jaipur - India, February 26-28, 2019.

[6] M.F. Shakeel, N.A. Bajwa, A.M. Anwaar, A. Sohail, A. Khan, Haroon-ur-Rashid, "Detecting Driver Drowsiness in Real Time Through Deep Learning Based Object Detection", Advances in Computational Intelligence, IWANN 2019 Lecture Notes in Computer Science, vol 11506, 2019.

[7] R. Ahmed, K. E. Emon, M. F. Hossain, "Robust driver fatigue recognition using image processing", 2014 International Conference on Informatics, Electronics & Vision (ICIEV), pp. 1-6, 2014.

[8] S. Abtahi, M. Omidyeganeh, S. Shirmohammadi, B. Hariri, YawDD, "A yawning detection dataset", ACM International Conference on Multimedia Systems, Singapore, Singapore, March 19 - 21, 2014.

[9] C. H. Weng, Y. H. Lai, S. H. Lai, "Driver Drowsiness Detection via a Hierarchical Temporal Deep Belief Network", Asian

Conference on Computer Vision Springer, pp. 117-133, 2016.

[10] R. Jabbar, M. Shinoy, M. Kharbeche, K. Al-Khalifa, M. Krichen, K. Barkaoui, "Driver Drowsiness Detection Model Using Convolutional Neural Networks Techniques for Android Application", 2020 IEEE International Conference on Informatics, IoT, and Enabling Technologies (ICIoT), pp. 237-242, 2020.

[11] S. Ramachandran, S. G. R. Rao, T. Sunder, "Drowsiness Detection Using Image Processing Techniques", International Research Journal of Engineering and Technology (IRJET), vol. 5, no. 6, 2018.

[12] A. I. Gaidar, P. Y. Yakimov, "Real-time fatigue features detection", In: Journal of Physics: Conference Series, vol. 1368, no. 5, 2017.

[13] J. Yu, S. Park, S. Lee, M. Jeon, "Driver Drowsiness Detection Using Condition-Adaptive Representation Learning Framework", IEEE Transactions on Intelligent Transportation Systems, vol. 20 no. 11, pp. 4206-4218, 2019.

SAKARYA ÜNİVERSİTESİ
FEN BİLİMLERİ ENSTİTÜSÜ DERGİSİ

Sakarya University Journal of Science
SAUJS

e-ISSN 2147-835X Period Bimonthly Founded 1997 Publisher Sakarya University
http://www.saujs.sakarya.edu.tr/

Title: Transition Gas Flow Between Two Parallel Plates with a Slit-Type Obstacle of Various Geometry by Event-Driven Molecular Dynamics Simulation

Authors: Mustafa KOÇ, İlyas KANDEMİR, Volkan Ramazan AKKAYA

Recieved: 2022-03-02 00:00:00

Accepted: 2022-06-01 00:00:00

Article Type: Research Article

Volume: 26
Issue: 4
Month: August
Year: 2022
Pages: 720-744

How to cite
Mustafa KOÇ, İlyas KANDEMİR, Volkan Ramazan AKKAYA; (2022), Transition Gas Flow Between Two Parallel Plates with a Slit-Type Obstacle of Various Geometry by Event-Driven Molecular Dynamics Simulation. Sakarya University Journal of Science, 26(4), 720-744, DOI: 10.16984/saufenbilder.1081717
Access link
http://www.saujs.sakarya.edu.tr/en/pub/issue/72361/1081717

Sakarya University Journal of Science 26(4), 720-744, 2022

Transition Gas Flow Between Two Parallel Plates with a Slit-Type Obstacle of Various Geometry by Event-Driven Molecular Dynamics Simulation

Mustafa KOÇ*[1], İlyas KANDEMİR[2], Volkan Ramazan AKKAYA[3]

Abstract

In this study, pressure-driven flow through a slit-type obstacle with various lengths (L) and heights (H) placed in between two parallel plates was investigated by Event-Driven Molecular Dynamics (EDMD) simulation. Mach number, temperature and pressure distributions were obtained along the channel in the transition regime. The change in these macroscopic properties and flow rate were examined for different cases created by changing Knudsen number (Kn) of the flow, the geometry of the slit and the outlet/inlet pressure ratio of the flow. Collision of gas molecules with plates and the obstacle were modeled with diffusive reflection boundary condition. The flow rate showed a sudden change in the transition regime and significant differences in the molecular regime depending on the pressure ratio. Except for the Kn, H and L dimensions were found to be effective in Mach disc formation. Pressure drops at the exit of the slit were shaped differently in normalized pressure profiles depending on Kn, H and L dimensions. In addition, the structure of the vortices formed at the entrance and exit of the slit varies depending on Kn. Some of the results obtained were confirmed to be consistent with similar studies in the literature.

Keywords: Event-Driven Molecular Dynamic Simulation, Knudsen Number, Slit Flow, Mach Discs, Transition Regime, Vorticity.

1. INTRODUCTION

Gas flow due to pressure difference through a slit is one of the major problems in rarefied gas dynamics. Flow through a slit between parallel plates occurs in different technological applications such as spacecraft, micro-propulsion systems, micro nozzle flows, electronic microscopy, MEMS or measurement of sudden and rapid pressure change in vacuum gauges [1-3]. To understand and solve such problems, flow through a narrow section of a channel should be studied. Even small or large pressure differences have significant importance in the design and optimization of various industrial equipment types [4]. Even the rarefied gas flow between two parallel plates of finite length is of practical importance in membrane applications [5].

* Corresponding author: phd.mustafakoc@gmail.com
1 Beykent University, Vocational School, Department of Mechanical and Technologies
ORCID: https://orcid.org/0000-0002-5417-2604
2 Gebze Technical University, Faculty of Aeronautics an d Astronautics
E-mail: kandemir@gtu.edu.tr
ORCID: https://orcid.org/0000-0002-8773-6541
3 Mugla Sıtkı Kocman University, Faculty of Technology, Department of Energy Systems Engineering
E-mail: m.kahyalar@tirsankardan.com.tr
ORCID: https://orcid.org/0000-0002-5052-8554

Rarefied gas flow observed in different technological areas including high altitude and space dynamics [6]. Examination of such flows is characterized by Knudsen number which is a dimensionless parameter defined as ratio of molecular mean free path to the scale of physical domain.

The numerical calculation of high Kn number flow regimes cannot be modeled with the Navier-Stokes equations (N-S), which approach the fluids as a bulk mass movement. For this, the equations based on the Kinetic Theory, which considers the fluid as the motion of the molecular, need to be solved numerically. Molecular simulation models such as Direct Simulation Monte Carlo (DSMC), Lattice Boltzmann (LBM) and Molecular Dynamics (MD) are available for such simulations.

Unlike CFD studies, which rely on solving Navier-Stokes equations, a molecular dynamics (MD) simulation does not require solving a set of differential equations. Instead, it detects and determines the type of each intermolecular interaction, and from these interactions it reveals the entire macroscopic behavior of the flow.

The DSMC method [7] uses several representative molecules to simulate a larger number of real molecules. The movements of the molecules are certain, but the determination of collisions is probabilistic. On the other hand, MD simulations are much more realistic and accurate because each particle represents a real molecule and its position and velocity are known exactly. Due to its time-oriented nature, it contains algorithms suitable for the integration of Newton's equation of motion for many time steps for multi-particle systems. The main disadvantages of standard MD simulations based on the continuous interaction potential (the most widely used being the Lennard-Jones potential) are the limitations in simulation time and size. The computation becomes more difficult as the number of molecules increases, because the interacting particles and their positions must be calculated for each interaction. The integration time step is so small that during a simulation of ten microseconds, even ten thousand molecules representing a very small volume require too many time steps and a collision test at each step.

Thanks to the hard-sphere assumption, where the interaction potential is considered to be discrete (zero except for the moment of contact), collision times can be predicted analytically, allowing the simulation to be treated as asynchronous sequences of events. This is called Event Driven Molecular Dynamics (EDMD) simulations and allows simulation of larger systems for longer periods of time than time-based simulations. It has been shown that this approach produces consistent results in the calculation of transport coefficients for rare gases [8-10]. Unlike in DSMC, molecular trajectories, determination of collision pairs and post-collision velocities are calculated deterministically in EDMD. Also, all collisions are real and predictable, no collision is neglected. Since the first introduction of EDMD simulations [11], the development of more efficient algorithms has further improved the performance of EDMD [8, 12, 13]. With the computing power of a desktop computer, simulation of millions of particles is possible for longer periods [14]. Another advantage of the EDMD method is that it is as deterministic as other classical MD methods and allows working with as many molecules as the DSMC method. Rather than relying on data from a very small number of molecules simulated as in DSMC, it treats all molecules in this physical space as real molecules and all interactions as real interactions, using the entire simulation space as physical space. Thanks to these assumptions and improvements in EDMD, computing performance can compete with DSMC.

LBM, which is a class of CFD, models the liquid as fictitious particles and such particles perform sequential propagation and collision operations on a separate lattice network. LBM solves a simplified version of kinetic equation and does not track each particle as in classical MD. It uses the equation with single particle velocity to simulate fluid flows. Unlike EDMD, the velocity, position and momentum states of the system are calculated probabilistically in the phase space. LBM simulates behavior of fluid flows with macroscopic fluid dynamics of an imaginary ensemble of particles whose motion and interactions are confined to a regular space-time lattice. Particle velocities are constrained by assuming that particles at each location can only

move along a finite number of directions. In addition, slip boundary conditions need to be added to simulate rarefied flow range in LBM. Unlike LBM, all particles are real, and motion and collision detection is calculated by analytical Newton's laws, also it can simulate high Knudsen number rarefied flows without any boundary conditions in EDMD.

Flow properties in a slit connecting reservoirs with two different pressures are studied with DSMC method [15] in the literature. This connection is sometimes a very short pipe and sometimes an infinitely thin border. Since these reservoirs are assumed to be infinitely large, their pressure does not change during the flow. The calculation is made by dividing the slit and the regions close to the slit into small domains. In common results, velocity, number density and temperature undergo a sudden change only in the slit region. These parameters of the molecules that cross the slit come to their states in the upstream region after a certain distance. Briefly reviewing the literature: In the studies of Danilatos [16], Sharipov [17] and [18], Wang and Li [19], Varoutis et al.[5], Argon, Helium and Nitrogen gases were used in a wide range of Kn-related flow regimes, especially in the transition regime, studied the flow through an orifice or slit channel. They investigated the distribution of number and density, velocity, temperature, pressure and flow rates along the flow axis and their variations according to pressure ratios, L/H ratios or only L or H dimensions. Sharipov and Strapasson [20], on the other hand, investigated the same problem with the DSMC method based on ab-initio potential and added krypton to the monoatomic gases. In addition to macroscopic distributions and flow rates, Graur et al. [21] also obtained the velocity profile in the orifice cross-section. But none of them changed the H height. Rahmati and Ehsani [22] obtained streamwise velocity profiles by using LBM method [23] in slip condition. Misdanitis et al. [24] conducted a similar study using the BGK. Pantazis and Valougeorgis [4], who conducted the same flow study, used the BGK model [25] that conforms to the Maxwell specular-diffuse boundary condition. Comparing DSMC simulations with their experimental studies, Gimelshein [26] and Lilly [27] also examined the effect of L geometry and surface interaction on impulse and propulsion. Lindström et al. [28] analyzed the mass flow rate of flow at various pressure ratios and different orifice geometries using a solver based on Navier-Stokes equations. Sharipov [29] calculated mass flow rate, temperature and velocity distributions based on time in transition and steady regime and also evaluated the times when the flow became steady in various regimes. Similarly, Polikarpov and Graur [2] and Ho and Graur [30], who made time-dependent calculations, investigated dependence of time to steady on various parameters in the entire Kn regime. In the study of Varoutis et al. [5], the flow rate between two parallel plates was examined depending on the L/H ratio. However, they did not place any obstacles in the channel. In the literature, molecule-wall interactions are generally modeled as specular or diffuse.

Flow between two parallel plates is in the literature, but the flow through an obstacle between the plates has not been studied yet. Also, the effect of H on the flow together with Kn and outlet/inlet pressure ratio is missing in the literature. Therefore, the macroscopic flow properties of these problems were investigated in this study. EDMD method has been applied for the first time to model such a flow considering all its advantages.

In 2nd section, the calculations and assumptions used for modeling the EDMD simulation will be explained. In 3rd section, the problem of present study will be defined and the setup of the simulation will be mentioned. In 4th section, simulation results will be given together with the validations and the results will be interpreted. Conclusion part and a detailed summary will be given in 5th section.

2. COMPUTATIONAL METHODS OF EDMD SIMULATION

The classical MD method needs a large computational power due to the continuous potential. Monoatomic molecules are modeled as hard-spheres in EDMD. For hard-sphere model, interaction potential between molecules is discrete and only exists in case of contact. Only binary

collisions are considered. No external force field exists, hence the resulting trajectories are linear and molecular velocity between the two collisions is constant. Thus, unlike conventional MD, there is a discrete potential approach instead of a continuous potential. Therefore, molecular trajectories, determination of collision pairs and post-collision velocities can be calculated deterministically in EDMD. Also, all collisions are real and predictable, no collision is neglected.

For the two molecules moving along their trajectories to collide, the contact condition must be met:

$$\sum_{k=1}^{3}\left(x_{j,k}^{*}-x_{i,k}^{*}\right)^{2}=\frac{\left(d_{m,j}+d_{m,i}\right)^{2}}{4} \tag{1}$$

Here i and j denote the pair of the molecules to collide, x_k^* position component, d is diameter of the molecules. The positions of the molecules when the collision occurs are calculated from the following formula:

$$\begin{aligned} x_{i,k}^{*} &= x_{i,k}+c_{i,k}(t-t_i) \\ x_{j,k}^{*} &= x_{j,k}+c_{j,k}\left(t-t_j\right) \end{aligned} \tag{2}$$

where c_k is velocity component, t_i and t_j are separate time variable held for each molecule. If Eq. (1) is substituted in Eq. (2), the following is obtained.

$$\begin{aligned} \sum_{k=1}^{3}\Big(x_{i,k}+c_{i,k}(t-t_i)-x_{j,k} \\ -c_{j,k}\left(t-t_j\right)\Big)^{2}=d^{2} \end{aligned} \tag{3}$$

To get a simpler form of Eq. (3), Δx_k and Δc_k are defined:

$$\begin{aligned} \Delta x_k &= c_{j,k}\Delta t_{i,j}+x_{j,k}-x_{i,k} \\ \Delta c_k &= c_{j,k}-c_{i,k} \end{aligned} \tag{4}$$

Hence, Eq. (4) would be as follows:

$$\begin{aligned} \sum_{k=1}^{3}(\Delta c_k)^2(t-t_i)^2+2\Delta x_k\Delta c_k(t-t_i) \\ +(\Delta x_k)^2=d^2 \end{aligned} \tag{5}$$

For a simpler representation $A=\sum_{k=1}^{3}(\Delta c_k)^2$, $B=\sum_{k=1}^{3}\Delta x_k\Delta c_k$ and $C=\sum_{k=1}^{3}(\Delta x_k)^2-d^2$ are defined. So, the collision time becomes the following quadratic form:

$$A(t-t_i)^2+2B(t-t_i)+C=0 \tag{6}$$

In case of no real roots, the trajectories do not intersect. If positive real roots exist, the smallest one gives the collision time. This allows one to estimate the collision times deterministically. Thus, the simulation consists of a series of asynchronous events. Due to its event-driven nature, time can advance discretely from one event to subsequent one in simulation.

On the initialization, thermal equilibrium is assured for for entire domain after a certain amount of time. Since monoatomic molecules have only translation energy mode, relationship between the kinetic temperatures and the average translational kinetic energies of molecules in thermal equilibrium is given as:

$$\frac{3}{2}k_bT=\frac{1}{2}m\langle c^2\rangle \tag{7}$$

Here $\langle c^2\rangle$ is the average of thermal velocity squares of molecules. According to Kinetic Theory, the velocities of molecules in a system at thermal equilibrium are sampled from the Boltzmann distribution. The most probable speed according to this distribution is as follows.

$$c_{mp}=\sqrt{\frac{2}{3}\langle c^2\rangle} \tag{8}$$

Thus, the thermal velocity components sampled from the distribution are as follows.

$$u_{th} = c_{mp}\sqrt{-ln(R_1)}\,sin(2\pi R_2)$$
$$v_{th} = c_{mp}\sqrt{-ln(R_3)}\,sin(2\pi R_4) \quad (9)$$
$$w_{th} = c_{mp}\sqrt{-ln(R_5)}\,sin(2\pi R_6)$$

When a collision occurs, post-collision velocities are determined analytically by conservation of energy and momentum. The type of molecule pair that participates in the collision determines the collision characteristic. Since intermolecular collisions are elastic, mass, translational energy, and momentum are conserved.

$$m_A + m_B = m'_A + m'_B$$
$$m_A c_A + m_B c_B = m'_A c'_A + m'_A c'_B \quad (10)$$
$$m_A|c_A|^2 + m_B|c_B|^2 = m'_A|c'_A|^2 + m'_A|c'_B|^2$$

Here $'$ indicates post-collision state. m and c indicate mass and velocity vector of the molecule, respectively. Accordingly, the post-collision velocities of the molecule pair are expressed as follows.

$$c'_A = c_A - \frac{2\mu_{AB}}{m_A}\epsilon\langle\epsilon, c_A - c_B\rangle$$
$$c'_B = c_B - \frac{2\mu_{AB}}{m_A}\epsilon\langle\epsilon, c_A - c_B\rangle \quad (11)$$

Here the inner product is shown as$\langle\cdot,\cdot\rangle$. μ_{AB} is reduced mass and ϵ is the unit vector passing through the molecule centers when two molecules are in contact.

$$\mu_{AB} = \frac{m_A m_B}{m_A + m_B}$$
$$\epsilon = \frac{x_A - x_B}{|x_A - x_B|} \quad (12)$$

Generally, three types of computational domain boundary models are considered sufficient to model a flow in micro- and nano-channels. These are periodicity, wall interaction and flow boundary conditions. In the presence of periodic boundaries simulation domain is modelled as an infinite lattice by repeating the calculation region along the boundary direction. When a molecule physically crosses a periodic boundary, it leaves the computational domain and enters the opposite boundary at the same velocity components. As a result of specular reflection of a molecule, the tangential velocity components remain the same while the normal velocity component, which conserves the tangential momentum, is reversed. In real life, the wall surface is rough, and molecules are projected at random angles from the wall. Diffuse reflection is the most common model representing these surfaces. The post-collision velocity of the molecule is largely independent of the incoming velocity and is stochastically determined from a distribution based on wall temperature (T_W).

Molecules reaching both ends of the system (upstream or downstream) leave the computational domain permanently. New molecules are inserted into the computational domain according to local domain properties. For both flow boundaries, the molecular flux entering the calculation domain is determined by the Maxwell distribution function:

$$F_j = \frac{n_j}{2\sqrt{\pi\beta_j}}\left[\begin{matrix} e^{-s_j^2 cos^2\phi} + \\ \sqrt{\pi}s_j cos\,\phi\left(1 + erf\left(s_j cos\,\phi\right)\right)\end{matrix}\right] \quad (13)$$

where $s_j = U_j\beta_j$, $\beta_j = 1/c_{mp,j} = 1/\sqrt{2k_bT_j\,/\,m}$. Here, U, T, n_j and c_{mp} are streamwise velocity, local temperature, number density of molecules in the cell and the most probable speed, respectively. This molecular flux should be calculated for each cell surface of each flow boundary cell j. The value of ϕ is 0 for upstream and π for downstream. The number of molecules entering the calculation domain from the cross-sectional area (A) of the boundary surface per unit time (Δt) gives the following relation:

$$N_{in,j} = F_j\Delta t A_j \quad (14)$$

The tangential velocity components (v and w) of the incoming molecules that are independent of streamwise are produced as follows:

$$v = V + c_{mp}\frac{R_n}{\sqrt{2}}$$
$$w = W + c_{mp}\frac{R'_n}{\sqrt{2}} \quad (15)$$

Here, V and W are mean tangential velocity components, and R_n and R'_n are randomly generated numbers from a normal distribution with zero mean and unit variance.

When the streamwise velocity (U) is zero, normal component is expressed as:

$$u = c_{mp}\sqrt{-logR_u} \quad (16)$$

Here, R_u is random number generated from uniform distribution of interval [0,1). For $U \neq 0$, Garcia and Wagner [31] introduce several efficient acceptance-rejection methods with the general form:

$$u = U - f\left(\frac{U}{c_{mp}}\right)c_{mp} \quad (17)$$

Here, $f(U/c_{mp})$ is a randomly selected number from the acceptance-rejection method. In this study, recommended method for low-speed flows ($-0.4c_{mp} < U < 1.3c_{mp}$) was used.

The inlet pressure (p_{in}) and temperature (T_{in}) are known for the upstream boundary. V_{in} and W_{in} are set to zero. The molecular number density is calculated from the ideal gas equation:

$$n_{in} = \frac{p_{in}}{k_b T_{in}} \quad (18)$$

Streamwise velocity perpendicular to the surface is expressed as a function of the mean flow velocity (U_j), pressure (p_j), density (ρ_j) and sound velocity (a_j) of the computational domain:

$$(U_{in})_j = U_j + \frac{p_{in} - p_j}{\rho_j a_j} \quad (19)$$

Only the outlet pressure (p_e) is known at the downstream boundary. Other flow properties are calculated by extrapolating from neighboring cell:

$$(n_e)_j = n_j + \frac{p_e - p_j}{(a_j)^2}$$
$$(U_e)_j = U_j + \frac{p_j - p_e}{\rho_j a_j} \quad (20)$$
$$(T_e)_j = -\frac{p_e}{(n_e)_j k_b}$$

The tangential components of the average flow velocity components are calculated similarly for the upstream:

$$(V_e)_j = V_j$$
$$(W_e)_j = W_j \quad (21)$$

No macroscopic information, except for the initial conditions and boundary conditions, is imposed on the system in EDMD simulations. Defining the fluid as an ensemble of molecules allows all macroscopic features of the system to be calculated from the instantaneous velocity, position and energy information of each molecule. The number of molecules inserted into the calculation domain from the flow boundary and their respective velocities are calculated by means of local flow properties such as temperature, pressure, molecular density and average velocity.

In the pioneering work of this study [10], Event-Driven Molecular Dynamic Simulation (EDMD) model to simulate rarefied gas flow was developed with Object-Oriented C# programming in Visual Studio. In order to reduce computational complexity of EDMD simulation, a cell division method [8] was used. In this method, each molecule is placed in a cell according to its position and a cell has 27 neighbor cells in 3D. For an intermolecular collision, the distance between two molecules must be less than the width of the cell. So they have to cross the cell border before they collide. So that only molecules of the same or neighboring cells are possible collision candidates at a given time, and it is unnecessary to check

whole computational domain. No collision is missed thanks to this multi-cell method. The simulation aims to find the earliest event and to process it. For this, the priority queue method [32], [33] is implemented in EDMD by Akkaya and Kandemir [10] and reduces the computational complexity to *O*(logN). For data reduction, the calculation domain was divided into small sub-domains (bins) and the average of the snapshots of these bins at a certain time intervals were taken. The implicit treatment method (IBT) for flow boundary is first introduced for DSMC simulations by Liou and Fang [34] and adapted for present EDMD simulations by Akkaya and Kandemir [10]. After implementing the necessary boundary conditions, shear-driven and pressure-driven flow were simulated. In the next development, flow through the porous media modeled with spherical particles and at various porosities was simulated in the transition flow regime [35]. In this study, the problem mentioned in 3rd section was investigated and the simulation was modeled for different cases.

3. PROBLEM DEFINITION AND SETUP OF EDMD SIMULATION

This study focuses on rarefied gas flow through a slit-type obstacle between two parallel plates. The effect of various slit size and inlet/outlet pressure ratio on flow properties are examined in numerous cases. The lower and upper plates and the slit between them, slit gap H and slit length L are shown in Figure 1. L/H has been taken into account while creating different cases for the slit geometry. $L/H = 0$ means L is zero regardless of H. $L/H = 2$ means that L is 2 times H regardless of H. In addition, the effect of separate dimensions of L and H were examined. Entire channel volume is computational domain. The gas pressure p_{in} and temperature T_{in} at the channel inlet and the pressure p_{out} and temperature T_{out} at the outlet are assigned when the simulation is initialized. The temperature of the lower and upper plates and the temperature inside the channel is $300K$ initially. Wall temperature is constant throughout the simulation, but the temperature of the channel is developed due to expansion throughout the simulation. Monatomic Argon gas has been selected as the working fluid. Total number of simulated molecules is 200000. All molecule-wall collisions were modeled as diffuse reflection.

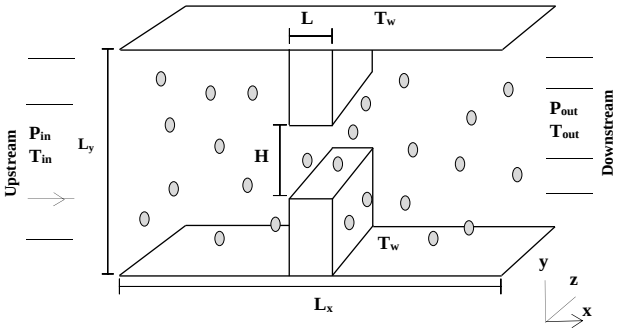

Figure 1. Geometry of computation domain slit and location of slit

While calculating the distribution of macroscopic properties, the channel was divided into 51 regions (bins) in the x − y plane. All 1D distributions are obtained along the channel mid-line in the x-axis by averaging the y and z axes. The properties within each bin were averaged along the z-axis for 2D data. In order to minimize numerical error, non-dimensionalization have been applied by scaling magnitudes with Boltzmann constant k_B=1.38×10^{-23}, reference mass $m = 1.5 \times 10^{-27}$kg and diameter $d = 0.5 \times 10^{-10}$m. Therefore, length of plates is $L_x = 10000 \times d$ and distance between them is L_y =5000× d. Since the z-axis is periodic, the width of the plates is infinite. The local Mach number is calculated with the local root mean square velocity (c_{rms}) and the temperature (T). The macroscopic properties have been calculated for each bin. For the purpose of qualitative comparison, Mach number (M), velocity (u_x), temperature (T), pressure (p) and density (n) distributions in all simulations have been nondimensionalized by normalizing with $2.5M$, $540m/s$, $330K$, $8\times10^6 Pa$ and $2.26\times10^6 m^{-3}$, respectively. Different pressure ratios and Kn are selected for different simulation setups. The slit is placed at position 0.16 L_x to take into account the fluid behavior at the slit entrance and also to follow the behavior at the slit exit to a certain distance.

Pressures at the inlet and inside the channel are initially same. In order to prevent molecule accumulation at the inlet and to obtain a steady flow rapidly, flow is created by applying low pressure only at the channel outlet.

At the initialization, the molecules have been randomly distributed into the channel according to the given pressure and number density. Their velocities are randomly assigned from a distribution function with respect to initial temperature. Specular reflection boundary condition has been valid for channel walls and no slit has been present. Thus, molecules have been allowed to collide enough to reach thermal equilibrium. Then a slit of the desired geometry has been created at the specified location of the channel and the corresponding reflection boundary conditions have been applied to the channel walls (diffusive in the y-axis and periodic in the z-axis). Finally, the pressure boundary condition has been applied to the downstream flows along the x-axis.

To calculate the flow rate ($\dot{m}$), the number of molecules entering (N_{in}) and leaving (N_{out}) the slit of width L are counted in a certain time period (Δt) and m_{mol} is the mass of a single molecule.

$$\dot{m} = \frac{N_{out} + N_{in}}{2\Delta t} m_{mol} \tag{22}$$

Flow rate and macroscopic properties were obtained at different Knudsen numbers (Kn) which can be described as the ratio of molecule's mean free path (λ) to the characteristic length (L_y).

$$Kn = \frac{\lambda}{L_y} \tag{23}$$

Since the H height is a control parameter in this study, it will not be appropriate to use it in Kn calculation. Therefore, Kn was calculated through L_y (channel length). In this way, the effect of the height H on the flow could be examined independently of Kn.

For each simulation, the pressure and density distributions are normalized to their values at the channel inlet. Hence, qualitative comparison of the results has been possible in different Kn, in other words, in density.

4. RESULTS AND DISCUSSION

In the flow rates were obtained according to Kn of transition regime at pressure ratios (p_o/p_i)=0.1 and 0.5 for L/H=0 (L=0) - H=500 and L/H=2 (L=1000) - H=500. As Kn is changing from 0.04 to 10, flow rate decreases. As Kn increases, the flow rate is almost constant until the transition regime. After that, a sudden decrease is observed in mass flow rate. This behaviour remains throughout the transition regime. In the molecular flow regime, it is almost constant. When the pressure ratio (p_o/p_i) increases from 0.1 to 0.5, the flow rate also decreases. This difference in flow rate due to pressure rate is not constant over the entire Kn range. It increases towards the molecular regime and decreases towards the continuum regime. L/H ratio also affects the flow rate. Increasing L creates a thin channel in the slit. This not only causes a decrease in the flow rate for the entire transition regime, but also changes Kn of the transition regime. As L increases, this range shifts towards smaller Kn values. Similar results at low Kn were observed in some DSMC studies [36] with a fixed H height and without top and bottom plates. The effect that creates the difference in high Kn is the increase of momentum transfer between individual molecules and upper and lower plate walls.

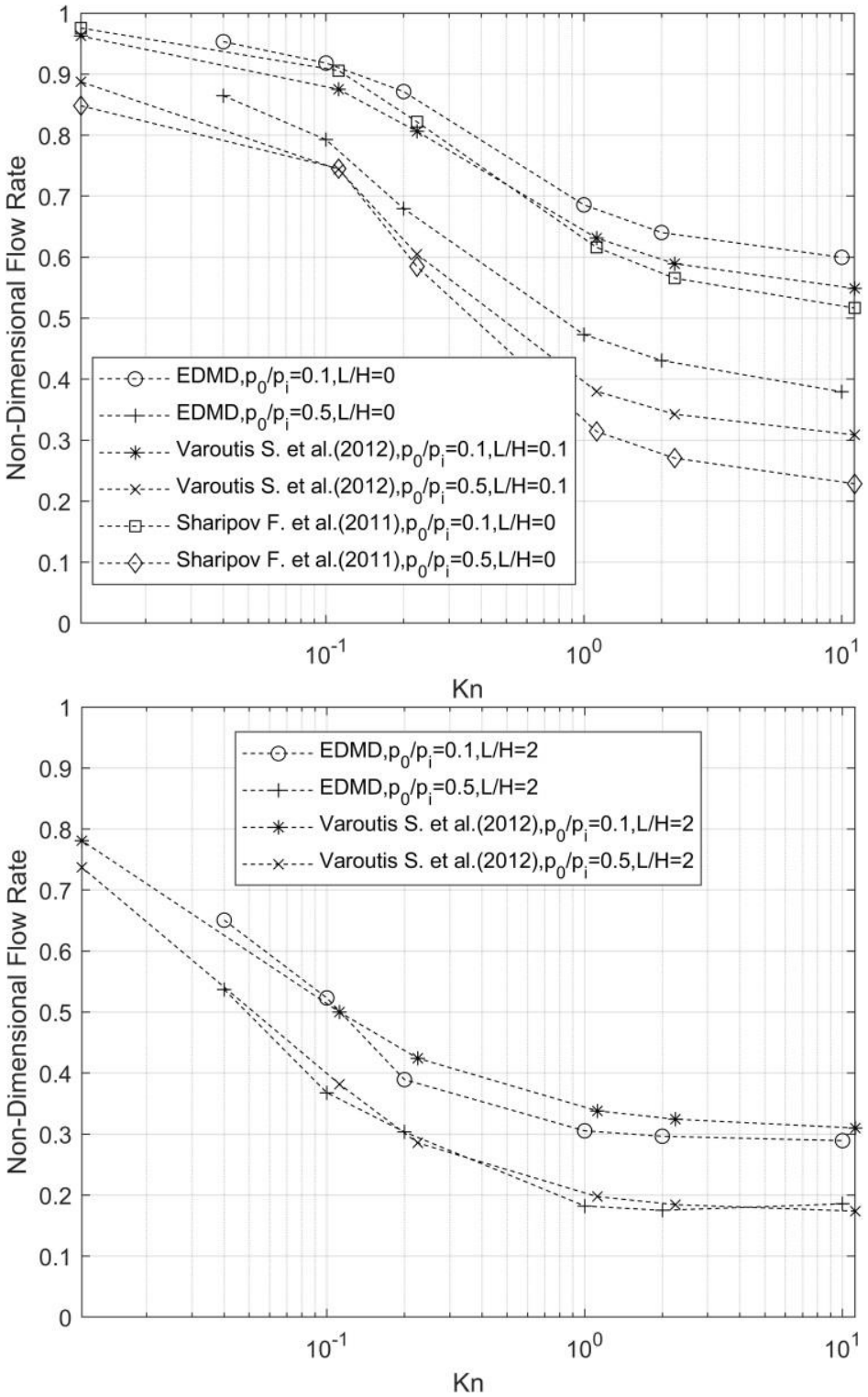

Figure 2 *Kn* vs. Non-Dimensional Flow Rate. p_o/p_i = 0.1 and 0.5 were compared for *L/H*=0(top) and 2(below).

In Figure 3, Mach number (M), temperature (T) and pressure (p) distribution along x/L_x were obtained under flow conditions p_o/p_i=0.1 and 0.5, H=500 and L=0 at Kn in transition regime. As Kn approaches to the continuous regime, the velocity at the slit outlet increases. While the temperature approaches to the initial value towards the channel outlet in low Kn, it decreases further (lower than the initial value) in high Kn. In steady-state flows, a sudden pressure drop is expected at the slit outlet due to the increase in

cross-sectional area. But as the Kn increases, this behavior disappears.

Mach number (M), temperature (T), pressure (p), density (n) contour plots and streamlines of the flow case in Figure 3 are shown in Figure 4 and 5, respectively. At low Kn, more pronounced vortex formations are noticeable at the slit outlet. There are even backflow vortex at the inlet of the slit due to the slit wall obstacle. As Kn increases, the vortex decreases at the slit outlet and begins to form at the slit inlet. For the case of H=500, Mach disk structure did not occur due to the maximum critical M being 0.7 at the outlet of the slit.

p_o/p_i=0.1, H=500 and L=0

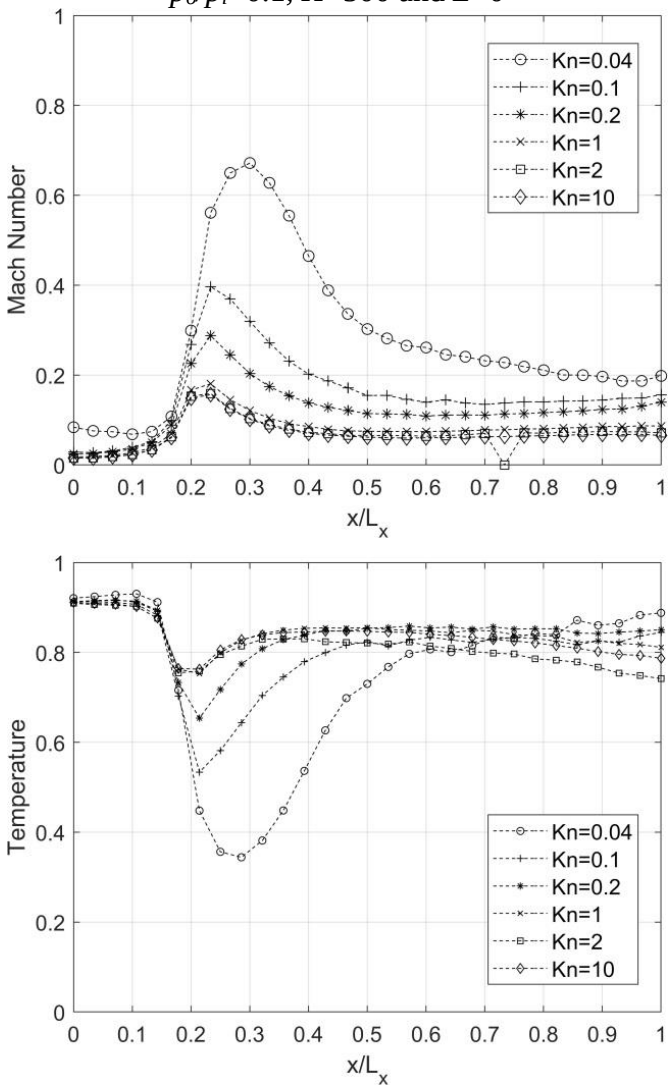

p_o/p_i=0.5, H=500 and L=0

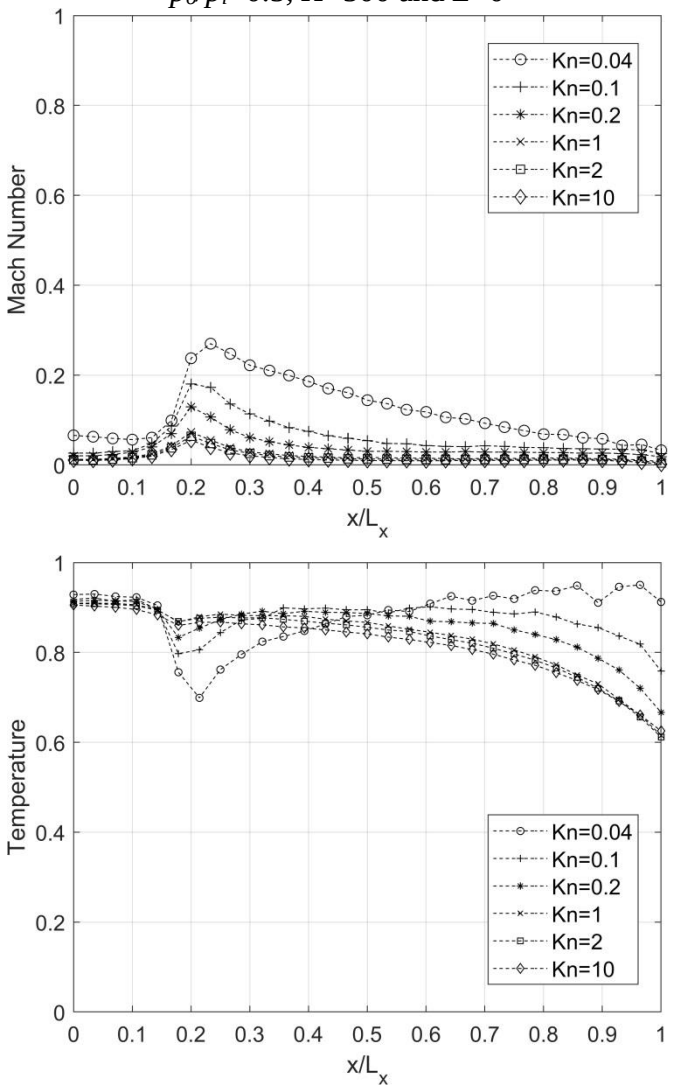

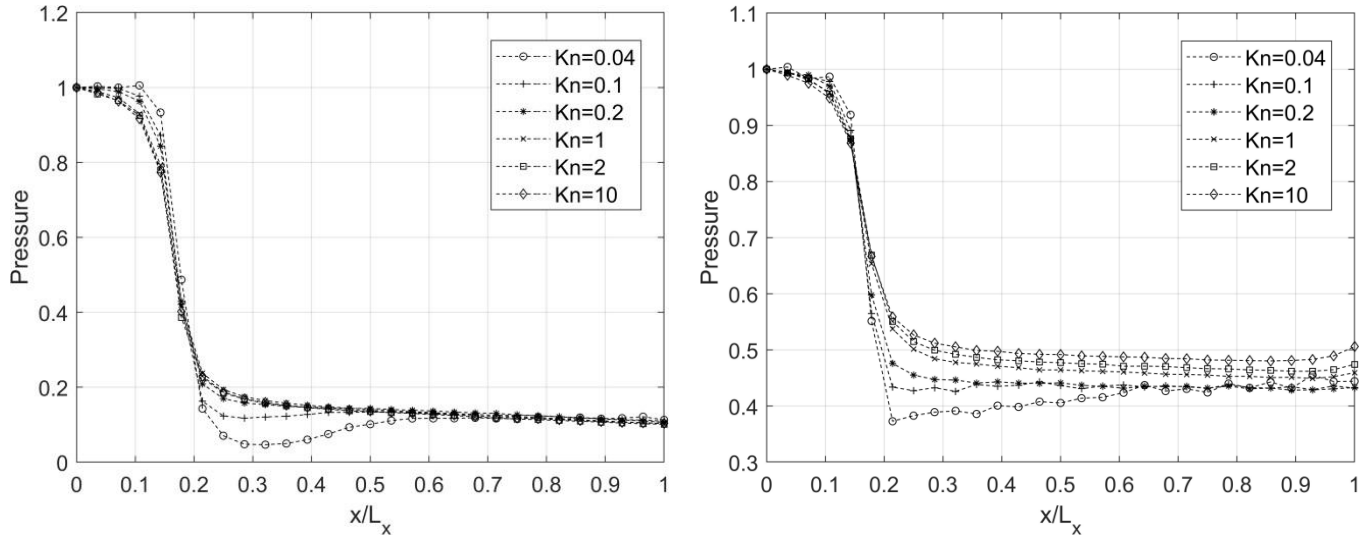

Figure 3 *M*, *T* and *p* distributions along L_x depending on *Kn*. Flow conditions are p_o/p_i=0.1(left) and p_o/p_i=0.5(right), *H*=500 and *L*=0.

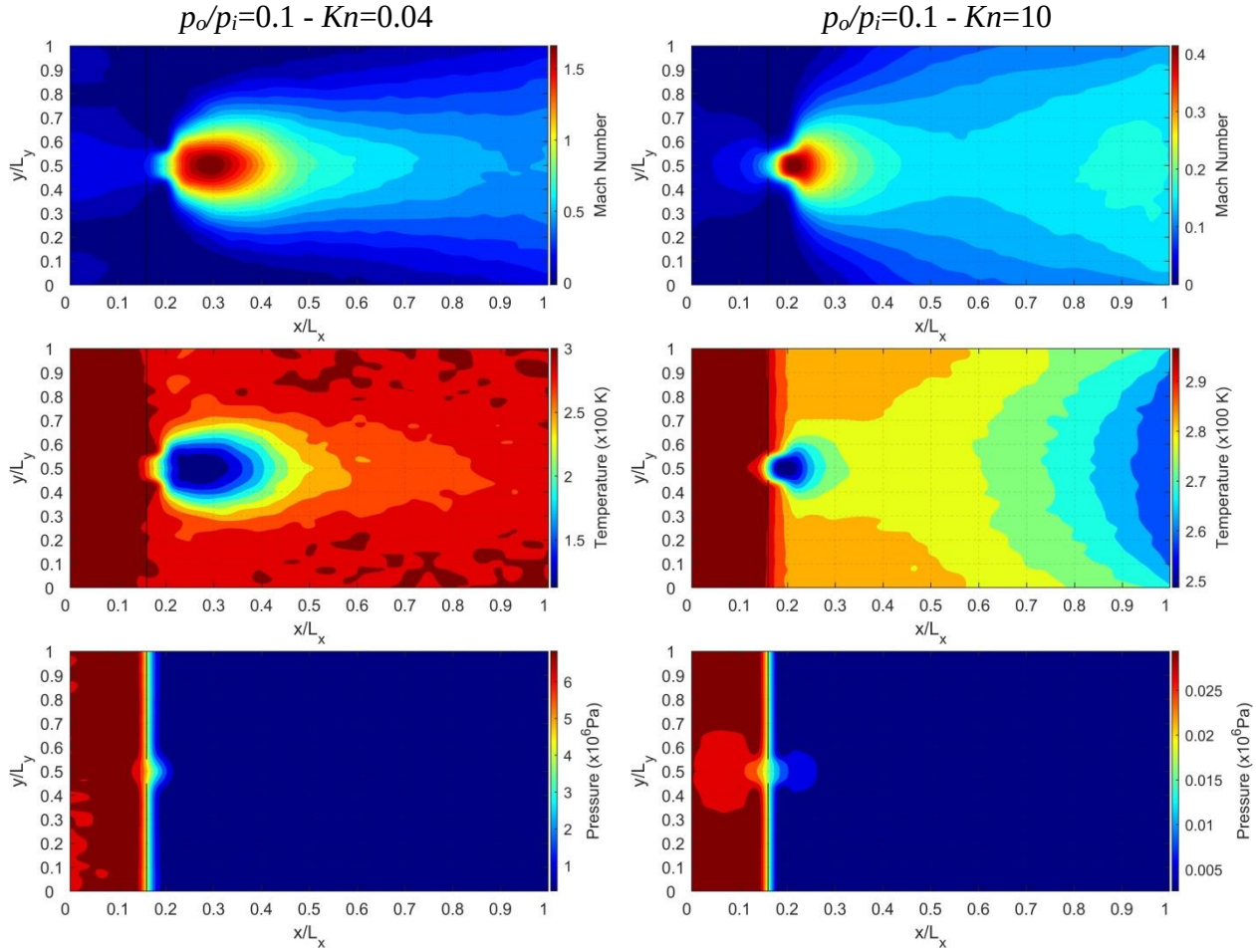

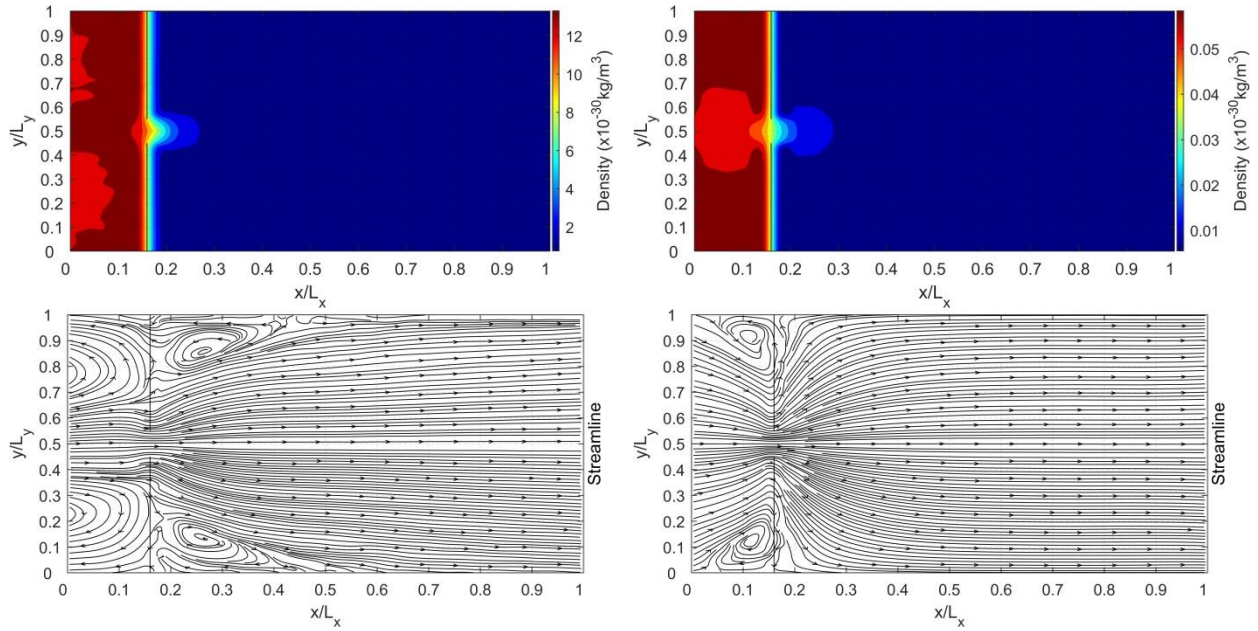

Figure 4 Contour plots of mach number, temperature, pressure, density and streamline. For H=500 - L=0: p_o/p_i=0.1 - Kn=0.04(Left Column), p_o/p_i=0.1 - Kn=10(Right Column).

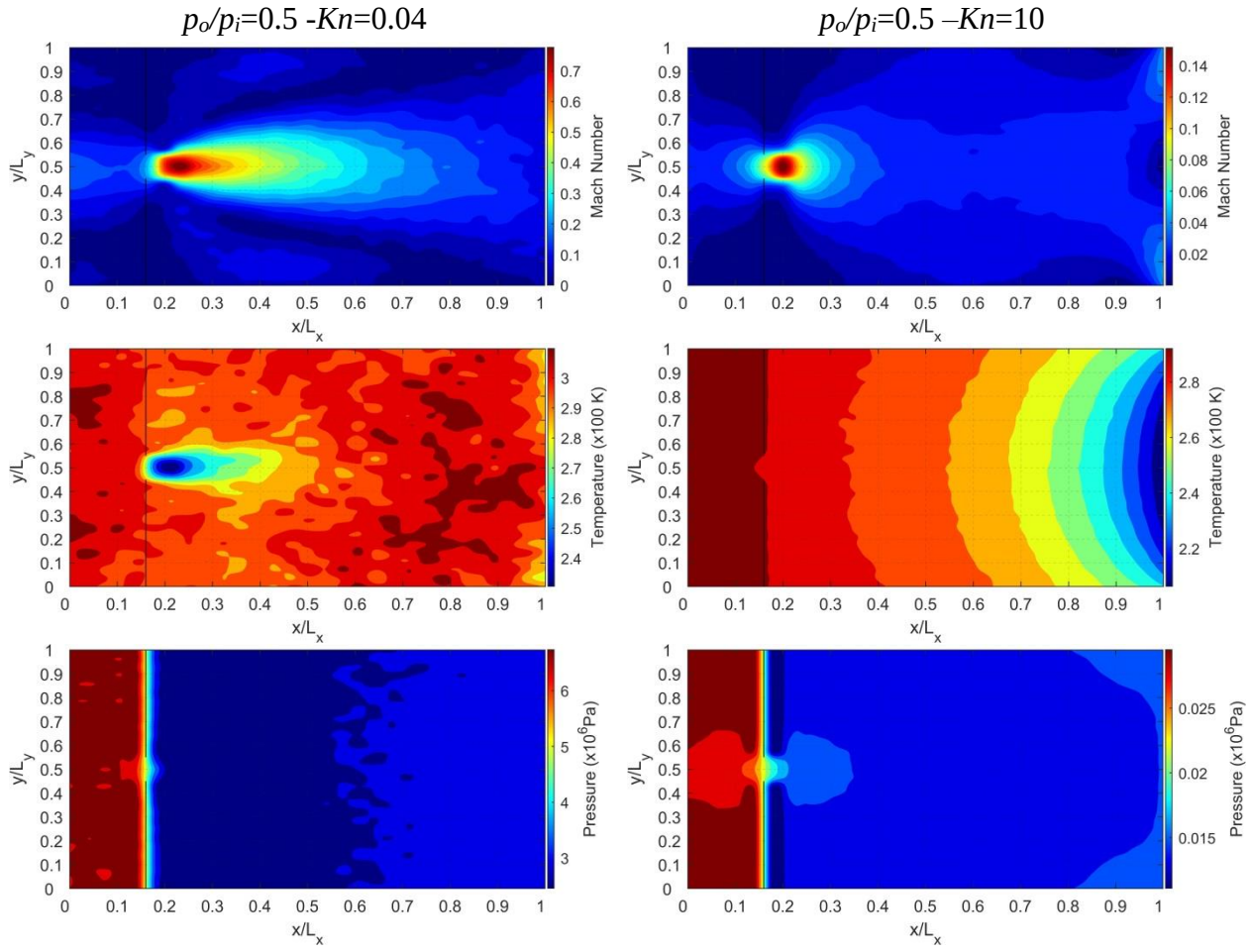

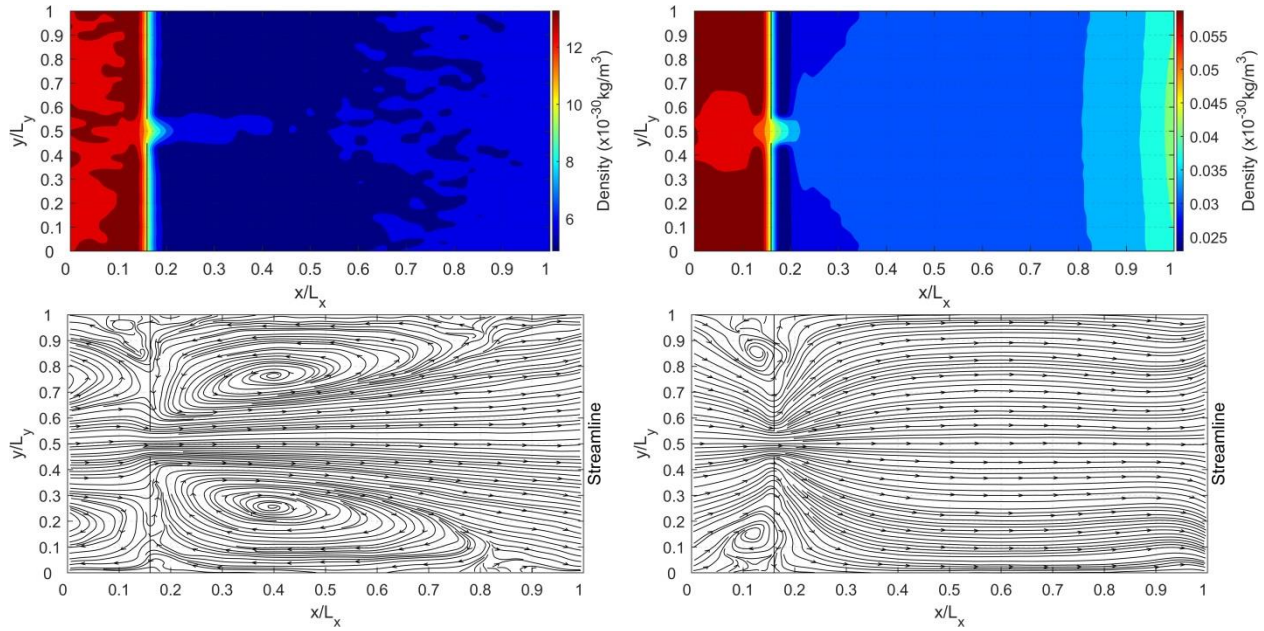

Figure 5 Contour plots of mach number, temperature, pressure, density and streamline. For H=500 - L=0: p_o/p_i=0.5 - Kn=0.04(Left Column), p_o/p_i=0.5 - Kn=10(Right Column).

In Figure 6, Mach number (M), temperature (T) and pressure (p) distributions are presented along x/L_x of the channel at Kn in transition regime for p_o/p_i=0.1 and 0.5, H=1000 and L=0. When the pressure ratio increases 5 times, Mach number doubles at the slit exit for Kn=0.04. Mach number is nearly 1 at the slit outlet. The midline distribution of Mach, temperature and pressure shows more dramatic changes than H=500 at outlet of the slit. Pressure drop at outlet of the slit in case of at H=1000 and p_o/p_i=0.5 for Kn =0.04 is more than H=500 but not valid for p_o/p_i=0.1. In addition, vortices size at outlet of slit in the case of H=500 is smaller than H=1000 especially for lower pressure ratio p_o/p_i=0.5.

p_o/p_i=0.1, H=1000 and L=0

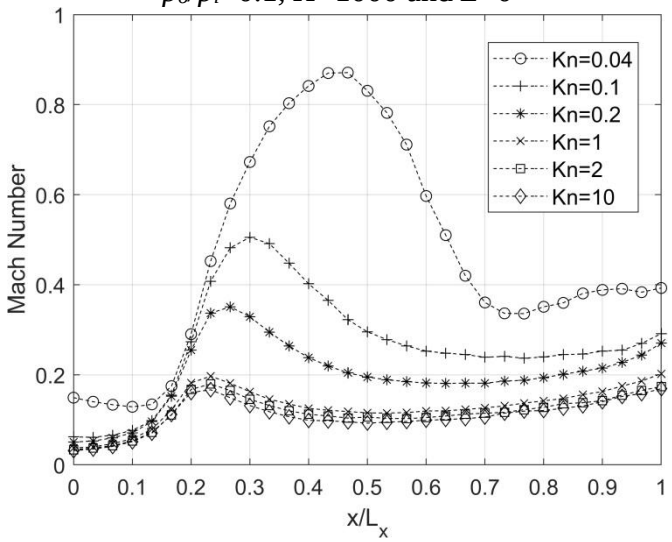

p_o/p_i=0.5, H=1000 and L=0

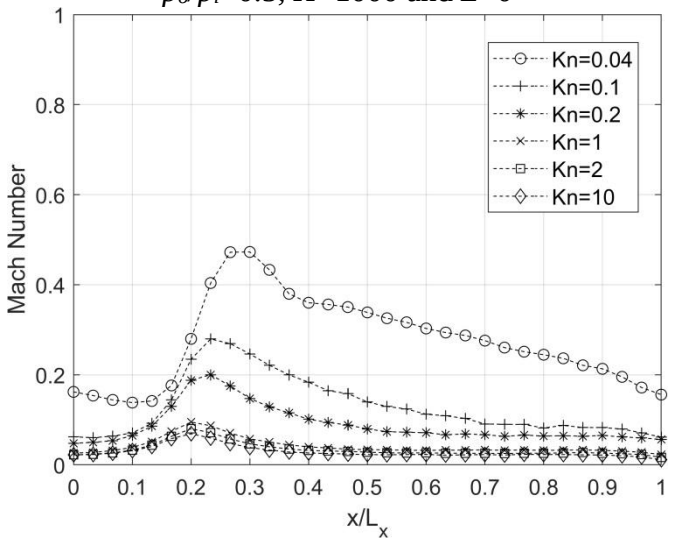

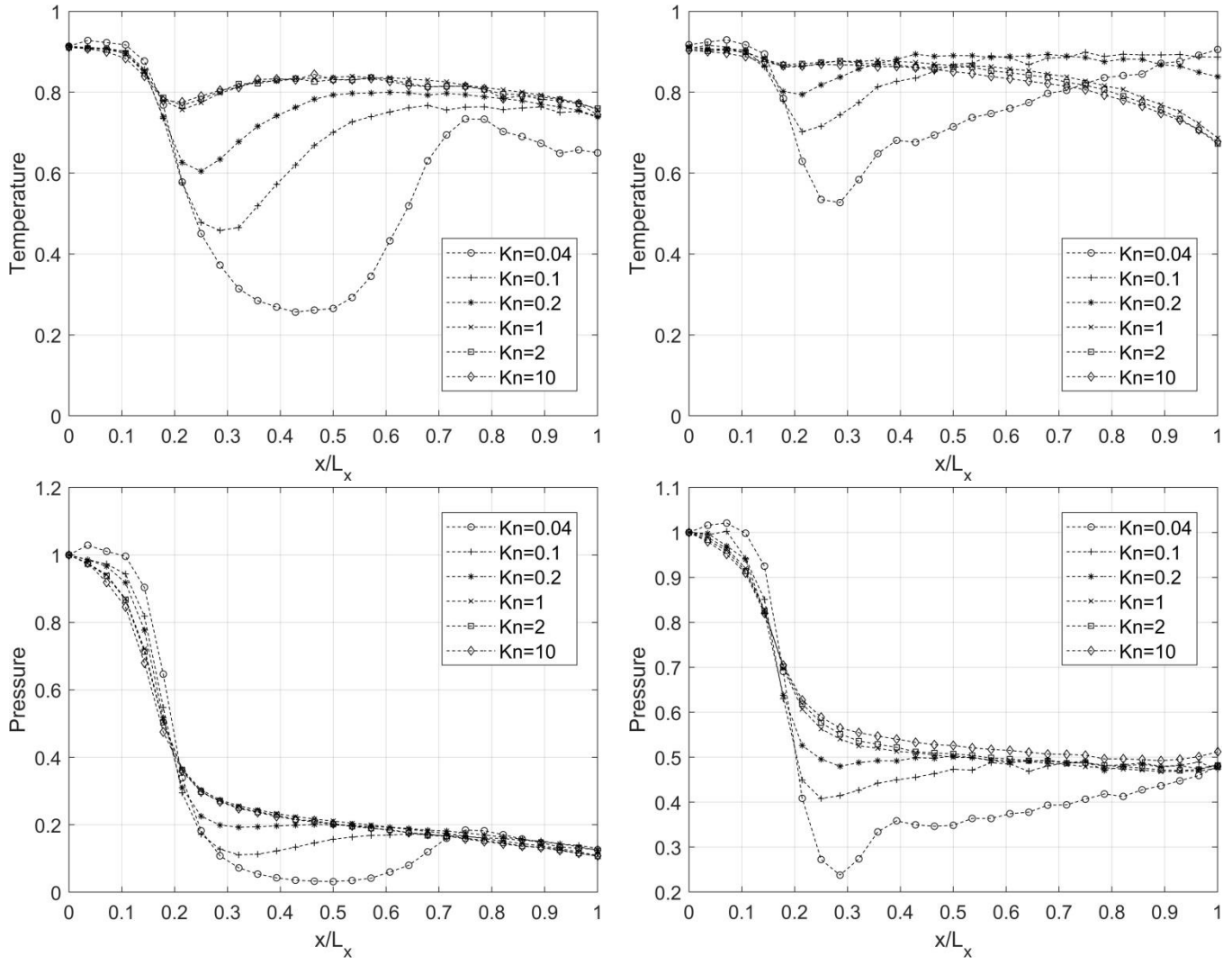

Figure 6 *M*, *T* and *p* distributions along L_x depending on *Kn*. Flow conditions are p_o/p_i=0.1(left) and p_o/p_i=0.5(right), *H*=1000 and *L*=0.

Mach number (M), temperature (T), pressure (p), density (n) contour plots and streamlines of the flow case in Figure 6 are shown in Figure 7 and 8, respectively. Mach discs started to be seen around x=0.75-0.8 at Kn=0.04. Mach disks are characterized by sudden fluctuations in Mach number, velocity, pressure, temperature and density distributions. At the outlet of the slit, a zone of silence is formed, where there is a sudden decrease in pressure and temperature, and a sudden increase in velocity. Then a normal shock occurs by decreasing the velocity. With this, there is a sudden increase in pressure and temperature. The silence zone and normal shock are delimited by the barrel shock. The flow re-thermalizes and is of relatively high density. It has a slightly supersonic flow rate. Flow slows down after barrel shock [21, 37]. Only enlargement of the H dimension caused this. This effect can also be seen in the changes in the x-axis in Figure 6. In the literature, the main factors in the formation of these discs are given as pressure ratio and Kn. Due to the effect of the simulation on the calculation power, only one Mach disc could be seen, since the length of the channel after the slit could not be extended too much and the Kn could not be further reduced. According to the pressure distribution along the channel, the sudden pressure drop at the slot outlet was smaller and farther than the H=500. Thus, it has been revealed that a certain distance is required for the formation of barrel shocks.

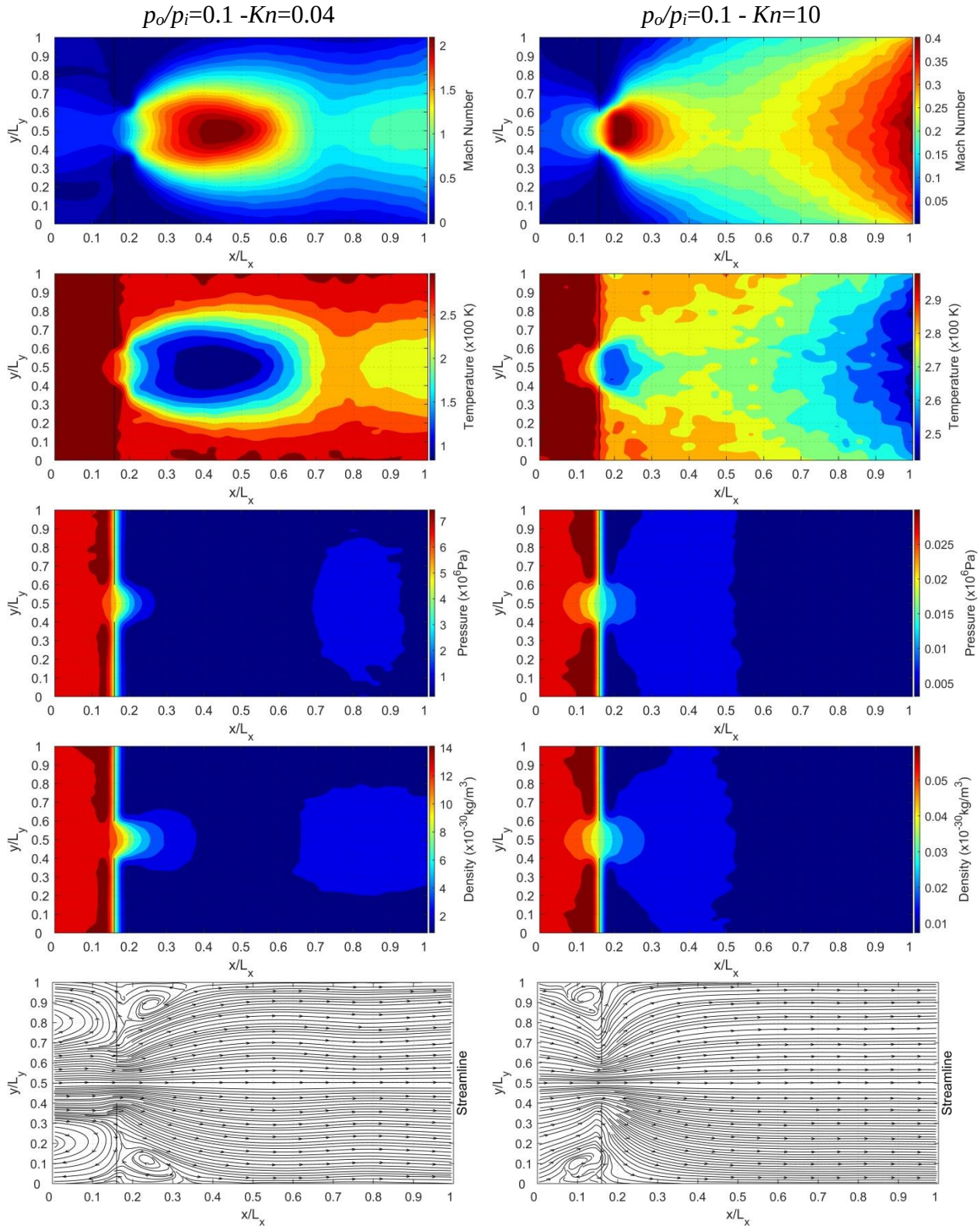

Figure 7 Contour plots of mach number, temperature, pressure, density and streamline. For H=1000 - L=0: p_o/p_i=0.1 - Kn=0.04(Left Column), p_o/p_i=0.1 - Kn=10(Right Column).

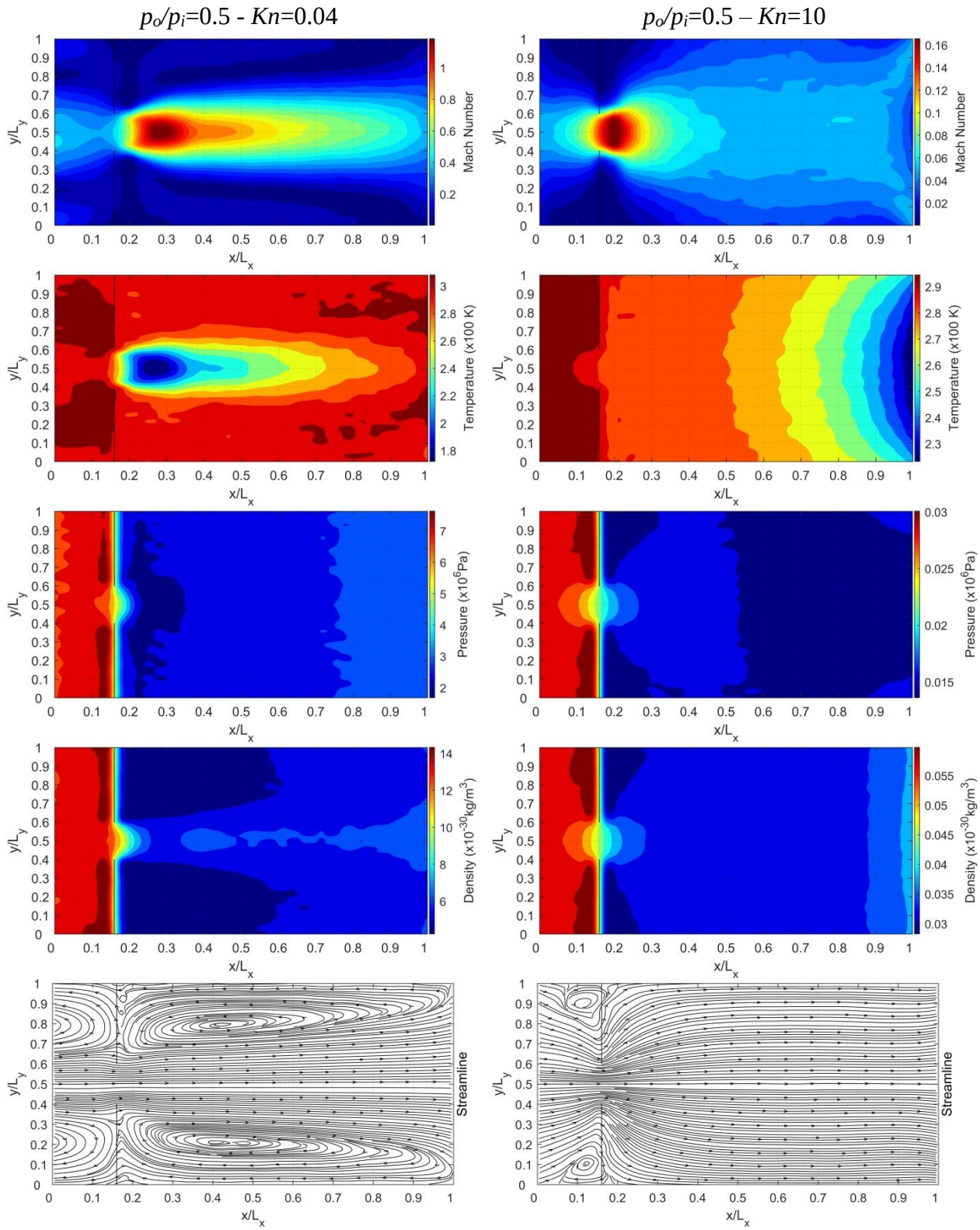

Figure 8 Contour plots of mach number, temperature, pressure, density and streamline. For H=1000 - L=0: p_o/p_i=0.5 - Kn=0.04(Left Column), p_o/p_i=0.5 - Kn=10(Right Column).

In Figure 9, Mach number (M), temperature (T) and pressure (p) changes along x/L_x for different Kn and p_o/p_i=0.1 and 0.5, H=500 and L=1000. Increasing L decreases Mach number at the slit exit. However, it causes vortex formation after the slit to spread longer along the x-axis. The pressure drop at the slit exit was smaller than that of L=0 for the same H. Mach number (M), temperature (T), pressure (p), density (n) contour plots and

streamlines of the flow case in Figure 9 are shown in Figure 10 and 11, respectively.

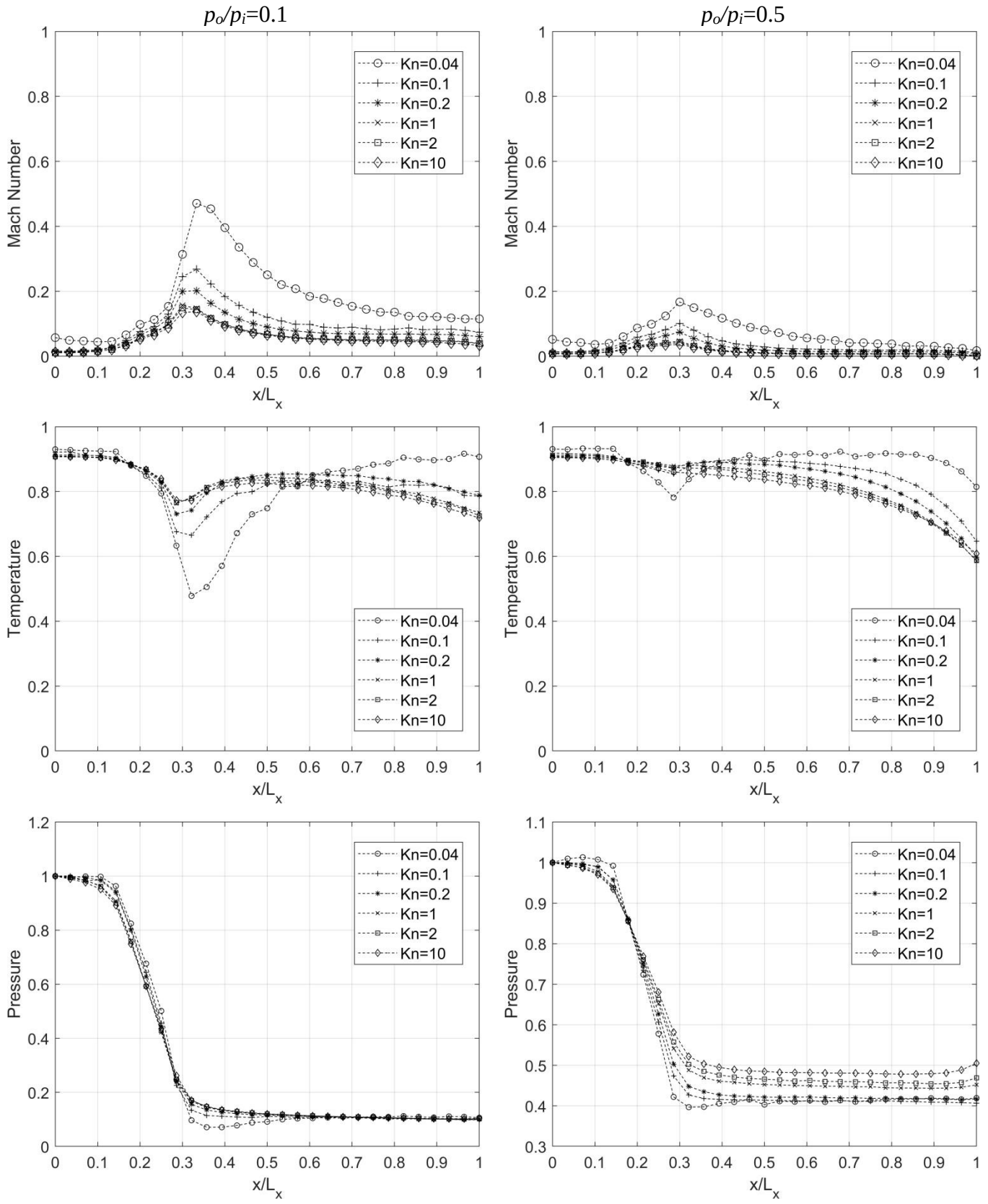

Figure 9 M, T and p distributions along L_x depending on Kn. Flow conditions are p_o/p_i=0.1(left) and p_o/p_i=0.5(right), H=500 and L=1000.

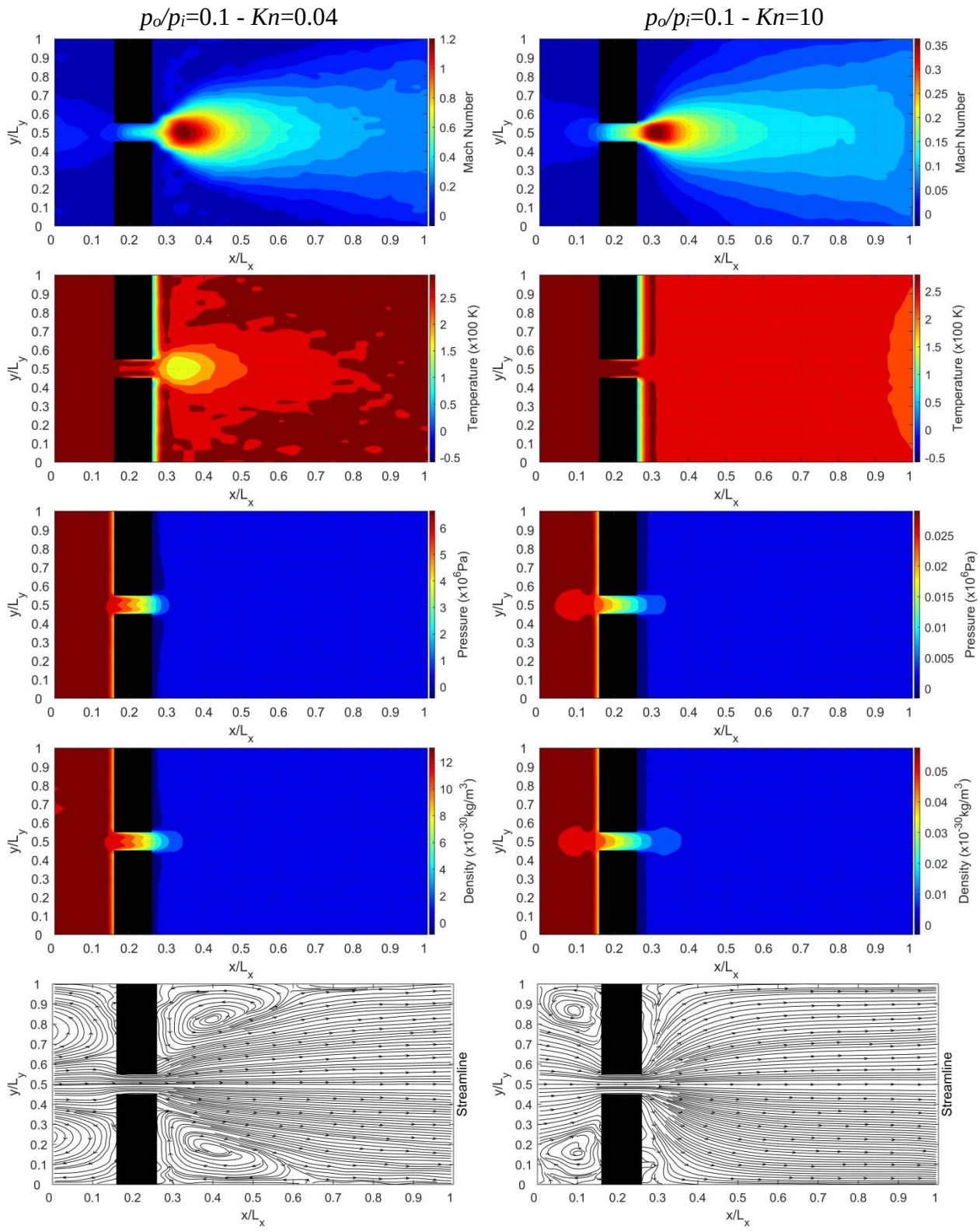

Figure 10 Contour plots of Mach number, Temperature, pressure, density and streamline. For H=500 - L=1000: p_o/p_i=0.1 - Kn=0.04(Left Column), p_o/p_i=0.1 - Kn=10(Right Column).

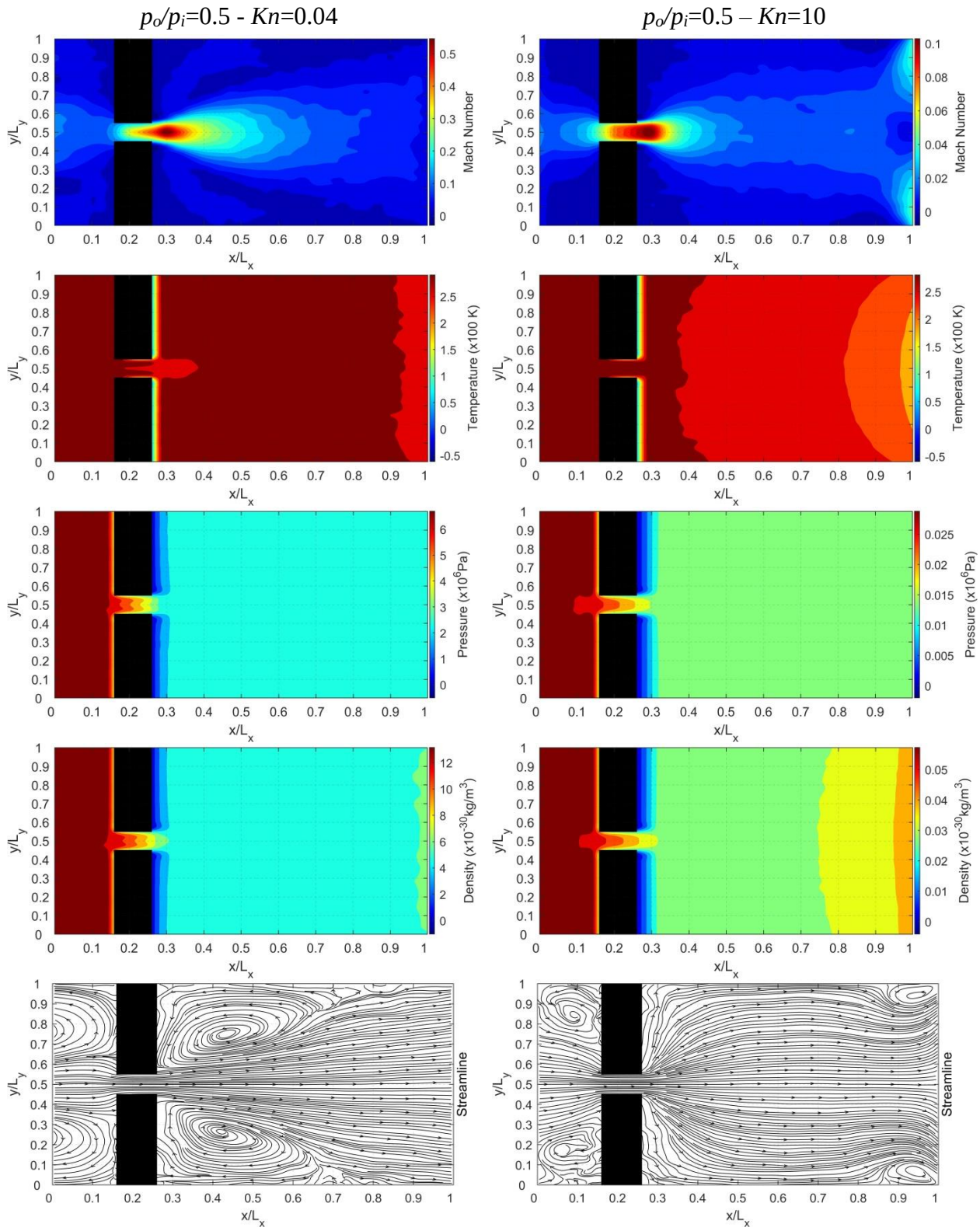

Figure 11 Contour plots of Mach number, Temperature, pressure, density and streamline. For H=500 - L=1000: p_o/p_i=0.5 - Kn=0.04(Left Column), p_o/p_i=0.5 - Kn=10(Right Column).

For Kn=0.04, H=1000 and L=0, pressure ratio p_o/p_i = 0.01-0.1-0.5 was applied in Figure 12. Increasing the pressure ratio by 100 times did not cause a big change in flow properties and Mach disc structure due to chocked flow. The most notable change in the contour plot is a slight increase in the length of the barrel shock along the channel. Changing the pressure ratio from p_o/p_i =

0.1 to 0.5, Mach number disproportionately doubled at the same Kn.

p_o/p_i for Kn=0.04

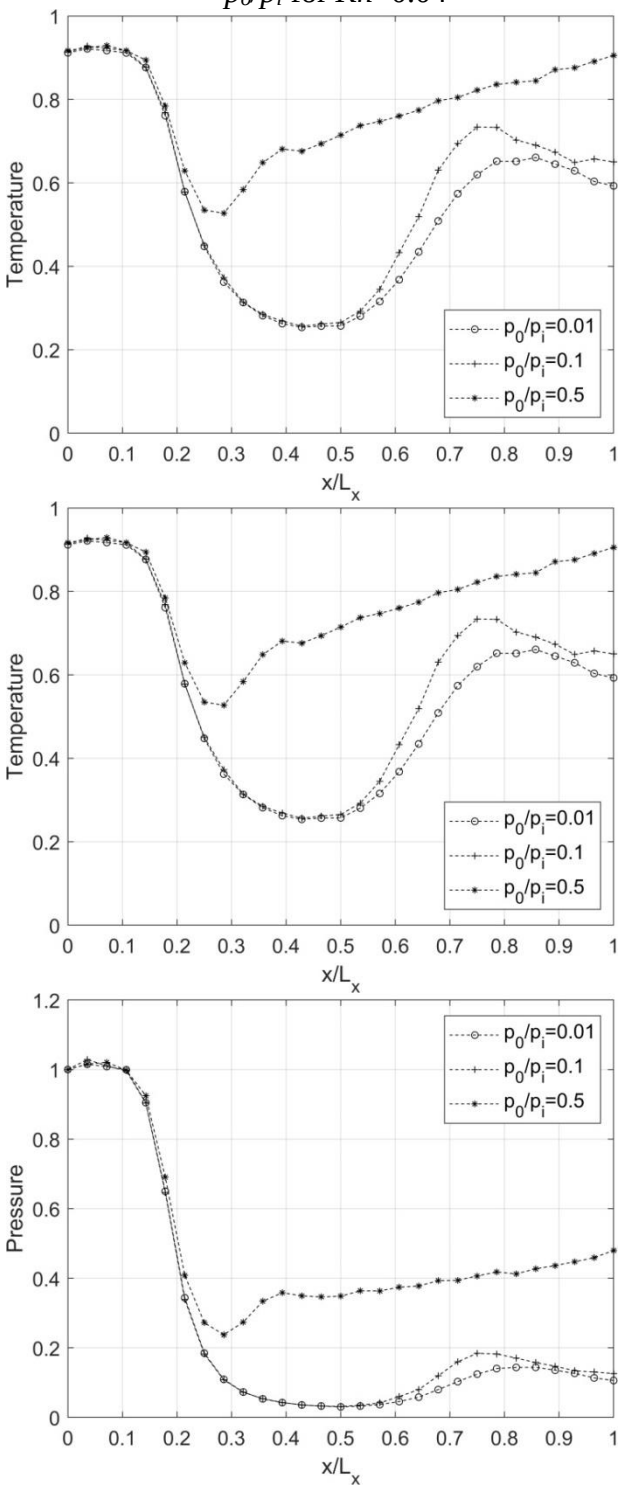

p_o/p_i=0.01

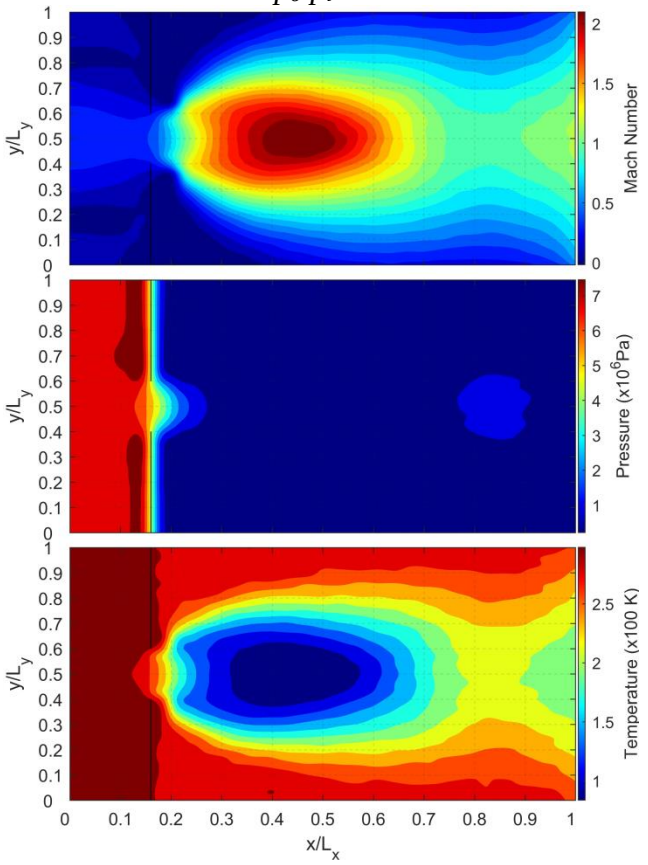

p_o/p_i=0.1

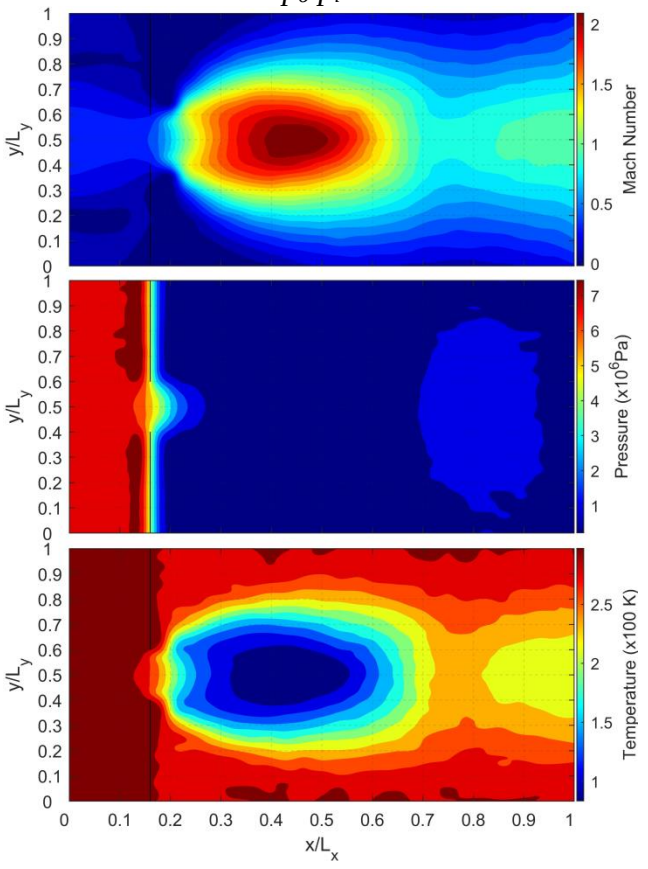

Figure 12 M, T and p distributions and contour plots depending on p_o/p_i for Kn=0.04, H=1000 and L=0. Top contour and bottom contour plots are p_o/p_i =0.01 and 0.1, respectively.

The enlargement of L reduced the pressure drop at the slit outlet. For H=250-500-1000, M, T and p distributions are given along the channel at Kn=0.04-10 in Figure 13. Fluctuation in the property distributions at the slit outlet is less at H=250. Thus, the settling of the flow properties was shorter at given Kn compared to high H. The positions of the Mach disc on the x-axis of the channel were similar to the study in Kn=0.01 [37]. However, the presence of plates and the difference in Kn caused sudden property changes at the slit outlet to be softer in EDMD.

In the distributions for some cases in this paper, the continuous decrease of the properties especially pressure and density from slit outlet to the channel outlet is because of low-pressure ratio is applied only to channel outlet.

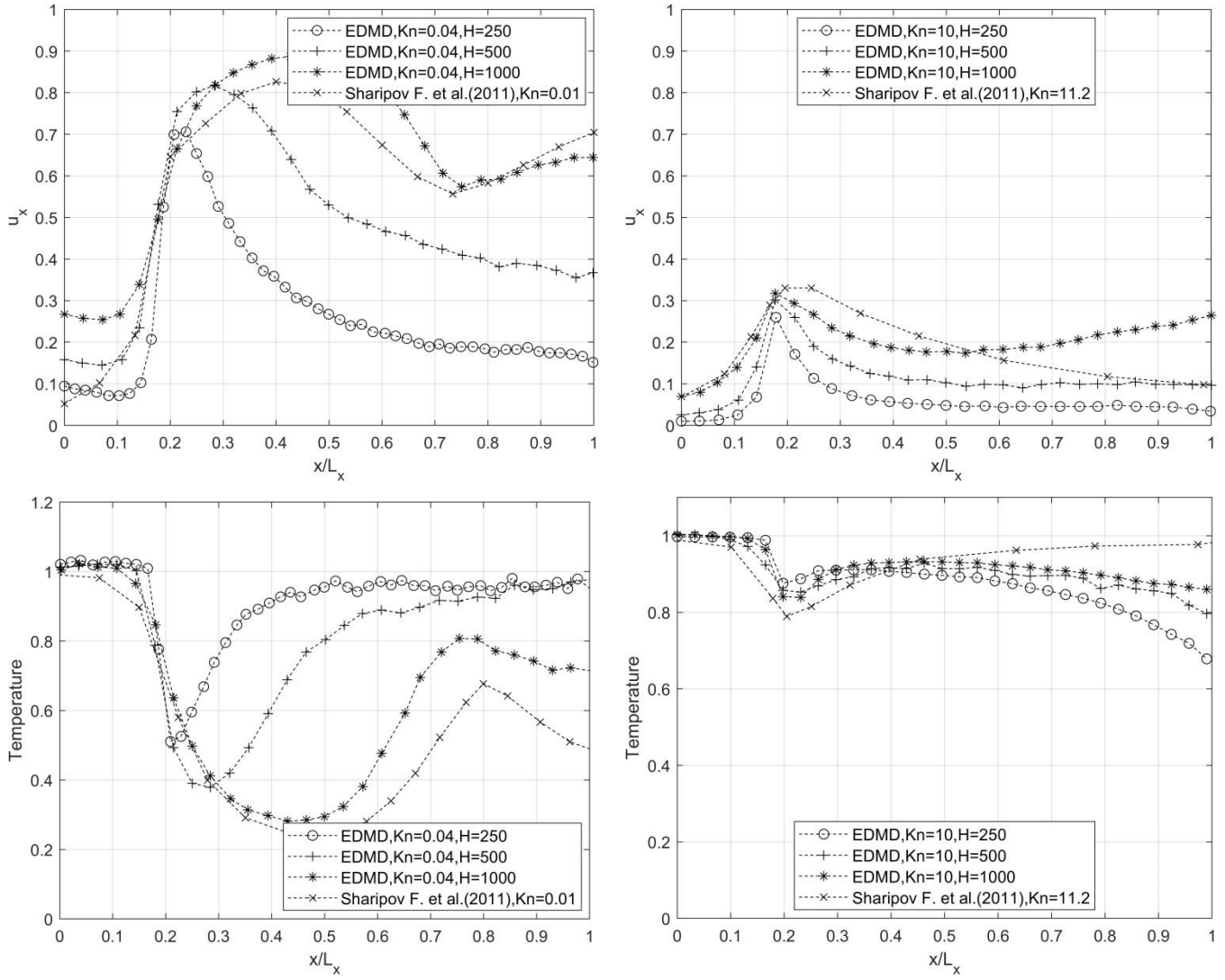

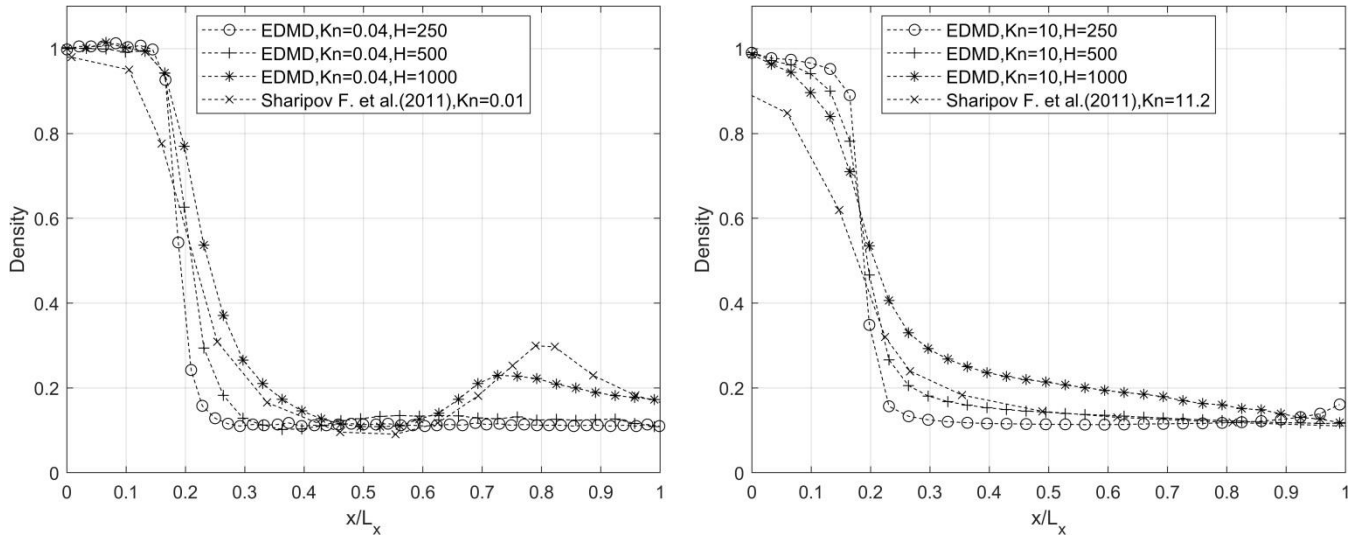

Figure 13 Distribution depending on Kn along L_x for dimensionless u_x, T and n. Kn=0.04(top) and Kn=10(bottom), p_o/p_i=0.1 for H=250, H=500 and H=1000 (L=0).

5. CONCLUSION

Effects of Kn and pressure ratio as well as H and L on the flow rate and flow property distributions along the channel have been investigated in the flow through a slit-type obstacle placed between two parallel plates. Simulations have been carried out for different cases, considering various L and H dimensions. The flow rate according to L/H ratio was examined in the transition regime and compared qualitatively with the literature.

Until the Kn number reaches the transition regime, the flow rate does not change significantly, but it decreases rapidly from the transition to the molecular regime. The flow rate typically increases as the pressure ratio increases for the same Kn. The difference between pressure ratios decreases as it approaches the steady state. While increasing the H increases the flow rate for high Kn, it has been observed that this difference decreases towards the continuous regime. While the increase in L/H ratio decreases the flow rate regardless of the pressure ratio and Kn, it has also been observed that it shifts the transition regime towards smaller Kn. In a case of different Kn, increasing of Kn results in increasing flow velocity. Because as Kn decreases, the inlet and outlet pressure difference (Δp) increases even if the pressure ratio remains constant.

Regardless of the pressure ratio, the formation of Mach discs is not observed as the flow regime passes from the continuous regime to the transition regime. For the same Kn in continuum regime, increasing the pressure ratio triggers the disc formation, but increasing the pressure ratio excessively will cause the flow to be chocked, and since the flow rate will no longer increase, there will be no serious change in the shape of the disc. Although the formation of Mach discs is directly dependent to Kn and the pressure ratio, H and L dimensions also play an important role for this phenomenon. For the same simulation case, an increase in H triggers disc formation, while an increase in L prevents disc formation as it decreases Mach and flow rate.

The characteristic of the vortices formed behind and in front of the slit is determined for different Kn, pressure ratio, H and L. Accordingly, it has been observed that increasing Kn decreases the size of the vortices and even almost loses and changes its position from the back of the slit (downstream direction) to the front (upstream direction). Although the H values given in the literature are not quantitatively specified, similar results were obtained at H=1000 according to the distribution data in the x-direction obtained for different H based on the L_y / H ratio. Thus, the effects of H and L variation on flow properties, streamlines and Mach disk structure are revealed independently of Kn and pressure ratio.

This study is important to understand vortices formation and shapes at inlet and outlet of the slit depending on Kn, pressure ratio and the slit gap geometry and showed that Mach disc, which is known to depend only on pressure ratio and Kn, can actually be controlled by H and L dimensions. It can also be important for controlling or measuring sudden pressure changes in similar applications.

Funding

The author (s) has no received any financial support for the research, authorship or publication of this study.

The Declaration of Conflict of Interest/ Common Interest

No conflict of interest or common interest has been declared by the authors.

Authors' Contribution

The authors contributed equally to the study.

The Declaration of Ethics Committee Approval

This study does not require ethics committee permission or any special permission.

The Declaration of Research and Publication Ethics

The authors of the paper declare that they comply with the scientific, ethical and quotation rules of SAUJS in all processes of the paper and that they do not make any falsification on the data collected. In addition, they declare that Sakarya University Journal of Science and its editorial board have no responsibility for any ethical violations that may be encountered, and that this study has not been evaluated in any academic publication environment other than Sakarya University Journal of Science.

REFERENCES

[1] P. J. Abbott, Z. J. Jabour, "Vacuum technology considerations for mass metrology," Journal of Research of the National Institute of Standards and Technology, vol. 116, no. 4, pp. 689–702, 2011.

[2] A. P. Polikarpov, I. Graur, "Unsteady rarefied gas flow through a slit," Vacuum, vol. 101, pp. 79–85, 2014.

[3] K. Jousten, S. Pantazis, J. Buthig, R. Model, M. Wüest, J. Iwicki, "A standard to test the dynamics of vacuum gauges in the millisecond range," Vacuum, vol. 100, pp. 14–17, 2014.

[4] S. Pantazis, D. Valougeorgis, "Rarefied gas flow through a cylindrical tube due to a small pressure difference," European Journal of Mechanics, B/Fluids, vol. 38, pp. 114–127, Mar. 2013.

[5] S. Varoutis, C. Day, F. Sharipov, "Rarefied gas flow through channels of finite length at various pressure ratios," Vacuum, vol. 86, no. 12, pp. 1952–1959, Jul. 2012.

[6] A. A. Alexeenko, D. A. Levin, S. F. Gimelshein, M. S. Ivanov, A. D. Ketsdever, "Numerical and experimental study of orifice flow in the transitional regime," 35th AIAA Thermophysics Conference, 2001.

[7] G. A. Bird, "Molecular gas dynamics and the direct simulation of gas flows," Oxford: Clarendon Press, 1994.

[8] I. Kandemir, "A multicell molecular dynamics method [Ph.D. thesis]," Case Western Reserve University, Cleveland, Ohio, USA, 1999.

[9] I. Greber, C. Sleeter, I. Kandemir, "Molecular dynamics simulation of unsteady diffusion," in AIP Conference Proceedings, Aug. 2001, vol. 585, pp. 396–400.

[10] V. R. Akkaya, I. Kandemir, "Event-driven molecular dynamics simulation of hard-sphere gas flows in microchannels," Mathematical Problems in Engineering, vol. 2015, 2015.

[11] B. J. Alder, T. E. Wainwright, "Phase transition for a hard sphere system," The Journal of Chemical Physics, vol. 27, no. 5. pp. 1208–1209, 1957.

[12] D. C. Rapaport, "The event scheduling problem in molecular dynamic simulation," Journal of Computational Physics, vol. 34, no. 2, pp. 184–201, 1980.

[13] A. Donev, A. L. Garcia, B. J. Alder, "Stochastic Event-Driven Molecular Dynamics," Journal of Computational Physics, vol. 227, no. 4, pp. 2644–2665, Feb. 2008.

[14] M. N. Bannerman, R. Sargant, L. Lue, "DynamO: A free O(N) general event-driven molecular dynamics simulator," Journal of Computational Chemistry, vol. 32, no. 15, pp. 3329–3338, Nov. 2011.

[15] G. A. Bird, "Molecular Gas Dynamics and the Direct Simulation of Gas Flows, " Oxford: Clarendon Press, 1994.

[16] G. D. Danilatos, "Direct simulation Monte Carlo study of orifice flow," in AIP Conference Proceedings, Aug. 2001, vol. 585, pp. 924–932.

[17] F. Sharipov, "Rarefied Gas Flow Through an Orifice at Finite Pressure Ratio," in AIP Conference Proceedings, Jun. 2003, vol. 663, pp. 1049–1056.

[18] F. Sharipov, "Numerical simulation of rarefied gas flow through a thin orifice," Journal of Fluid Mechanics, vol. 518, pp. 35–60, Nov. 2004.

[19] M. Wang, Z. Li, "Simulations for gas flows in microgeometries using the direct simulation Monte Carlo method," International Journal of Heat and Fluid Flow, vol. 25, no. 6, pp. 975–985, Dec. 2004.

[20] F. Sharipov, J. L. Strapasson, "Ab initio simulation of rarefied gas flow through a thin orifice," Vacuum, vol. 109, pp. 246–252, 2014.

[21] I. A. Graur, A. P. Polikarpov, F. Sharipov, "Numerical modelling of rarefied gas flow through a slit at arbitrary pressure ratio based on the kinetic equation," Zeitschrift fur Angewandte Mathematik und Physik, vol. 63, no. 3, pp. 503–520, Jun. 2012.

[22] A. R. Rahmati, R. Ehsani, "Simulation of Micro-Channel and Micro-Orifice Flow Using Lattice Boltzmann Method with Langmuir Slip Model," Nano Micro Scales, vol. 5, no. 1, pp. 1–8, 2017.

[23] J. Zhang, "Lattice Boltzmann method for microfluidics: Models and applications," Microfluidics and Nanofluidics, vol. 10, no. 1. Springer Verlag, pp. 1–28, Jan. 01, 2011.

[24] S. Misdanitis, S. Pantazis, D. Valougeorgis, "Pressure driven rarefied gas flow through a slit and an orifice," Vacuum, vol. 86, no. 11, pp. 1701–1708, May 2012.

[25] P. L. Bhatnagarp, E. P. Gross, A. M. Krook, "Model for Collision Processes in Gases. I. Small Amplitude Processes in Charged and Neutral One-Component Systems~," 1954.

[26] S. F. Gimelshein, G. N. Markelov, T. C. Lilly, N. P. Selden, A. D. Ketsdever, "Experimental and numerical modeling of rarefied gas flows through orifices and short tubes," in AIP Conference Proceedings, May 2005, vol. 762, pp. 437–443.

[27] C. T. Lilly, F. S. Gimelshein, D. A. Ketsdever, N. G. Markelov, "Measurements and computations of mass flow and momentum flux through short tubes in rarefied gases," Physics of Fluids, vol. 18, no. 9, 2006.

[28] J. Lindström, J. Bejhed, J. Nordström, "Measurements and numerical modelling of orifice flow in microchannels," 41st AIAA Thermophysics Conference, 2009.

[29] F. Sharipov, "Transient flow of rarefied gas through an orifice," Journal of Vacuum Science & Technology A: Vacuum, Surfaces, and Films, vol. 30, no. 2, p. 021602, Mar. 2012.

[30] M. T. Ho, I. Graur, "Numerical study of unsteady rarefied gas flow through an

orifice," Vacuum, vol. 109, pp. 253–265, 2014.

[31] A. L. Garcia, W. Wagner, "Generation of the Maxwellian inflow distribution," Journal of Computational Physics, vol. 217, no. 2, pp. 693–708, Sep. 2006.

[32] G. Paul, "A Complexity O(1) priority queue for event driven molecular dynamics simulations," Journal of Computational Physics, vol. 221, no. 2, pp. 615–625, Feb. 2007.

[33] M. Marín, P. Cordero, "An empirical assessment of priority queues in event-driven molecular dynamics simulation," Computer Physics Communications, vol. 92, no. 2–3, pp. 214–224, 1995.

[34] W. W. Liou, Y. C. Fang, "Implicit boundary conditions for direct simulation Monte Carlo method in MEMS flow predictions," CMES - Computer Modeling in Engineering and Sciences, 2000.

[35] M. Koc, I. Kandemir, V. R. Akkaya, "An Investigation of Transition Flow in Porous Media by Event Driven Molecular Dynamics Simulation," Journal of Applied Fluid Mechanics, vol. 14, no. 1, pp. 23–36, 2020.

[36] S. Varoutis, O. Sazhin, D. Valougeorgis, and F. Sharipov, "Rarefied gas flow into vacuum through a short tube," 51st IUVSTA Workshop on Modern Problems and Capability of Vacuum Gas Dynamics.

[37] F. Sharipov, D. V. Kozak, "Rarefied gas flow through a thin slit at an arbitrary pressure ratio," European Journal of Mechanics, B/Fluids, vol. 30, no. 5, pp. 543–549, Sep. 2011.

SAKARYA ÜNİVERSİTESİ
FEN BİLİMLERİ ENSTİTÜSÜ DERGİSİ

Sakarya University Journal of Science
SAUJS

ISSN 1301-4048 | e-ISSN 2147-835X | Period Bimonthly | Founded: 1997 | Publisher Sakarya University | http://www.saujs.sakarya.edu.tr/

Title: Conformational Analysis of Tyrosyl-Lysyl-Threonine Tripeptide Using MM, MD and QM Methods and Its Hyperpolarizability Study

Authors: Bilge BIÇAK, Serda Kecel GÜNDÜZ

Recieved: 2021-11-19 00:00:00

Accepted: 2022-06-15 00:00:00

Article Type: Research Article

Volume: 26
Issue: 4
Month: August
Year: 2022
Pages: 745-756

How to cite
Bilge BIÇAK, Serda Kecel GÜNDÜZ; (2022), Conformational Analysis of Tyrosyl-Lysyl-Threonine Tripeptide Using MM, MD and QM Methods and Its Hyperpolarizability Study. Sakarya University Journal of Science, 26(4), 745-756, DOI: 10.16984/saufenbilder.1025541
Access link
http://www.saujs.sakarya.edu.tr/en/pub/issue/72361/1025541

Sakarya University Journal of Science 26(4), 745-756, 2022

Conformational Analysis of Tyrosyl-Lysyl-Threonine Tripeptide Using MM, MD and QM Methods and Its Hyperpolarizability Study

Bilge BIÇAK*[1], Serda KECEL GÜNDÜZ[1]

Abstract

Peptides are important structures that offer important opportunities for therapeutic interventions in various diseases. Tyrosyl-Lysyl-Threonine is an important peptide structure that contains the antiviral, antioxidant, and anticancer properties of the amino acids in its structure. Examination of the conformational structure, which has great importance on both the ability of the molecule to fulfill its biological functions and electronic properties, is important for molecular studies. In this study, the determination of the stable conformations and optimization of the most stable structure of the Tyrosyl-Lysyl-Threonine molecule was carried out using molecular mechanical and quantum mechanical methods. With molecular dynamics simulation studies, the changes in conformational structure, RMSD, and Rg values in different environments were monitored for 10 ns. Additionally, the hyperpolarizability study of Tyrosyl-Lysyl-Threonine was carried out. As a result of this study, it was aimed to determine the optimized geometry of the tripeptide, its conformational changes, and nonlinear optical properties.

Keywords: Peptide, conformational analysis, hyperpolarizability

1. INTRODUCTION

Peptides are important structures that can be used as therapeutic compounds in the medicinal studies of diseases. Peptides that can trigger various biological activities such as anticancer, anti-inflammatory, immunomodulator, antidiabetic [1-4], are accepted internationally due to their therapeutic effects and are used effectively in different disease areas [5].

Tyrosyl-Lysyl-Threonine (YKT or Tyr-Lys-Thr) has $C_{19}H_{30}N_4O_6$ formula and 410.47 relative molecular mass. Structures containing tyrosine are neurotransmitter precursors [6,7] with the ability to increase the levels of plasma neurotransmitters. It also exhibits antioxidant properties [8,9]. Structures containing lysine also have antiviral effects as well as antioxidant properties like tyrosine [9,10]. In addition, it has been seen in studies in the literature that poly-lysine structures have antimicrobial, and antitumor properties [11]. It is known that

* Corresponding author: bbicak@istanbul.edu.tr
[1] İstanbul University, Faculty of Science
E-mail: skecel@istanbul.edu.tr
ORCID: https://orcid.org/0000-0003-1147-006X, https://orcid.org/0000-0003-0973-8223

structures containing threonine also have antibacterial properties [12], and support cardiovascular, hepatic, central nervous, and immune system functions. It has an important role in inhibiting apoptosis, synthesizing mucin, and maintaining the integrity of the intestinal barrier [13-15]. It is also an essential molecule for the synthesis of glycine and serine amino acids, which are important in collagen, elastin, and muscle tissue production [16]. Tyr-Lys dipeptide is an important peptide structure that has analgesic effects [17], and induces necrosis [18,19]. Considering both experimental and theoretical studies performed with Tyr-Lys-Thr, it was determined that Tyr-Lys-Thr tripeptide has a cytotoxic effect on prostate, breast and cervical cancer cells (Mat-LyLu, MCF-7, and HeLa cell lines) and has an anti-cancer potential in vitro studies. In molecular docking studies, it was determined that it made strong bindings with androgen, estrogen, progesterone, and EGFR receptors, supporting the experimental studies [20-22].

The conformations, which are of great importance in the estimation of biological activity and physicochemical properties of Tyr-Lys-Thr tripeptide with drug potential, were determined in this study. Different conformations of the tripeptide were investigated in depth by MM, MD and QM methods. Theoretical conformational analysis, optimization, molecular dynamics simulations and hyperpolarizability studies were realized to determine and evaluate the structural properties of YKT tripeptide.

2. MATERIAL METHODS

2.1. Theoretical Conformational Analysis

The conformational analysis of YKT tripeptide was realized with FORTRAN program [23]. The conformations having low energies of tripeptide were obtained with the help of the Ramachandran maps [24,25]. The conformational potential energies of YKT were obtained as the sum of Van der Waals, electrostatic, torsional, and hydrogen bond energies. The most stable conformation determined was accepted as the first data for geometry optimization performed by DFT method.

2.2. Optimization and Hyperpolarizability Analyses

Optimization in molecules provides to obtain a well-arranged structure by minimizing system energy. Different molecular geometries due to the arrays of atoms and the binding energies of the bonds affect the behavior of molecules (physical, chemical) [26]. Nonlinear-optical properties are important in the optoelectronic and laser technology areas [27]. The hyperpolarizability study of YKT tripeptide was achieved to predict the nonlinear-optical property. The optimization and hyperpolarizability studies of YKT were carried out using Gaussian09 software program [28] with the density functional theory method at B3LYP theory level and 6-311++G(d,p) basis set.

2.3. MD Analysis

The molecular dynamics (MD) simulations were carried out in the vacuum, water, and methanol environments for 10 ns using GROMOS96 43a1 force field [29] by GROningen MAchine for Chemical Simulations (GROMACS) software [30] to investigate the conformational change on the optimized structure. Before the MD production runs, further energy minimization calculations of the solvated systems were carried out and the systems were equilibrated with the help of NVT (for 50 ps) and NPT (for 500 ps) ensembles, employing the V-rescale thermostat [31] and the isotropic Parrinello-Rahman barostat [32] at 310 K and 1 bar. Only a simulation in an NVT ensemble was done for the vacuum medium for 100 ps. Molecular Dynamics (MD) simulations were conducted with 2 fs time steps and periodic boundary conditions. Root Mean Square Deviation (RMSD), Radius of Gyration (Rg), and H-bond information were obtained from the 10ns-long simulations.

YKT tripeptide was placed in the box and was adjusted as 3 x 3 x 3 nm. The cubic boxes were filled with 1061 moles of SPC (simple point charge) type water and 525 moles of methanol for solvent-containing environments. Na^+ and Cl^-

ions were included in the water and methanol systems to neutralize the systems. Energy minimization calculations using the steepest-descent algorithm were completed in 59 steps (for vacuum), 172 steps (for water), and 113 steps (for methanol). The NVT studies were carried out for 25,000 (for vacuum) and 50,000 (for water and methanol) steps with a 2-femtosecond time. For water and methanol environments, the NPT studies were realized for 250,000 steps with a 2 femtoseconds time. MD simulations were achieved for 5,000,000 steps with a 2 femtoseconds time in all environments.

Obtained graphics were plotted by Xmgrace plotting tool [33]. Images of conformational changes during 10 ns were obtained with VMD program [34].

3. RESULT AND DISCUSSION

3.1. Theoretical Conformational Analysis Result

The determination of the stable conformations of the YKT tripeptide was first started by performing the theoretical conformation analysis with the FORTRAN program. With this analysis, stable conformations of the tripeptide were tried to be determined. In the theoretical conformation analysis, the atoms forming the peptide, bond lengths, angles, angle values, and charge information were entered into the input file. The possible conformations and the energy values of these conformations were obtained by entering the dihedral angle values of the conformation regions with the help of the conformation regions formed by Ramachandran of the amino acids that make up the peptide (cf. Figure 1). 105462 conformations of YKT tripeptide were examined and it was observed that the conformation with the lowest energy was in the BBB (B1B3B1) region and had an energy value of 6.37 kcal/mol (cf. Table 1). While Van der Waals energy contributed the most to this energy value with -11.34 kcal/mol, the electrostatic and torsion energy values contributing to the total energy were calculated as 15.63 kcal/mol and 2.08 kcal/mol, respectively. When the most stable geometry was examined, it was seen that the biggest changes were in the χ_{13} (OH region in tyrosine side chain), φ_2 (between amino and Cα in lysine), and χ_{21} (between C_α and side chain in lysine) regions. When the input and output torsional angles were compared, it was seen that the biggest change was in the χ_{13} changed from -60.000 to -1.950 (cf. Table 2). The other changes were from 180.000 to 200.667 for χ_{21} and from -120.000 to -101.809 for φ_2.

Table 1 For the Tyr-Lys-Thr tripeptide, the conformation numbers examined for all conformation regions and the conformation region with the minimum energy (global energy)

Conformational Regions	Conformation numbers	Global energy (kcal/mol)
BBB	*13122*	***6.37***
BBR	*13122*	*6.99*
BRB	*13122*	*8.38*
BRL	*486*	*12.04*
BRR	*13122*	*9.21*
RRB	*13122*	*8.90*
RRR	*13122*	*9.53*
RBB	*13122*	*7.25*
RBR	*13122*	*8.08*
	Total: 105462	

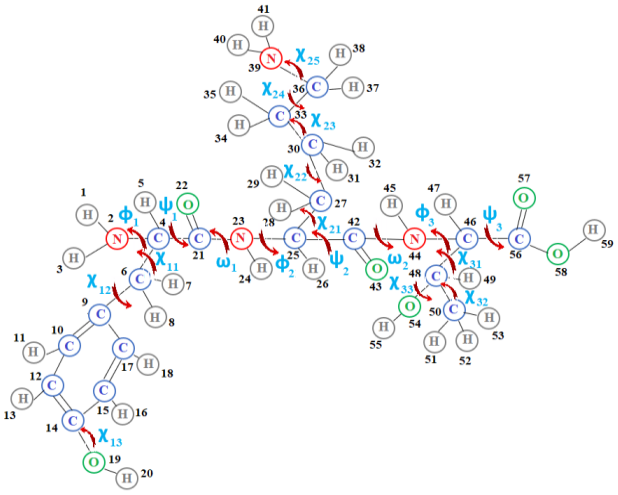

Figure 1 The structure of YKT

Table 2 For the Tyr-Lys-Thr tripeptide, the conformation numbers examined for all conformation regions and the conformation region with the minimum energy (global energy)

Angles (Y)	PHI_1	CH_{11}	CH_{12}	CH_{13}	PSI_1	W_2
In	-115.0	180.00	-90.00	-60.0	160.00	180.00
Out	-117.045	179.449	-98.51	-1.95	149.699	181.981

Ang. (K)	PHI_2	CH_{21}	CH_{22}	CH_{23}	CH_{24}	CH_{25}	PSI_2	W_3
In	-120.0	180.0	-60.0	180.0	180.0	180.0	100.0	180.0
Out	-101.809	200.667	-61.846	188.926	183.543	177.249	107.552	181.429

Ang. (T)	PHI_3	CH_{21}	CH_{22}	CH_{23}	PSI_2
In	-100.00	60.000	180.000	180.000	150.00
Out	-83.190	57.482	182.432	177.413	136.429

3.2. Optimization

Tyrosyl-Lysyl-Threonine (Tyr-Lys-Thr) tripeptide consists of 59 atoms and contains three different amino acids that are polar (tyr,thr) and positively charged (lys). The determined stable conformation with 6.37 kcal/mol energy obtained by Theoretical Conformation Analysis was introduced to the Gaussian09 program, and the optimization study was achieved using the DFT-B3LYP theory level and 6-311++G(d,p) basis set. The non-optimized (Figure 2a) and optimized (Figure 2b) geometries of YKT tripeptide were shown in Figure 2 with the names and numbers of the atoms and the energy values of the optimized geometry of YKT were given in Table 3. The parameters belonging to the bonds, angles, and dihedrals of the YKT tripeptide were obtained by Gaussian09 package program and given in Tables 4, 5, and 6. The bond lengths in the molecule structure take values from 0.96 Å to 1.56 Å. It was found that two of the peptide bonds in the tripeptide had a value of about 1.36 Å.

Table 3 The energy values of optimized geometry of YKT tripeptide

DFT/B3LYP		
Monomer	**Energy (a.u.)**	**Energy (kcal/mol)**
6-311++ G (d,p)	-1412.91298118	-886616.471001598

Table 4 Optimized bond lengths (Å) values of the Tyr-Lys-Thr tripeptide

Bond	**6-311++G(d,p)**
H1-N2	1.0134
N2-H3	1.016
N2-C4	1.4579
C4-H5	1.096
C4-C6	1.5642
C4-C21	1.5373
C6-H7	1.0953
C6-H8	1.0944
C6-C9	1.5121
C9-C10	1.3973
C9-C17	1.4026
C10-H11	1.0838
C10-C12	1.3928
C12-H13	1.0856
C12-C14	1.394
C14-C15	1.396
C14-O19	1.3697
C15-H16	1.0834
C15-C17	1.3902
C17-H18	1.086
O19-H20	0.963
C21-O22	1.2282
C21-N23	1.3555
N23-H24	1.0097
N23-C25	1.4659
C25-H26	1.0932
C25-C27	1.5377
C25-C42	1.5472
C27-H28	1.0951
C27-H29	1.0951
C27-C30	1.5376
C30-H31	1.098
C30-H32	1.0966
C30-C33	1.533
C33-H34	1.0973
C33-H35	1.0932
C33-C36	1.5364
C36-H37	1.0961
C36-H38	1.0962
C36-N39	1.4661
N39-H40	1.0156
N39-H41	1.0165
C42-O43	1.2236

C42-N44	1.3584
N44-H45	1.0105
N44-C46	1.4426
C46-H47	1.0934
C46-C48	1.5421
C46-C56	1.5337
C48-H49	1.0953
C48-C50	1.5247
C48-O54	1.4341
C50-H51	1.0948
C50-H52	1.0938
C50-H53	1.0918
O54-H55	0.9623
C56-O57	1.202
C56-O58	1.3543
O58-H59	0.9691

Table 5 Optimized angle values (degrees) of the Tyr-Lys-Thr tripeptide

Angle	**6-311++G(d,p)**
H1-N2-H3	109.0402
H1-N2-C4	111.5289
H3-N2-C4	109.6419
N2-C4-H5	108.7168
N2-C4-C6	114.1771
N2-C4-C21	106.7859
H5-C4-C6	107.497
H5-C4-C21	108.6947
C6-C4-C21	110.8524
C4-C6-H7	106.2763
C4-C6-H8	108.6473
C4-C6-C9	114.9046
H7-C6-H8	106.6946
H7-C6-C9	108.9465
H8-C6-C9	110.963
C6-C9-C10	121.8126
C6-C9-C17	120.5854
C10-C9-C17	117.5767
C9-C10-H11	119.9932
C9-C10-C12	121.5093
H11-C10-C12	118.4907
C10-C12-H13	119.7226
C10-C12-C14	119.8385
H13-C12-C14	120.4301
C12-C14-C15	119.7762
C12-C14-O19	122.7269
C15-C14-O19	117.4969
C14-C15-H16	119.1497
C14-C15-C17	119.6097
H16-C15-C17	121.2404
C9-C17-C15	121.688
C9-C17-H18	119.5106
C15-C17-H18	118.799
C14-O19-H20	109.6253
C4-C21-O22	121.1574
C4-C21-N23	116.4264
O22-C21-N23	122.4161
C21-N23-H24	118.9176
C21-N23-C25	122.6811
H24-N23-C25	118.0877
N23-C25-H26	106.467
N23-C25-C27	109.2816
N23-C25-C42	109.4584
H26-C25-C27	109.7535
H26-C25-C42	109.3118
C27-C25-C42	112.3924
C25-C27-H28	106.7791
C25-C27-H29	108.5171
C25-C27-C30	115.3374
H28-C27-H29	107.4238
H28-C27-C30	108.1394
H29-C27-C30	110.3151
C27-C30-H31	108.879
C27-C30-H32	107.4403
C27-C30-C33	115.969
H31-C30-H32	105.7544
H31-C30-C33	109.4353
H32-C30-C33	108.8686
C30-C33-H34	109.536
C30-C33-H35	110.6931
C30-C33-C36	112.9308
H34-C33-H35	106.462
H34-C33-C36	109.3515
H35-C33-C36	107.6457
C33-C36-H37	109.2229
C33-C36-H38	110.01
C33-C36-N39	115.5531
H37-C36-H38	106.1393
H37-C36-N39	107.5508
H38-C36-N39	107.9313
C36-N39-H40	110.4995
C36-N39-H41	109.9592
H40-N39-H41	106.7414
C25-C42-O43	121.7987
C25-C42-N44	114.8015
O43-C42-N44	123.3873
C42-N44-H45	119.5286
C42-N44-C46	122.8268
H45-N44-C46	117.3628
N44-C46-H47	107.8202
N44-C46-C48	111.2584
N44-C46-C56	111.3009
H47-C46-C48	108.8582
H47-C46-C56	106.4297
C48-C46-C56	110.974
C46-C48-H49	107.3631
C46-C48-C50	112.9346
C46-C48-O54	104.9393
H49-C48-C50	109.8307
H49-C48-O54	109.5859
C50-C48-O54	111.9751
C48-C50-H51	109.8952
C48-C50-H52	110.5358
C48-C50-H53	111.162
H51-C50-H52	107.3302

H51-C50-H53	108.5576
H52-C50-H53	109.2601
C48-O54-H55	109.363
C46-C56-O57	126.2832
C46-C56-O58	110.6868
O57-C56-O58	123.0141
C56-O58-H59	107.3715

Table 6 Optimized dihedral values (degrees) of the Tyr-Lys-Thr tripeptide

Dihedral	**6-311++G(d,p)**
H1-N2-C4-H5	-83.5707
H1-N2-C4-C6	36.4338
H1-N2-C4-C21	159.3202
H3-N2-C4-H5	155.5545
H3-N2-C4-C6	-84.4409
H3-N2-C4-C21	38.4455
N2-C4-C6-H7	-43.5887
N2-C4-C6-H8	70.8911
N2-C4-C6-C9	-164.151
H5-C4-C6-H7	77.0972
H5-C4-C6-H8	-168.423
H5-C4-C6-C9	-43.4652
C21-C4-C6-H7	-164.2365
C21-C4-C6-H8	-49.7566
C21-C4-C6-C9	75.2012
N2-C4-C21-O22	-34.3865
N2-C4-C21-N23	145.6829
H5-C4-C21-O22	-151.5101
H5-C4-C21-N23	28.5593
C6-C4-C21-O22	90.5503
C6-C4-C21-N23	-89.3803
C4-C6-C9-C10	-94.5552
C4-C6-C9-C17	83.5711
H7-C6-C9-C10	146.3614
H7-C6-C9-C17	-35.5124
H8-C6-C9-C10	29.1822
H8-C6-C9-C17	-152.6915
C6-C9-C10-H11	-1.274
C6-C9-C10-C12	177.7612
C17-C9-C10-H11	-179.4542
C17-C9-C10-C12	-0.419
C6-C9-C17-C15	-178.0405
C6-C9-C17-H18	2.5285
C10-C9-C17-C15	0.1632
C10-C9-C17-H18	-179.2679
C9-C10-C12-H13	-178.6091
C9-C10-C12-C14	0.3171
H11-C10-C12-H13	0.4401
H11-C10-C12-C14	179.3663
C10-C12-C14-C15	0.0522
C10-C12-C14-O19	-179.9301
H13-C12-C14-C15	178.9707
H13-C12-C14-O19	-1.0116
C12-C14-C15-H16	179.5174
C12-C14-C15-C17	-0.3013
O19-C14-C15-H16	-0.4994
O19-C14-C15-C17	179.6819
C12-C14-O19-H20	1.2508
C15-C14-O19-H20	-178.7318
C14-C15-C17-C9	0.1927
C14-C15-C17-H18	179.6277
H16-C15-C17-C9	-179.6222
H16-C15-C17-H18	-0.1872
C4-C21-N23-H24	7.678
C4-C21-N23-C25	-178.88
O22-C21-N23-H24	-172.2517
O22-C21-N23-C25	1.1903
C21-N23-C25-H26	39.6895
C21-N23-C25-C27	158.1649
C21-N23-C25-C42	-78.3561
H24-N23-C25-H26	-146.8169
H24-N23-C25-C27	-28.3415
H24-N23-C25-C42	95.1375
N23-C25-C27-H28	-39.5693
N23-C25-C27-H29	75.95
N23-C25-C27-C30	-159.7383
H26-C25-C27-H28	76.8356
H26-C25-C27-H29	-167.6451
H26-C25-C27-C30	-43.3334
C42-C25-C27-H28	-161.2939
C42-C25-C27-H29	-45.7746
C42-C25-C27-C30	78.5371
N23-C25-C42-O43	-74.6105
N23-C25-C42-N44	104.145
H26-C25-C42-O43	169.1347
H26-C25-C42-N44	-12.1098
C27-C25-C42-O43	47.0134
C27-C25-C42-N44	-134.2311
C25-C27-C30-H31	54.8175
C25-C27-C30-H32	168.9098
C25-C27-C30-C33	-69.0804
H28-C27-C30-H31	-64.6043
H28-C27-C30-H32	49.4881
H28-C27-C30-C33	171.4978
H29-C27-C30-H31	178.1839
H29-C27-C30-H32	-67.7238
H29-C27-C30-C33	54.286
C27-C30-C33-H34	-56.4681
C27-C30-C33-H35	60.6261
C27-C30-C33-C36	-178.6009
H31-C30-C33-H34	179.9232
H31-C30-C33-H35	-62.9826
H31-C30-C33-C36	57.7904
H32-C30-C33-H34	64.7812
H32-C30-C33-H35	-178.1245
H32-C30-C33-C36	-57.3515
C30-C33-C36-H37	-55.8643
C30-C33-C36-H38	60.2574
C30-C33-C36-N39	-177.243
H34-C33-C36-H37	-178.1006
H34-C33-C36-H38	-61.9788
H34-C33-C36-N39	60.5208
H35-C33-C36-H37	66.6287
H35-C33-C36-H38	-177.2495

H35-C33-C36-N39	-54.7499
C33-C36-N39-H40	-62.4679
C33-C36-N39-H41	55.1101
H37-C36-N39-H40	175.258
H37-C36-N39-H41	-67.1641
H38-C36-N39-H40	61.1301
H38-C36-N39-H41	178.708
C25-C42-N44-H45	-4.5522
C25-C42-N44-C46	-178.2907
O43-C42-N44-H45	174.181
O43-C42-N44-C46	0.4426
C42-N44-C46-H47	16.5177
C42-N44-C46-C48	135.8167
C42-N44-C46-C56	-99.8552
H45-N44-C46-H47	-157.3482
H45-N44-C46-C48	-38.0492
H45-N44-C46-C56	86.2789
N44-C46-C48-H49	177.2415
N44-C46-C48-C50	-61.5436
N44-C46-C48-O54	60.6942
H47-C46-C48-H49	-64.0806
H47-C46-C48-C50	57.1343
H47-C46-C48-O54	179.3721
C56-C46-C48-H49	52.729
C56-C46-C48-C50	173.9439
C56-C46-C48-O54	-63.8184
N44-C46-C56-O57	-2.2479
N44-C46-C56-O58	176.325
H47-C46-C56-O57	-119.4691
H47-C46-C56-O58	59.1038
C48-C46-C56-O57	122.2406
C48-C46-C56-O58	-59.1866
C46-C48-C50-H51	-179.511
C46-C48-C50-H52	-61.2267
C46-C48-C50-H53	60.2885
H49-C48-C50-H51	-59.7052
H49-C48-C50-H52	58.5791
H49-C48-C50-H53	-179.9057
O54-C48-C50-H51	62.2861
O54-C48-C50-H52	-179.4296
O54-C48-C50-H53	-57.9144
C46-C48-O54-H55	-170.2305
H49-C48-O54-H55	74.76
C50-C48-O54-H55	-47.3714
C46-C56-O58-H59	179.977
O57-C56-O58-H59	-1.395

Additionally, intramolecular hydrogen bonds of YKT were determined as a result of MM, and QM calculations, shown in Figure 2 and Table 7.

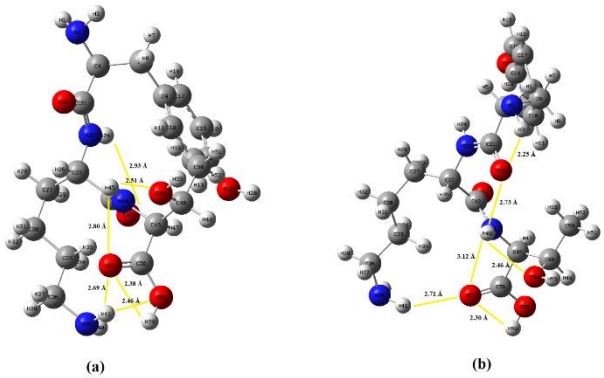

Figure 2 The structure of YKT

Table 7 Intramolecular hydrogen bond lengths of YKT

(a) as a result of MM calculations (non-optimized geometry)	
Atoms	**Bond Lengths (Å)**
O43-H24	2.93
O54-H45	2.51
O57-H41	2.69
O57-H45	2.80
O57-H59	2.38
O58-H41	2.46
(b) as a result of QM calculations (optimized geometry)	
Atoms	**Bond Lengths (Å)**
O22-H3	2.25
O22-H45	2.73
O54-H45	2.46
O57-H41	2.71
O57-H45	3.12
O57-H59	2.30

3.3. MD Results

Molecular dynamics simulations were successfully achieved in the vacuum, water, and methanol. Potential energies were converged to -2.1324930 x 10^2 kJ/mol (for vacuum), -5.2986488 x 10^4 kJ/mol (for water) and -1.9647314 x 10^4 kJ/mol (for methanol), shown in Figure 3. MD simulations were achieved in the vacuum, water, and methanol environment, and kinetic, potential, and total energies for 10 ns were shown in Figure 4.

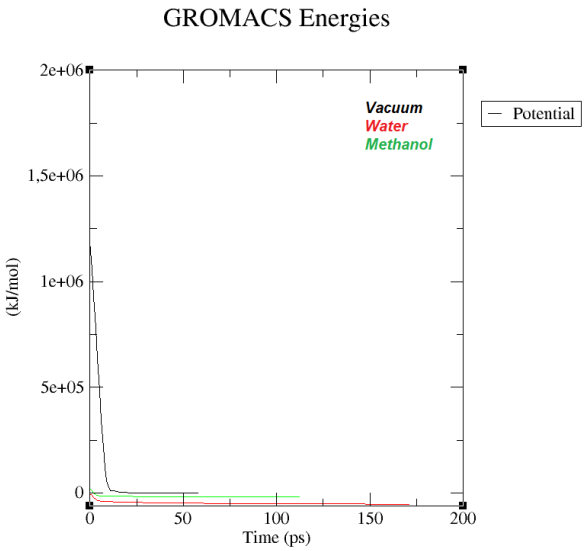

Figure 3 The potential energies of the system as a function of the minimization step using Steepest Descent algorithm

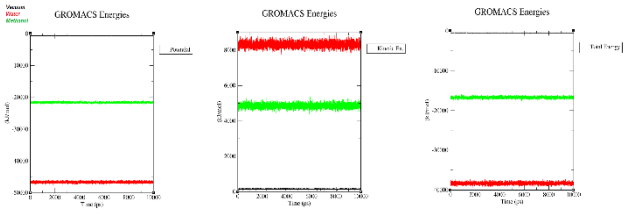

Figure 4 The potential, kinetic and total energies of all systems

For the changes in the molecular structure, using the trajectory files, the conformation of the molecule in each nanosecond was determined in the vacuum, water, and methanol environment, shown in Figure 5.

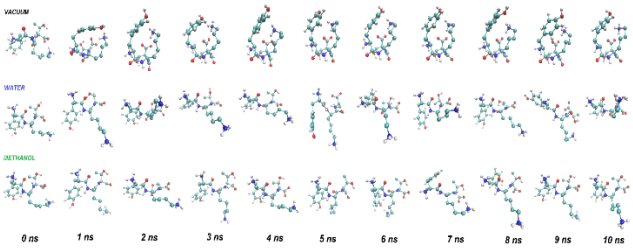

Figure 5 The conformation of the YKT in each nanosecond in the vacuum, water and methanol environment

RMSD, Rg, and hydrogen bond values of all systems were determined as a result of MD studies. RMSD values provide information on how much the system deviates from the initial structure [35]. Values less than 0.2 nm indicate that the structure is not subjected to a major structural change compared to the first structure. Looking at the RMSD values for all systems, the highest RMSD value was obtained in the vacuum environment and its value is 0.15 nm. In the water and methanol environments, these values are 0.12 nm and 0.11 nm, respectively. According to these values, it was observed that the structure tended to retain its first structure for 10 ns in all environments shown in Figure 6a.

Rg of the peptide is a measure of its compactness. When Figure 5 and Figure 6 were interpreted together, Figure 5 showed that the peptide is quite stable with folded structure in the vacuum environment, and it was seen in the RMSD and radius of gyration graphs (Figure 6) that this stable structure remains stable from 2 ns to 10 ns. In the water and methanol environment, extended structures clearly showed the reason for the fluctuation of the radius of gyration graph within the simulation period.

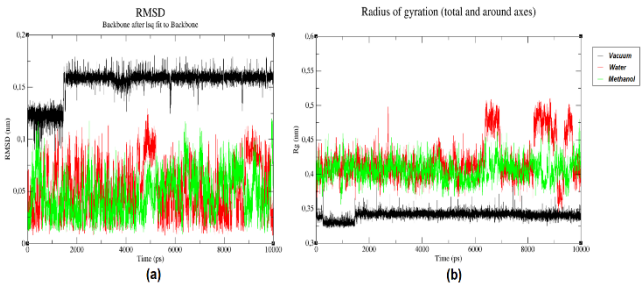

Figure 6 RMSD values (a) and Radius of gyration values (b) of YKT tripeptide in different environments

In the vacuum medium, due to the folded structure of the peptide (cf. Figure 5), atoms with high electronegativity and hydrogens bound to these atoms have more interactions and tended to make intramolecular H-bonds. It is observed in Figure 7 that the tendency to make hydrogen bonds is mostly in the vacuum medium.

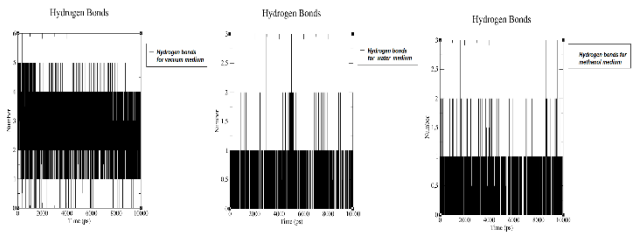

Figure 7 Hydrogen bond values of YKT tripeptide in different environments

As a result of all structural analyzes performed using MM, MD, and QM methods, the energy values of YKT tripeptide were calculated as -6.37 kcal/mol, -117.26 kcal/mol, and -886616.47 kcal/mol, respectively.

3.4. Hyperpolarizability

First-order hyperpolarizability (β_0), polarizability (α), and dipole moment (μ) data of Tyr-Lys-Thr (YKT) tripeptide were obtained with DFT/B3LYP method using 6-311++G(d,p) basis set.

The dipole moment, polarizability, and hyperpolarization values obtained in the studies using the DFT / B3LYP / 6-311 ++ G (d, p) basis set in the Gaussian 09 program are given in the following Table 8.

The dipole moment value obtained is 1.6968023 D and the hyperpolarization value is $2.6114151629 \times 10^{-30}$ esu. Urea values of μ, α, and β in the literature were obtained as 1.373D, 3.8312×10^{-24} esu, and 0.37289×10^{-30} esu using the B3LYP / 6-31G (d) basis set [36-38]. When the values of YKT tripeptide were compared with the literature data, μ, α, and β_0 values of the tripeptide were obtained 1.2358, 10.775, and 7.0031 times that of urine, respectively.

Table 8 First-order hyperpolarizability (β_0), polarizability (α), and dipole moment (μ) table of YKT tripeptide

Parameters			
μ_x	-0.7736091	β_{xxx}	-45.1187173
μ_y	1.1058228	β_{xxy}	3.9859085
μ_z	-1.0285052	β_{xyy}	-107.2066633
μ	**1.6968023**	β_{yyy}	205.1883547
α_{xx}	301.183032	β_{xxz}	-29.7750615
α_{xy}	4.5501607	β_{xyz}	3.3650559
α_{yy}	280.3586188	β_{yyz}	56.0279763
α_{xz}	-13.5298548	β_{xzz}	-15.1125743
α_{yz}	18.6290357	β_{yzz}	40.1568576
α_{zz}	254.1346634	β_{zzz}	7.9961513
$<\alpha_o>$	**278.5587714**	β_o	302.2821117
$<\alpha_{top(esu)}>$	41.28241×10^{-24}	$\beta_{o(esu)}$	$2611.4151629 \times 10^{-33}$
		$\beta_{o(esu)}$	$2.6114151629 \times 10^{-30}$
(α:1 a.u. = 0.1482×10^{-24} esu ; β:1 a.u. = 8.639×10^{-33} esu)			

4. CONCLUSIONS

In this study, the stable conformations of Tyrosyl-Lysyl-Threonine were obtained by the theoretical conformational analysis, firstly. And then, the optimized geometry and energy values of the determined structure as the most stable conformation of YKT tripeptide by theoretical conformational analysis were obtained and bond, angle, and dihedral data of tripeptide were determined and shared. Additionally, the intramolecular H-bonds of the structure obtained from MM and QM calculations were determined. The conformational change of YKT tripeptide in the vacuum, water, and methanol environments was investigated by molecular dynamics methods for 10 ns. Additionally, the energy values obtained using MM, MD, and QM methods are presented comparatively. μ, α, and β_0 values of YKT were calculated by Gaussian09 software program. With this study, a study about the structural properties of YKT tripeptide was brought to the literature.

Acknowledgments

We thank Prof Dr Petra Imhof and her team for their advice on MD studies.

Funding

This study was supported by the Research Funds of Istanbul University. Project Number: FDK-2018-32253 and it was supported by International Research Scholarships for Research Assistants scholarship of The Council of Higher Education.

The Declaration of Conflict of Interest/ Common Interest

No conflict of interest or common interest has been declared by the authors.

Authors' Contribution

The authors contributed equally to the study. B.B: data collection, literature research, writing. S.K.G: writing, editing, literature research.

The Declaration of Ethics Committee Approval

This study does not require ethics committee permission or any special permission.

The Declaration of Research and Publication Ethics

The authors of the paper declare that they comply with the scientific, ethical and quotation rules of SAUJS in all processes of the paper and that they do not make any falsification on the data collected. In addition, they declare that Sakarya University Journal of Science and its editorial board have no responsibility for any ethical violations that may be encountered, and that this study has not been evaluated in any academic publication environment other than Sakarya University Journal of Science.

REFERENCES

[1] D. Agyei, I. Ahmed, Z. Akram, M. N. Iqbal, H. and M. K. Danquah, "Protein and peptide biopharmaceuticals: an overview," Protein and peptide letters, vol. 24, no. 2, pp. 94-101, 2017.

[2] D. Agyei and M. K. Danquah, "Industrial-scale manufacturing of pharmaceutical-grade bioactive peptides," Biotechnology advances, vol. 29, no. 3, pp. 272-277, 2011.

[3] K. Fosgerau and T. Hoffmann, "Peptide therapeutics: current status and future directions," Drug discovery today, vol. 20, no. 1, pp. 122-128, 2015.

[4] R. E. Hancock and H. G. Sahl, "Antimicrobial and host-defense peptides as new anti-infective therapeutic strategies," Nature biotechnology, vol. 24, no. 12, pp. 1551-1557, 2006.

[5] S. S. Usmani, G. Bedi, J. S. Samuel, S. Singh, S. Kalra, P. Kumar, ... & G. P. Raghava, "THPdb: Database of FDA-approved peptide and protein therapeutics," PloS one, vol. 12, no. 7, e0181748, 2017.

[6] H. R. Lieberman, S. Corkin, B. J. Spring, R. J. Wurtman and J. H. Growdon, "The effects of dietary neurotransmitter precursors on human behavior," The American journal of clinical nutrition, vol. 42, no. 2, pp. 366-370, 1985.

[7] D. D. Rasmussen, B. Ishizuka, M. E. Quigley and S. S. C. Yen, "Effects of tyrosine and tryptophan ingestion on plasma catecholamine and 3, 4-dihydroxyphenylacetic acid concentrations," The Journal of Clinical Endocrinology & Metabolism, vol. 57, no. 4, pp. 760-763, 1983.

[8] I. Gülçin, "Comparison of in vitro antioxidant and antiradical activities of L-tyrosine and L-Dopa," Amino acids, vol. 32, no. 3, pp. 431, 2007.

[9] H. M. Chen, K. Muramoto, F. Yamauchi and K. Nokihara, "Antioxidant activity of designed peptides based on the antioxidative peptide isolated from digests of a soybean protein. Journal of agricultural and food chemistry," vol. 44, no. 9, pp. 2619-2623, 1996.

[10] R. W. Tankersley, "Amino acid requirements of herpes simplex virus in human cells," Journal of bacteriology, vol. 87, no. 3, pp. 609-613, 1964.

[11] N. A. El-Sersy, A. E. Abdelwahab, S. S. Abouelkhiir, D. M. Abou-Zeid and S. A. Sabry, "Antibacterial and Anticancer activity of ε-poly-L-lysine (ε-PL) produced by a marine Bacillus subtilis sp.," Journal of basic microbiology, vol. 52, no. 5, pp. 513-522, 2012.

[12] P. Simic, H. Sahm and L. Eggeling, "L-Threonine export: use of peptides to identify a new translocator from Corynebacterium glutamicum," Journal of bacteriology, vol. 183, no. 18, pp. 5317-5324, 2001.

[13] P. Li, Y. L. Yin, D. Li, S. W. Kim and G. Wu, "Amino acids and immune function," British Journal of Nutrition, vol. 98, no. 2, pp. 237-252, 2007.

[14] R. F. Bertolo, C. Z. Chen, G. Law, P. B. Pencharz and R. O. Ball, "Threonine requirement of neonatal piglets receiving total parenteral nutrition is considerably lower than that of piglets receiving an identical diet intragastrically," The Journal of nutrition, vol. 128, no. 10, pp. 1752-1759, 1998.

[15] W. W. Wang, S. Y. Qiao and D. F. Li, "Amino acids and gut function," Amino acids, vol. 37, no. 1, pp. 105-110, 2009.

[16] K. A. Bala, M. Dogan, T. Mutluer, S. Kaba, O. Aslan, R. Balahoroglu, ... & S. Kocaman, "Plasma amino acid profile in autism spectrum disorder (ASD)," Eur Rev Med Pharmacol Sci, vol. 20, no. 5, pp. 923-929, 2016.

[17] P. Chen, N. Bodor, W. M. Wu, and L. Prokai, "Strategies to target kyotorphin analogues to the brain," Journal of medicinal chemistry, vol. 41, no. 20, pp. 3773-3781, 1998.

[18] B. N. P. Sah, T. Vasiljevic, S. Mckechnie and O. N. Donkor, "Identification of anticancer peptides from bovine milk proteins and their potential roles in management of cancer: a critical review," Comprehensive Reviews in Food Science and Food Safety, vol. 14, no. 2, pp. 123-138, 2015.

[19] H. Otani, and H. Suzuki, "Isolation and characterization of cytotoxic small peptides, α-casecidins, from bovine αs1-casein digested with bovine trypsin," Animal Science Journal, vol. 74, no. 5, pp. 427-435, 2003.

[20] B. Bicak, S. Kecel Gunduz, Y. Budama Kilinc, P. Imhof, B. Gok, G. Akman, and A. E. Ozel, "Structural, spectroscopic, in silico, in vitro and DNA binding evaluations of tyrosyl-lysyl-threonine," Journal of Biomolecular Structure and Dynamics, 1-17, 2021.

[21] B. Bicak, Y. Budama Kilinc, S. Kecel Gunduz, T. Zorlud, and G. Akman, "Peptide based nano-drug candidate for cancer treatment: Preparation, characterization, in vitro and in silico evaluation," Journal of Molecular Structure, 1240, 130573, 2021.

[22] B. Bicak, S. Kecel Gunduz, Y. Budama Kilinc, and B. Ozdemir, "Molecular docking studies of YKT tripeptide and drug delivery system with poly (ε-caprolactone) nanoparticles," Archiv der Pharmazie, e2100437, 2022.

[23] I. S. Maksumov, L. I. Ismailova and N. M. Godzhaev, "A program for the semiempirical calculation of the conformations of molecular complexes on a computer," Journal of structural chemistry, vol. 24, no. 4, pp. 647-648, 1984.

[24] C. M. Venkatachalam and G. N. Ramachandran, "Conformation of polypeptide chains," Annual review of biochemistry, vol. 38, no. 1, pp. 45-82, 1969.

[25] G. T. Ramachandran and V. Sasisekharan, "Conformation of polypeptides and proteins," Advances in protein chemistry, vol. 23, pp. 283-437, 1968.

[26] G. Friesecke and F. Theil, "Molecular geometry optimization, models," Encyclopedia of Applied and Computational Mathematics, pp. 951-957, 2015.

[27] A. Janaki, V. Balachandran and A. Lakshmi, "First order molecular hyperpolarizabilities and intramolecular charge transfer from vibrational spectra of NLO material: 2, 6-dichloro-4-nitroaniline," vol. 51, no. 09, pp. 601-614, 2013.

[28] M. J. Frisch, G. W. Trucks, H. B. Schlegel, G. E. Scuseria, M. A. Robb, J. R. Cheeseman, ... & D. J. Fox, Gaussian 09; Gaussian, Inc. Wallingford, CT, vol. 32, pp. 5648-5652, 2009.

[29] W. F. van Gunsteren, S. R. Billeter, A. A. Eising, P. H. Hünenberger, P. K. H. C. Krüger, A. E. Mark, ... & I. G. Tironi, "Biomolecular simulation: the GROMOS96 manual and user guide," Vdf Hochschulverlag AG an der ETH Zürich, Zürich, vol. 86, pp. 1-1044, 1996.

[30] D. Van Der Spoel, E. Lindahl, B. Hess, G. Groenhof, A. E. Mark and H. J. Berendsen, "GROMACS: fast, flexible, and free," Journal of computational chemistry, vol. 26, no. 16, pp. 1701-1718, 2005.

[31] G. Bussi, D. Donadio and M. Parrinello, "Canonical sampling through velocity rescaling," The Journal of chemical physics, vol. 126, no. 1, pp. 014101, 2007.

[32] M. Parrinello and A. Rahman, "Polymorphic transitions in single crystals: A new molecular dynamics method," Journal of Applied physics, 52(12), 7182-7190, 1981.

[33] P. J. Turner, "XMGRACE, Version 5.1. 19." Center for Coastal and Land-Margin Research, Oregon Graduate Institute of Science and Technology, Beaverton, OR. 2005.

[34] W. Humphrey, A. Dalke and K. Schulten, "VMD: visual molecular Dynamics," Journal of molecular graphics, vol. 14, no. 1, pp. 33-38, 1996.

[35] D. van der Spoel, "Structure and dynamics of peptides: theoretical aspects of protein folding," Doctoral Thesis, 1996.

[36] Y. X. Sun, , Q. L. Hao, , W. X. Wei, , Z. X. Yu, , L. D. Lu, X. Wang and Y. S. Wang, "Experimental and density functional studies on 4-(3, 4-dihydroxybenzylideneamino) antipyrine, and 4-(2, 3, 4-trihydroxybenzylideneamino) antipyrine," Journal of Molecular Structure: THEOCHEM, vol. 904, no. 1-3, pp. 74-82, 2009.

[37] E. V. Shah and D. R. Roy, "A comparative DFT study on electronic, thermodynamic and optical properties of telluride compounds," Computational materials science, vol. 88, pp. 156-162, 2014.

[38] S. Kecel-Gunduz, B. Bicak, S. Celik, S. Akyuz and A. E. Ozel, "Structural and spectroscopic investigation on antioxidant dipeptide, l-Methionyl-l-Serine: A combined experimental and DFT study," Journal of Molecular Structure, vol. 1137, pp. 756-770, 2017.

SAKARYA ÜNİVERSİTESİ
FEN BİLİMLERİ ENSTİTÜSÜ DERGİSİ

Sakarya University Journal of Science
SAUJS

ISSN 1301-4048 | e-ISSN 2147-835X | Period Bimonthly | Founded: 1997 | Publisher Sakarya University | http://www.saujs.sakarya.edu.tr/

Title: Synthesis and Characterization of Thiazole Compounds in the Presence of Various Reagents, Catalysts and Solvents

Authors: Nurcan BERBER

Recieved: 2021-06-11 00:00:00

Accepted: 2022-06-15 00:00:00

Article Type: Research Article

Volume: 26
Issue: 4
Month: August
Year: 2022
Pages: 757-767

How to cite
Nurcan BERBER; (2022), Synthesis and Characterization of Thiazole Compounds in the Presence of Various Reagents, Catalysts and Solvents. Sakarya University Journal of Science, 26(4), 757-767, DOI: 10.16984/saufenbilder.950016
Access link
http://www.saujs.sakarya.edu.tr/en/pub/issue/72361/950016

Sakarya University Journal of Science 26(4), 757-767, 2022

Synthesis and Characterization of Thiazole Compounds in the Presence of Various Reagents, Catalysts and Solvents

Nurcan BERBER *[1]

Abstract

The reaction medium plays a key role in organic synthesis and pharmaceutical research. There are many opinions on choosing the best condition, including cost and environmental implications, but the main requirement is that they have the necessary interaction with solvents to cause dissolution, precipitation, stabilization, or instability. For this purpose, in this article synthesis of the thiazole ring was made under various reaction conditions. So new compounds 2-(isoquinolin-5-ylimino)-3-phenylthiazolidin-4-one (1), (4-amino-3-phenylthiazol-2(3H)-ylidene) isoquinolin-5-amine (2), (4-amino-3-phenylthiazol-2(3H)-ylidene) isoquinolin-5-amine (3) were synthesized from the reaction between thiourea derivative and monochloroacetic acid, diethyloxalate and chloro acetonitrile. For this synthesizes were created in various reaction conditions, using different bases (sodium acetate/sodyum etoksit/ triethylamine or pyridine) and solvents (1,4-dioxane, toluene, acetic acid, ethanol, tetrahydrofuran, dimethyl formamide). At the end of these reactions, the best efficiency was obtained with the one-pot reaction using THF/DMF, Et_3N. The structures of all novel compounds reported herein were established using FT-IR, ^1H NMR, and ^{13}C NMR spectra as well as elemental analysis technique.

Keywords: 5-aminoisoquinoline, thioureas, one-pot reaction, thiazole rings

1. INTRODUCTION

Hetero-cyclic compounds or ring structures have an important role in organic chemistry due to their wide range of pharmacological properties [1-3]. Heterocyclic compounds are widely distributed in nature. Many of them show drug active properties have increased the importance of such compounds and led organic synthesizers to make various reactions.

Six-membered hetero-cyclic compounds, pyridine and benzo derivatives, especially quinoline and isoquinoline derivatives are widely used in many chemical syntheses due to their biological activities [4-6]. They play are key structural components due to their various

* Corresponding author: nberber@comu.edu.tr
[1] Çanakkale Onsekiz Mart University
ORCID: https://orcid.org/0000-0002-1595-585X

biological activities such as antimalarial [7], antibacterial [8], antifungal [9], antidepressant [10, 11], anticonvulsant [12, 13], anti-inflammatory [14], antidiabetic [15], antiviral [16], antihistamine [17], anticarcinogen and antioxidant [18]. For example, quinine was isolated from the bark of Cinchona trees and has been used for the treatment of malaria [19]. Its structure determination and SAR studies resulted in the discovery of newer antimalarial drugs like chloroquine, primaquine, mefloquine [20]. Besides, nitrogen and sulfur-containing aromatic heterocyclic compounds such as thiazole are widely used in many types of treatments due to their interesting physicochemical properties and pronounced biological activities [21-26]. Some important heterocyclic compound derivatives are given (Figure 1). Also, thioureas and substituted thioureas play important roles in the formation of these heterocyclic systems [27-29].

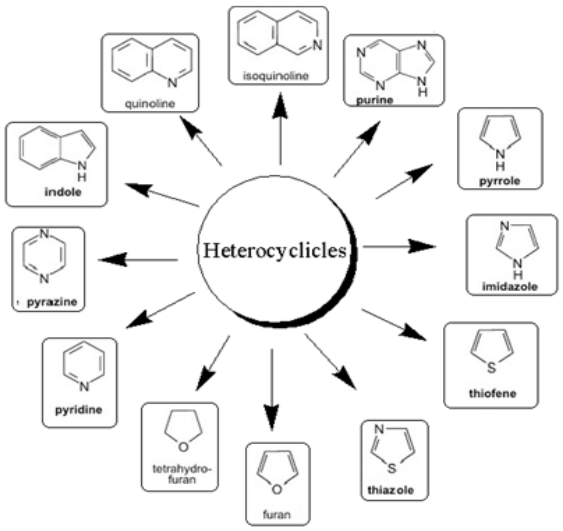

Figure 1 Some important heterocyclic compounds derivatives

The conventional synthesis in previous work several methods have been reported for the preparation of thiazole rings for example ethanol/ sodium ethoxide [30], ethanol/ anhydrous sodium acetate [31, 32], acetic acid/ anhydrous sodium acetate [33], dioxane/ anhydrous sodium acetate [34], solvent/scavenger-free conditions [35]. This article describes of synthesis of new heteroaryl isoquinoline derivatives [2-(isoquinolin-5-ylimino)-3-phenylthiazolidin-4-one (1), (4-amino-3-phenylthiazol-2(3H)-ylidene) isoquinolin-5-amine (2), (4-amino-3-phenylthiazol-2(3H)-ylidene) isoquinolin-5-amine (3)] under various conditions. For this purpose, the thiazole ring was formed from adding monochloroacetic acid, chloroacetonitrile, diethyl oxalate in the using three different bases (EtONa, AcONa, Pyridine) and solvents (1,4-dioksan, Toluene, AcOH).

2. EXPERIMENTAL

All starting materials and reagents were purchased from commercial suppliers. Reactions were monitored by TLC; the plates were visualized with short wave UV fluorescence (k = 254 nm). Melting points were taken on a Yanagimoto micromelting point apparatus. FT-IR spectra (ν, cm^{-1}) were measured on a SHIMADZU Prestige21 (200 VCE) spectrometer. ^{1}H NMR and ^{13}C NMR spectra were taken on JEOL NMR-400 MHz instrument in DMSO-d6 using TMS as the internal standard. All chemicals were purchased from Merck (Darmstadt, Germany) and Sigma-Aldrich (Taufkirchen, Germany). The ele-mental analysis was carried out with a Leco CHNS-932 (St. Joseph,Michigan)instrument.

2.1. General synthesis of the new heteroaryl isoquinoline derivatives (1-3)

Synthesis from thiourea: A solution of the appropriate 1-(isoquinolin-5-yl)-3-phenylthiourea (1mmol) in 1,4-dioxane/ toluene/ acetic acid/ ethanol/ tetrahydrofuran or dimethylformamide (10mL) was refluxed with the appropriate monochloroacetic acid (1mmol)/chloro acetonitrile(1mmol), or diethyl oxalate(1mmol) in the presence of base EtONa/AcONa/ Pyridine or Et_3N (2mmol) for 24 h. The reaction mixture was then cooled poured into ice and the oily residue was recrystallized into ethanol/10% HCl mixture (Scheme 1).

One-pot synthesis from amine: To a solution of 5-aminoisoquinoline (1mmol) in THF/DMF (5/0,5mL) was added Phenyl isothiocyanate (1mmol), monochloroacetic acid (1mmol)/chloro acetonitrile (1mmol), or diethyl oxalate (1mmol) and triethylamine (3drop). The reaction mixture

was heated at 80 ˚C for 24 h. The reaction mixture was cooled and poured into ice. And then the oily residue was transferred to another vessel and precipitated in EtOH / 10% HCl mixture.

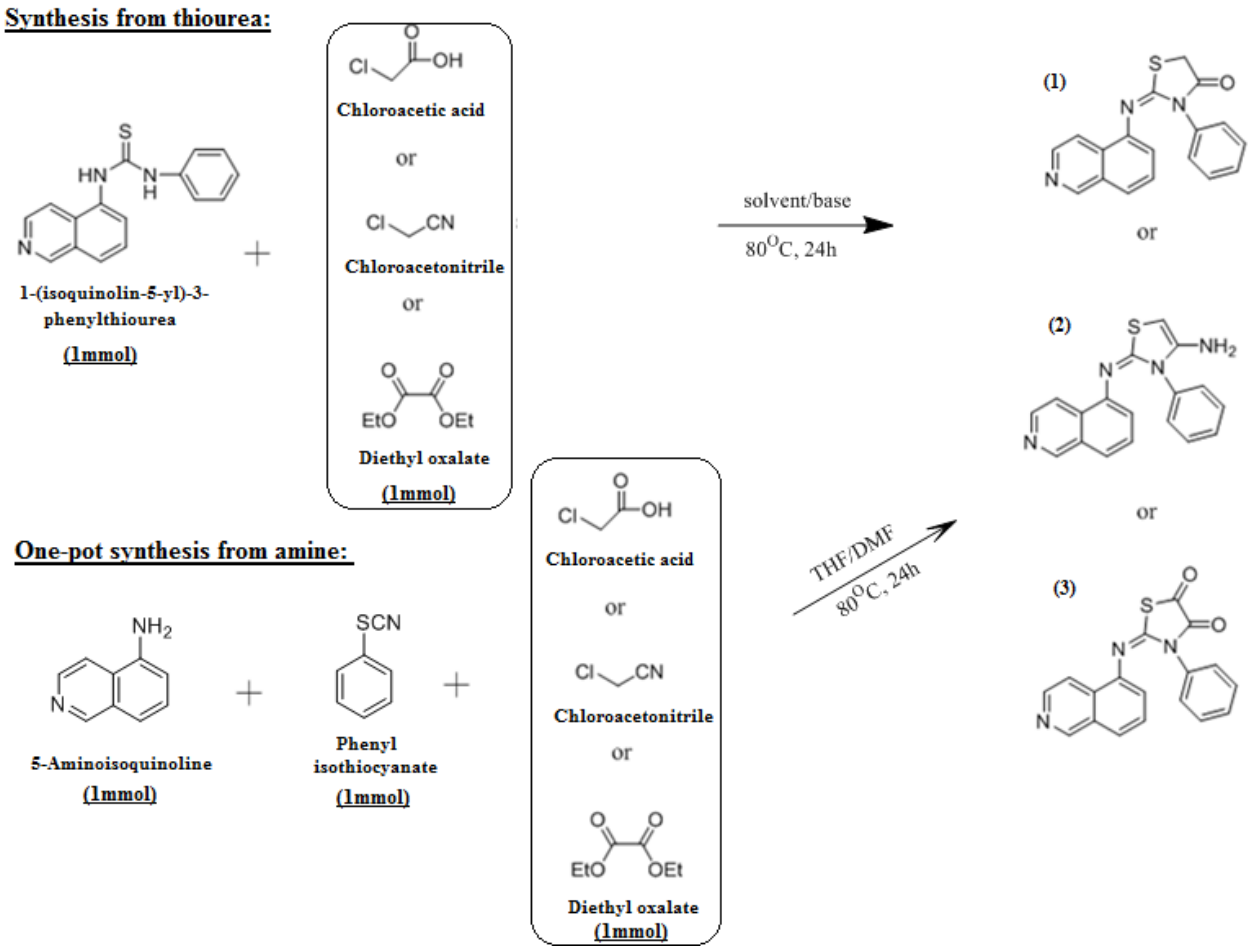

Scheme 1 General reaction condituons of thiazole ring

2-(isoquinolin-5-ylimino)-3-phenylthiazolidin-4-one (1): Yellow solid, **y**ield based on one-pot synthesis from amine reaction; %65, mp. 205-208°C. IR (KBr, cm^{-1}) ν = 3070-3040 (Ar CH), 1670 (CO); ^{1}H NMR (DMSO-d6) δ = 9.68-7.40 (11H, m, Ar H), 4.25 (2H, s, CH_2); ^{13}C NMR (DMSO-d6) δ = 170.24 (CO), 156.60 (-N=C-), 150.60-126.06 (Ar C), 34.20 (CH_2); Anal. Calcd. For. $C_{18}H_{13}N_3OS$ (319.38): C, 67.69; H, 4.10; N, 13.16; found. C, 67.83; H, 4.37; N, 13.31.

(4-amino-3-phenylthiazol-2(3H)-ylidene) isoquinolin-5-amine (2): Brown solid, yield based on one-pot synthesis from amine reaction %77, mp. 189-191°C. IR (KBr, cm^{-1}) ν = 3271 (NH_2), 3075-3012 (Ar CH); ^{1}H NMR (DMSO-d6) δ = 9.70-7.76 (11H, m, Ar H), 6.95 (1H, s, CH), 5.69, (2H, s, NH_2); ^{13}C NMR(DMSO-d6) δ = 169.62 (-N=C-), 150.60-126.06 (Ar C), 60.05 (-CH=); Anal. Calcd. For. $C_{18}H_{14}N_4S$ (318.40): C, 67.90; H, 4.43; N, 17.60; found. C, 68.05; H, 4.87; N, 17.81.

(4-amino-3-phenylthiazol-2(3H)-ylidene) isoquinolin-5-amine (3): Dark Brown solid, Yield based on one-pot synthesis from amine reaction; %83, mp. 181-183°C. IR (KBr, cm^{-1}) ν = 3113-3081 (Ar CH), 1683,1675 (CO); ^{1}H NMR (DMSO-d6) δ = 9.80-7.45 (11H, m, Ar H); ^{13}C NMR(DMSO-d6) δ = 183.40, 170.11 (CO), 160.30 (-N=C-), 150.60-126.06 (Ar-C); Anal. Calcd. For. $C_{18}H_{11}N_3O_2S$ (333.37): C, 64.85; H, 3.33; N, 12.61; found. C, 65.05; H, 3.51; N, 12.83.

3. RESULTS AND DISCUSSION

This study was designed to synthesize and characterize the new heteroaryl isoquinoline derivatives (1-3) from both 1-(isoquinolin-5-yl)-3-phenylthiourea and 5-aminoisoquinoline (in one-pot). Firstly, the designed compound was synthesized by condensation of 1-(isoquinolin-5-yl)-3-phenylthiourea with monochloroacetic acid/chloro acetonitrile, or diethyl oxalate using polar/apolar solvents (1,4-dioxane/ toluene/ acetic acid/ ethanol/ tetrahydrofuran or dimethylformamide) and bases (EtONa/ AcONa/ Pyridine or Et_3N) for 24 h. In apolar solvents, toluene and 1,4-dioxane, product (a) was obtained in higher yields, whereas it was obtained in lower yields in polar solvents such as tetrahydrofuran, acetic acid. Also, the synthesis of heteroaryl isoquinoline derivatives (1-3) used different bases such as sodium ethoxide, triethylamine, pyridine, or sodium acetate. The best yield was obtained with sodium acetate in the apolar solvent. When the reaction was carried out at 80 ° C under base-free conditions, no reaction took place. The results obtained were given in Table 1.

Table 1 Effect of base on synthesis (E)-2-(isoquinolin-5-ylimino)-3-phenylthiazolidin-4-one (a)

	Base	**Solvent**	**Base**	**Chloro acetic Acid**	**Yield (%)**
1	Pyridine	1,4-Dioksane	2	1	40
2	NaOAc	1,4-Dioksane	2	1	55
3	NaOEt	1,4-Dioksane	2	1	45
4	Pyridine	Toluene	2	1	36
5	NaOAc	Toluene	2	1	40
6	NaOEt	Toluene	2	1	25
7	NaOAc	AcOH	2	1	35
8	-	1,4-Dioksane	-	1	-

Secondly, the one-pot reaction has been achieved by condensation of 5-aminoisoquinoline, phenyl isothiocyanate with monochloroacetic acid/chloro acetonitrile or diethyl oxalate using THF/DMF(5/0,5mL) and Et_3N (3 drops) for 24 h. Compounds (1-3) were achieved with the one-pot reaction at a higher yield of 70-75%. The oily residue obtained at the end of the reaction was recrystallized with Ethanol/10% HCl mixture. It is known that such one-pot reactions are used in many thiazole derivatives synthesis because of mild reaction conditions, shorter reaction times, high efficiencies, and facile isolation of the desired product. [35-37]. A plausible mechanism for these syntheses is shown in Scheme 2. Also, it is varies depending on the pKa of the amine attached to the thiourea moiety with acylation taking place toward the amine having a lower pKa [38-41]. The measured pKa of 5-aminoisoquinoline and aniline respectively are 5.48 and 4.58. For unsymmetrical 1-(isoquinolin-5-yl)-3-phenylthiourea, aniline nitrogen is more basic compared with isoquinoline nitrogen of the carbodiimide intermediate. Thus, the former is acylated from aniline nitrogen (in Scheme 2). Also, asymmetric attack of acetic acid to carbodiimide will lead to protonation towards the amine with higher pKa without affecting the imine group on the other side [38].

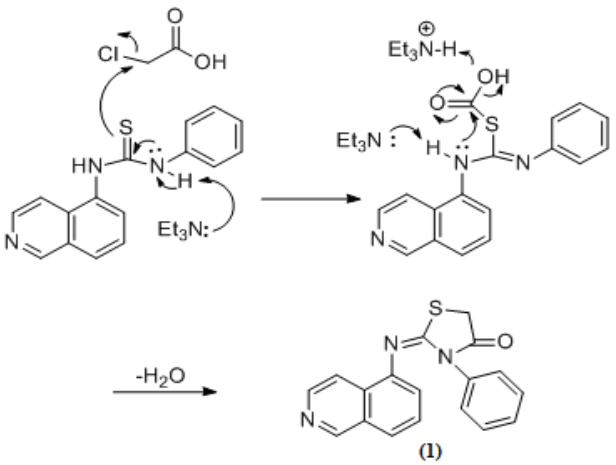

Scheme 2 A plausible mechanism for the formation of 2-(isoquinolin-5-ylimino)-3-phenylthiazolidin-4-one

The structural analysis of the obtained molecules was made using FT-IR, ^{1}H NMR, ^{13}C NMR, spectroscopy and elemental analysis techniques. In the infrared spectrum of compound (2) displayed a significant vibrational band at 3271 cm^{-1} for the presence of amine [26,27]. In aromatic compounds, the C–H stretching vibrations appear to be between 3113 and 3012 cm^{-1}. In compound (1-3), in addition to aromatic compound bonds, there are isoquinoline and phenyl aromatic rings, C=C, C-C, and C-N bonds. These stretching vibrations have been observed between 1675-1450 cm^{-1} [42]. Also, the absorption of C=O stretching vibrations was seen around 1670-1683 cm^{-1} in compounds (1) and (3) [37]. Also, important IR absorptions of the synthesized molecules are given in Table 2.

In ^{1}H NMR spectrum of all the compounds showed the signals of the aromatic protons of isoquinoline and phenyl ring at 7,40- 9.80 ppm [43]. The ^{1}H NMR spectrum of compounds (1) and (2) gave signals at 4.25 and 6.95 ppm attributed to thiazole ring CH_2 (H30-H31) and CH (H30), respectively [32]. Also, the signal belongs the NH_2 (H36-H37) on the thiazole ring in compound 2 was shown at 5.69 ppm. In their ^{13}C NMR spectra, the signal due to the thiazole carbonyl carbon (C14-O18, C15-O24) appeared at 170.11–183.40 ppm. Also -C=N- (C12-N11) signals were seen around 160 ppm [26,27]. The isoquinoline and phenyl carbons resonated at the range 125.90−168.31and 118.95−160.87 ppm, respectively. All spectra and elemental analyses support the structure of the synthesized compounds.

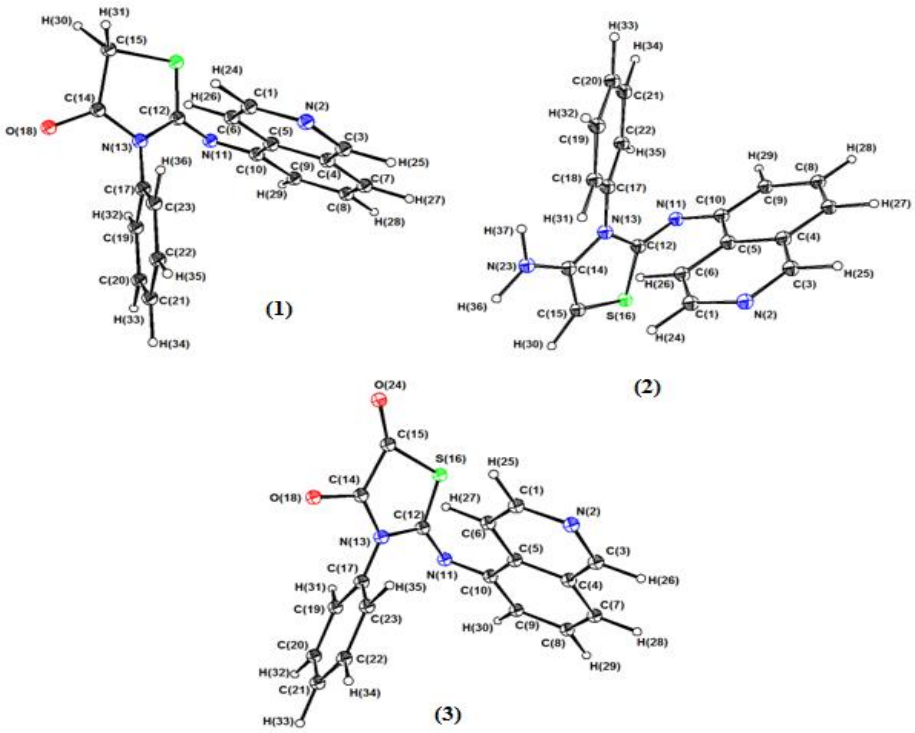

Scheme 3 ORTEP plot of the molecular structure of compound (1-3)

Table 2 ^{1}H and ^{13}C NMR (ppm) spectral data of compounds (1-3)

Compd.	IR (cm^{-1})			^{1}H NMR (PPM)			^{13}C (PPM)	
	NH_2	Ar CH	CO	Ar H (m)	thiazole CH_2 or CH	NH_2	-C=O	-N=C-
(1)	-	3070-3040	1670	9.68-7.40	4.25	-	170.24	156.60
(2)	3271	3075-3012	-	9.70-7.76	6.95	5.69	-	169.62
(3)	-	3113-3081	1683,1675	9.80-7.45	-	-	170.11, 183.40	160.30

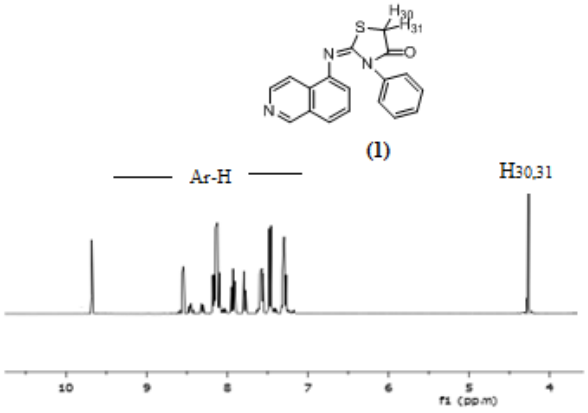

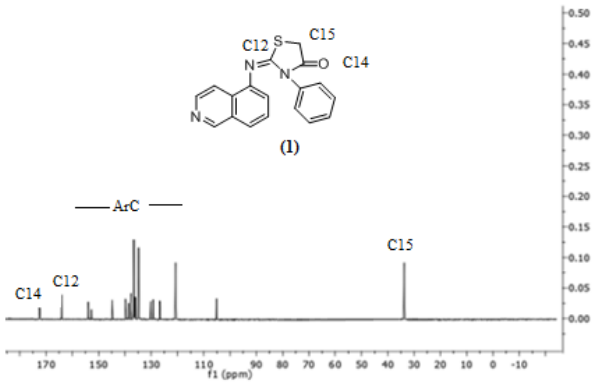

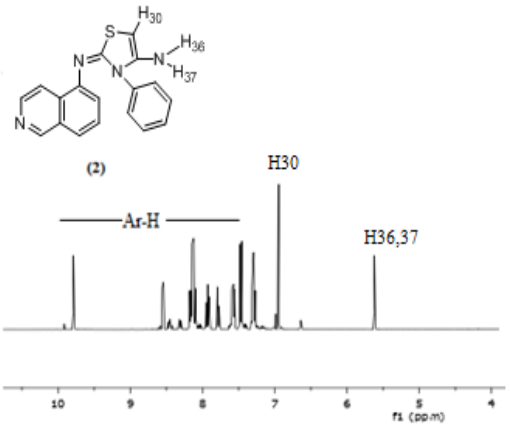

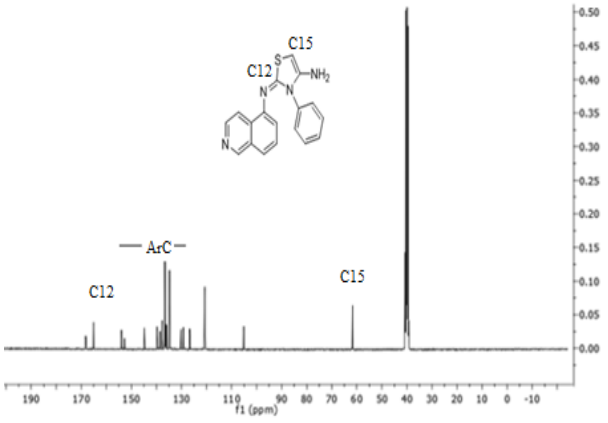

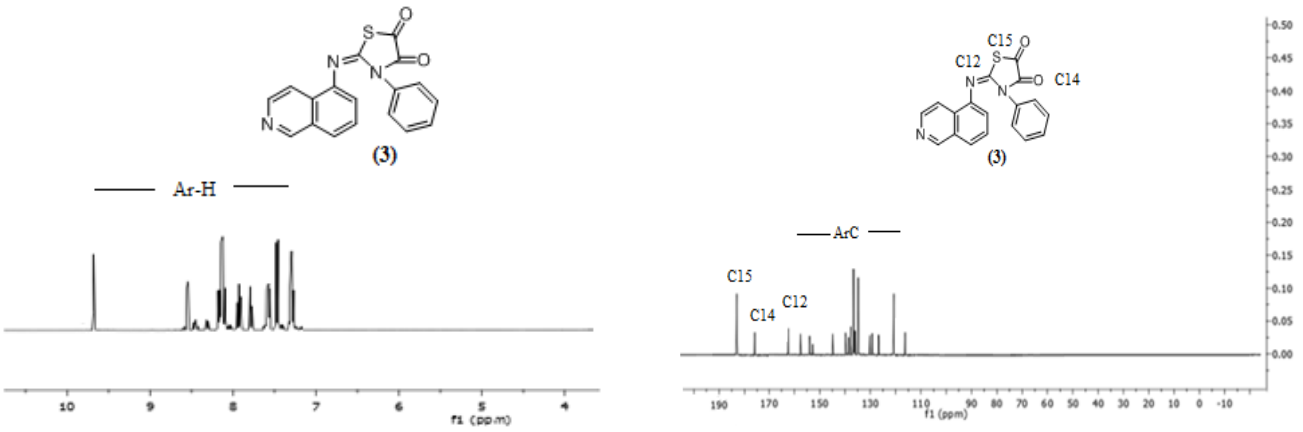

Scheme 4 ^{1}H and ^{13}C NMR spectrum of Compound (1-3)

4. CONCLUSIONS

In conclusion, a one-pot reaction protocol for the new heteroaryl isoquinoline derivatives (1-3) has been reported. The optimum conditions were found to be with 1 equivalent of phenyl isothiocyanate with monochloroacetic acid/chloro acetonitrile or diethyl oxalate using THF/DMF(5/0,5mL) and Et_3N (3 drops) affording a good yield of the new heteroaryl isoquinoline derivatives (1-3). Mild reaction conditions, shorter reaction times, high efficiencies, and facile isolation of the desired product make the present methodology a most suitable alternative. Unlike the one-pot reaction, the reaction stage increases in reactions carried out over thiourea, because firstly you must synthesis thiourea structure. Also, compounds are taken with a lower yield. Within the scope of literature studies, it has been observed for unsymmetrical thioureas in which amine attached to the thiourea having lower pKa is a part of the imino component and the amine having higher pKa is the contributor to the other heterocyclic nitrogen.

Acknowledgements

The author would like to thank the Çanakkale Onsekiz Mart University Scientific Research Projects Commission (BAP) for contributing to the financial portion of the project.

Funding

This work was supported by Research Fund of the Çanakkale Onsekiz Mart University. Project Number: FHD-2020-3440.

The Declaration of Conflict of Interest/ Common Interest

No conflict of interest or common interest has been declared by the authors.

Authors' Contribution

The author solemly performed the computations and wrote the manuscript.

The Declaration of Ethics Committee Approval

The author declare that this study does not require an ethics committee approval or any special permission.

The Declaration of Research and Publication Ethics

The authors of the paper declare that they comply with the scientific, ethical and quotation rules of SAUJS in all processes of the paper and that they do not make any falsification on the data collected. In addition, they declare that Sakarya

University Journal of Science and its editorial board have no responsibility for any ethical violations that may be encountered, and that this study has not been evaluated in any academic publication environment other than Sakarya University Journal of Science.

REFERENCES

[1] T. Akiyama, J. Iwai, "Scandium trifluoro-methanesulfonate-catalyzed chemoselective allylation reactions of carbonyl compounds with tetraallylgermane in aqueous media," Tetrahedron, vol. 55, no. 24, pp. 7499-7508, 1999.

[2] M. S. Saini, A. Kumar, J. Dwivedi, R. Singh, "A review: biological significances of heterocyclic compounds," International Journal of Pharma Sciences and Research, vol. 4, no. 3, pp. 66-77, 2013.

[3] Y. Cheng, Z. T. Huang, M. X. Wang, "Heterocyclic enamines: The versatile intermediates in the synthesis of heterocyclic compounds and natural products," Current Organic Chemistry, vol. 8, no. 4, pp. 325-51, 2004.

[4] N. Kaur "Review on the synthesis of six-membered N, N-heterocycles by microwave irradiation," Synthetic Communications, vol. 45, no. 10, pp. 1145-82, 2015.

[5] N. Kaur "Photochemical reactions: synthesis of six-membered N-heterocycles," Current Organic Synthesis, vol. 14, no. 7, pp. 972-98, 2017.

[6] M. Haji "Multicomponent reactions: A simple and efficient route to heterocyclic phosphonates," Beilstein Journal of Organic Chemistry, vol. 12, no. 1, pp. 1269-1301, 2016.

[7] S. Sarkar, A. A. Siddiqui, S. J. Saha, De. Rudranil, S. Mazumder, C. Banerjee, M. S. Iqbal, S. Nag, S. Adhikari, U. Bandyopadhyay, "Antimalarial Activity of small-molecule benzothiazole hydrazones," Antimicrob Agents Chemother, vol. 60, no. 7, pp. 4217-28, 2016.

[8] G. Negri, C. Kascheres, A. J. Kascheres, "Recent development in preparation reactivity and biological activity of enamino ketones and enamino thiones and their utilization to prepare heterocyclic compounds," Journal of Heterocyclic Chemistry, vol. 41, no. 4, pp. 461-491, 2004.

[9] A. Hazra, S. Mondala, A. Maitya, S. Naskara, P. Sahaa, R. Pairaa, K. B. Sahua, P. Pairaa, S. Ghoshb, C. Sinhab, A. Samanta, S. Banerjeea, N. B. Mondal, "Amberlite–IRA-402 (OH) ion exchange resin mediated synthesis of indolizines, pyrrolo [1, 2-a] quinolines and isoquinolines: Antibacterial and antifungal evaluation of the products," European Journal of Medicinal Chemistry, vol. 46, no. 6, pp. 2132-40, 2011.

[10] S. Saeed, N. Rashid, P. G. Jones, M. Ali, R. Hussain, "Synthesis, characterization and biological evaluation of some thiourea derivatives bearing benzothiazole moiety as potential antimicrobial and anticancer agents," European Journal of Medicinal Chemistry, vol. 45, no. 4, pp. 1323-31, 2010.

[11] P. Zajdel, A. Partyka, K. Marciniec, A. J. Bojarski, M. Pawlowski, A. Wesolowska, "Quinoline-and isoquinoline-sulfonamide analogs of aripiprazole: novel antipsychotic agents?," Future Medicinal Chemistry, vol. 6, no. 1, pp. 57-75, 2014.

[12] D. C. Liu, H. J. Zhang, C. M. Jin, Z. S. Quan, "Synthesis and biological evaluation of novel benzothiazole derivatives as potential anticonvulsant agents," Molecules, vol. 21, no. 3, pp. 164, 2016.

[13] E. G. Paronikyan, A. S. Noravyan, S. F. Akopyan, I. A. Dzhagatspanyan, I. M. Nazaryan, R. G. Paronikyan, "Synthesis and anticonvulsant activity of pyrano [4′, 3′: 4,

5] pyrido [2, 3-b] thieno [3, 2-d] pyrimidine derivatives and pyrimido [5′, 4′: 2, 3]-thieno [2,3-c] isoquinoline derivatives," Pharmaceutical Chemistry Journal, vol. 41, no. 9, pp. 466-9, 2007.

[14] S. Shafia, M. Mahboob, A. Naveen, M. Chaitanya, M. G. Vanajad, A. M. Kalled, R. Pallud, M.S.Alama, "Synthesis of novel 2-mercapto benzothiazole and 1,2,3-triazole based bis-heterocycles: their anti-inflammatory and anti-nociceptive activities," European Journal of Medicinal Chemistry, vol. 49, no. 2012, pp. 324-33, 2012.

[15] V. S. Patilac, K. P. Nandreb, S. Ghoshd, V. J., Rao, B. A. Chopadede, B. Sridharf, S. V. Bhosaleg, S. V. Bhosaleab, "Synthesis, crystal structure and antidiabetic activity of substituted (E)-3-(Benzo[d]thiazol-2-ylamino)phenylprop-2-en-1-one," European Journal of Medicinal Chemistry, vol. 59, no. 2013, pp. 304-9. 2013.

[16] E. Pitta, A. Geronikaki, S. Surmava, P. Eleftheriou, V. P. Mehta, E. V. Van der Eycken, "Synthesis and HIV-1 RT inhibitory action of novel (4/6-substituted benzo[d]thiazol-2-yl) thiazolidin-4-ones Divergence from the non-competitive inhibition mechanism," Journal of Enzyme Inhibition and Medicinal Chemistry, vol. 28, no. 1, pp. 113-22, 2013.

[17] W. Krzysztof, R. Guryn, O. P. Zuiderveld, H. Timmerman, "Non-imidazole histamine H3 ligands, Part 2: new 2-substituted benzothiazoles as histamine H3 antagonists," Archiv der Pharmazie, vol. 332, no. 11, pp. 389-98, 1999.

[18] K. J. Wilson, C. R. Illig, N. Subasinghe, J. B. Hoffman, M. J. Rudolph, R. Soll, C. J. Molloy, R. Bone, D. Green, T. Randall, M. Zhang, F. A. Lewandowski, Z. Zhou, C. Sharp, D. Maguire, B. Grasberger, R. L. DesJarlais, J. Spurlino, "Synthesis of thiophene-2-carboxamidines containing 2-aminothiazoles and their biological evaluation as urokinase inhibitors," Bioorganic and Medicinal Chemistry Letters, vol. 11, no. 7, pp. 915-18, 2001.

[19] N. El-Ket, E. Kendjo, M. Thellier, L. Assoumou, V. Potard, A. Taieb, I. Tantaoui, E. Caumes, R. Piarroux, C. Roussel, P. Buffet, D. Costagliola, S. Jauréguiberry, "Propensity score analysis of artesunate versus quinine for severe imported Plasmodium falciparum malaria in France," Clinical Infectious Diseases, vol. 70, no. 2, pp. 280-87, 2020.

[20] S. D'Alessandro, D. Scaccabarozzi, L. Signorini, F. Perego, D. P. Ilboudo, P., Ferrante, S. Delbue, "The use of antimalarial drugs against viral infection," Microorganisms, vol. 8, no. 1, pp. 85, 2020.

[21] H. N. Karade, B. N. Acharya, M. Sathe, M. P. Kaushik, "Design, synthesis, and antimalarial evaluation of thiazole-derived amino acids," Medicinal Chemistry Research, vol. 17, no. 1, pp. 19–29, 2008.

[22] P. Ghosh, M. J. Deka, A. K. Saikia, "Lewis acid mediated intramolecular C–O bond formation of alkanol-epoxide leading to substituted morpholine and 1, 4-oxazepane derivatives: total synthesis of (±) – viloxazinec," Tetrahedron, vol. 72, no. 5, pp. 690-698, 2016.

[23] R. M. Abdel-Rahman "Role of uncondensed 1,2,4-triazine compounds and related heterobicyclic systems as therapeutic agents: a review," Pharmazie, vol. 56, no. 1, pp. 18-22, 2001.

[24] A. R. Surray "4-Thiazolidones.IV. The preparation of some 3-alkylaminoalkyl-2-aryl derivatives," Journal of the American Chemical Society, vol. 71, no. 10, pp. 3354–56, 1949.

[25] N. G. Voznesenskaia, O. I. Shmatova, M. M. Ilyin, M. M. Ilyin Jr, V. G. Nenajdenko, "Enantioselective synthesis of thiazole-derived α-perfluoroalkylated 5–7-membered amines," European Journal of

Organic Chemistry, vol. 2019, no. 9, pp. 1893-903, 2019.

[26] N. Berber, M. Arslan, F. Vural, A. Ergun, N. Gençer, O. Arslan, "Synthesis of new series of thiazol-(2(3H)-ylideneamino) benzene- sulfonamide derivatives as carbonic anhydrase inhibitors," Journal of Biochemical and Molecular Toxicology, vol. 34, no. 12, pp. e22596, 2020.

[27] N. Berber, M. Arslan, Ç. Bilen, Z. Sackes, N. Gencer, O. Arslan, "Synthesis and evaluation of new phthalazine substituted β-lactam derivatives as carbonic anhydrase inhibitors," Russian Journal of Bioorganic Chemistry, vol. 41, no. 4 pp. 414-20, 2015.

[28] N. Berber "Synthesis of certain new morpholine derivatives bearing a thiazole moiety," Sakarya University Journal of Science and Technology, vol. 23, no. 4, pp. 554-58, 2019.

[29] S. Kılıcaslan, M. Arslan, Z. Ruya, Ç. Bilen, A. Ergün, N. Gençer, O. Arslan, "Synthesis and evaluation of sulfonamide-bearing thiazole as carbonic anhydrase isoforms hCA I and hCA II," Journal of Enzyme Inhibition and Medicinal Chemistry, vol. 31, no. 6, pp. 1300-1305, 2016.

[30] H. Saad "The synthesis of some new sulfur-bearing various heterocyclic systems derived from asymmetrical n,n′-disubstituted thiourea derivatives," Phosphorus, Sulfur, and Silicon, vol. 181, no. 7, pp. 1557-1567, 2006.

[31] H. A. Abdel-Azız, H. S. El-Zahabi, K. M. Dawood, "Microwave-assisted synthesis and in-vitro anti-tumor activity of 1,3,4-triaryl-5-N-arylpyrazole carboxamides," European Journal of Medicinal Chemistry, vol. 45, no. 6, pp. 2427-2432, 2010.

[32] H. M. Abumelha "Synthesis and antioxidant assay of new nicotinonitrile analogues clubbed thiazole, pyrazole and/or pyridine ring systems," Journal of Heterocyclic Chemistry, vol. 57, no. 3, pp. 1011-1022, 2020.

[33] Y. Feng, X. Ding, T. Chen, L. Chen, F. Liu, X. Jia, X. Luo, X. Shen, K. Chen, H. Jiang, H. Wang, H. Liu, D. Liu, "Design, synthesis, and interaction study of quinazoline-2 (1 H)-thione derivatives as novel potential Bcl-xL inhibitors," Journal of Medicinal Chemistry, vol. 53, no. 9, pp. 3465-3479, 2010.

[34] H. A. Morsy, A. H. Moustafa "A facile approach for synthesis of thiazines-, thiazoles-and triazoles-annulated 6-styryl-2-thiouracil derivative," Journal of the Iranian Chemical Society, vol. 17, no. 1, pp. 119-125, 2020.

[35] M. Sathishkumar, S. Nagarajan, P. Shanmugavelan, M. Dinesh, A. Ponnuswamy, "A facile, rapid, one-pot regio/stereoselective synthesis of 2-iminothiazolidin-4-ones under solvent/ scavenger-free conditions," Beilstein Journal of Organic Chemistry, vol. 9, no. 1, pp. 689-697, 2013.

[36] A. R. Sayed, S. M. Gomha, E. A. Taher, Z. A. Muhammad, H. R. El-Seedi, H. M. Gaber, M. M. Ahmed, "One-pot synthesis of novel thiazoles as potential anti-cancer agents," Drug Design, Development and Therapy, vol. 14, no. 2020, pp. 1363, 2020.

[37] M. El-Naggar, W. M. Eldehna, H. Almahli, A. Elgez, M. Fares, M. M. Elaasser, H. A. Abdel-Aziz, "Novel thiazolidinone/ thiazolo [3,2-a] benzimidazolone-isatin conjugates as apoptotic anti-proliferative agents towards breast cancer: one-pot synthesis and in vitro biological evaluation," Molecules, vol. 23, no. 6, pp. 1420, 2018.

[38] C. B. Singh, H. Ghosh, S. Murru, B. K. Patel, "Hypervalent iodine (III)-mediated regioselective N-acylation of 1, 3-disubstituted thioureas," The Journal of Organic Chemistry, vol. 73, no. 7, pp. 2924-2927, 2008.

[39] T. Wirth, M. Ochiai, V. V. Zhdankin, G. F. Koser, H. Tohma, Y. Kita, "Topics in Current Chemistry: Hypervalent iodine chemistry-modern developments in organic synthesis," Wirth, T, vol. 2002, pp. 1-248. 2002.

[40] R. Yella, H. Ghosh, B. K. Patel, "It is "2-imino-4-thiazolidinones" and not thiohydantoins as the reaction product of 1,3-disubstituted thioureas and chloroacetylchloride," Green Chemistry, vol. 10, no. 12, pp. 1307-1312, 2008.

[41] H. Ghosh, S. Sarkar, A. R. Ali, B. K. Patel, "Oxidative desulfurization of disubstituted thioureas using Pb (II) salts and investigation of p K a-dependent regioselective N-acylation," Journal of Sulfur Chemistry, vol. 31, no. 1, pp. 1-11, 2010.

[42] V. Krishnakumar, N. Surumbarkuzhalı, S. Muthunatesan "Scaled quantum chemical studies on the vibrational spectra of 4-bromo benzonitrile," Spectrochimica Acta Part A: Molecular and Biomolecular Spectroscopy, vol. 71, no. 5, pp. 1810-1813, 2009.

[43] N. Subramanian, N. Sundaraganesan, J. Jayabharathi "Molecular structure, spectroscopic (FT-IR, FT-Raman, NMR, UV) studies and first-order molecular hyperpolarizabilities of 1, 2-bis (3-methoxy-4-hydroxybenzylidene) hydrazine by density functional method," Spectrochimica Acta Part A: Molecular and Biomolecular Spectroscopy, vol. 76, no. 2, pp. 259-269, 2010.

SAKARYA ÜNİVERSİTESİ
FEN BİLİMLERİ ENSTİTÜSÜ DERGİSİ

Sakarya University Journal of Science
SAUJS

e-ISSN 2147-835X Period Bimonthly Founded 1997 Publisher Sakarya University
http://www.saujs.sakarya.edu.tr/

Title: Metal-containing Coordination Complexes (MCCs): Assessment of Biological Activity with Helicobacter pylori Caused Gastric Ulcer

Authors: Dursun KISA, Yusuf CEYLAN, Merve YILDIRIM, Sümeyra DURGUN, Nesrin KORKMAZ

Recieved: 2022-02-05 00:00:00

Accepted: 2022-06-16 00:00:00

Article Type: Research Article

Volume: 26
Issue: 4
Month: August
Year: 2022
Pages: 768-775

How to cite
Dursun KISA, Yusuf CEYLAN, Merve YILDIRIM, Sümeyra DURGUN, Nesrin KORKMAZ; (2022), Metal-containing Coordination Complexes (MCCs): Assessment of Biological Activity with Helicobacter pylori Caused Gastric Ulcer. Sakarya University Journal of Science, 26(4), 768-775, DOI: 10.16984/saufenbilder.1068212
Access link
http://www.saujs.sakarya.edu.tr/en/pub/issue/72361/1068212

Sakarya University Journal of Science 26(4), 768-775, 2022

Metal-containing Coordination Complexes (MCCs): Assessment of Biological Activity with *Helicobacter pylori* Caused Gastric Ulcer

Dursun KISA*[1], Yusuf CEYLAN[1], Merve YILDIRIM[1],
Sümeyra DURGUN[1], Nesrin KORKMAZ[2]

Abstract

The ulcer is a vital disease that unfavorably affects human health globally. *Helicobaster pylori*, which causes ulcers and some stomach disorders, survives by using the urease enzyme. Metal coordination complexes (MCCs) are used in numerous industrial areas and the health field. Cyanide bridged metal complexes are also applied in several applications. In the current study, antibacterial characteristic of (C1), $[Ni(bishydeten)_2Ag(CN)_2][Ag(CN)_2].H_2O$), and (C2), $([Ni(hydeten)_2Ag(CN)_2][Ag(CN)_2]$, MCCs were analyzed by disk diffusion, broth dilution and urease enzyme inhibition assays were performed. As a result of both antibacterial tests, C1 and C2 were observed to provide favorable effects. The synthesized compounds have effective inhibitory potential with IC_{50} values between 26.65±1.21 and 12.37±0.87 µM for urease.

Keywords: Metal coordination complexes, *Helicobacter pylori*, antibacterial, urease, enzyme inhibition

1. INTRODUCTION

H. pylori is a pathogenic Gram (-) bacterium that attacks the gastric epithelial surface and results in lifelong chronic gastritis unless treated with antimicrobial drugs. *H. pylori* is a microorganism that influences approximately 50% of the global population, and research on its eradication has been rising in previous years [1].

The bacterial urease enzyme is of particular impact, a potent virulence factor. The enzyme secreted by *H. pylori* in the mucus layer of the stomach converts urea into ammonia and carbamate [2]. In the presence of the urease, the hydrolysis of urea raises approximately tenfold. The bacterium thus preserves itself from the harmful impacts of stomach acid by establishing an alkaline habitat [3]. Urea is the main source of pathologies caused by *H. pylori* and therefore plays a fundamental role in the pathology of

* Corresponding author: dkisa@bartin.edu.tr
[1] Bartın University, Faculty of Science, Department of Molecular Biology and Genetics
E-mail: ysf.cyln@gmail.com, mervee.yildirim9@gmail.com, sdurgun141@gmail.com
ORCID: https://orcid.org/0000-0002-7681-2385, https://orcid.org/ 0000-0001-8186-7252, https://orcid.org/0000-0003-1427-9666, https://orcid.org/ 0000-0001-6437-5512
[2] Yozgat Bozok University, Hemp Research Institute
E-mail: nesrinokumus@gmail.com
ORCID: https://orcid.org/0000-0002-7896-1042

gastric and peptic ulcers. Excessive urease activity gives rise to cell death, kidney disorders, renal calculus formation, ulcer, hepatic, and urinary system diseases [4].

Enzymes, biological molecules responsible for the metabolic process, are synthesized by living cells and perform chemical reactions [5]. Enzymes reach optimum pH, temperature, substrate concentration, enzyme amount, activator, and inhibitory substances. Enzymes are used as biomarkers in hospital routine tests to diagnose various diseases [6].

Enzyme inhibition is a crucial step in pharmaceutical research since it has led to the detection of several curative drugs for many diseases [5]. Specific inhibitors interact with enzymes and block their activity. Urease (Ureamidohydrolase; EC 3.5.1.5), a crucial factor of the nitrogen cycle, is a nickel-containing metalloenzyme found in animals, plants, bacteria, and fungi [1,4].

Metal-containing coordination complexes (MCCs) have been used in several fields long ago, and one of the most critical areas of that is in the medical field. Papers have risen in this direction by increasing MCC availability in the industry. MCC is among the compounds researchers notice with this approach [7].

It is known that MCCs demonstrate various biological activities such as antitumor, antimicrobial, antifungal, analgesic, anti-inflammatory, anti-HIV, carbonic anhydrase inhibition, and local anesthetic [8]. Enzymes are responsible for almost all biochemical reactions to maintain homeostasis. Metal complexes carrying –OH groups on their active surfaces have more enzyme inhibition effects. The effects of MCC on the inhibition of enzymes have been initiated to be examined in recent years [9]. Cyano bridged metal complexes among the complex coordination compounds are one-, two- or three-dimensional macromolecules arranged in the form of metal-metal or metal-ligand-metal. Cyano complexes containing transition metals take part in material chemistry due to their various bonding, structural properties, and broad usage areas [10].

Cyano-bridged homo- and heteronuclear compounds are among the molecules that attract attention due to their different properties and application areas. Various coordination compounds are still used as anticancer drugs [11-16]. In conclusion, coordination compounds are promising complexes in anticancer and antimicrobial therapies.

H. pylori is sensitive to many antibiotics *in vitro*, although it is resistant to *in vivo* conditions. Currently, antibiotics such as lansoprazole, amoxicillin, metronidazole, and clarithromycin and inhibitory agents such as urea C-13 are applied for the eradication of *H. pylori* and the inhibition of the urease enzyme. It has been reported that the urease secreted by *H. pylori* is found in the cytoplasm in freshly prepared cultures and the outer membrane in old cultures [17-18].

Urease inhibitors are one of the targets for new antiulcer drugs. Studying the synthesis of new urease inhibitors that can suppress the urease enzyme and new coordination complexes with antimicrobial effects against *H. pylori* to treat such diseases is a promising approach to disease treatment. This study aimed to minimize the formation of ammonia, which has a vital role in the *H. pylori* life cycle, by inhibiting the urease function of the newly synthesized MCC and analyzing its usage as an antibacterial agent. Our research group will examine the effect of MCCs, which were previously shown to have inhibitory effects on AChe, BChE, and carbonic anhydrase on urease, for the first time with this study [19].

2. EXPERIMENTAL

2.1. Disc Diffusion Method

Previously synthesized MCCs ($[Ni(hydeten)_2Ag(CN)_2][Ag(CN)_2]$ and $[Ni(bishydeten)_2Ag(CN)_2][Ag(CN)_2].H_2O$) were dissolved in sterile distilled water and five different concentrations (1000 µg/mL, 500 µg/mL, 250 µg/mL, 100 µg/mL and 50 µg/mL) were prepared under sterile conditions. Different concentrations of MCCs were absorbed into sterile discs. *Helicabter pyolori* (ATCC 700824)

used in the current study was obtained from the Microbiology Reference Laboratories and Biological Products Department of the Ministry of Health of the Republic of Turkey. Modification of Kirby and Bauer's disk diffusion assay was practiced because of the use of blood agar instead of Mueller Hinton agar [20]. Bacterial growth was calibrated 0.5 McFarland turbidity ($1.5x10^{8}$ cell/mL). Bacteria were seeded into blood agar (LabM), and discs were placed on the petri dishes and incubated overnight at 37°C. After incubation, the inhibition zones around the discs were measured, and the study was performed with three replicates.

2.2. Broth Microdilution Assay

The modified Minimal Inhibition Concentration (MIC) test was applied for antibacterial activity of MCCs against *H. pylori* that were cultured in Tryptic Soy Broth (LabM). The concentration of bacterial suspension was adjusted to 0.5 McFarland in %9 sterile NaCl. Chemicals were dispersed in 10% DMSO and diluted to 500 µg/mL concentration, and serial two-fold dilution was performed among 15.625 µg/mL. MIC and Minimal Bactericidal Concentration (MBC) values of MCCs were identified against *H. pylori* [21].

2.3. Urease Inhibition Assay

The urease inhibition study of MCCs was carried out using the indophenols method to quantify ammonia [22]. In brief, the reaction mixtures comprise 50 µL of phosphate buffer (100 mM, pH 8.2), which contains 100 mM urea µL, 25 µL of jack bean urease solution, and 20 µL of MCCs were incubated in a 96 well microplate at 37 °C for 15 min. Then, the ammonia liberated was allowed to complex with 45 µL of a phenol reagent (1% w/v phenol and 0.005% w/v sodium nitroprusside - $Na_2[Fe(CN)_5NO]\cdot 2H_2O$), and 70 µL of an alkali reagent (0.5% w/v NaOH and 0.1% NaOCl). After the mixture was incubated for 20 min, the absorbance of the color change was spectrophotometrically measured at 630 nm using the microplate reader. (MultiskanGO Microplate Reader, Thermo Scientific).

3. RESULTS AND DISCUSSION

3.1. Disc Diffusion Method

H. pylori is one pathogenic bacteria that significantly influence human health globally. Since *H. pylori* are sensitive to antibiotics *in vivo* conditions, research on inhibiting or eradicating the bacteria continues. In current paper, different concentrations (1000 µg/mL, 500 µg/mL, 250 µg/mL, 100 µg/mL and 50 µg/mL) of **C1** (bishydeten) and **C2** (hydeten) compounds were analyzed and tetracycline antibiotic was used as positive control (Table 1). The largest zone was measured at the concentration of 1000 µg/mL concentration, the highest dose for both compounds (Figure 1). The highest dose for compound **C1** and **C2** was measured at 1000 µg/mL concentrations at 10±0,24 mm and 14±1,00 mm, respectively. On the other hand, tetracycline formed a zone diameter of 27 mm. When previous studies were viewed, it was observed that chemical compounds with similar structures had a lower zone diameter than the antibiotic used as a positive control [10, 23-25]. As the concentrations of **C1** and **C2** compounds of *H. pylori* reduced, it was revealed that the diameter of the effect zone narrowed. Both chemical compounds were assessed effectively against bacteria.

Table 1 Inhibitory zone diameter (mm) for different concentration of C1 and C2 against *H. pylori* by disc diffusion method

Conc. (µg/mL)	C1	C2
1000	10±0.24	14±1.00
500	8±0.47	10±0.31
250	8±0.28	8±0.20
100	7±0.16	NE

NE: No effect

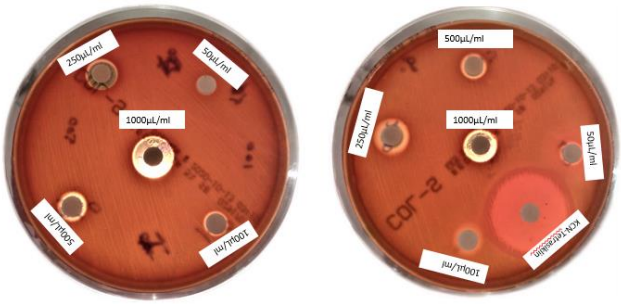

Figure 1 Photograph showing antibacterial C1 and C2 screening on blood agar

3.2. Broth Microdilution Assay

C1 and **C2** were subjected to MIC and MBC analysis. The results are served in Figures 2 and 3. As seen in Figure, both chemicals demonstrated MBC and MIC characteristics at 500 µg/mL and 250 µg/mL concentrations, respectively. Like the disc diffusion method, it was observed that the bacteriostatic and bacterial effects increased with increasing chemical concentration. According to MIC results of EUCAST Clinical Breakpoint, Fluoroquinolones and tetracyclines shows MIC breakpoints at 1 mg/mL concentration [26]. Antibacterial properties of the MCCs possibly be clarified by the many essential factors like hydrophilicity, hydrophobicity, metal ion, metal ion coordination site can possess an appreciable effect on the antibacterial effect. The activities of MCCs can be ascribed to their susceptibility to experience different ligand substitute reactions with the biological ligands such as DNA and protein [27-29].

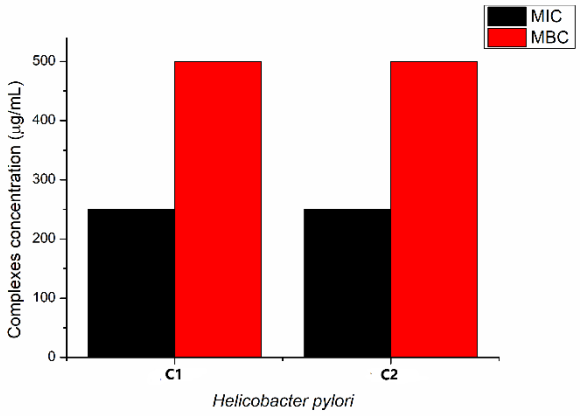

Figure 2 Minimum inhibition and minimum bacteriostatic/bactericidal concentration of C1 and C2 against *H. pylori*

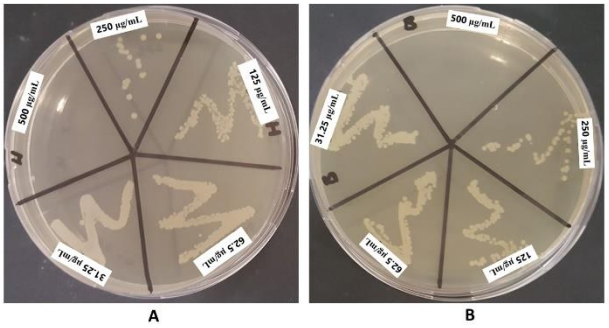

Figure 3 Results of minimum bactericidal concentration against *H. pylori*

3.3. Urease Inhibition Ability of MCCs

In this study, the inhibition effects of MCCs on urease enzyme associated with *H. pylori* were evaluated, and their IC_{50} values are shown in Figure 4 and Table 2 below. The synthesized compound C1 has effective inhibitory potential with an IC_{50} value at 12.37±0.87 µM. The urease inhibitory potential of the compound C2 was 12.37±0.87 µM for IC_{50} value. The compounds inhibited urease activity in micromolar concentration. A previous study on inhibition of urease with metal compounds of schiff base ligands demonstrated that transition metals had exhibited different abilities, and their IC_{50} value changed between 0.37-100 µM for urease inhibition [30]. The inhibitory activity of complexes containing metals such as Cu, Ni, Zn, and Co against urease activity declared that their synthesized complexes have IC_{50} values between 2.14± 0.12 – 100 µM for urease [31]. Another study expressed that some metal complexes show medium urease inhibitory ability, with IC_{50} values of 35.7±3.1, and 41.5±2.7 µmol·L^{-1}, respectively [32]. The obtained compounds should be assessed as urease inhibitors according to previous studies. The inhibitory potential of molecules against enzymes has been associated with the structure of compounds, allowing them to interact between enzymes and substances [33].

Table 2 Inhibition values of dicyanidosilver complexes on urease

Compounds	IC_{50} (µM)	r^2
$[Ni(hydeten)_2Ag(CN)_2][Ag(CN)_2]$ (C2)	26.65±1.21	0.897
$[Ni(bishydeten)_2Ag(CN)_2][Ag(CN)_2].H_2O$ (C1)	12.37±0.87	0.904

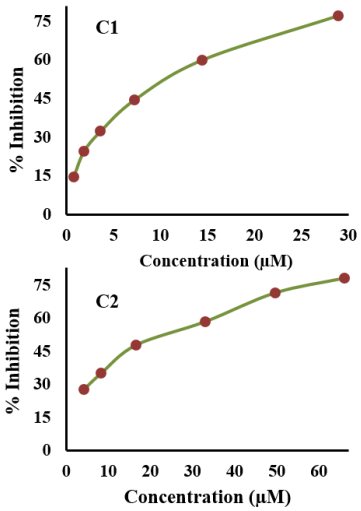

Figure 4 Inhibition ability of MCCs on the studied urease enzyme

4. CONCLUSION

Health issues caused by *H. pylori* are diseases that adversely affect many world populations. It is concluded that MCCs have antibacterial effects against *H. pylori* and anti-urease activity. The eradication of *H. pylori* by enzyme inhibition has prompted researchers to attempt new solutions to inhibit urease activity. MCCs are applied in several fields and the health sector, such as antifungal, antibacterial, anticancer, and antitumor. The current paper analyzed the antibacterial effect of C1 and C2 compounds against *H. pylori* by disc diffusion and broth dilution methods.

Acknowledgments

We would like to thank TÜBİTAK for supporting this project.

Funding

"This study is supported by TÜBİTAK TÜBİTAK 2209-A - Research Project Support Programme for Undergraduate Students. Project Number: 1919B011902147."

The Declaration of Conflict of Interest/ Common Interest

The authors have declared no conflict of interest or common interest.

Authors' Contribution

The authors contributed equally to the study.

The Declaration of Ethics Committee Approval

The author declares that this document does not require approval from the ethics committee or any special permission.

The Declaration of Research and Publication Ethics

The authors of the paper declare that they comply with the scientific, ethical, and quotation rules of SAUJS in all the article processes and that they do not falsify the data collected. In addition, they declare that Sakarya University Journal of Science and its editorial board have no responsibility for any ethical violations that may be encountered and that this study has not been evaluated in any academic publication environment other than Sakarya University Journal of Science.

REFERENCES

[1] J. E. Everhart, "Recent developments in the epidemiology of Helicobacter pylori,"

Gastroenterology Clinics of North America, vol. 29, no. 3, pp. 559-578, 2000.

[2] P. Malfertheiner, F. Megraud, C. A. O'morain, J. P. Gisbert, E. J. Kuipers, A. T. Axon, E. M. El-Omar, "Management of Helicobacter pylori infection—the Maastricht V/Florence consensus report," Gut, vol. 66, no.1, pp. 6-30, 2017.

[3] W. R. Gransden, "Topley and Wilson's Microbiology and Microbial Infections, (CD-ROM)," Journal of Clinical Pathology, vol. 52, no. 3, pp. 237, 1999.

[4] F. Mégraud, "Advantages and disadvantages of current diagnostic tests for the detection of Helicobacter pylori," Scandinavian journal of gastroenterology, vol 31, no. sup215, pp. 57-62, 1996.

[5] P. Taslimi, I. Gulcin, B. Ozgeris, S. Goksu, F. Tumer, S. H. Alwasel, C. T. Supuran, "The human carbonic anhydrase isoenzymes I and II (hCA I and II) inhibition effects of trimethoxyindane derivatives," Journal of enzyme inhibition and medicinal chemistry, vol. 31, no. 1, pp. 152-157, 2016.

[6] D. Barman, V. Kumar, S. Roy, S.C. Mandal, "Clinical enzymes and their application," Aquaculture. pp. 12-13, 2011.

[7] X. Huang, S. Jiang, M. Liu, "Metal ion modulated organization and function of the Langmuir− Blodgett films of amphiphilic diacetylene: photopolymerization, thermochromism, and supramolecular chirality," The Journal of Physical Chemistry B, vol. 109, no. 1, pp. 114-119, 2005.

[8] H. Aghabozorg, F. Manteghi, S. Sheshmani, "A brief review on structural concepts of novel supramolecular proton transfer compounds and their metal complexes," Journal of the Iranian Chemical Society, vol. 5, no. 2, pp. 184-227, 2008.

[9] H. İlkimen, C. Yenikaya, "Salisilik asit türevleri ile 2-aminobenzotiyazol türevlerinin karışık ligandlı Cu (II) komplekslerinin sentezi ve karakterizasyonu," Pamukkale Üniversitesi Mühendislik Bilimleri Dergisi, vol. 23, no. 7, pp. 899-907, 2017.

[10] N. Korkmaz, A. Aydın, A. Karadağ, Y. Yanar, Y. Maaşoğlu, E. Şahin, Ş. Tekin, "New bimetallic dicyanidoargentate (I)-based coordination compounds: Synthesis, characterization, biological activities, and DNA-BSA binding affinities," Spectrochimica Acta Part A: Molecular and Biomolecular Spectroscopy, vol. 173, pp. 1007-1022, 2017.

[11] L. Ronconi, P. J. Sadler, "Using coordination chemistry to design new medicines," Coordination Chemistry Reviews, vol. 251, no. 13-14, pp. 1633-1648, 2007.

[12] E. Meggers, "Exploring biologically relevant chemical space with metal complexes," Current opinion in chemical biology, vol. 11 no. 3, pp. 287-292, 2007.

[13] P. C. Bruijnincx, P. J. Sadler, "New trends for metal complexes with anticancer activity," Current opinion in chemical biology, vol. 12, no. 2, pp. 197-206, 2008.

[14] I. Ott, R. Gust, "Non platinum metal complexes as anti-cancer drugs," Archiv der Pharmazie: An International Journal Pharmaceutical and Medicinal Chemistry, vol. 340, no. 3, pp. 117-126, 2007.

[15] E. R. T. Tiekink, "Anti-cancer potential of gold complexes," Inflammopharmacology, vol. 16, no. 3, pp. 138-142, 2008.

[16] I. Kostova, "Ruthenium complexes as anticancer agents," Current Medicinal Chemistry, vol. 13, no. 9, pp. 1085-1107, 2006.

[17] D. Y. Graham, M. Miftahussurur, "*Helicobacter pylori* urease for diagnosis of *Helicobacter pylori* infection: A mini-review," Journal of Advanced Research, vol. 13, pp. 51-57, 2018.

[18] G. M. El-Sherbiny, M. K. Elbestawy, "A review–plant essential oils active against *Helicobacter pylori*," Journal of Essential Oil Research, pp. 1-13, 2022.

[19] D. Kısa, N. Korkmaz, P. Taslimi, B. Tuzun, Ş. Tekin, A. Karadag, F. Şen, "Bioactivity and molecular docking studies of some nickel complexes: New analogues for the treatment of Alzheimer, glaucoma and epileptic diseases," Bioorganic Chemistry, vol. 101, no. 104066, 2020.

[20] J. Hudzicki, "Kirby-Bauer disk diffusion susceptibility test protocol" 2009.

[21] J.M. Andrews, Determination of minimum inhibitory concentrations, Journal of Antimicrobial Chemotherapy, vol. 49, pp. 1049–1049, 2002.

[22] M. Ikram, S. Rehman, F. Subhan, M. N. Akhtar, M. O. Sinnokrot, "Synthesis, characterization, thermal degradation and urease inhibitory studies of the new hydrazide based Schiff base ligand 2-(2-hydroxyphenyl)-3-{[(E)-(2-hydroxyphenyl)methylidene]amino}-2,3-dihydroquinazolin-4(1H)-one," Open Chemistry, vol. 15, pp. 308–319, 2017.

[23] N. Korkmaz, A. Karadağ, A. Aydın, Y. Yanar, İ. Karaman, Ş. Tekin, "Synthesis and characterization of two novel dicyanidoargentate (I) complexes containing N-(2-hydroxyethyl) ethylenediamine exhibiting significant biological activity," New Journal of Chemistry, vol. 38, no. 10, pp. 4760-4773, 2014.

[24] A. Karadağ, N. Korkmaz, A. Aydın, Ş. Tekin, Y. Yanar, Y. Yerli, Ş. A. Korkmaz, "In vitro biological properties and predicted DNA–BSA interaction of three new dicyanidoargentate (i)-based complexes: synthesis and characterization," New Journal of Chemistry, vol. 42, no. 6, pp. 4679-4692, 2018.

[25] A. Karadağ, N. Korkmaz, A. Aydın, H. Akbaş, Ş. Tekin, Y. Yerli, F. Şen, "Metalo components exhibiting significant anticancer and antibacterial properties: a novel sandwich-type like polymeric structure," Scientific reports, vol. 10, no. 1, pp. 1-17, 2020.

[26] EUCAST (2022). The European Committee on Antimicrobial Susceptibility Testing. Breakpoint tables for interpretation of MICs and zone diameters. Version 12.0, 2022. http://www.eucast.org.

[27] S. Ahmad, S. Nadeem, A. Anwar, A. Hameed, S. A. Tirmizi, W. Zierkiewicz, M. A. Alotaibi, "Synthesis, characterization, DFT calculations and antibacterial activity of palladium (II) cyanide complexes with thioamides," Journal of Molecular Structure, vol. 1141, pp. 204-212, 2017.

[28] S. Aslam, A. A. Isab, M. A. Alotaibi, M. Saleem, M. Monim-ul-Mehboob, S. Ahmad, N. Trendafilova, "Synthesis, spectroscopic characterization, DFT calculations and antimicrobial properties of silver (I) complexes of 2, 2′-bipyridine and 1, 10-phenanthroline," Polyhedron, vol. 115, pp. 212-218, 2016.

[29] M. N. Uddin, J. Akter, M. A. Manchur, "Cyano Bridged Bimetallic Compounds of the Type M2+-NC-Fe3+ (M= Co, Ni, Cu, Zn, Cd) Using the [Fe (CN) 6] 3-Building Block and their Antibacterial Evaluation," Orbital: The Electronic Journal of Chemistry, vol. 5, no. 4, pp. 257-263, 2014.

[30] W. Chen, Y. Li, Y. Cui, X. Zhang, H. L. Zhu, Q. Zeng, "Synthesis, molecular docking and biological evaluation of Schiff base transition metal complexes as potential urease inhibitors," European Journal of Medicinal Chemistry, vol. 45, pp. 4473–4478, 2010.

[31] Y. Cui, X. Dong, Y. Li, Z. Li, W. Chen, "Synthesis, structures and urease inhibition studies of Schiff base metal complexes derived from 3,5-dibromosalicylaldehyde," Eur. J. Med. Chem., vol. 58, pp. 323–331, 2012.

[32] Z. You, H. Yu, Z. Li, W. Zhai, Y. Jiang, A. Li, S. Guo, K. Li, C. Lv, C. Zhang, "Inhibition studies of Jack bean urease with hydrazones and their copper(II) complexes," Inorganica Chimica. Acta., vol. 480, pp. 120–126, 2018.

[33] J. Matysiak, A. Skrzypek, M. Karpińska, K. Czarnecka, P. Szymański, M. Bajda, A. Niewiadomy, "Biological evaluation, molecular docking, and sar studies of novel 2-(2,4-dihydroxyphenyl)-1h- benzimidazole analogues," Biomolecules, vol. 9, pp. 1–17, 2019.

SAKARYA ÜNİVERSİTESİ
FEN BİLİMLERİ ENSTİTÜSÜ DERGİSİ

Sakarya University Journal of Science
SAUJS

ISSN 1301-4048 | e-ISSN 2147-835X | Period Bimonthly | Founded: 1997 | Publisher Sakarya University | http://www.saujs.sakarya.edu.tr/

Title: Potential Use of Lactobacillus gasseri G10 Isolated from Human Vagina along with Intrauterine Devices (IUD) to Prevent Pathogen Colonization

Authors: Büşra AKTAŞ

Recieved: 2022-03-30 00:00:00

Accepted: 2022-06-20 00:00:00

Article Type: Research Article

Volume: 26
Issue: 4
Month: August
Year: 2022
Pages: 776-788

How to cite
Büşra AKTAŞ; (2022), Potential Use of Lactobacillus gasseri G10 Isolated from Human Vagina along with Intrauterine Devices (IUD) to Prevent Pathogen Colonization. Sakarya University Journal of Science, 26(4), 776-788, DOI: 10.16984/saufenbilder.1095584
Access link
http://www.saujs.sakarya.edu.tr/en/pub/issue/72361/1095584

Sakarya University Journal of Science 26(4), 776-788, 2022

Potential Use of *Lactobacillus gasseri* G10 Isolated from Human Vagina along with Intrauterine Devices (IUD) to Prevent Pathogen Colonization

Büşra AKTAŞ *[1]

Abstract

Intrauterine devices (IUDs), well effective long-term contraception methods used around the world, are potential reservoir for pathogens and carry risk of reproductive-tract infections such as bacterial vaginosis and vulvovaginal candidiasis. A healthy vagina is dominated by *Lactobacillus* involved in protecting reproductive system against pathogens. This study aims to investigate the impact of *L. gasseri* G10 (G10), a vaginal isolate, and its Exopolysaccharide (EPS) on adherence of *Staphylococcus aureus* and *Candida albicans* to IUD-tail. Three conditions were simulated to examine if G10 with/without EPS is capable of displacing, excluding, and competing pathogen adhesion to IUD. Inhibitory impact of EPS at various concentrations on pathogen adherence was also evaluated with co-incubation. G10 blocked by co-incubation (97%) and displacement (46%) of S. aureus adherence to IUD tail and displaced *C. albicans* attached to IUD with about 99%. Compared with *S. aureus*, the biofilm formation by *C. albicans* was highly susceptible to EPS. All concentrations of EPS inhibited the adherence of *C. albicans* (81-97%); however, no significant reductions were observed in *S. aureus* adherence. Moreover, G10 and EPS together reduced the adherence of both *S. aureus* (>99%) and *C. albicans* (94-98%) through all three mechanisms. This study indicates that G10 and its EPS have the ability to inhibit adhesion of *S. aureus* and *C. albicans* to IUD and potential use in intravaginal products to prevent/manage IUD associated infections in women. The results suggest development of a new way of applying IUD along with probiotic agents alone or as synbiont.

Keywords: *Lactobacillus gasseri*, intrauterine devices (IUD), *Staphylococcus aureus*, *Candida albicans*, vaginal probiotics

1. INTRODUCTION

The intrauterine device (IUD) is one of the long term reversible contraception methods, which found to have the lowest failure rate of among other contraception methods which is less than 1% [1]. IUD has been used commonly around the world especially in less developed regions and easy to access in most of the countries [2, 3]. Copper-releasing IUDs with T-shaped frame is one of the frequently used IUD choice for women which last more than 10 years [4]. Since it is a long term contraception method, IUD use has

* Corresponding author: baktas@mehmetakif.edu.tr
[1] Mehmet Akif Ersoy University
ORCID: https://orcid.org/0000-0001-9863-683X

raised concern for decades as a potential risk for infections in reproductive and urinary system [5], [6].

During IUD use, IUD has been colonized by anaerobic and aerobic bacteria and change the genital tract microbiota, which then may increase the prevalence of genital tract infection [7–9]. 9% of the bacterial species that human body hosts are associated with the urogenital tract [10]. A disruption in the well-balanced relationship between the genital microbiota and the host immune system maintaining homeostasis in healthy urogenital system can lead to health problems in genital tract such as persistent infection and cervical cancer [11]. Microbiota studies on women with IUD have been shown that IUD is associated with bacterial vaginosis and cervical infection [8, 12, 13]. Additionally, inflammatory infiltrates including leukocytes counting in cervical samples collected from women using copper IUD and control group of women not using contraception was found to be significantly more frequent in women with IUD compared to the control [12].

Bacterial vaginosis is a common dysbiosis in vagina of women at reproductive age [14]. It is characterized by replacement of lactobacilli with opportunistic bacteria and has found to be associated with adverse health problem including sexually transmitted diseases, preterm delivery, intrauterine infection and pelvic inflammatory disease. No matter when the genital tract infection occurs, either before IUD insertion or after the insertion, IUD is a potential reservoir for pathogen microorganisms including *Escherichia coli*, *Candida* spp., *Staphylococcus aureus* and *Pseudomonas aeruginosa*, which then could lead to antibiotic resistance and persistent infections in IUD users [8, 15–18]. Although toxic shock syndrome has been rarely seen due to IUD use, a few cases has been reported [19–21].

Vaginal dysbiosis may also lead to yeast infection such as vulvovaginal candidiasis which is considered the most common cause of vaginitis after bacterial vaginosis [22–24] . Most of the cases are originated by *Candida albicans* strains [22, 25]. IUD use as contraception method also has found to be associated with vulvovaginal candidiasis due to biofilm production by candida species [22, 26–30]. It has been reported that the presence of a foreign object such as cervical sutures or IUD seems to be the most crucial risk factor for the congenital systemic candidiasis and early preterm birth [31]. Studies reported that *C. albicans* are capable of adhering strongly to the different parts of IUD including copper head and the tail, which attached the most, and produce biofilm on IUD [26, 29, 32].

A healthy genital tract is usually dominated by *Lactobacillus* which one of the main genera commonly used as probiotics [33]. *Lactobacillus* lower the risk of infection and improve vaginal health. One of the species primarily found in the vaginal microbiota is *L. gasseri*, which are several health benefits attributed to its cells and cell fractions including protecting respiratory and reproductive system against pathogens and improving immune system [33–35]. In a double-blind, randomized, placebo-controlled study, 100 of women with bacterial vaginosis were received a vaginal cream containing clindamycin followed by a vaginal capsule containing 2 lactobacilli strains from *L. gasseri* and *L. rhamnosus* at $10^{8\text{-}9}$ CFU/capsules for 10 days during 3 menstrual cycles [36]. Probiotic treatment showed a 65% cure rate compared to the control with 46% and women treated with lactobacilli remained free of bacterial vaginosis at the end of the 6-month follow up. In a study including twenty women with candida vulvovaginitis, a probiotic gel with 3 selected lactobacilli strains was applied for 10 days [25]. Around 45% of the women with acute candida vulvovaginitis were treated successfully and they suggested that this lactobacilli mix can be used as an antimycotics adjuvant or as a preventive agent in patients with recurrent vulvovaginal candidosis. Parolin et al. explored the functionality of vaginal lactobacilli strains isolated from healthy premenopausal women against different *Candida* spp. adhered to HeLa cells [37]. The results of exclusion, competition, and displacement assays showed that *L. gasseri* strains were the most effective ones in reducing pathogen adhesion to the HeLa cells. In another study, vaginal lactobacilli have found to inhibit the attachment of *S. aureus*, which is an urogenital pathogen, to the vaginal epithelium cells [38].

Moreover, *S. aureus* infection and adherence to surgical implants have been inhibited by *L. fermentum* RC-14 in a rat model [39].

Previously our research group screened *L. gasseri* strains isolated from a healthy human vagina, and their EPSs for their impact on cervical cancer cell growth and immune response in addition to their adhesion capability to the HeLa cells [11]. *L. gasseri* G10 was the most adhesive strain and found to inhibit the cell proliferation of HeLa cells with the impact of EPS. In this study, we explored the potential use of *L. gasseri G10* and its EPS either alone or together as synbiont along with IUD and examined its inhibitory effect on both *S. aureus* and *C. albicans* with competition, exclusion, and displacement assays.

2. MATERIALS AND METHODS

2.1. Microbial strains and culture conditions

Previously described *L. gasseri* G10 (G10) isolated from a healthy human vagina was used in this study [40, 41]. Stock cultures were maintained at -30°C in de Man, Rogosa and Sharpe (MRS) broth (Merck, Germany), with 10% (v/v) glycerol. Working cultures were prepared from frozen stocks by 2 sequential transfers in MRS broth and incubations were carried out at 37°C for 24 h and 18 h, respectively. The culture was harvested by centrifugation at 3006 x g for 15 min at room temperature. The pellet was re-suspended in 0.9% NaCl (w/v) and the optical density at 600 nm (OD600) was determined. A volume of washed cells (based upon the OD600) sufficient to yield a 25 mL-cell suspension was harvested by centrifugation at 3006 x g for 15 min and washed with 0.9% NaCl. The resulting pellet was suspended in 25 mL of brain-heart infusion (BHI) (Neogen, UK) to obtain a final concentration of ~10^8 CFU/mL. Similarly, stock cultures of pathogen strains including *C. albicans* 10231 and *S. aureus* ATCC 6538, were maintained at -30°C in Malt Extract (Merck, Germany) and Tryptic Soy Broth (Merck, Germany), respectively, with 10% (v/v) glycerol. Working cultures were prepared from frozen stocks by 2 sequential transfers in broth medium and incubations were conducted at 37°C for 24 h and 18 h, respectively. The culture at early stationary phase was harvested by centrifugation at 3006 x g for 15 min at room temperature. The pellet was re-suspended in 0.9% NaCl (w/v) and the optical density at OD600 for *C. albicans* and at OD595 for *S. aureus* were determined. The pellets were washed twice with 0.9% NaCl and finally resuspended in BHI at a concentration of ~10^6 CFU/mL. The final culture solution of G10, *S. aureus* and *C. albicans* was enumerated on MRS, Mannitol Salt, and Malt extract agar, respectively, to confirm the concentration.

2.2. Isolation and lyophilization of exopolysaccharide

The method of Frengova et al. was followed to isolate G10 EPS [42]. The growth culture was heated at 100°C for 15 min. After cooling, the cell suspension was treated with 17% (v/v) of 85% trichloracetic acid solution and centrifuged at 16000 x g for 20 min to remove cells and proteins. The exopolysaccharide was precipitated using one volume of cold absolute ethanol followed by centrifugation at 16000 x g for 15 min. The exopolysaccharide was precipitated using 2 volume of cold absolute ethanol followed by centrifugation at 16000 x g for 15 min. The resulting pellet containing EPS was suspended in deionized water. The EPS isolated was lyophilized in Christ Alpha 2–4 freeze dryer (Marin Christ Co. FL, USA). The freeze-dried EPS powder was stored at 4°C.

2.3. Inhibition of *Staphylococcus aureus* and *Candida albicans* adherence to IUD tails by *Lactobacillus gasseri* G10

Tail of a commercially available IUD (T380A) was aseptically cut into 1 cm-pieces to use in adherence assays. Three different procedure was used to evaluate the ability of G10 to inhibit the adherence of *S. aureus* and *C. albicans* to IUD tail including exclusion, competition, and displacement assays. In the competition or co-incubation assay, G10 was added simultaneously with the pathogens to each well of a sterile 24-well plates (SPL life Science, Korea) containing 1 cm-piece of IUD tail and incubated in BHI at 37°C for 24h. In the displacement assay, *S. aureus* or *C. albicans* was initially incubated for 24 h at

37°C in BHI with 1 cm IUD tail sample. Then, non-adherent cells were removed from the tail by gently washing with 0.9% NaCl (w/v) 2 times. Precoated tails with pathogens were immediately inoculated with G10 and incubated at 37°C for another 24h. In the exclusion assay, G10 was initially incubated for 24 h at 37°C in BHI with 1 cm IUD tail sample. Then, non-adherent cells were removed from the tail by gently washing with 0.9% NaCl (w/v) 2 times. Precoated tails with G10 were immediately inoculated with *S. aureus* or *C. albicans* and incubated at 37°C for another 24h. The inhibitory activity of G10 was evaluated by enumerating the viable cells adhered on the IUD tail. After the plates were incubated at 37°C for 24 h, the samples were placed into a sterile 24-well plate and gently washed with 0.9% NaCl (w/v) 2 times to remove loosely adherent bacterial cells. The samples were then placed in 1 mL of 0.9% NaCl (w/v) and vortexed vigorously for 2 min to remove bacteria adhered to the IUD tail surface. Vortexed solution was enumerated by plate count on the MRS, Mannitol Salt, or Malt extract agar. Cultures of *S. aureus* and *C. albicans* incubated with the tail alone were used as control. Each enumeration was performed in triplicate and the assay experiments were carried out in 4 replicates.

2.4. Inhibition of *Staphylococcus aureus* and *Candida albicans* adherence to IUD tails by lactobacilli EPS or live cells + EPS

EPS isolated from G10 was dissolved in BHI and filter sterilized (0.2 μm). Inhibitory impact of EPS of G10 on *S. aureus* and *C. albicans* was evaluated with co-incubation assays. EPSs at various concentration (500, 750, and 1000 μg/mL) were added simultaneously with *S. aureus* and *C. albicans* to each well of a sterile 12-well plates containing 1 cm-piece of IUD tail and incubated at 37°C for 24h. Additionally, synbiotic effect of EPS at 750 μg/mL and live G10 cells was evaluated with exclusion, competition, and displacement assays as described above.

2.5. Statistical analysis

Statistical differences of the bacterial adhesion were assessed with the Each Pair Student's Test using JMP version 12 (SAS Institute Inc., Cary, NC) and were presented as the mean ± SEM. Statistical difference was determined at a P value of 0.05 or less.

3. RESULTS

3.1. *Lactobacillus gasseri* G10 mediated inhibition of *Staphylococcus aureus* and *Candida albicans adherence* to IUD tails

IUD acts as a microbial reservoir and induces microbial infection and biofilm formed by these microorganisms, it, therefore, has been thought to be one of the main reason of persistent infection in IUD users [17]. *S. aureus* and *C. albicans* are among the predominant pathogens found to be associated with IUD [15–17, 26, 43]. Since the tail of IUD serves as a bridge between external environment and vagina, we investigated the impact of *L. gasseri* G10 isolated from a healthy woman vagina, on adherence of *S. aureus* and *C. albicans* to IUD tail. The ability of *L. gasseri* G10 to inhibit *S. aureus* and *C. albicans* adhered to IUD was evaluated with exclusion, competition, and displacement assays by enumerating the number of bacteria on the tail surface. As shown in Fig. 1, the vaginal lactobacilli G10 was able to prevent the adherence of *S. aureus* and *C. albicans* at different extents via competing or displacing. G10 cells had no statistically significant inhibitory effect on any of the pathogen strains studied via exclusion. *S. aureus* is one of the organisms predominantly associated with biofilms formed on IUDs especially during long term use [15, 17, 18]. There was a significant reduction ($P<0.05$) in *S. aureus* cells adhered to IUD with the exposure of lactobacilli strain. G10 blocked by co-incubation and displacement 9% and 46% of *S. aureus* adherence to IUD tail, respectively. The greatest inhibition of *S. aureus* adhesion was produced when *S. aureus* was added together with G10 (competition). On the contrary, there was no significant reduction in the adhesion of *S. aureus* with G10 under the condition of exclusion. After bacterial vaginosis, vulvovaginal candidiasis is one of the most common microbial vaginitis and *C. albicans* is the most common cause [24]. *C. albicans* also have found to be associated with IUD infection [32]. The impact of vaginal lactobacilli G10 on *C. albicans* adherence

to IUD tail was evaluated and the results showed that G10 displaced the candida attached to IUD significantly ($P<0.05$) with more than 2 logs, corresponding to about 99% inhibition [44].

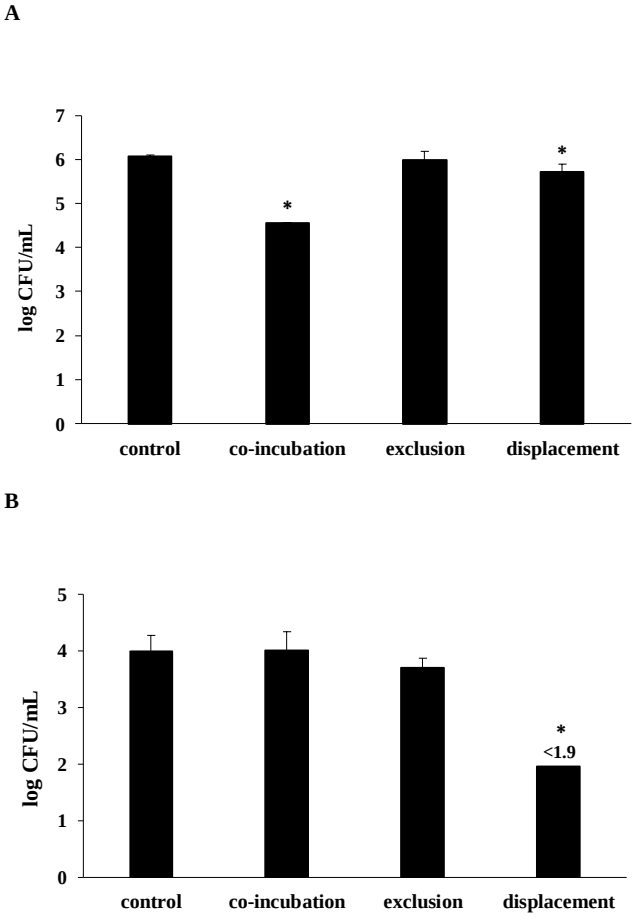

Figure 1 Inhibitory abilities of *Lactobacillus gasseri* G10 against *Staphylococcus aureus* 6538 (A) and *Candida albicans* 10231 (B). Log reduction in pathogenic cells adhered to IUD tail was calculated after competition, exclusion, and displacement with *L. gasseri* G10 and compared with *S. aureus* 6538 or *C. albicans* 10231 adherence alone. **P<0.05*: significant differences from the control

3.2. Lactobacilli EPS mediated inhibition of *Staphylococcus aureus* and *Candida albicans* adherence to IUD tails

Not only live cells but also polysaccharides produced by lactobacilli have found to be capable of inhibiting both biofilm production and growth of pathogens [45]. Moreover, combining live cells with polysaccharides as prebiotics may increase the probiotic effect [46]. To investigate the contribution of EPS on inhibition of urogenital pathogens, we co-incubated the pathogens together with the EPSs produced by G10 at various concentrations (500, 750, and 1000 µg/mL) and enumerated the number of bacteria on the tail surface. Additionally, we performed exclusion, competition, and displacement assays with the EPS at 750 µg/mL together with the live cells of G10 to evaluate the synbiotic effect on adherence. The results showed that G10 EPSs at all concentrations tested inhibited the adherence of *C. albicans* on IUD significantly ($P<0.05$) as seen in Fig. 2; however, no significant reductions were observed in the number of staphylococcal cells when co-incubated with G10 EPS (data not shown). Compared with *S. aureus*, the biofilm formation by *C. albicans* was highly susceptible to G10 EPS. Reduction of candida adherence by G10 EPS was significantly high with 97, 95, and 81% at the concentration of 500, 750, and 1000 µg/mL, respectively.

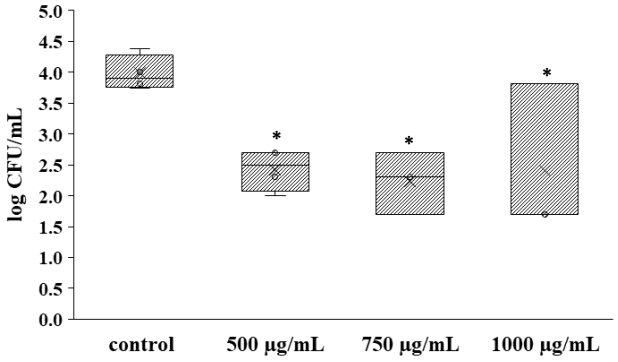

Figure 2 Inhibitory abilities of EPS isolated from *Lactobacillus gasseri* G10 against *Candida albicans* 10231. Log reduction in pathogenic cells adhered to IUD tail was calculated after co-incubation with EPSs at varying concentration which are 500 µg/mL, 750 µg/mL, and 1000 µg/mL and compared with *C. albicans 10231* adherence alone. **P< 0.05*: significant differences from the control

Moreover, a large reduction in adherence of both *S. aureus* and *C. albicans* through all 3

mechanisms were observed when G10 was added together with its EPS. The synbiotic impact of G10 and EPS on the adherence of *S. aureus* and *C. albicans* inhibition are shown in Fig. 3. G10 and EPS together caused about 3-log reduction and significantly (P<0.05) reduced the adhesion of *S. aureus* with more than 99% (Fig. 3). Co-incubation with G10 and EPS resulted in a 2-log reduction in the number of adhered *C. albicans* CFU (P<0.05). This was followed by about a log reduction in adherence with exclusion and displacement (Fig. 3). G10 and EPS together have a synbiotic inhibitory impact on candida adherence to IUD with 98, 90 and 94% reduction through co-incubation, exclusion, and displacement, respectively.

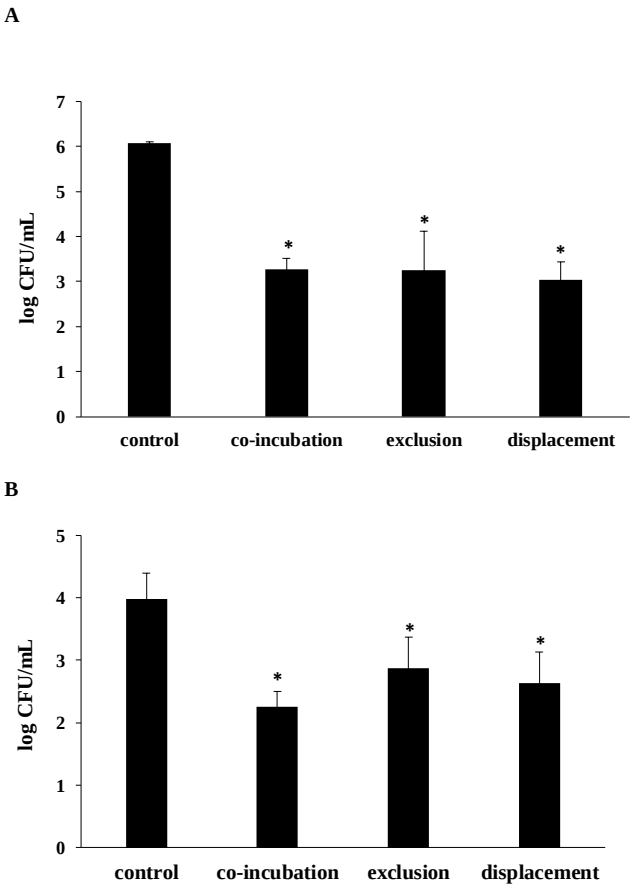

Figure 3. Synbiotic inhibitory effect of *Lactobacillus gasseri* G10 with EPS against *Staphylococcus aureus* 6538 (A) and *Candida albicans* 10231 (B). Log reduction in pathogenic cells adhered to IUD tail was calculated after competition, exclusion, and displacement with *L. gasseri* G10 together with EPS and compared with *S. aureus* 6538 or *C. albicans 10231* adherence alone. **P<0.05*: significant differences from the control

4. DISCUSSION

Various bacterial genera have been detected in vaginal microbiota and a healthy vaginal microbiota is dominated by *Lactobacillus* spp. including *L. crispatus*, *L. gasseri*, and *L. iners* [47]. Studies showed that replacement of *Lactobacillus* spp. in the vaginal microbiota with potential pathogens such as *Staphylococcus* spp., has been associated with vaginal dysbiosis resulting bacterial vaginosis and vaginitis [48]. The vaginal mucosa is populated by both bacteria and fungi, which normally exist together in a balance. When this balance breaks, the ecological state of vaginal microbiota may turn into a pathological state. Another common infection caused by vaginal dysbiosis is *Candida* spp. associated infections. Vulvovaginal candidiasis, a symptomatic vaginitis, affect around 75% of reproductive age women at least once in their lifespan [49].

Studies showed that *Lactobacillus* spp. have an antimicrobial impact on growth of *S. aureus*, which may cause toxic shock syndrome by colonizing and producing biofilm on intravaginal products, and *C. albicans* in addition to preventing their attachment to vaginal epithelium [21, 38, 50]. Ten different lactobacilli strains have been evaluated for development of vaginal tablets used to treat vaginal infections as replacement for antibiotics [51]. One of the best lactobacilli strains they chose for the preparation of vaginal tablets was belonging to *L. gasseri* which adhered to epithelial cells better and displaced the vaginal pathogens. In another study on biosurfactant produced by *L. brevis*, they showed that lactobacilli biosurfactant has the ability to slow down the adhesion of *C. albicans* to silicone surfaces and reported that lactobacilli metabolites are promising as antiadhesive coating products to prevent medical device associated fungal infection [52].

The presence of IUDs supplies a solid surface for microbial attachment and an ideal environment to grow and form biofilm. Although vaginal lactobacilli strains have been studied commonly for their probiotic effect, their application on intravaginal products are limited such as ability to adhere to the vaginal products and impact on

vaginal pathogens colonized on intravaginal devices [33–35]. Here we showed that a vaginal isolate *L. gasseri* G10 studied previously for their probiotic potential is capable of inhibiting adherence of vaginal pathogens including *S. aureus* and *C. albicans* on IUD and have a potential for alternative application with devices used in reproductive system. In an old study, IUDs in 2-year use were removed from 6 women with signs for neither uterine nor cervical infection to detect bacterial colonization and they revealed that microbial biofilms exist on prosthetic devices consisting of indigenous microorganisms with no symptom of an infection [53]. Moreover, they tested the attachment of *L. acidophilus*, *L. casei,* and *L. fermentum* strains to IUD and urinary catheters within 24h. They found that lactobacilli strains adhered to the surface of prosthetic devices in a strain-dependent manner and pointed out the clinical importance of lactobacilli having potential to prevent onset of infection. Similarly, in another study, the impact of *Lactobacillus* strains on the adhesion of *S. aureus* and *C. albicans* on urinary catheter were examined [54]. They showed that co-presence of lactobacilli significantly reduced the *S. aureus* adhesion and *C. albicans* adhesion was significantly reduced in presence of *S. aureus* and suggested that lactobacilli could be used as displacement agent in urinary catheters. Anti-biofilm effect of lactobacilli strains on *S. aureus* have been shown in different studies [55]. *L. brevis* strains recovered from milk tanks were tested for their inhibitory effect on biofilm formation by pathogenic microorganisms recovered from the milk tanks including the *S. aureus* on stainless steel surfaces [56]. They reported 5 *L. brevis* strains restricted the *S. aureus* adhesion on abiotic surfaces and suggested to use as natural barrier in the food processing sector.

Vaginal isolate G10 was able to displace the attached *S. aureus* on IUD tail and decreased the adherence with 46%. Moreover, the reduction in *S. aureus* adherence was 97% when they co-incubate together. The results suggest that the presence of G10 cells could not only inhibit the initial adherence of *S. aureus* but also suppress the development of a mature biofilm.

It has been reported that IUD use increases the risk of vulvovaginal candidiasis since candida species are capable of adhering to medical devices and promote reoccurrence over time [22], [23]. Candida cells have been shown to adhere strongly to the different parts of IUD including the tail [29]. Although different parts of the IUD promote yeast to stay in the genital tract, the tail is the part where *C. albicans* and non-albicans species adhered the most, indicating the tail is the key area for pathogen colonization [32]. Alternative strategies have been tried to prevent biofilm formation by *Candida* spp. on IUDs. Shanmughapriy et al. suggested a combination therapy of tyrosol with amphotericin to inhibit candida biofilm along with IUD use and pointed to need of a future work on such biomaterials to improve IUD devices [57]. While the combined inhibitory effect of tyrosol and amphotericin was 90%, individual inhibition was around 50%. Vaginal lactobacilli G10 showed a significant reduction in the *C. albicans* adherence with 99% by displacing the previously attached pathogen.

Studies showed that not only the live lactobacilli cells but also cell free supernatant or a specific metabolite could have inhibitory effect on growth of pathogens or biofilm production on a surface [37, 45, 55]. In another study, cell-free supernatant of *L. acidophilus* and *L. casei* strains have shown to inhibit the growth of *S. aureus* and remove the biofilm produced by *S. aureus* on polystyrene and glass surfaces in a species and concentration dependent manner [55]. EPS is one of the bacterial metabolites helping lactic acid bacteria to have a good adherence capability to host epithelial cells and to exhibit antimicrobial activity on pathogens [45, 58, 59]. Released EPSs produced by *L. acidophilus* strain have found to hamper biofilm production by a wide range of Gr (+) and Gr (-) pathogens [45].

Here in this study, although EPS from vaginal *L. gasseri* G10 alone had no inhibitory effect on *S. aureus* cell attachment to IUD, there was 97% reduction in *C. albicans* adherence to IUD when they were co-incubated with EPS. However, inhibitory impact on vaginal pathogens was much higher when EPS and live cells applied together. While synbiotic inhibitory effect of G10 with its

EPS on candida adherence to IUD ranged from 94% to 98%, G10 and EPS together reduced the *S. aureus* adherence with more than 99% showing that G10 has a high inhibitory impact on pathogen adherence to IUD with its EPS together. Combination of probiotics and prebiotics is called synbiotics and studies showed that synbiotics may confer better health benefit compared to the application of a probiotic alone and increase the adhesion capability of probiotics [46].

A few different mechanisms have been described for construction of multicellular clusters. Studies suggest that cells normally clusters mature and organize larger microcolonies to form biofilms; however, in the presence of a bacterial metabolites as antimicrobial agent, these organized microcolonies are reduced due to modified cell surface and decreased cell to cell surface interactions [45]. Cell surface hydrophobicity is one of the factors involving in cell adhesion and affecting the autoaggregation, coaggregation, and biofilm formation ability of a strain [60]. Previously, G10 was shown to have a high autoaggregation ability and coaggregates with *C. albicans* strongly, indicating to have a lower hydrophobic surface [40, 41]. Additionally, Kim et al. investigated the inhibitory impact of released EPS from *L. acidophilus* on biofilm formation by *E. coli* and performed a transcriptomic analysis [45]. Interestingly, they found that lactobacilli EPS decreased the expression of curli production genes involved in the attachment and biofilm formation of *E. coli* strains and chemotaxis gene. They suggest that EPS has the ability to control biofilm formation via regulation of biofilm associated virulence factors in pathogens. Quorum-sensing molecules are also involved in regulation of the biofilm production and metabolites produced by probiotics such as EPSs are able to diminish the quorum signals produced by pathogens that are essential for biofilm formation [45], [46].

5. CONCLUSION

IUD is one of the effective long-term contraception method commonly used around the world, serving as reservoir for pathogens and carries risk of reproductive tract infections such as bacterial vaginosis and vulvovaginal candidiasis. Probiotic lactobacilli strains have been studied commonly for their probiotic impact; however, their ability to adhere and compete with vaginal pathogens and their application on intravaginal products are limited, although bacterial adhesion to abiotic materials such as suture and prostheses have been the study objects for many researchers. Alternative way of probiotic delivery through female hygiene or intravaginal products have been getting attention recently. In view of potential application of the vaginal isolate *Lactobacillus* strain as vaginal probiotics, we explored the potential use in intravaginal products such as IUD to prevent or manage IUD associated urogenital tract infections in women. The results showed that both G10 and its EPS either alone or together as synbiont have a clear inhibitory effect on urogenital pathogen adherence to IUD and have a potential for alternative use with devices for reproductive system.

Acknowledgments

The bacterial strains were kindly provided by Prof. Belma Aslim (Biotechnology Lab, Department of Biology, Gazi University).

Funding

The author has no received any financial support for the research, authorship or publication of this study.

The Declaration of Conflict of Interest/ Common Interest

No conflict of interest or common interest has been declared by the authors.

Authors' Contribution

The author contributed100% to the manuscript.

The Declaration of Ethics Committee Approval

This study does not require ethics committee permission or any special permission.

The Declaration of Research and Publication Ethics

The authors of the paper declare that they comply with the scientific, ethical and quotation rules of SAUJS in all processes of the paper and that they do not make any falsification on the data collected. In addition, they declare that Sakarya University Journal of Science and its editorial board have no responsibility for any ethical violations that may be encountered, and that this study has not been evaluated in any academic publication environment other than Sakarya University Journal of Science.

REFERENCES

[1] A. Sundaram, B. Vaughan, K. Kost, A. Bankole, L. Finer, S. Singh, J. Trussell, "Contraceptive Failure in the United States: Estimates from the 2006-2010 National Survey of Family Growth" Perspectives on sexual and reproductive health, vol. 49, no. 1, pp. 7–16, 2017.

[2] M. L. Kavanaugh, J. Jerman, "Contraceptive method use in the United States: trends and characteristics between 2008, 2012 and 2014" Contraception, vol. 97, no. 1, pp. 14–21, 2018.

[3] K. J. Buhling, N. B. Zite, P. Lotke, and K. Black, "Worldwide use of intrauterine contraception: A review" Contraception, vol. 89, no. 3, pp. 162–173, 2014.

[4] A. N. Aksoy, G. T. Sarikas, E. G. Gozgec, "The effect of copper intrauterine device use duration on uterine and ovarian blood flow parameters: A prospective cross-sectional study" Journal of Clinical Ultrasound, vol. 49, no. 2, pp. 124–128, 2021.

[5] K. Peebles, F. M. Kiweewa, T. Palanee-Phillips, C. Chappell, D. Singh, K. E. Bunge, L. Naidoo, B. Makanani, N. Jeenarain, D. Reynolds, S. L. Hillier, E. R. Brown, J. M. Baeten, J. E. Balkus, "Elevated Risk of Bacterial Vaginosis Among Users of the Copper Intrauterine Device: A Prospective Longitudinal Cohort Study" C linical Infectious Diseases, vol. 73, no. 3, pp. 513–520, 2021.

[6] S. Caddy, M. H.Yudin, J. Hakim, D. M. Money, "Best Practices to Minimize Risk of Infection With Intrauterine Device Insertion" Journal of Obstetrics and Gynaecology Canada, vol. 36, no. 3, pp. 258–265, 2014.

[7] A. D. Saidu, K. A. Tunau, A. A. Panti, E. I. Nwobodo, Y. Mohammed, J. Amin, J. Garba, "Effect of hormonal and copper IUDs on genital microbial colonisation and clinical outcomes in North-Western Nigeria" International Journal of Reproduction, Contraception, Obstetrics and Gynecology, vol. 6, no. 6, pp. 2143–2147, 2017.

[8] S. Abd, A.-K. Al-Kattan, D. T. Burhan, S. T. Burhan, "Biofilm Formation on Intrauterine Device and Associated Infections" Iraqi Postgraduate Medical Journal, vol. 12, no. 4, pp. 562–567, 2013.

[9] S. L. Achilles, M. N. Austin, L. A. Meyn, F. Mhlanga, Z. M. Chirenje, S. L. Hillier, "Impact of contraceptive initiation on vaginal microbiota" American Journal of Obstetrics & Gynecology, vol. 218, no. 6, pp. 622.e1-622.e10, 2018.

[10] The NIH HMP Working Group, "The NIH Human Microbiome Project" Genome Research, vol. 19, pp. 2317–2323, 2009.

[11] T. Sungur, B. Aslim, C. Karaaslan, B. Aktas, "Impact of Exopolysaccharides (EPSs) of Lactobacillus gasseri strains isolated from human vagina on cervical tumor cells (HeLa)" Anaerob*e*, vol. 47, pp. 137–144, 2017.

[12] J. Eleuterio, P. C. Giraldo, A. K. Silveira Gonçalves, R. M. Nunes Eleuterio, "Liquid-based cervical cytology and microbiological analyses in women using cooper intrauterine device and levonorgestrel-releasing intrauterine system" European Journal of Obstetrics & Gynecology and Reproductive Biology, vol. 255, pp. 20–24, 2020.

[13] T. Madden, J. M. Grentzer, G. M. Secura,

J. E. Allsworth, and J. F. Peipert, "Risk of Bacterial Vaginosis in Users of the Intrauterine Device: A Longitudinal Study" Sexually Transmitted Diseases, vol. 39, no. 3, pp. 217–222, 2012.

[14] J. Ravel, I. Moreno, C. Simón, "Bacterial vaginosis and its association with infertility, endometritis, and pelvic inflammatory disease" American Journal of Obstetrics & Gynecology, vol. 224, no. 3, pp. 251–257, 2021.

[15] A. E.-S. Abdou, E. A. E. A. Mohamad, A. M. Tawfiek, "Bacterial Infections and Biofilm Formation Associated with Intra Uterine Contraceptive Device among Females Attending Al-Glaa Teaching Hospital in Cairo" Egyptian Journal of Hospital Medicine, vol. 70, no. 5, pp. 882–890, 2018.

[16] A. A. Elsharkawy, R. S. Abdel-latif, M. A. Kamel, "Biofilm Forming Bacteria Isolated from Intrauterine Devices and Their Susceptibility to Antibiotics" Egyptian Journal of Medical Microbiology, vol. 26, no. 3, pp. 145–152, 2017.

[17] V. Pruthi, A. Al-Janabi, B. M. J. Pereira, "Characterization of biofilm formed on intrauterine devices" Indian Journal of Medical Microbiology, vol. 21, no. 3, pp. 161–165, 2003.

[18] Z. Pa´l, E. Urba´n, E. Do´sa, A. Pa´l, E. Nagy, "Biofilm formation on intrauterine devices in relation to duration of use" Journal of Medical Microbiology, vol. 54, pp. 1199–1203, 2005.

[19] E. E. Cho D. Fernando, "Fatal streptococcal toxic shock syndrome from an intrauterine device" Journal of Emergency Medicine, vol. 44, pp. 777–780, 2013.

[20] M. Gottlieb, B. Long, A. Koyfman, "The Evaluation and Management of Toxic Shock Syndrome in the Emergency Department: A Review of the Literature" Journal of Emergency Medicine, vol. 54, no. 6, pp. 807–814, 2018.

[21] C. D. Klug, C. R. Keay, and A. A. Ginde, "Fatal Toxic Shock Syndrome From an Intrauterine Device" Annals of Emergency Medicine, vol. 54, no. 5, pp. 701–703, 2009.

[22] E. A. Omran, N. E. S. Youssef, A. H. Abdelfattah, S. A. Esmail, and A. M. Fouad, "Copper IUD increases virulence of non-albicans Candida species isolated from women with vulvovaginal candidiasis" European Journal of Contraception & Reproductive Health Care, vol. 25, no. 2, pp. 120–125, 2020.

[23] J. de Cássia Orlandi Sardi, D. R. Silva, P. C. Anibal, J. J. C. M. de Campos Baldin, S. R. Ramalho, P. L. Rosalen, M. L. R. Macedo, J. F. Hofling, "Vulvovaginal Candidiasis: Epidemiology and Risk Factors, Pathogenesis, Resistance, and New Therapeutic Options" Current Fungal Infection Reports, vol. 15, no. 1, pp. 32–40, 2021.

[24] B. Gonçalves, C. Ferreira, C. T. Alves, M. Henriques, J. Azeredo, and S. Silva, "Vulvovaginal candidiasis: Epidemiology, microbiology and risk factors" Critical Reviews in Microbiology, vol. 42, no. 6, pp. 905–927, 2016.

[25] G. Donders, G. Bellen, E. Oerlemans, I. Claes, K. Ruban, T. Henkens, F. Kiekens, S. Lebeer "The use of 3 selected lactobacillary strains in vaginal probiotic gel for the treatment of acute Candida vaginitis: a proof-of-concept study" European Journal of Clinical Microbiology & Infectious Diseases, vol. 39, no. 8, pp. 1551–1558, 2020.

[26] K. M. Zahran, M. N. Agban, S. H. Ahmed, E. A. Hassan, and M. A. Sabet, "Patterns of candida biofilm on intrauterine devices" Journal of Medical Microbiology, vol. 64, no. 4, pp. 375–381, 2015.

[27] M. E. Auler, D. Morreira, F. F. O. Rodrigues, M. S. Abr Ão, P. F. R. Margarido, F. E. Matsumoto, E. G. Silva, B. C. M. Silva, R. P. Schneider, C. R. Paula "Biofilm formation on intrauterine devices in patients with recurrent vulvovaginal

candidiasis Biofilm formation on IUDs in patients with vulvovaginal candidiasis" Medical Mycology, vol. 48, no. 1, pp. 211–216, 2010.

[28] P. Lal, V. Agarwal, P. Pruthi, B. M. J. Pereira, M. R. K. Vikas, "Biofilm formation by Candida albicans isolated from intrauterine devices" Indian journal of microbiology, vol. 48, no. 4 , pp. 438–444, 2008.

[29] F. Chassot, M. F. N. Negri, A. E. Svidzinski, L. Donatti, R. M. Peralta, T. I. E. Svidzinski, M. E. L.Consolaro "Can intrauterine contraceptive devices be a Candida albicans reservoir?" Contraception, vol. 77, no. 5, pp. 355–359, 2008.

[30] B. Pippi, G. da R. M. Machado, V. Z. Bergamo, R. J. Alves, S. F. Andrade, and A. M. Fuentefria, "Clioquinol is a promising preventive morphological switching compound in the treatment of Candida infections linked to the use of intrauterine devices" Journal of Medical Microbiology, vol. 67, no. 11, pp. 1655–1663, 2018.

[31] T. A. Georgescu, A.-C. Lisievici, O. Munteanu, F. L. Furtunescu, O. G. Bratu, C. Berceanu, R. E. Bohîlţea "Congenital systemic candidiasis: A comprehensive literature review and meta-analysis of 44 cases" Romanian Journal of Morphology and Embryology, vol. 61, no. 3, pp. 673–680, 2020.

[32] L. C. F. Paiva, L. Donatti, E. V. Patussi, T. I. E. Svizdinski, M. E. Lopes-Consolaro, "Scanning electron and confocal scanning laser microscopy imaging of the ultrastructure and viability of vaginal Candida albicans and non-albicans species adhered to an intrauterine contraceptive device" Microscopy and Microanalysis, vol. 16, no. 5, pp. 537–549, 2010.

[33] M. I. Petrova, "Lactobacillus species as biomarkers and agents that can promote various aspects of vaginal health" Frontiers in Physiology, vol. 6, p. 81, 2015.

[34] L. Stoeker, S. Nordone, S. Gunderson, L. Zhang, A. Kajikawa, A. LaVoy, M. Miller, T. R. Klaenhammer, G. A. Dean "Assessment of Lactobacillus gasseri as a candidate oral vaccine vector" Clinical and Vaccine Immunology, vol. 18, no. 11, pp. 1834–1844, Sep. 2011.

[35] E. Motevaseli, M. Shirzad, S. M. Akrami, A. S. Mousavi, A. Mirsalehian, M. H. Modarressi, "Normal and Tumour cervical cells respond differently to vaginal lactobacilli, independent of pH and lactate" Journal of Medical Microbiology, vol. 62, pp. 1065–1072, 2013.

[36] P.-G. Larsson, B. Stray-Pedersen, K. R. Ryttig, S. Larsen, "Human lactobacilli as supplementation of clindamycin to patients with bacterial vaginosis reduce the recurrence rate; a 6-month, double-blind, randomized, placebo-controlled study" BMC Womens. Health, vol. 8, p. 3, 2008.

[37] C. Parolin, A. Marangoni, L. Laghi, C. Foschi, R. A. Ñ. Palomino, N. Calonghi, R. Cevenini, B. Vitali "Isolation of Vaginal Lactobacilli and Characterization of Anti-Candida Activity" PLoS One, vol. 10, no. 6, p. e0131220, 2015.

[38] G. Zárate M. E. Nader-Macias, "Influence of probiotic vaginal lactobacilli on in vitro adhesion of urogenital pathogens to vaginal epithelial cells" Letters in Applied Microbiology, vol. 43, no. 2, pp. 174–180, 2006.

[39] B. S. Gan, J. Kim, G. Reid, P. Cadieux, J. C. Howard, "Lactobacillus fermentum RC-14 Inhibits Staphylococcus aureus Infection of Surgical Implants in Rats" Journal of Infectious Diseases, vol. 185, no. 9, pp. 1369–1372, 2002.

[40] H. Ekmekci, B. Aslim, D. O. Darilmaz, "Some factors affecting the autoaggregation ability of vaginal lactobacilli isolated from Turkish women" Archives of Biological Sciences, vol. 61, no. 3, pp. 407–412, 2009.

[41] H. Ekmekçi, B. Aslim, and D. Önal Darilmaz, "Factors affecting the

coaggregation ability of vaginal lactobacilli with Candida spp" Annals of Microbiology, vol. 59, no. 1, pp. 163–167, 2009.

[42] G. I. Frengova, E. D. Simova, D. M. Beshkova, Z. I. Simov, "Production and monomer composition of exopolysaccharides by yogurt starter cultures" Canadian Journal of Microbiology, vol. 46, no. 12, pp. 1123–1127, 2000.

[43] G. Tsanadis, S. N. Kalantaridou, A. Kaponis, E. Paraskevaidis, K. Zikopoulos, E. Gesouli, N. Dalkalitsis, I. Korkontzelos, E. Mouzakioti, D. E. Lolis "Bacteriological cultures of removed intrauterine devices and pelvic inflammatory disease" Contraception, vol. 65, pp. 339–342, 2002.

[44] K. K. Foarde, D. W. Vanosdell, R. S. Steiber, "Investigation of gas-phase ozone as a potential biocide" Applied Occupational and Environmental Hygiene, vol. 12, no. 8, p. 535, 1997.

[45] Y. Kim, S. Oh, S. H. Kim, "Released exopolysaccharide (r-EPS) produced from probiotic bacteria reduce biofilm formation of enterohemorrhagic Escherichia coli O157:H7" Biochemical and Biophysical Research Communications, vol. 379, no. 2, pp. 324–329, 2009.

[46] S. Bikric, B. Aslim, İ. Dincer, Z. Yuksekdag, S. Ulusoy, S. Yavuz, "Characterization of Exopolysaccharides (EPSs) Obtained from Ligilactobacillus salivarius Strains and Investigation at the Prebiotic Potential as an Alternative to Plant Prebiotics at Poultry" Probiotics and Antimicrobial Proteins, vol. 14, no. 1, pp. 49–59, 2022.

[47] M. Aldunate, D. Srbinovski, A. C. Hearps, C. F. Latham, P. A. Ramsland, R. Gugasyan, R.A. Cone, G. Tachedjian "Antimicrobial and immune modulatory effects of lactic acid and short chain fatty acids produced by vaginal microbiota associated with eubiosis and bacterial vaginosis" Frontiers in Physiology, vol. 6, p. 164, 2015.

[48] S. Borges, J. Silva, P. Teixeira, "The role of lactobacilli and probiotics in maintaining vaginal health" Archives of Gynecology and Obstetrics, vol. 289, pp. 479–489, 2014.

[49] X. Zhou, T. Li, S. Fan, Y. Zhu, X. Liu, X. Guo, Y. Liang "The efficacy and safety of clotrimazole vaginal tablet vs. oral fluconazole in treating severe vulvovaginal candidiasis" Mycoses, vol. 59, no. 7, pp. 419–428, 2016.

[50] M. Chiaruzzi, A. Barbry, A. Muggeo, A. Tristan, Is. Jacquemond, C. Badiou, L. Cluzeau, S. Bourdeau, T. Durand, A. Engelmann, D. Bosquet, M. Bes, C. Prigent-Combaret, J. Thioulouse, D. Muller, G. Lina "Vaginal Tampon Colonization by Staphylococcus aureus in Healthy Women Myriam" Applied and Environmental Microbiology, vol. 86, no. 18, pp. 1–9, 2020.

[51] P. Mastromarino, P. Brigidi, S. Macchia, L. Maggi, F. Pirovano, V. Trinchieri, U "Characterization and selection of vaginal Lactobacillus strains for the preparation of vaginal tablets" Journal of Applied Microbiology, vol. 93, no. 5, pp. 884–893, 2002.

[52] C. Ceresa, F. Tessarolo, I. Caola, G. Nollo, M. Cavallo, M. Rinaldi, L. Fracchia "Inhibition of Candida albicans adhesion on medical-grade silicone by a Lactobacillus-derived biosurfactant" Journal of Applied Microbiology, vol. 118, no. 5, pp. 1116–1125, 2015.

[53] G. Reid, L.-A. Hawthorn, R. Mandatorifl, R. L. Cook, H. S. Beg, "Adhesion of Lactobacilli to Polymer Surfaces In Vivo and In Vitro" Microbial Ecology, vol. 16, pp. 241–251, 1988.

[54] G. Reid C. Tieszer, "Use of lactobacilli to reduce the adhesion of Staphylococcus aureus to catheters" International Biodeterioration & Biodegradation, vol. 34, no. 1, pp. 73–83, 1994.

[55] M. Koohestani, M. Moradi, H. Tajik, A. Badali, "Effects of cell-free supernatant of

Lactobacillus acidophilus LA5 and Lactobacillus casei 431 against planktonic form and biofilm of Staphylococcus aureus" Veterinary Research Forum, vol. 9, no. 4, pp. 301–306, 2018.

[56] F. Ait Ouali, I. Al Kassaa, B. Cudennec, M. Abdallah, F. Bendali, D. Sadoun, N.-E. Chihib, D. Drider "Identification of lactobacilli with inhibitory effect on biofilm formation by pathogenic bacteria on stainless steel surfaces" International Journal of Food Microbiology, 191, pp. 116–124, 2014.

[57] S. Shanmughapriya, H. Sornakumari, A. Lency, S. Kavitha, K. Natarajaseenivasan, "Synergistic effect of amphotericin B and tyrosol on biofilm formed by Candida krusei and Candida tropicalis from intrauterine device users" Med. Mycol., vol. 52, no. 8, pp. 853–861, 2014.

[58] G. Donnarumma, A. Molinaro, D. Cimini, C. De Castro, V. Valli, V. De Gregorio, M. De Rosa, C. Schiraldi "Lactobacillus crispatus L1: high cell density cultivation and exopolysaccharide structure characterization to highlight potentially beneficial effects against vaginal pathogens" BMC Microbiology, vol. 14, no. 1, p. 137, 2014.

[59] D. Ren, C. Li Y. Qin, R. Yin, S. Du, F. Ye, C. Liu, H. Liu, M. Wang, Y. Li, Y. Sun, X. Li, M. Tian, N. Jin "Invitro evaluation of the probiotic and functional potential of Lactobacillus strains isolated from fermented food and human intestine" Anaerobe, vol. 30, pp. 1–10, 2014.

[60] J. Woo J. Ahn, "Probiotic-mediated competition, exclusion and displacement in biofilm formation by food-borne pathogens" Letters in Applied Microbiology, vol. 56, no. 4, pp. 307–313, 2013.

SAKARYA ÜNİVERSİTESİ
FEN BİLİMLERİ ENSTİTÜSÜ DERGİSİ

Sakarya University Journal of Science
SAUJS

ISSN 1301-4048 | e-ISSN 2147-835X | Period Bimonthly | Founded: 1997 | Publisher Sakarya University | http://www.saujs.sakarya.edu.tr/

Title: Preparation and Characterization of Intrinsically Fluorescent Polyphosphazene Microspheres

Authors: Simge METİNOĞLU ÖRÜM

Recieved: 2022-01-28 00:00:00

Accepted: 2022-06-21 00:00:00

Article Type: Research Article

Volume: 26
Issue: 4
Month: August
Year: 2022
Pages: 789-798

How to cite
Simge METİNOĞLU ÖRÜM; (2022), Preparation and Characterization of Intrinsically Fluorescent Polyphosphazene Microspheres . Sakarya University Journal of Science, 26(4), 789-798, DOI: 10.16984/saufenbilder.1064432
Access link
http://www.saujs.sakarya.edu.tr/en/pub/issue/72361/1064432

Sakarya University Journal of Science 26(4), 789-798, 2022

Preparation and Characterization of Intrinsically Fluorescent Polyphosphazene Microspheres

Simge METİNOĞLU ÖRÜM *[1]

Abstract

The novel polyphosphazene and cyclomatrix type microspheres were synthesized via a one-pot self-assembly polycondensation method. Octachlorocyclotetraphosphazene and two fluorescent compounds; fluorescein and curcumin were used as a crosslinker and monomers, respectively. The prepared microspheres were characterized by SEM, EDX, FTIR, XRD, UV-vis techniques. Also, the fluorescence properties of the microspheres were investigated. The microspheres exhibited fluorescence emissions both in ethanol and as solid-state when excited at 470 nm. The optimum pH was determined as 9.0 for fluorescence measurements. Owing to fluorescent properties of the microspheres, the delivery of curcumin from the prepared microspheres, and cell imaging can be investigated in the future. It is thought that the obtained intrinsically fluorescent polyphosphazene microspheres have the potential for use as sensors and labels, also.

Keywords: Polyphosphazene, fluorescence, fluorescein, curcumin, microsphere

1. INTRODUCTION

Polyphosphazenes are inorganic-organic hybrid polymers that include alternating –P=N– groups [1]. Cyclomatrix type polyphosphazenes are highly crosslinked materials that can be facilely prepared via a one-pot polycondensation and self-assembly process. A cross-linker phosphazene compound (hexachlorocyclotriphosphazene; HCCP or octachlorocyclotetraphosphazene; OCCP) and monomer including two or more donor atoms are used in their synthesis [2]. Owing to the substitution of organic side groups for phosphorous atoms of phosphazene rings, phosphazene compounds have been gain various features such as catalysts [3], flame retardants [4], adsorbents [5], protic ionic liquids (PILs) [6], organic light-emitting diodes [7], fluorescent chemosensors [8], bioactive agents (such as antituberculosis [9], anticancer [10], DNA cleavage and antimicrobial agents [11]), biomaterials [12]. Additionally, due to being biodegradable and biocompatible, they are used for tissue engineering [13], drug delivery [14] and controlled drug release [15] applications.

* Corresponding author: simge.metinoglu@gmail.com
[1] Burdur Mehmet Akif Ersoy University
ORCID: https://orcid.org/0000-0003-4166-4973

In recent years, apart from these applications of the polyphosphazenes, their fluorescence properties and applications have been attracted attention. Especially, in the past decade, intrinsically fluorescent cyclomatrix and highly cross-linked polyphosphazene nano/microspheres were synthesized containing amine [16, 17] or hydroxyl [18-20] derivative monomers. Their fluorescent applications such as sensor to detection of metal ions (Fe^{3+}, Hg^{2+}) [17, 21], picric acid [22], nitroaromatic explosives [16], dopamine [23]; cell or tumor imaging [24, 25] and drug delivery [26] were investigated.

Fluorescein is the most popular organic fluorescent dye. It is generally used as a fluorescent sensor or label. But, it can not be used with all solvents and its photobleaching property is not good [27]. Also, its leakage from the host is still a serious problem when encapsulated in nanomaterials [28]. On the other hand, curcumin is a natural anticancer drug and biologically active compound besides, it is also a fluorescent molecule. It can be used for confocal imaging [29], cell tracking [30], and sensing [31].

The aims of this study are to obtain cross-linked polyphosphazene microspheres that are novel, highly cross-linked, intrinsically fluorescent, and containing an anticancer drug. For this purpose, novel cyclomatrix polyphosphazene microspheres were prepared by self-assembly polycondensation using fluorescein, curcumin, and OCCP as monomers and crosslinker. Fluorescein was used to gain fluorescence properties to the microspheres. Curcumin was chosen both as an anticancer drug and as a fluorescent compound. The microspheres were obtained just in 4 hours using an ultrasonic bath. The microspheres gained fluorescent features by means of monomers. It was determined that they exhibited fluorescence emissions both as ethanolic dispersion and as solid-state. The optimum pH was determined as 9.0. It is thought that the delivery of curcumin from the synthesized microspheres, and monitoring fluorescently can be investigated in the future. In addition, the prepared novel and intrinsically fluorescent polyphosphazene microspheres will open a gate for preparing new fluorescent polymers and they have great potential for sensor applications.

2. EXPERIMENTAL

2.1. Materials and Methods

Octachlorocyclotetraphosphazene (OCCP) was used after recrystallization using n-heptane. Curcumin, fluorescein, triethylamine (TEA), acetone and ethanol were purchased from Sigma-Aldrich.

Scanning Electron Microscopy (SEM) images and Energy-Dispersive X-ray analysis (EDX) of prepared microspheres were recorded by ZEISS geminiSEM 500 electron microscope at an accelerating voltage of 3 kV. Perkin Elmer FTIR Spectrometer Spotlight 400 Imaging System was used for Fourier Transform Infrared Spectroscopy (FTIR) measurements of the microspheres, OCCP, curcumin and fluorescein. X-ray diffraction (XRD) pattern was recorded by using a Bruker AXS, D8 Advance instrument equipped with Cu Kα radiation at 40 kV and 40 mA. The UV–vis spectra of curcumin, fluorescein and microspheres were measured by the PG Instruments T60 Model UV–vis spectrophotometer. The fluorescence experiments were performed by the LS-55 Fluorescence Spectrometers.

2.2. Synthesis of the Microspheres

Fluorescein (0.072 g; 0.216 mmol), curcumin (0.080 g; 0.216 mmol) and OCCP (0.100g; 0.216 mmol) were dissolved in 50 mL acetone in a round bottom flask using ultrasonic irradiation (53 kHz, 150 W). After 15 minutes, TEA (3mL) was added to the reaction. The colour of the reaction medium changed to red from orange. The reaction was finished 4 hours later. The precipitated yellow product was separated by centrifugation at 4500 rpm, for 10 min and washed with acetone, distilled water and ethanol, respectively. Finally, the obtained polyphosphazene microspheres were dried under vacuum at 45 °C.

3. RESULTS AND DISCUSSIONS

3.1. Preparation of the Microspheres

The synthesized reaction and crosslinked structure of the prepared microspheres are illustrated in Figure 1. The fluorescent compounds; fluorescein and curcumin were reacted with phosphazene; OCCP to obtain intrinsically fluorescent polyphosphazene microspheres via a one-pot self-assembly polycondensation. In the synthesis procedure, TEA was used as a catalyst and an acid acceptor which absorb HCl and form TEA.HCl salt during the reaction [32]. In the formation mechanism of the microspheres, hydroxyl groups of fluorescein and curcumin react with phosphorous atoms of OCCP rings. In this way, the crosslinked oligomeric species are formed. Then, the oligomers aggregate together and primary nucleus particles are obtained. The stable particles generate via aggregation of the primary nucleus particles by hydrogen bonds. The stable particles grow by absorbing oligomers and highly crosslinked, solid, inorganic-organic hybrid, and contained hydroxyl groups on their surfaces polyphosphazene spheres are obtained [33].

3.2. Characterization

The characterization of the microspheres was performed by SEM, EDX, XRD, FTIR, and UV-vis techniques. SEM images of the synthesized polyphosphazene particles are seen in Figure 2. It was determined that the particles were spherical and micro-sized. In Figure 3, EDX results show that the microspheres have fluorescein and curcumin in their structures due to including 60 % C, 19.48 % O. Phosphorus and nitrogen atoms belonging to OCCP rings were determined as 7.94 % and 10.25 %, respectively. Also, the microspheres contain just 2.32 % unreacted Cl atoms owing to steric hindrance. Thus, it was seen that the microspheres were highly crosslinked.

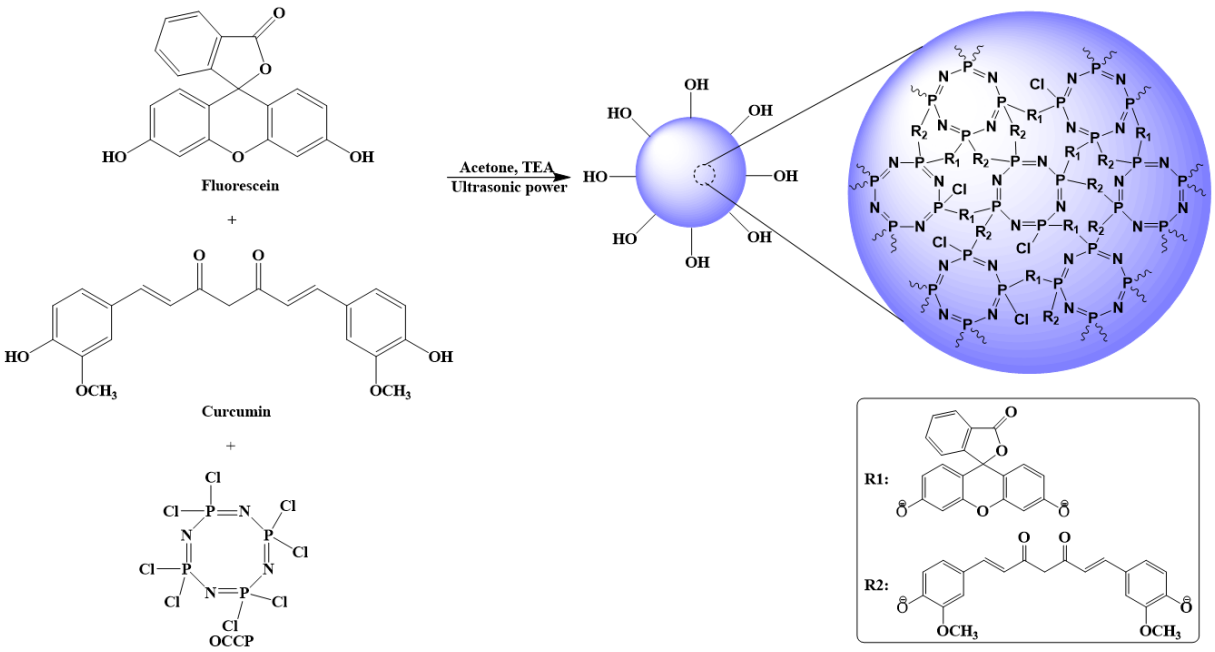

Figure 1The synthesis reaction and crosslinked structure of the polyphosphazene microspheres

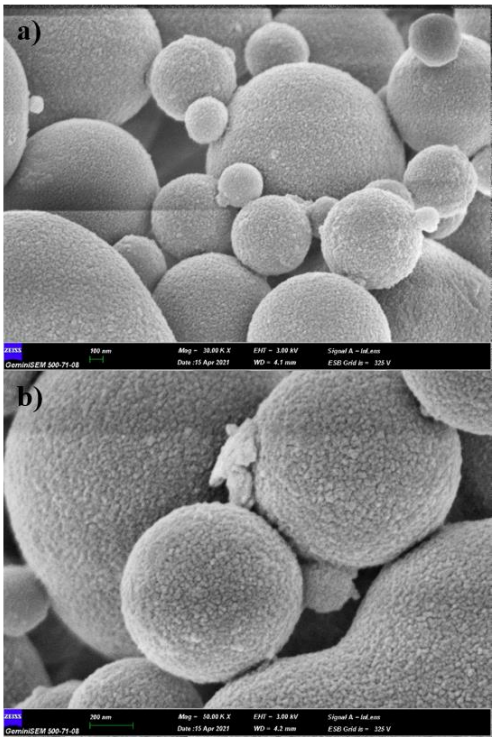

Figure 2 SEM images of synthesized polyphosphazene microspheres at different magnifications a) 30.00 KX, b) 50.00 KX.

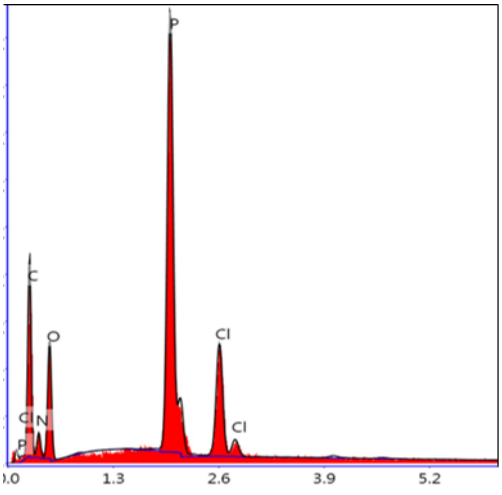

Element	Weight %	Atomic %
C K	47.91	60
N K	9.55	10.25
O K	20.72	19.48
P K	16.34	7.94
ClK	5.48	2.32

Figure 3 EDX results of the microspheres

XRD pattern of the microspheres is illustrated in Figure 4. The wide diffraction peak at about 24 θ showed that the microspheres were amorphous. The peaks of the fluorescein, curcumin and TEA.HCl salt were not seen in the XRD pattern. Hence, it is seen that the microspheres were purified from monomers and salt [34].

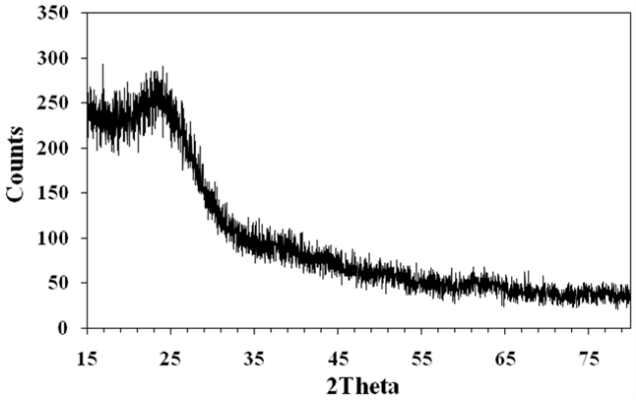

Figure 4 XRD pattern of the microspheres

The FTIR spectra of the curcumin, fluorescein OCCP and the obtained microspheres were recorded to explain the bonding of monomers with OCCP (Figure 5). The peak at 1766 cm^{-1} (a) indicates the carbonyl group arising from the lactone ring based on fluorescein. It is understood that the microspheres have fluorescein moieties. The absorbance at 1600 cm^{-1} (b) is attributed to the C=C bond. It is seen that the absorbances at 1498 cm^{-1} (c) and 1155 cm^{-1} (f) which corresponded to C=O and C-O (O-CH_3) bonds of curcumin, respectively, demonstrated including curcumin of the microspheres. The peaks at 1239 cm^{-1} (d) and 1213 cm^{-1} (e) belong to the P=N group of the OCCP ring in the crosslinked structure of the microspheres. The most important absorbance at 970 cm^{-1} (g) is attributed to P-O-Ar shows that bonded of curcumin and fluorescein to OCCP rings. Also, the peak at 494 cm^{-1} (h) corresponds to the P-Cl bond demonstrating that the microspheres have a few amounts of unreacted chloride atoms owing to steric hindrance. It is understood from the FTIR results that the bonding and polycondensation between OCCP, curcumin and fluorescein were accomplished successfully.

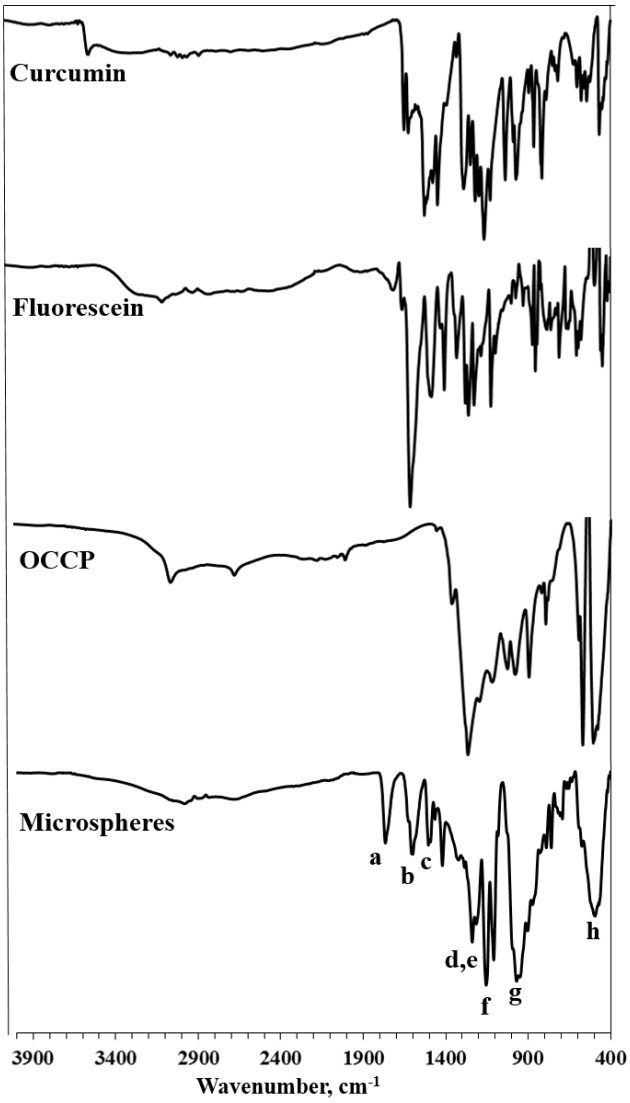

Figure 5 FTIR spectra of curcumin, fluorescein, OCCP and the microspheres

In Figure 6, UV-vis spectra of the microspheres, fluorescein and curcumin in ethanol are seen. It was determined that fluorescein, curcumin and the microspheres demonstrated absorbance peaks at 457, 485; 425; 458 nm, respectively. Due to the highly crosslinked structure, the microspheres show a wide absorbance spectrum.

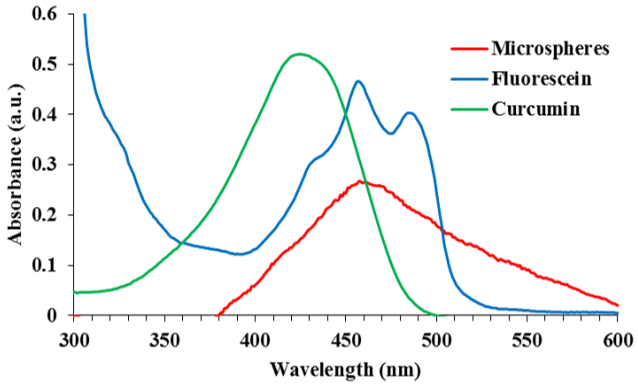

Figure 6 Uv-vis spectra of the microspheres (1.0 mg/mL), fluorescein and curcumin

3.3. Fluorescence Studies

The fluorescence emissions of the microspheres, fluorescein and curcumin were compared in ethanol and solid-state, in Figure 7. As can be seen in Figure 7a, the microspheres, fluorescein and curcumin exhibited fluorescence emissions at 528, 515 and 525 nm, in ethanol, when excited at 470 nm light, respectively. It was thought that the fluorescence emission peak of the microspheres is red-shifted due to the bonding of curcumin and fluorescein changing the energy gap for the electron transition of curcumin and fluorescein in the microspheres [24].

The microspheres exhibited wide fluorescence emission at 536 nm as solid when excited at 470 nm, in Figure 7b. The fluorescein and curcumin showed very weak fluorescence emissions at 619 and 562 nm, respectively, due to aggregation-induced quenching when compared with the microspheres.

The OCCP rings are nonconjugated systems for electron transfer without any resonance between alternating P−N and P=N bonds. Thus, they are photochemically inert and act as spacers to isolate fluorescein and curcumin in the microspheres [26]. So, the electron and energy transfer between the fluorescein and curcumin were blocked effectively in microspheres. Hence, the microspheres exhibited fluorescence emissions-reducing fluorescence quenching in both ethanol and solid states.

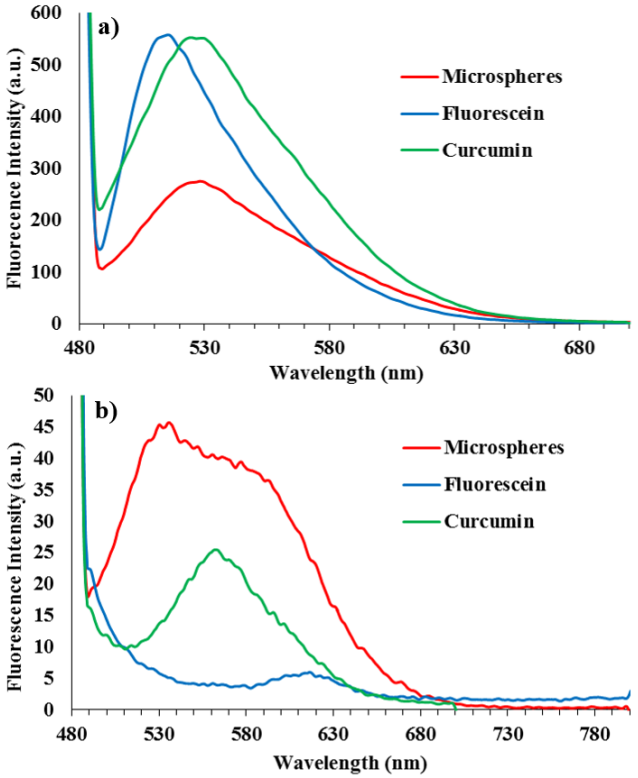

Figure 7 a) Fluorescence emission spectra of synthesized microspheres (1.0 mg/mL), fluorescein and curcumin in ethanol and b) solid state

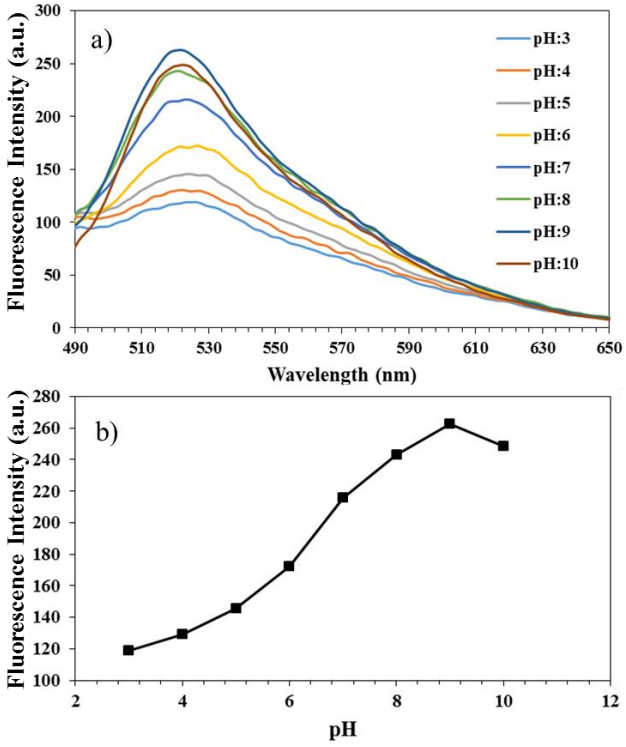

Figure 8 a)The pH dependent fluorescence spectra of the microspheres in different pH (1.0 mg/mL). b) the graph of fluorescence intensity versus pH

The fluorescence emissions of aqueous dispersions of the microspheres dependent on pH were investigated between pH 3-10, in Figure 8a and 8b. The hydroxyl groups of the curcumin and fluorescein, and nitrogen atoms of the OCCP in the microspheres have lone-pair-electrons. The hydroxyl groups and nitrogen atoms can transfer electrons to curcumin and fluorescein in a basic medium. So, the microspheres exhibited higher fluorescence emissions at the basic medium and showed a maximum emission peak at pH: 9.0. But, in an acidic medium, owing to the protonation of hydroxyl groups and nitrogen atoms, the electron transfer is eliminated and weakened fluorescence emissions are observed [17].

Fluorescein as an organic fluorescent dye can leak from the host when encapsulated in nanomaterials. In this study, this problem was eliminated due to the bonding of fluorescein covalently to phosphorus atoms of OCCP rings by a nucleophilic substitution reaction.

The prepared microspheres have hydroxyl groups on their surfaces due to fluorescein and curcumin compounds. In previous reports, hydroxyl derivated crosslinked polyphosphazene nano/microspheres such as including oxyresveratrol [18], phloroglucinol [19], 4,4′-sulfonyldiphenol [20] were synthesized and fluorescence properties were investigated. In addition, the applications of the prepared polyphosphazene nano/microspheres using the monomers containing lone-pair electrons arising from amine or hydroxyl groups, such as fluorescence sensors to detect Fe^{3+}, Hg^{2+} metal ions [17, 21], nitroaromatic explosives [16] and dopamine [23] were investigated.

By taking into consideration above studies, when the prepared microspheres interacted with metal ions, chemical or biological compounds, the fluorescence intensity of the microspheres can be quenched or increased by compounds. Hence, it is thougth that the obtained polyphosphazene

microspheres have great potential for sensor applications due to having hydroxyl groups.

In the literature, curcumin was reacted with hexachlorocyclotriphosphazene (HCCP) and researched usage as a fluorescent sensor for the detection of picric acid [22]. Besides, the hollow polyphosphazene nanospheres were synthesized using fluorescein and HCCP. The cell imaging and drug delivery properties of the synthesized fluorescent nanospheres were investigated [26]. In this study, OCCP was used as a crosslinker instead of HCCP. Curcumin and fluorescein were reacted together with OCCP to synthesize microspheres. In this way, the microspheres both gained fluorescent properties and contained curcumin as an anticancer drug. Thus, the curcumin delivery from the synthesized microspheres and cell imaging owing to fluorescence property of the microspheres can be investigated as a further study.

3. CONCLUSIONS

In summary, the one-pot synthesis of the novel polyphosphazene microspheres was performed via polycondensation polymerization. The microspheres were obtained facilely with bonding between OCCP and fluorescent compounds; fluorescein and curcumin in an ultrasonic bath, for just 4 hours. They were characterized by SEM, EDX, FTIR, XRD, and UV-vis techniques. The microspheres gained fluorescence property through fluorescein and curcumin bonding to phosphorous atoms of the OCCP rings. The microspheres exhibited fluorescence emissions in both ethanol and as solid-state. The optimum pH was determined as 9.0. The prepared highly crosslinked and fluorescent polyphosphazene microspheres have the potential to be used as sensors to detect metals, and biological or chemical compounds, and also to deliver curcumin, and to image cells due to the fluorescence properties.

Funding

The author has no received any financial support for the research, authorship or publication of this study.

The Declaration of Conflict of Interest/ Common Interest

No conflict of interest or common interest has been declared by the author.

REFERENCES

[1] S. Rothemund, I. Teasdale, “Preparation of polyphosphazenes: a tutorial review”, Chemical Society Reviews, vol. 45, pp. 5200-5215, 2016.

[2] C. Wan, X. Huang, “Cyclomatrix polyphosphazenes frameworks (Cyclo-POPs) and the related nanomaterials: synthesis, assembly and functionalization”, Materials Today Communications, vol. 11 pp. 38–60, 2017.

[3] J. Fu, S, Wang, J. Zhu, K. Wang, M. Gao, X. Wang, Q. Xu, "Au-Ag bimetallic nanoparticles decorated multi-amino cyclophosphazene hybrid microspheres as enhanced activity catalysts for the reduction of 4-nitrophenol", Materials Chemistry and Physics, vol. 207, pp. 315-324, 2018.

[4] Y. Sui, H. Sima, W. Shao, C. Zhang, "Novel bioderived cross-linked polyphosphazene microspheres decorated with FeCo-layered double hydroxide as an all-in-one intumescent flame retardant for epoxy resin", Composites Part B, vol. 229, pp. 109463, 2022.

[5] W. Wei, R. Lu, H. Xie, Y. Zhang, X. Bai, L. Gu, R. Da, X. Liu, "Selective adsorption and separation of dyes from an aqueous solution on organic–inorganic hybrid cyclomatrix polyphosphazene submicro-spheres", Journal of Materials Chemistry A, vol. 3, pp. 4314, 2015.

[6] G. Elmas, A. Okumuş, Z. Kılıç, P. Özbeden, L. Açık, B. Ç. Tunalı, M. Türk, N. A. Çerçi, T. Hökelek, "Phosphorus-nitrogen compounds. Part 48. Syntheses of the phosphazenium salts containing 2-pyridyl pendant arm: Structural characterizations, thermal analysis, antimicrobial and cytotoxic activity studies", Indian Journal of Chemistry -Section A, vol. 59A, pp.533-550, 2020.

[7] S. P. Mucur, B. Canımkurbey, P. Kavak, H. Akbaş, A. Karadağ, "Charge carrier performance of phosphazene-based ionic liquids doped hole transport layer in organic light-emitting diodes", Applied Physics A, vol. 126 (12), pp. 923, 2020.

[8] S. O. Tümay, "A novel selective "turn-on" fluorescent chemosensor based on thiophene appended cyclotriphosphazene schiff base for detection of Ag+ ions", ChemistrySelect, vol. 6(39), pp. 10561-10572, 2021.

[9] A. Okumuş, G. Elmas, Z. Kılıç, A. Binici, N. Ramazanoğlu, L. Açık, B. Çoşut, T. Hökelek, R. Güzel, B. Ç. Tunalı, M. Türk, H. Şimşek, "The comparative reactions of 2-cis-4-ansa and spiro cyclotetraphosphazenes with difunctional ligands: Structural and stereogenic properties, electrochemical, antimicrobial and cytotoxic activity studies", Applied Organometallic Chemistry, vol. 35 (4), pp. e6150, 2021.

[10] A. Binici, G. Elmas, A. Okumuş, S. Erden Tayhan, T. Hökelek, L. Açık, B. N. Şeker, Z. Kılıç, "Phosphorus-nitrogen compounds. part 58. syntheses, structural characterizations and biological activities of 4-fluorobenzyl-spiro(N/O)cyclotriphosphazene derivatives", Journal of Biomolecular Structure and Dynamics, 2021.

[11] G. Elmas, Z. Kılıç, B. Çoşut, G. Keşan, L. Açık, M. Çam, B. Ç. Tunalı, M. Türk, T. Hökelek, "Synthesis of bis(2,2,3,3-tetrafluoro-1,4-butanedialkoxy)-2-trans-6-bis(4-fluorobenzyl)spiro cyclotetraphosphazene: structural characterization, biological activity and dft studies", Journal of Chemical Crystallography, vol. 51, pp. 235-250, 2020.

[12] L. C. Xu, C. Chen, J. Zhu, M. Tang, A. Chen, H. R. Allcock, C. A. Siedlecki, "New cross-linkable poly[bis(octafluoropentoxy) phosphazene] biomaterials: synthesis, surface characterization, bacterial adhesion, and plasma coagulation responses", Journal of Biomedical Materials Research Part A, vol.108(8), pp. 3250-3260, 2020.

[13] H. R. Allcock, "The background and scope of polyphosphazenes as biomedical materials", Regenerative Engineering and Translational Medicine, vol. 7, pp. 66–75, 2021.

[14] K. S. Ogueri, K. S. Ogueri, H. R. Allcock, C.T. Laurencin,"Polyphosphazene polymers: the next generation of biomaterials for regenerative engineering and therapeutic drug delivery", Journal of Vacuum Science and Technology B, vol. 38, pp. 030801, 2020.

[15] S. Mehmood, L. Wang, H. Yu, F. Haq, S. Fahad, B. Amin, M. A. Uddin, M. Haroon, "Recent progress on the preparation of

cyclomatrix-polyphosphazene based micro/nanospheres and their application for drug release", Chemistry Select, vol. 5, pp. 5939 –5958, 2020.

[16] W. Wei, X. Huang, K. Chen, Y. Tao, X. Tang, "Fluorescent organic–inorganic hybrid polyphosphazene microspheres for the trace detection of nitroaromatic explosives", RSC Advances, vol. 2, pp. 3765–3771, 2012.

[17] K. Chen, Y. Liu, Y. Hu, M. Yuan, X. Zheng, X. Huang, "Facile synthesis of amino-functionalized polyphosphazene microspheres and their application for highly sensitive fluorescence detection of Fe^{3+}", Journal of Applied Polymer Science, vol. 137, no. 32, pp. 48937, 2020.

[18] S. Hong, J. Li, X. Huang, H.Liu, "A facile approach to generate cross-linked poly(cyclotriphosphazeneco-oxyresveratrol) nanoparticle with intrinsically fluorescence", Journal of Inorganic and Organometallic Polymers and Materials, vol. 28, pp. 2258–2263, 2018.

[19] T. Pan, X. Huang, H. Wei, W. Wei, X. Tang, "Intrinsically fluorescent microspheres with superior thermal stability and broad ultraviolet-visible absorption based on hybrid polyphosphazene material", Macromolecular Chemistry and Physics, vol. 213, pp. 1590−1595, 2012.

[20] W. Liu, X. Huang, H. Wei, X. Tang, L. Zhua, "Intrinsically fluorescent nanoparticles with excellent stability based on a highly crosslinked organic–inorganic hybrid polyphosphazene material", Chemical Communications, vol. 47, pp. 11447–11449, 2011.

[21] Y. Hu, L. Meng, Q. Lu, "Fastening porphyrin in highly cross-linked polyphosphazene hybrid nanoparticles: powerful red fluorescent probe for detecting mercury ion", Langmuir, vol. 30, pp. 4458−4464, 2014.

[22] W. Wei, R. Lu, S. Tang, X. Liu, "Highly cross-linked fluorescent poly(cyclotriphosphazene-co-curcumin) microspheres for the selective detection of picric acid in solution phase", Journal of Materials Chemistry A, vol. 3, pp. 4604-4611, 2015.

[23] D. Wang, Y. Hu, L. Meng, X. Wang, Q. Lu, "One-pot synthesis of fluorescent and cross-linked polyphosphazene nanoparticles for highly sensitive and selective detection of dopamine in body fluids", RSC Advances, vol. 5, pp. 92762, 2015.

[24] L. Meng, C. Xu, T. Liu, H. Li, Q. Lu, J. Long, "One-pot synthesis of highly cross-linked fluorescent polyphosphazene nanoparticles for cell imaging", Polymer Chemistry, vol. 6, pp. 3155, 2015.

[25] Z. Wang, M. Hu, S. Hu, J. Han, Z. Wang, Y. Chen, C. Huang, L. Fu, Z. Zhang, "Facile one-pot synthesis of multifunctional polyphosphazene nanoparticles as multifunctional platform for tumor imaging", Analytical and Bioanalytical Chemistry vol. 410, pp. 3723–3730, 2018.

[26] L. Sun, T. Liu, H. Li, L. Yang, L. Meng, Q. Lu, J. Long, "Fluorescent and cross-linked organic−inorganic hybrid nanoshells for monitoring drug delivery", ACS Applied Materials and Interfaces, vol. 7, pp. 4990−4997, 2015.

[27] K.S.B Sam, L. George, SYN, A. Varghese. "Fluorescein based fluorescence sensors for the selective sensing of various analytes", Journal of Fluorescence, vol. 31, pp. 1251 – 1276, 2021.

[28] T. Preiß, A. Zimpel, S. Wuttke, J.O. Rädler, "Kinetic analysis of the uptake and release of fluorescein by metal-organic framework nanoparticles", Materials, vol. 10, no. 2, pp. 216, 2017.

[29] A. Kumar, L. Li, A. Chaturvedi, J. Brzostowski, J. Chittigori, S. Pierce, L. A. Samuelson, D. Sandman, J. Kumar, "Two-photon fluorescence properties of curcumin as a biocompatible marker for confocal

imaging", Applied Physics Letters, vol. 100, pp. 203701, 2012.

[30] B. F. Mogharbel, J. C. Francisco, A. C. Irioda, D. S. M. Dziedzic, P. E. Ferreira, D. Souza, C. M. C. O. Souza, N. B. Neto, L. C. Guarita-Souza, C. R. C. Franco, C. V. Nakamura, V. Kaplum, L. Mazzarino, E. Lemos-Senna, R. Borsali, P. A. Soto, P. Setton-Avruj, E. Abdelwahid, K. A. T. Carvalho, "Fluorescence properties of curcumin-loaded nanoparticles for cell tracking", International Journal of Nanomedicine, vol. 13, pp. 5823–5836, 2018.

[31] M. Y. Khorasania, H. Langaric, S. B. T. Sany, M. Rezayib, A. Sahebkar, "The role of curcumin and its derivatives in sensory applications", Materials Science & Engineering C, vol. 103, pp. 109792, 2019.

[32] F. Chang, X. Huang, H, Wei, K. Chen, C. Shan, X. Tang, "Intrinsically fluorescent hollow spheres based on organic–inorganic hybrid polyphosphazene material: synthesis and application in drug release", Materials Letters, vol. 125, pp. 128–131, 2014.

[33] S. Metinoğlu Örüm, "Novel cyclomatrix polyphosphazene nanospheres: preparation, characterization and dual anticancer drug release application", Polymer Bulletin.

[34] Y. Wang, J. Mu, L. Li, L. Shi, W. Zhang, Z. Jiang, "Preparation and properties of novel fluorinated cross-linked polyphosphazene micro-nano spheres", High Performance Polymers, vol. 24, pp. 229, 2012.

SAKARYA ÜNİVERSİTESİ
FEN BİLİMLERİ ENSTİTÜSÜ DERGİSİ

Sakarya University Journal of Science
SAUJS

ISSN 1301-4048 | e-ISSN 2147-835X | Period Bimonthly | Founded: 1997 | Publisher Sakarya University | http://www.saujs.sakarya.edu.tr/

Title: Mechanical and Structural Evaluation of LiSrH3 Perovskite Hydride for Solid State Hydrogen Storage Purposes

Authors: Selgin AL, Çağatay YAMÇIÇIER

Recieved: 2022-02-14 00:00:00

Accepted: 2022-06-22 00:00:00

Article Type: Research Article

Volume: 26
Issue: 4
Month: August
Year: 2022
Pages: 799-804

How to cite
Selgin AL, Çağatay YAMÇIÇIER; (2022), Mechanical and Structural Evaluation of LiSrH3 Perovskite Hydride for Solid State Hydrogen Storage Purposes. Sakarya University Journal of Science, 26(4), 799-804, DOI: 10.16984/saufenbilder.1073242
Access link
http://www.saujs.sakarya.edu.tr/en/pub/issue/72361/1073242

Sakarya University Journal of Science 26(4), 799-804, 2022

Mechanical and Structural Evaluation of $LiSrH_3$ Perovskite Hydride for Solid State Hydrogen Storage Purposes

Selgin AL*[1], Çağatay YAMÇIÇIER[2]

Abstract

Increasing catastrophic climate events, energy needs, human population lead to look for clean, cheap and environmentally friendly energy production methods and sources. International agreements have been made to lower carbon emissions and support carbon free way of energy productions. Hydrogen technology is suggested as one excellent way of accomplishing these aims. Hydrogen is an excellent energy carrier with almost zero carbon emission and high efficiency. There are four steps to make hydrogen energy ready for usage: production, transportation, storage and converting it to electricity. Each step has its own obstacles to be overcome. Among the storage methods, solid state storage of hydrogen is very promising since it allows us to store hydrogen in high content and safely. Thus, there are intense ongoing research on this area. Therefore, this study adopts a well proved, time and cost saving method density functional theory to search and evaluate mechanical and electronic properties of $LiSrH_3$ perovskite hydride with space group $Pm\bar{3}m$ (221) for hydrogen storage purposes. Two critical parameters gravimetric hydrogen density and hydrogen desorption temperature along with elastic constants, Poisson's ratio, Shear, bulk, Young modulus are collected and discussed. The mechanical evaluation is demonstrated that $LiSrH_3$ is a mechanically stable material, however, elastic constant evaluation is showed that it is a brittle material which can be an obstacle when handling the material. The electronic band structure is also obtained which demonstrated an indirect band gap of 3.65 eV.

Keywords: Solid state, hydrogen storage, mechanical stability, elastic properties.

1. INTRODUCTION

Our daily lives require energy which depicts a rising pattern due to increasing life standards and world's population. In the current situation, this energy is produced from coal, natural gas and oil. These sources are limited and have been creating pollution which causes catastrophic climate

* Corresponding author: selgin.al@idu.edu.tr
[1] İzmir Democracy University
ORCID: https://orcid.org/0000-0003-2496-1300
[2] Osmaniye Korkut Ata University
E-mail: cagatay1050@gmail.com
ORCID: https://orcid.org/0000-0003-3033-168X

changes and disasters such as flood, drought and heat. In addition, the prices of oil, natural gas and oil are going up with the demand. All these reasons are led to search for cheap, safe, carbon free energy sources and methods to decrease climate change effects and prices. International agreements have been made such as Paris Agreement to tackle with high carbon emissions [1]. Several environmentally friendly energy production methods have been suggested and implemented for this purpose. Among them, hydrogen has taken great attention due to being abundant, cheap, and carbon free.

Currently, hydrogen has been produced from steam-methane reforming reactions, coal, natural and water electrolysis [2]. The efficiency of water electrolysis is around 70%. When the excess energy from solar or wind power is used to produce hydrogen via electrolysis, this process can be very effective. Besides production, hydrogen storage and transportation of it, is a critical step, too There are several ways to store hydrogen such as gas, liquid and solid-state storage. Among them, storing hydrogen in a solid host material seems to be much promising compared to compressed gas and liquid storage due to easy transportation, safety, high content, reversibility and high kinetics. Solid state hydrogen storage materials can be used in various applications such as fuel cells which can also be used in stationary or portable devices. These materials include hydrides, alloys and complex materials. ABH_3 materials has taken great interest owing to its perovskite structure. Thus, perovskite hydrides are studied intensely recently. The electronic and elastic behaviors of $KSrH_3$ and $RbSrH_3$ are studied using first principles calculations for hydrogen storage purposes by Raza et al. [3]. Their result suggested a mechanical and thermodynamic stability with a brittle nature for these hydrides. The electronic structures indicated semiconductor nature. The phase stabilities of several hydrides $MBeH_3$ (Li, Na, K. Rb, Cs) are investigated [4]. $LiBeH_3$ and $NaBeH_3$ are reported to be as brittle materials in another study [5]. Elastic, electronic and optical properties of $KMgH_3$ is investigated using density functional theory calculations for different phases and only perovskite structure is reported to be stable [6]. The target for storing hydrogen in solid material is determined as 4 wt. % by the US Energy Department. Materials with higher gravimetric hydrogen density than this value are great of interest such as lithium containing materials. Lithium based host materials are studied extensively since these materials are light and exist in our world in large quantities. $LiSrH_3$ is one of these host materials which is not examined before as host material and its properties are not investigated. Therefore, revealing electronic and elastic features of these hydrides are critical since it is linked to their stabilities. For example, if the host material is brittle, it will be difficult to handle it. Also, the bonding features of host material can affect the bonding of hydrogen to the host material. Thus, this study is adopted first principles calculations to investigate electronic, elastic and hydrogen storage properties of $LiSrH_3$. The stability and bonding properties of $LiSrH_3$ will be examined in great detail.

2. METHOD OF COMPUTATION

All the calculations in this study were done by using Siesta 4.0 package program [7]. First principles calculation was adopted to reveal elastic and electronic features of $LiSrH_3$. Perdew-Burke-Ernzerhof generalised gradient approximation (PBE-GGA) was taken for the exchange correlation potential [8]. A 8x8x8 k-points mash was taken to sample the Brillouin zone. The structure was formed by relaxing all the atoms with residual force smaller than 0.01 eV/Å on each atom. The electronic wave functions were expanded in plane-wave basis to set up a kinetic energy cut off to 35 Ry, while the cut off energy for the electronic charge density was set to 350 Ry. In order to obtain optimized lattice vectors and atomic positions, the stress tolerance and maximum atomic force were taken less than 0.5 GPa and smaller than $0.01 \mathrm{eV\,Å^{-1}}$, respectively.

3. RESULTS AND DISCUSSION

3.1 Elastic Properties

The comprehensive elastic moduli of $LiSrH_3$ have been tabulated in Table 1 and 2 for the first time. To obtain elastic moduli of $LiSrH_3$, the elastic constants C_{ij} need to be calculated, the calculation details have been given in [9, 10]. A material's elastic tensor defines its response to an external stress. For a cubic crystal, there are three elastic constants are defined due to the symmetry, C_{11}, C_{12}, C_{44}. The well-known Born stability condition for this kind of materials is [11]:

$$(C_{11} - C_{12}) > 0,\ C_{11} > 0,\ C_{44} > 0,\ (C_{11} + 2C_{12}) > 0 \quad (1)$$

It can be deduced as;

$$C_{12} < B < C_{11} \quad (2)$$

Based on the equations 1&2, it seen that $LiSrH_3$ meets the stability criteria, thus $LiSrH_3$ can be categorized as a mechanically stable material. C_{11} describes material's resistance to linear compression along the x-axis. By comparing elastic constants, it is noticed that C_{11} is larger than other elastic constants, suggesting a harder compressibility along the x-axis. Also, it seen that the value of C_{11} is higher than that of C_{44}. This suggests that $LiSrH_3$ will show greater resistance to unidirectional compression than shear deformation compression [12].

Cauchy pressure (C_p), Pugh's ratio (B/G), and Poisson's ratio are an indication of material's failure such as ductility/brittleness. Thus, these parameters are also computed. Cauchy pressure tells us about the nature of the materials. Ductile materials can be distorted easily whereas brittle materials can easily change their volumes. It is known that the negative Cauchy pressure implies brittle nature and the positive one implies ductile nature [13]. As Table 1 displays that Cauchy pressure of $LiSrH_3$ has a negative Cauchy pressure of -9.78 and indicates a brittle nature. This can be an obstacle when handling the material in portable applications. Another index that illustrates the nature of the material is that Pugh's ratio. Ductile materials take apart from brittle ones by the ratio of 1.75. The value higher than that indicates ductility and lower value indicates brittleness [14]. In addition to these parameters, Poisson's ratio, $\sigma \sim 0.26$ defines a border line. Lower than this line will be classified as brittle and higher values will be classified as ductile [15]. The obtained Cauchy pressure is negative, the ratio of B/G is lower than 1.75 and Poisson's ratio is around 0.26, thus it can be concluded that $LiSrH_3$ is brittle in nature. This property will not be an issue in stationary applications whereas it can create an obstacle when it is decided to be used in portable applications. Therefore, it will require a great attention when handling it.

Additionally, bonding characteristics within $LiSrH_3$ is assessed using Poisson's ratio. Generally, if the Poisson's ratio is close to 0.1, the solid shows covalent bonding characteristics, if it is close to 0.25, it displays ionic bonding properties [16]. By examining the Poisson's ratio of $LiSrH_3$, it may be anticipated that covalent bonding is dominant for $LiSrH_3$.

Table 1 The calculated lattice constants (*a, Å*), Bulk modulus (*B, GPa*), elastic constants (C_{11}, C_{12}, C_{44}, GPa) and Cauchy Pressure (C_P) of $LiSrH_3$.

Material	a	B	C_{11}	C_{12}	C_{44}	C_{12}-C_{44}
$LiSrH_3$	4.63	7.87	22.55	0.53	10.31	-9.78
Raza et al.[17]	4.58		-	-	-	-

Table 2 The calculated Bulk modulus (B), Shear modulus (G), B/G ratios, Poisson's ratios (σ) and Young's modulus (E) of $LiSrH_3$.

Material	B	G	B/G	σ	E
$LiSrH_3$	7.87	10.59	0.74	0.036	21.93

Bulk modulus, B, is utilised to assess resistance against fracture whereas shear modulus, G, is utilised to assess resistance against plastic deformation. Bulk modulus represents a degree of resistivity towards volume change which is executed by an applied pressure. This can provide substantial information about average bound strength because of having a strong correlation

with cohesive and binding energies of material`s atoms [18, 19]. Higher bulk modulus means higher resistivity against volume change [20]. Also, higher C_{44} value results in higher shear modulus [21]. Moreover, shear modulus is much related to hardness than bulk modulus. Based on the Table 2, it can be predicted that $LiSrH_3$ has a slight hardness and will show resistivity towards volume change. Young modulus, E, reflects the stiffness of materials. Higher Young modulus represents better stiffness of materials [22]. Young modulus of $LiSrH_3$ is 21.93 GPa thus it can be predicted that $LiSrH_3$ shows some stiffness.

3.2 Electronic Properties

The electronic band structure of $LiSrH_3$ along the high symmetry directions in the Brillouin zone using the generalized gradient approximation (GGA) is demonstrated in Figure 1. The Fermi energy level is set to 0 V by extracting Fermi energy value from electronic band energies and displayed as dot lines in Figure 1.

As can be noticed from Figure 1 that a gap exists between the valence and conduction band with the value of 3.65 eV. Thus, it can be concluded that $LiSrH_3$ is a non-metallic material.

In order to assess the electronic features of $LiSrH_3$, total and partial density of states (DOS) is plotted in Figure 2. From total and partial densities of the states, it is noticed that the main contribution to valence band comes from H-1s states.

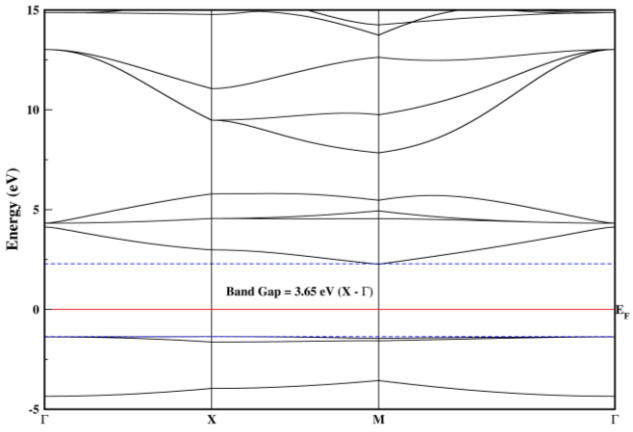

Figure 1 Electronic band structure of $LiSrH_3$.

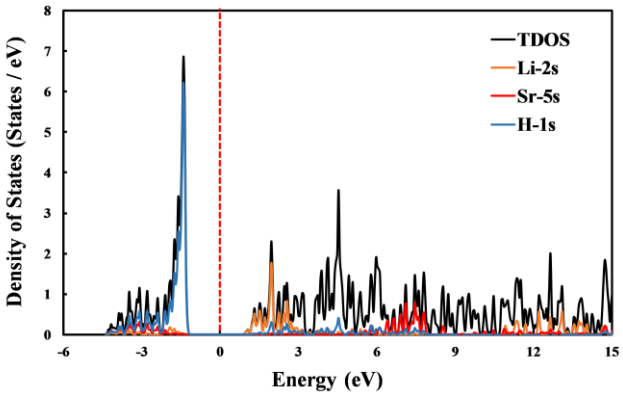

Figure 2 The total and partial density of states of $LiSrH_3$.

3.3 Hydrogen Storage Properties

The gravimetric hydrogen density (GHD) is a critical index for storing hydrogen in a solid host material. The GHD of $LiSrH_3$ is collected using the equation below [16]:

$$C_{wt\%} = \left(\frac{(H/M)M_H}{M_{Host}+(H/M)M_H} \; x \; 100 \right) \% \qquad (3)$$

M_H and M_{host} describes molar mass of the materials and H and M describes the number of atoms of the element. The GHD value of $LiSrH_3$ is obtained as 3.97 wt.% which is in the range of the targeted value by the US Energy Department (4 wt.%). Another critical parameter that needs to be examined that the temperature at which hydrogen can be desorbed from the host material. That is called hydrogen desorption temperature. This temperature is computed as follows [16];

$$\Delta H = T_d \times \Delta S \qquad (4)$$

Where T_d is hydrogen desorption temperature and ΔS is hydrogen entropy change which is 130.7 J/mol. K [23, 24]. Based on this calculation, T_d is found to be as 90 K.

4. CONCLUSION

This research has assessed elastic, electronic and hydrogen storage features of $LiSrH_3$. Several elastic parameters are computed using elastic constants to assess its mechanical stability.

Evaluation of Cauchy pressure, Pugh's ratio and Poisson's ratio demonstrates that $LiSrH_3$ is a brittle material. Ductility and brittleness of the host material is another important parameter that needs to be taken into account when carrying the material. If the material is brittle, it will be difficult to use it in portable devices. Based on our calculations and evaluations, it is found that $LiSrH_3$ is a brittle material and not suitable for portable applications. It might be better to use this material in stationary applications. In addition, the electronic band structures of $LiSrH_3$ displays that this material is non-metallic due to a band gap between valence and conduction band. The hydrogen gravimetric density of $LiSrH_3$ is found to be 3.97 wt.% which is very close to the target value 4 wt.%. Finally,, the hydrogen desorption temperature has been calculated and found to be 90 K.

The Declaration of Conflict of Interest/ Common Interest

We declare no conflict or common interest.

Authors' Contribution

Both authors carried out equal work on this study.

REFERENCES

[1] C. Tarhan, M. A. Çil, "A study on hydrogen, the clean energy of the future: Hydrogen storage methods," Journal of Energy Storage, vol. 40, p. 102676, 2021.

[2] M. Hirscher, V.A. Yartys, M. Baricco, J.B. von Colbe, D. Blanchard, Jr, R.C. Bowman, D.P. Broom, C.E. Buckley, F. Chang, P. Chen, Y.W. Cho "Materials for hydrogen-based energy storage – past, recent progress and future outlook," Journal of Alloys and Compounds, vol. 827, p. 153548, 2020.

[3] H. H. Raza, G. Murtaza, Umm-e-Hani, N. Muhammad, S. M. Ramay, "First-principle investigation of $XSrH_3$ (X = K and Rb) perovskite-type hydrides for hydrogen storage," International Journal of Quantum Chemistry, vol. 120, no. 24, p. e26419, 2020.

[4] P. Vajeeston, P. Ravindran, H. Fjellvag, "Structural phase stability studies on $MBeH_3$ (M = Li, Na, K, Rb, Cs) from density functional calculations," (in English), Inorganic Chemistry, Article vol. 47, no. 2, pp. 508-514, 2008.

[5] B. Rehmat, M. A. Rafiq, Y. Javed, Z. Irshad, N. Ahmed, S. M. Mirza, "Elastic properties of perovskite-type hydrides $LiBeH_3$ and $NaBeH_3$ for hydrogen storage," International Journal of Hydrogen Energy, vol. 42, no. 15, pp. 10038-10046, 2017.

[6] A. H. Reshak, M. Y. Shalaginov, Y. Saeed, I. V. Kityk, S. Auluck, "First-Principles Calculations of Structural, Elastic, Electronic, and Optical Properties of Perovskite-type $KMgH_3$ Crystals: Novel Hydrogen Storage Material," The Journal of Physical Chemistry B, vol. 115, no. 12, pp. 2836-2841, 2011.

[7] P. Ordejón, E. Artacho, J. M. Soler, "Self-consistent order-N density-functional calculations for very large systems," Physical Review B, vol. 53, no. 16, p. R10441, 1996.

[8] J. P. Perdew, K. Burke, M. Ernzerhof, "Generalized Gradient Approximation Made Simple," Physical Review Letters, vol. 77, no. 18, pp. 3865-3868, 1996.

[9] G. D. Yıldız, Y. G. Yıldız, S. AL, A. İyigör, N. Arıkan, "Computational investigations of mechanic, electronic and lattice dynamic properties of yttrium based compounds," International Journal of Modern Physics B, vol. 32, no. 20, p. 1850214, 2018.

[10] S. Al, N. Arikan, S. Demir, A. Iyigör, "Lattice dynamic properties of Rh_2 XAl

(X= Fe and Y) alloys," Physica B: Condensed Matter, vol. 531, pp. 16-20, 2018.

[11] S. Al, A. Iyigor, "Structural, electronic, elastic and thermodynamic properties of hydrogen storage magnesium-based ternary hydrides," Chemical Physics Letters, vol. 743, p. 137184, 2020.

[12] S. Al, "Elastic and thermodynamic properties of cubic perovskite type $NdXO_3$ (X=Ga, In)," The European Physical Journal B, vol. 94, no. 5, p. 108, 2021.

[13] D. G. Pettifor, "Theoretical predictions of structure and related properties of intermetallics," Materials Science and Technology, vol. 8, no. 4, pp. 345-349, 1992.

[14] C. Kurkcu, S. Al, C. Yamcicier, "Ab-initio study of structural, electronic, elastic, phonon properties, and phase transition path of sodium selenite," Chemical Physics, vol. 539, p. 110934, 2020.

[15] M. Hadi, M. Nasir, M. Roknuzzaman, M. Rayhan, S. Naqib, A. Islam, "First-principles prediction of mechanical and bonding characteristics of new T2 superconductor Ta_5GeB_2," J physica status solidi, vol. 253, no. 10, pp. 2020-2026, 2016.

[16] S. Al, C. Kurkcu, C. Yamcicier, "Structural evolution, mechanical, electronic and vibrational properties of high capacity hydrogen storage TiH_4," International Journal of Hydrogen Energy, vol. 45, no. 55, pp. 30783-30791, 2020.

[17] H. H. Raza, G. Murtaza, R. M. A. Khalil, "Optoelectronic and thermal properties of $LiXH_3$ (X= Ba, Sr and Cs) for hydrogen storage materials: a first principle study," J Solid State Communications, vol. 299, p. 113659, 2019.

[18] S. Al, N. Arikan, A. Iyigör, "Investigations of Structural, Elastic, Electronic and Thermodynamic Properties of X_2TiAl Alloys: A Computational Study," Zeitschrift für Naturforschung A, vol. 73, no. 9, pp. 859-867, 2018.

[19] A. Iyigor, "Investigations of structural, elastic, electronic, vibrational and thermodynamic properties of RhMnX (X = Sb and Sn)," Materials Research Express, vol. 6, no. 11, p. 116110, 2019.

[20] P. Li, J. Zhang, S. Ma, Y. Zhang, H. Jin, S. Mao, "First-principles investigations on structural stability, elastic and electronic properties of Co_7M_6 (M= W, Mo, Nb) μ phases," Molecular Simulation, vol. 45, no. 9, pp. 752-758, 2019.

[21] S. Chen, Y. Sun, Y.-H. Duan, B. Huang,, M.-J. Peng, "Phase stability, structural and elastic properties of C15-type Laves transition-metal compounds MCo_2 from first-principles calculations," Journal of Alloys and Compounds, vol. 630, pp. 202-208, 2015.

[22] C. Kürkçü, Ç. Yamçıçıer, "Structural, electronic, elastic and vibrational properties of two dimensional graphene-like BN under high pressure," Solid State Communications, vol. 303-304, p. 113740, 2019.

[23] Q. Zeng, K. Su, L. Zhang, Y. Xu, L. Cheng, X. Yan, "Evaluation of the Thermodynamic Data of CH_3SiCl_3 Based on Quantum Chemistry Calculations," Journal of physical and chemical reference data, vol. 35, no. 3, pp. 1385-1390, 2006.

[24] S. Al, C. Kurkcu, C. Yamcicier, "High pressure phase transitions and physical properties of Li_2MgH_4; implications for hydrogen storage," International Journal of Hydrogen Energy, vol. 45, no. 7, pp. 4720-4730, 2020.

SAKARYA ÜNİVERSİTESİ
FEN BİLİMLERİ ENSTİTÜSÜ DERGİSİ

Sakarya University Journal of Science
SAUJS

ISSN 1301-4048 | e-ISSN 2147-835X | Period Bimonthly | Founded: 1997 | Publisher Sakarya University | http://www.saujs.sakarya.edu.tr/

Title: Effect of Iron on Some Parameters Recombinant Pseudomonas aeruginosa Carrying Vitreoscilla Hemoglobin Gene

Authors: Hüseyin KAHRAMAN

Recieved: 2022-03-31 00:00:00

Accepted: 2022-06-22 00:00:00

Article Type: Research Article

Volume: 26
Issue: 4
Month: August
Year: 2022
Pages: 805-812

How to cite
Hüseyin KAHRAMAN; (2022), Effect of Iron on Some Parameters Recombinant Pseudomonas aeruginosa Carrying Vitreoscilla Hemoglobin Gene. Sakarya University Journal of Science, 26(4), 805-812, DOI: 10.16984/saufenbilder.1096293
Access link
http://www.saujs.sakarya.edu.tr/en/pub/issue/72361/1096293

Sakarya University Journal of Science 26(4), 805-812, 2022

Effect of Iron on Some Parameters Recombinant *Pseudomonas aeruginosa* Carrying *Vitreoscilla* Hemoglobin Gene

Hüseyin KAHRAMAN *[1]

Abstract

In this study, the effects of iron presence on some bacterial parameters of *Pseudomonas aeruginosa* and its recombinant bacteria carrying *Vitreoscilla* hemoglobin on its chromosome were investigated for the first time. These parameters are; optical density, pH, glucose, trehalose production and biomass. Parameters; It was studied at 37 °C and 250 rpm ventilated conditions depending on time. Bacteria have developed mechanisms by which they can resist heavy metal stress with many other mechanisms, including making metals less toxic and excreting them out of the cell. The Efflux system is the most widely used mechanism. The bacterium that makes the best use of these mechanisms is *P. aeruginosa*, which has an environmental and versatile feature. In the presence of LB alone, an increase was observed in the first 48 hours and a decrease of 43% in the other time periods, especially in the 96th hour compared to the control. The highest increase was detected in the 48th time periods, up to 259% in the 3,32. When iron was added to the medium, significant increases were observed in all time periods compared to the controls and these increases reached 575% at 72 hours. In the same time periods, the maximum value of OD_{600} 4.55 was reached.

Keywords: *Pseudomonas aeruginosa*, *Vitreoscilla* Hemoglobin, Iron

1. INTRODUCTION

Iron is a cofactor for many enzymes involved in critical biological processes such as redox chemistry, tricarboxylic acid cycle, electron transport and DNA and RNA synthesis [1, 2]. The iron is not insoluble and bioavailability [3]. The iron is one of the elements necessary for the bacterial life and cannot be easily taken from the environment and may be below the concentration required for bacterial growth in many environments [4, 5]. Iron starvation can prevent bacterial growth. Recent studies have shown that these levels of metal function as a signal for biofilm development if there are enough irons to grow. It may be [6, 7]. It reacts with oxygen and water to form ferric (FeIII) oxides and hydroxides (e.g. rust) which limits the availability of living organisms [8]. For some microorganisms, it is also the key metal for the production of biological surfactants. Because of some bacteria may use

* Corresponding author: hkahraman71@gmail.com
[1] İnönü University, Faculty of Science And Literature, Department of Biology
ORCID: https://orcid.org/0000-0001-6235-5497

iron as electron donor or acceptor in the energy metabolism, in the structure and activator of some enzymes [1, 9].

Working with a pathogen such as *Pseudomonas aeruginosa* in iron-related limiting conditions is due to the fact those it is a suitable bacterium to understand its behavior (Jimenez et al., 2010). Recent studies have shown that this metal serves as a signal for biofilm development in iron concentrations that do not limit growth. The production of rhamnolipid is stimulated under iron-limiting conditions and this causes an increase in twitching mobility [1, 2, 4, 8].

P. aeruginosa is an opportunistic pathogenic bacterium. Although it is a soil bacterium, it can be found in almost any habitat. This bacterium is a non-fermenting gram negative bacterium and, is able to survive in a variety of metabolic environments. *P. aeruginosa* has a natural resistance mechanism. Therefore, it is resistant to antimicrobial agents. It can transfer these resistance mechanisms in other bacteria. Iron regulation in *P. aeruginosa* occurs through a complex regulatory network [8], which may contain numerous environmental stimuli that allow virulence factors to be expressed on time. *P. aeruginosa* with biofilm is able to live on biotic and abiotic surfaces [1, 10].

Vitreoscilla hemoglobin provides oxygen to the respiratory chain and facilitates oxygenated growth and biological product synthesis. *Vitreoscilla* hemoglobin heterologous expression has an enhancing effect on cell growth and protein synthesis needed [11].

2. MATERIAL AND METHODS

2.1. Chemicals

L-(+)-Rhamnose monohydrate was purchased from MP Chemicals (USA). Phenol, H_2SO_4, and $NaHCO_3$ were purchased from Carlo Erba Chemicals. NaCl, L-(+)-glucose, $FeCl_3$ was purchased from Merck. Yeast and peptone were purchased from Mast Diagnostics. Antrone was purchased from Sigma-Aldrich. All other chemicals used were of analytical grade.

2.2. Bacterial Strains

P. aeruginosa (NRRL B-771) and its transposon mediated *vgb* transferred recombinant strain was used.

2.3. Culturing

Cells were maintained on agar plates at 4 ºC with transfers at monthly intervals. The liquid media used throughout the study was Luria- Bertani (LB) broth medium (g l^{-1}); peptone (10), NaCl (10), and yeast extract (5). The final pH values were adjusted to 7.0. 250 µl of overnight cultures was inoculated into 50 ml of the same medium in 150 ml volume flasks and incubated in at 37 °C in a 200 rpm (24, 48, 72 and 96 h). The concentration of iron compound based in preliminary experiments; in LB was 150 ppm iron. Stock iron solution was prepared in dH_2O and autoclaved. These solutions were kept at 4 ºC, and no longer than 1 month.

2.4. Cell Densities and Dry Weight

The cell densities were measured at OD_{600} every 24 h using spectrophotometer. For determination of the cell dry weight, bacterial suspensions were centrifuged at 10.000 rpm for 20 min at 20 ºC, then cell pellets produced after centrifugation were dried at 105 ºC for 5 hours and then measuring the cell dry weight.

2.5. Glucose Detection

Soluble glucose was quantified according to the anthrone method. Colorimetric response was compared to a standard curve based on glucose, and total carbohydrate content was expressed as mg/ml of glucose [12, 13].

2.6. Rhamnose

Rhamnose concentration was using the phenol-sulphuric method [14, 15]. Rhamnose concentration was quantified by a colorimetric method as rhamnose content using a rhamnose standard [16-19].

2.7. Statistics

Student's *t*-test was used for comparing and significant difference was claimed when $P < 0.05$.

In the presence of LB alone, an increase was observed in the first 48 hours and a decrease of 43% in the other time periods, especially in the 96th hour compared to the control. The highest increase was detected in the 48th time periods, up to 259% in the 3,32. When iron was added to the medium, significant increases were observed in all time periods compared to the controls and these increases reached 575% at 72 hours. In the same time periods, the maximum value of OD_{600} 4.55 was reached.

3. RESULTS

3.1. OD_{600}

While wild bacteria caught the highest value at the 48th hour with 0.935 [in iron], recombinant bacteria (PaJC) reached the 72nd hour with a value of 4,55. Especially recombinant bacteria reach the value of 4,55 with an increase of 5 times after 48 hours. Likewise, a five-fold increase was observed in the wild bacteria at the 48th hour.

When we look at the graphics, recombinant bacteria give an advantageous OD_{600} value in the first 48 hours, while wild bacteria give this increase after 72nd hours. In the iron medium, an increase of OD_{600} up to 500% is observed from the 48th hour. In LB environment, recombinant bacteria reach the highest OD_{600} value with max 3,32, while wild bacteria reach 2,86 at 96th hour.

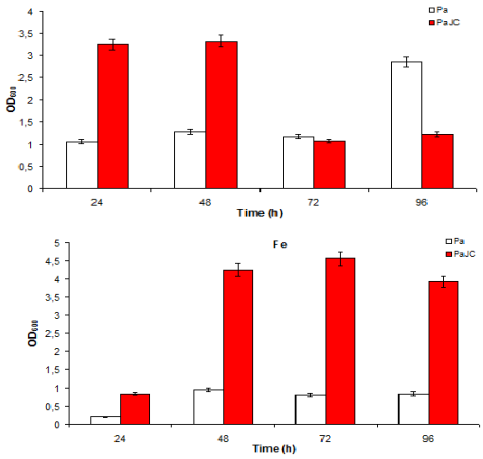

Figure 1 Growth rate of *P. aeruginosa* and its recombinant strain cells LB (top) and under LB+Fe-replete conditions (bottom).

In the presence of iron, the recombinant bacteria reach the OD_{600} value of 4.55 by the 72nd hour. Wild bacteria reach the 48th hour with 0.955 (Figure 1).

3.2. pH

Although there is an increase in the presence of PaJC in pH changes in LB environment, these increases are not significant. The highest pH increase was measured at PaJC with 8,9 at 96 hours. In the presence of iron, significant differences and pH increases occurred in the presence of PaJC. A pH increase of 133% was observed in the presence of PaJC at all times periods.

There was no significant difference in both wild bacteria and PAJC in all time frames. When wild bacteria and PaJC are compared, 1,33 times difference is seen as constant in all time frames. Wild tip bacteria reached the highest pH value again at the 96th hour with 6,71. Especially for recombinant bacteria, the pH value remained high in the presence of iron and did not show a significant change depending on the time (Figure 2).

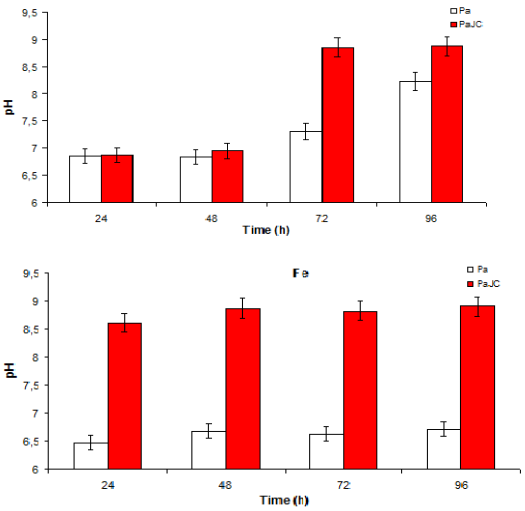

Figure 2 pH rate of *P. aeruginosa* and its recombinant strain cells LB (top) and under LB+Fe-replete conditions (bottom).

3.3. Glucose

While there were no significant differences in LB control environment, decreases in glucose production up to 712% compared to controls were recorded especially in the 96th period. In the presence of iron, the highest difference was obtained in PaJC with 204% and 387,01 mg / ml. These values decreased up to 3-fold according to LB environment. Iron reduces glucose production. Glucose production causes a decrease in both bacteria [in iron]. It is seen that it reaches the highest value with 387 mg / ml only in the presence of recombinant bacteria iron at 24 hours (Figure 3).

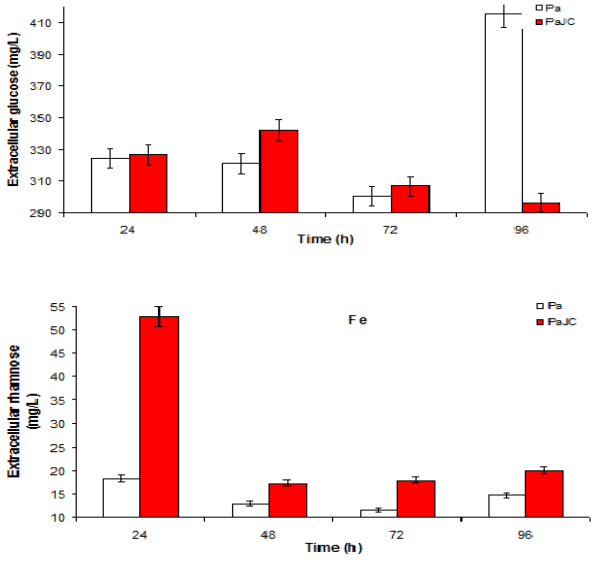

Figure 3 Extracellular glucose rate of *P. aeruginosa* and its recombinant strain cells LB LB (top) and under LB+Fe-replete conditions (bottom).

3.4. Rhamnose

Iron ramnose production decreased by 2-fold compared to the control environment. However, it appears to be advantageous in the presence of both LB and LB + iron compared to PaJC wild strain. The highest difference was 289% and 52,77 mg / ml and 24 hours in the presence of LB + iron. Rhamnose production decreases in the presence of both bacteria iron (Figure 4).

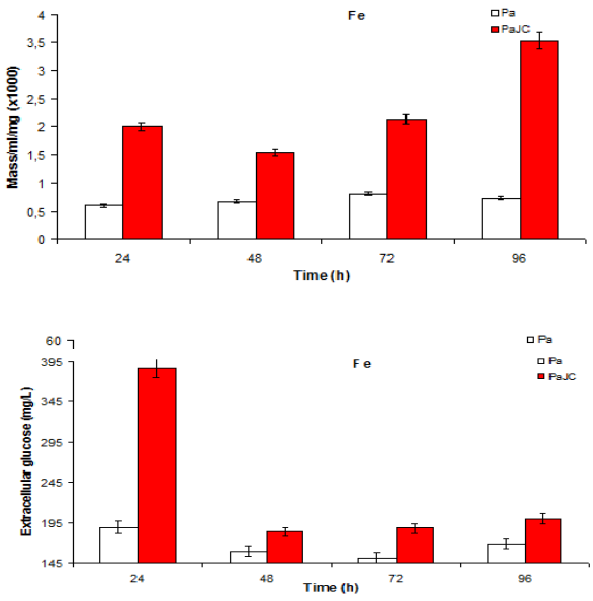

Figure 4 Extracellular rhamnose rate of *P. aeruginosa* and its recombinant strain cells LB (top) and under LB+Fe-replete conditions (bottom).

3.5. Mass

The addition of iron in the biomass measurement, one of the most important parameters, resulted in a difference between PaJC and wild strain. The difference was the highest with 204% and highest 500%. These ratios have reached only 288% in LB environment. PaJC showed differences in biomass growth up to 3-fold in the presence of LB and LB + iron. The highest biomass formation is reached by the 96th hour, by far, by recombinant bacteria. However, in the presence of iron, it causes an up to 3-fold decrease in wild-type bacteria (Figure 5).

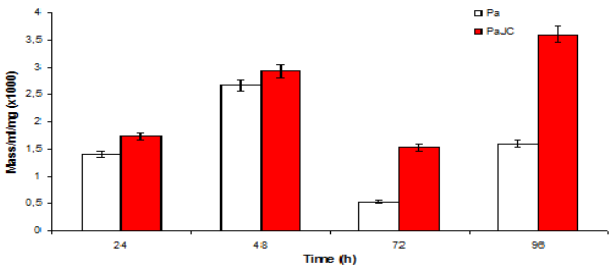

Figure 5 Biomass of *P. aeruginosa* and its recombinant strain cells LB (top) and under LB+Fe-replete conditions (bottom).

P. aeruginosa was chosen because it is widespread in nature and it has been often used in bioremediation studies [20].

4. DISCUSSION

Bacteria have developed mechanisms by which they can resist heavy metal stress with many other mechanisms, including making metals less toxic and excreting them out of the cell. The Efflux system is the most widely used mechanism. The bacterium that makes the best use of these mechanisms is *P. aeruginosa*, which has an environmental and versatile feature [21].

VHb contributes to aerobic growth and biological product synthesis by providing O_2 to the respiratory chain. Heterologous expression of VHb increases cell growth and total protein synthesis.

Iron plays a very important role in cell growth, especially in the presence of hydrobobic substrates. Some studies show that iron deficiency in the environment inhibits growth. In another study, it was stated that the growth of *P. syrigae* increased in the presence of iron. However, it has been reported that its excess causes toxicity. For example, ATCC15442 strain has been shown to affect gene expression in the presence of $FeCl_2$ and FCL_3 (0.025-0.075 and 0.1 g / L [16].

Iron is an essential growth factor for most microorganisms. *P. aeruginosa* has many iron absorbing systems to reduce under iron limited conditions. These systems; (1) siderophore system (reduces ferric iron via endogenous siderophores and xenosiderophores); (2) the heme system that obtains iron from the heme group, and (3) the iron-bearing iron-absorbing system [22, 23].

Iron restriction limits the growth rate of *P. aeruginosa*. This may be due to the iron-containing respiratory system. As a result, there is a decrease in the production of TCA cycle enzymes. Iron is already known to be a helpful factor in many biological processes. Iron is important for all organisms as it also increases resistance to DNA replication, electron transfer system and oxidative stress. Iron is essential to all organisms due to its role in DNA replication, electron transfer, and oxidative stress resistance etc [22, 24].

Due to its role in both electrons transfer and resistance to oxidative stress, it is vital that iron is present in a certain amount in microorganisms. It has been stated that the reasons for the decrease in the growth rate of *Pseudomas* produced in iron-limited conditions may be related to the decreased expression of iron-carrying TCA cycle enzymes (such as aconitase and succinate dehydrogenase). My work also supports this view (Fig. 1). Again, in this study, it is seen that the recombinant bacteria are not affected by this problem (Figure 1-5).

Apart from this, it was stated that there was a decrease in the biomass of *P. putida* grown in a limited iron environment and this was related to the ED pathway. No such determination was made in this study. On the contrary, I detected a decrease in biomass in the presence of iron (Fig. 5).

Rhamnose production decreases in the presence of both bacteria Fe. This causes a decrease in rhamnolipid formation. Although iron is a key nutrient for most organisms.

It causes an up to two-fold decrease in Fe-glucose production. We think this may be due to Cyt enzymes. It also causes a decrease in Fe-OD_{600} and mass; A decrease of up to three times is observed in the production of rhamnose.

5. CONCLUSION

While there is a stable pH in both bacteria in FE-pH, pH overlap occurs from the 72^{nd} hour in the LB environment. However, in the LB environment, the recombinant bacteria reach pH values in the presence of iron at 72 hours. This can be explained by the production of VHb to provide the oxygen needed.

In the presence of Fe, the recombinant bacterium seems to be more advantageous than the wild strain. This may be because the VHb molecule has reached a high level of iron binding capacity. As a result, has more oxygen uptake ability. Normally the presence of a plasmid or episome-shaped genetic load can be a burden for

metabolism in bacteria. However, we don't see that here.

Funding

This work was supported by a Grant (APYB 128/2011) from Research Fund Unit of Inonu University

The Declaration of Conflict of Interest/ Common Interest

No conflict of interest or common interest has been declared by the author.

Authors' Contribution

Author have contributed in experimental study and writing of the manuscript.

The Declaration of Ethics Committee Approval

Author declare that this study doesn't require ethics committee approval and any special permission.

The Declaration of Research and Publication Ethics

The authors of the paper declare that they comply with the scientific, ethical and quotation rules of SAUJS in all processes of the paper and that they do not make any falsification on the data collected. In addition, they declare that Sakarya University Journal of Science and its editorial board have no responsibility for any ethical violations that may be encountered, and that this study has not been evaluated in any academic publication environment other than Sakarya University Journal of Science.

REFERENCES

[1] A. Abalos, F. Maximo, M. A. Manresa, J. Bastida, "Utilization of response surface methodology to optimize the culture media for the production of rhamnolipids by *Pseudomonas aeruginosa* AT10," Journal of Chemical Technology and Biotechnology, vol. 77, pp. 777–784, 2002.

[2] K. R. A. Akbari, A. A. Ali, "Study of antimicrobial effects of several antibiotics and iron oxide nanoparticles on biofilm producing *Pseudomonas aeruginosa*," Nanomedical Journal, vol. 4, no.1, pp. 37–43, 2017.

[3] G. Aouada, J. L. Crovisier, V. A. Geoffroy, J-M. Meyer, P. Stille, "Microbially-mediated glass dissolution and sorption of metals by *Pseudomonas aeruginosa* cells and biofilm," Journal of Hazardous Materials B, vol. 136, pp. 889–895, 2006.

[4] E. Banin, M. L. Vasil, E.P. Greenberg, "Iron and *Pseudomonas aeruginosa* biofilm formation," PNAS, vol. 102, no. 31, pp. 11076–11081, 2005.

[5] M. Benincasa, J. Contiero, M. A. Manresa, I. O. Moraes, "Rhamnolipid production by *Pseudomonas aeruginosa* LBI growing on soapstock as the sole carbon source," Journal of Food Engineering, vol. 54, pp. 283–288, 2002.

[6] Y. Cai, R. Wang, M-M. An, B-B. Liang, "Iron-depletion prevents biofilm formation in *Pseudomonas aeruginosa* through twitching motility and quorum sensing," Brazilian Journal of Microbiology, vol. 41, pp. 37–41, 2010.

[7] E. V. Chandrasekaran, J. N. Bemiller, "Constituent analysis of glycosaminoglycans," In: Wrhiste L, Wolfrom ML. (eds) Methods in Carbohydrate Chemistry. New York: Vol III. Academic Press; pp. 89–97, 1980.

[8] W-J. Chen, T-Y. Kuo, F-C. Hsieh, P-Y. Chen, C-S. Wang, Y-L. Shih, Y-M. Lai, J-R. Liu, L-Y. Yang, M-C. Shih, "Involvement of type VI secretion system in secretion of iron chelator pyoverdine in

Pseudomonas taiwanensis," Scientific Reports, vol. 6:32950, pp. 1-14, 2016.

[9] S. G. V. A. O. Costa, M. Nitschke, R. Haddad, M. N. Eberlin, J. Contiero, "Production of *Pseudomonas aeruginosa* LBI rhamnolipids following growth on Brazilian native oils," Process Biochemistry, vol. 41, pp. 483–488, 2006.

[10] S. Çam, R. Brinkmeyer, "The effects of temperature, pH, and iron on biofilm formation by clinical versus environmental strains of *Vibrio vulnificus*," Folia Microbiologica, vol. 65, no.3, pp. 557–566, 2020.

[11] N. Gedara, J. Moutinho-Pereira, A. Malheiro, J. P. Coutinho, S. Bernardo, A. Luzio, L. Dinis, "Grapevine ecophysiology and berry's quality: Best adapted varieties in Douro region terroir," International Journal of Advances in Science Engineering and Technology, vol. 7, no. 4, pp. 65–70, 2019.

[12] R. Glick, C. Gilmour, J. Tremblay, S. Satanower, O. Avidan, E. De´ziel, P. Greenberg, K. Poole, E. Banin, "Increase in rhamnolipid synthesis under iron-limiting conditions influences surface motility and biofilm formation in *Pseudomonas aeruginosa*," Journal of Bacteriology, vol. 192, no. 12, pp. 2973–2980, 2010.

[13] P. N. Jimenez, G. Koch, E. Papaioannou, M. Wahjudi, J. Krzeslak, T. Coenye, R. H. Cool, W. J. Quax, "Role of PvdQ in *Pseudomonas aeruginosa* virulence under iron-limiting conditions," Microbiology, vol. 156, pp. 49–59, 2010.

[14] A. Leyva, A. Quintana, M. Sanchez, E. N. Rodriguez, J. Cremata, J. C. Sanchez, "Rapid and sensitive anthrone -sulfuric acid assay in microplate format to quantify carbohydrate in biopharmaceutical products: Method development and validation," Biologicals, vol. 36, no. 2, pp. 134–141, 2008.

[15] A. T. Nguyen, J. W. Jones, M. A. Ruge, M. A. Kane, A. G. Oglesby-Sherrouse, "Iron depletion enhances production of antimicrobials by *Pseudomonas aeruginosa*," Journal of Bacteriology, vol. 197, no. 14, pp. 2265–2275, 2015.

[16] A. A. Reinhart, A. G Oglesby-Sherrouse, "Regulation of *Pseudomonas aeruginosa* Virulence by distinct iron sources," Genes, vol. 7, no. 12, pp. 1–12, 2016.

[17] Z. Sahebnazar, D. Mowla, G. Karimi, **"**Enhancement of Pseudomonas aeruginosa growth and rhamnolipid production using iron-silica nanoparticles in low-cost medium," Journal of Nanostructures, vol. 8, no. 1, pp. 1–10, 2018.

[18] S. S. Sasnow, H. Wei, L. Aristilde, "Bypasses in intracellular glucose metabolism in iron-limited *Pseudomonas putida*," Microbiology Open, vol. 5, no. 1, pp. 3–20, 2016.

[19] K. T. Schiessl, E. M. Janssen, S. M. Kraemer, K. McNeill, M. Ackermann, "Magnitude and mechanism of siderophore-mediated competition at low iron solubility in the *Pseudomonas aeruginosa* pyochelin system," Frontiers in Microbiology, vol. 8: 1964, pp. 1–11, 2017.

[20] F. Shatila, M. M. Diallo, U. Şahar, G. Özdemir, H. T. Yalçın, The effect of carbon, nitrogen and iron ions on mono-rhamnolipid production and rhamnolipid synthesis gene expression by *Pseudomonas aeruginosa* ATCC 15442," Archives of Microbiology, vol. 202, pp. 1407–1417, 2020.

[21] S. N. R. L. Silva, C. B. B. Fariasb, R. D. Rufinob, J. M. Lunab, L. A. Sarubbo, "Glycerol as substrate for the production

of biosurfactant by *Pseudomonas aeruginosa* UCP0992," Colloidal Surface B, vol. 79, pp. 174–183, 2010.

[22] G. M. Teitzel, M. R. Parsek, "Heavy metal resistance of biofilm and planktonic *Pseudomonas aeruginosa*," Applied and Environmental Microbiolgy, vol. 69, pp. 2313–2320, 2003.

[23] R. Vyas, P. M. Maharshi, J. Pohnerkar, G. N. Kumar, "*Vitreoscilla* hemoglobin promotes biofilm expansion and mitigates sporulation in *Bacillus subtilis* DK1042," 3 Biotechonology, vol. 10:118: pp. 1–7, 2020.

[24] Y. Zhang, X. Pan, L. Wang, L. Chen, "Iron metabolism in *Pseudomonas aeruginosa* biofilm and the involved iron-targeted anti-biofilm strategies," Journal of Drug Targeting, vol. 29, no. 3, pp. 249–258, 2020.

SAKARYA ÜNİVERSİTESİ
FEN BİLİMLERİ ENSTİTÜSÜ DERGİSİ

Sakarya University Journal of Science
SAUJS

ISSN 1301-4048 | e-ISSN 2147-835X | Period Bimonthly | Founded: 1997 | Publisher Sakarya University | http://www.saujs.sakarya.edu.tr/

Title: Synchronization of Gursey System

Authors: Eren TOSYALI, Fatma AYDOĞMUŞ

Recieved: 2022-01-17 00:00:00

Accepted: 2022-06-24 00:00:00

Article Type: Research Article

Volume: 26
Issue: 4
Month: August
Year: 2022
Pages: 813-819

How to cite
Eren TOSYALI, Fatma AYDOĞMUŞ; (2022), Synchronization of Gursey System . Sakarya University Journal of Science, 26(4), 813-819, DOI: 10.16984/saufenbilder.1059043
Access link
http://www.saujs.sakarya.edu.tr/en/pub/issue/72361/1059043

Sakarya University Journal of Science 26(4), 813-819, 2022

Synchronization of Gursey System

Eren TOSYALI*[1], Fatma AYDOĞMUŞ[2]

Abstract

Gursey Model, the only possible four-dimensional pure spinor model, proposed as a possible basis for a unitary description of elementary particles. The model exhibits chaotic behaviors depending on the system parameter values. In this study, we investigate the synchronization of chaotic dynamic in the Gursey wave equation that has particle-like solutions derived classical field equations. Numerical results for synchronization of the Gursey system are performed to indicate the accuracy of the used method.

Keywords: Synchronization, Gursey, chaos

1. INTRODUCTION

The field equation proposed by Feza Gursey in 1956 is the first nonlinear spinor wave equation with conformal invariance [1]. Gursey Model is the first 4D conformal invariant fermionic model [1]. The exact solution of 4D Gursey Model via Heisenberg ansatz was found by Kortel. This exact solution had instantonic character [2]. Instantons are corresponding to classical topological solution with zero energy for the QCD (Quatum Chromo Dynamic) field equations [3]. In addition, soliton-type solutions are found by adding the mass term to the equation for certain values of the coupling constant [4, 5]. Also, soliton solutions of the expanded form of Gursey wave equation and Wu-Yang type monopole solutions were found [1, 4].

In nature, systems are well described by nonlinear equations, which have rich solutions such as regular or chaotic behavior. Therefore, chaos and nonlinear dynamics are widely used in many applied fields, from natural science (physics, biology …) to social science [6]. The Gursey system exhibits regular or chaotic behaviors depending on the system parameters. Recently, many studies have been done on the dynamics of the Gursey wave equation [7 - 9].

Synchronization in chaotic systems has been a topic of great interest in recent years. The first study on the coupling and synchronization of

* Corresponding author: eren.tosyali@bilgi.edu.tr
[1] İstanbul Bilgi University
ORCID: https://orcid.org/0000-0001-9118-851X
[2] İstanbul University
E-mail: fatmaa@istanbul.edu.tr
ORCID: https://orcid.org/0000-0003-1434-2143

identical chaotic systems was by Pecora-Carroll [10]. After the Pecora-Caroll studies, identical chaotic systems' synchronization problems get much popular in this field. Especially, active control method is used to synchronize chaotic flows and maps such as Lorenz, Duffing, Gross-Pitaevskii Equation (Bose-Einstein Condensate) and HIV-AIDS dynamical system [11-18]. In this paper, master-slave synchronization based on open-plus-closed-loop (OPCL) method is used to synchronize chaotic dynamic of Gursey wave equation. The OPCL method was proposed by Jackson and Grosu in 1995 [19]. They applied this method to synchronize chaotic identical Lorenz, Duffing and Chua systems. The effectiveness of the method was also investigated for complex network and hyper chaotic maps [20, 21]. In this paper, the synchronized and unsynchronized phase space diagrams and control-activated diagrams are given to show the effectiveness of the used method.

2. GURSEY MODEL

Gursey spinor wave equation is

$$i\partial\psi + g(\bar{\psi}\psi)\psi = 0. \tag{1}$$

here the fermion field ψ has scale dimension $\frac{3}{2}$ and g is the positive dimensionless coupling constant. The Heisenberg ansatz [22].

$$\psi = \left[\mathrm{i}x_\mu\, \gamma_\mu \chi(s) + \phi(s)\right]C, \tag{2}$$

here C is an arbitrary spinor constant; $\chi(s)$ and $\phi(s)$ are real functions of $s = x_\mu = r^2 + t^2 (x_1 = x, x_2 = y, x_3 = z, x_4 = t)$ in the Euclidean space-time, *i.e.* $r^2 = x_1^2 + x_2^2 + x_3^2$. Inserting Eq. (2) into Eq. (1) we obtain the following nonlinear differential equations system

$$4\chi(s) + 2s\frac{d\chi(s)}{ds} - \alpha[s\chi(s)^2 + \phi(s)^2]^{\frac{1}{3}}\phi(s) = 0 \tag{3a}$$

$$2\,\frac{d\phi(s)}{ds} + \alpha[s\chi(s)^2 + \phi(s)^2\,]^{\frac{1}{3}}\chi(s) = 0, \tag{3b}$$

here $\alpha = g(\bar{C}C)^{\frac{1}{3}}$ for short. Substituting $\chi = As^{-\sigma}F(u)$ and $\phi = Bs^{-\tau}\,G(u), u = \ln s$ and $\tau = \frac{3}{4}$ and $A^2 = B^2$ [2], the dimensionless form of the nonlinear coupled differential equations system is obtained as

$$2\frac{dF(u)}{du} + \frac{3}{2}F(u) - \alpha(AB)^{\frac{1}{3}}[F(u)^2 + G(u)^2]^{\frac{1}{3}}G(u) = 0, \tag{4a}$$

$$2\frac{dG(u)}{du} - \frac{3}{2}G(u) + \alpha(AB)^{\frac{1}{3}}[F(u)^2 + G(u)^2]^{\frac{1}{3}}F(u) = 0. \tag{4b}$$

Here F and G are dimensionless functions of u and A, B are constants [7].

3. MASTER SLAVE SYNCHRONIZATION METHOD

In this section, we describe our master-slave synchronization process based on OPCL method to synchronize identical systems. Let us consider two identical systems and relate them some coupling function. Systems are defined on $\mathbb{R}^3$, so they have three degrees of freedom. The generalized coordinates for master system are described by $\boldsymbol{x} \equiv (x, y, z)$ and slave system $\boldsymbol{x}_s \equiv (x_s, y_s, z_s)$. Their evolution is described by the same vector field $f: \mathbb{R}^3 \to \mathbb{R}^3$, then we have

$$\dot{\boldsymbol{x}}(t) = f\big(x(t)\big) \tag{7a}$$

$$\dot{\boldsymbol{x}}_s(t) = f\big(x_s(t)\big), \tag{7b}$$

The difference between master and slave systems named error function is given by $\boldsymbol{x} - \boldsymbol{x}_s$, with coefficients dependent on the master variables [23, 24], that is,

$$\boldsymbol{k}(x).(\boldsymbol{x} - \boldsymbol{x}_s) = \begin{pmatrix} k_{11}(x) & k_{12}(x) & k_{31}(x) \\ k_{21}(x) & k_{22}(x) & k_{32}(x) \\ k_{31}(x) & k_{23}(x) & k_{33}(x) \end{pmatrix}.\begin{pmatrix} x - x_s \\ y - y_s \\ z - z_s \end{pmatrix}. \tag{8}$$

This coupling function $\boldsymbol{k}(x).(\boldsymbol{x} - \boldsymbol{x}_s)$ is added to the slave subsystem. Therefore, this function generates a response which synchronize master and slave system

$$\dot{\boldsymbol{x}}(t) = f\big(\boldsymbol{x}(t)\big) \tag{9a}$$

$$\dot{\boldsymbol{x}}_s(t) = f(\boldsymbol{x}_s(t)) + k(x).(\boldsymbol{x} - \boldsymbol{x}_s), \quad (9b)$$

If $\boldsymbol{\xi}(t) = \boldsymbol{x}(t) - \boldsymbol{x}_s(t)$ go to zero, the system will reach asymptotically stable, implying that the states $\boldsymbol{x}(t)$ and $\boldsymbol{x}_s(t)$ will approach each other which means master and slave system is synchronized along the flow. If the regularity class of f is at least C^1, this is an easy consequence of the Mean Value Theorem in several variables and a judicious choice of the matrix k [21]: We consider it equal to

$$k = d_{\boldsymbol{x}(t)}\boldsymbol{f} - \boldsymbol{H}, \quad (10)$$

where $d_{\boldsymbol{x}(t)}\boldsymbol{f}$ is the differential of the vector field $\boldsymbol{f}$ evaluated along the trajectory $\boldsymbol{x}(t)$ of the master system, and $\boldsymbol{H}$ is a constant matrix all of whose eigenvalues have strictly negative real parts (this is known as a Hurwitz matrix). For any fixed t, subtracting Eq. 9b from the Eq. 9a we obtain

$$\dot{\boldsymbol{\xi}}(t) = \frac{d}{dt}(\boldsymbol{x}(t) - \boldsymbol{x}_s(t)) = \boldsymbol{f}(\boldsymbol{x}) - \boldsymbol{f}(\boldsymbol{x}_s) - \boldsymbol{k}.\boldsymbol{\xi} \cong (d_{\boldsymbol{x}(t)}\boldsymbol{f} - \boldsymbol{k}).\boldsymbol{\xi} = \boldsymbol{H}.\boldsymbol{\xi}, \quad (11)$$

here, $\boldsymbol{H}$ is Hurwitz implies that the exponential is a decaying one, leading to the asymptotic $\lim_{t\to\infty}\|\boldsymbol{\xi}(\mathbf{t})\| = 0$.

3.1. GURSEY SYNCHRONIZATION

Let us consider a driven and damped master Gursey system as given below,

$$\frac{dx_1}{du} = \left(-\frac{3}{4}\right)x_1 + 0.5y_1(x_1^2 + y_1^2)^{\frac{1}{3}}, \quad (12a)$$

$$\frac{dy_1}{du} = \frac{3}{4}y_1 - 0.5x_1(x_1^2 + y_1^2)^{\frac{1}{3}} + 0.5A\,Cos(wu) - 0.5\gamma y_1. \quad (12b)$$

For simplification we use (x_1, y_1) and (x_2, y_2) instead of (F_1, G_1) and (F_2, G_2) for master and slave systems, respectively. Jacobian matrix of master system is

$$detf = \begin{pmatrix} -\frac{3}{4} + \frac{0.333x_1y_1}{(x_1^2+y_1^2)^{(2/3)}} & \frac{0.333y_1^2}{(x_1^2+y_1^2)^{(2/3)}} + 0.5(x_1^2 + y_1^2)^{(1/3)} \\ \frac{0.419974x_1^2}{(x_1^2)^{(2/3)}} - 0.629961(x_1^2)^{(1/3)} & -\frac{3}{4} - 0.5\gamma \end{pmatrix}, \quad (13)$$

We take parameters and constants of Jacobi matrix (detf) as

$$\begin{pmatrix} -\frac{3}{4} + \mathrm{p} & 0 \\ 0 & -\frac{3}{4} - 0.5\gamma + p \end{pmatrix}. \quad (14)$$

Eigenvalues of Eq. 14 are $\lambda_1 = \frac{1}{4}(-3 + 4p)$ and $\lambda_2 = 0.75 + \mathrm{p} - 0.5\gamma$. The largest p value for the synchronization is 0.592 depending on $\lambda_1 < 0$ and $\lambda_2 < 0$. We took $p = -1$ which is smaller then 0.592 and $\gamma = 0.316$.

If we substitute the p and γ value into Eq. 14 we reach the H matrix which is given below,

$$\begin{pmatrix} -\frac{7}{4} & 0 \\ 0 & -0.408 \end{pmatrix}, \quad (15)$$

$\boldsymbol{k} = detf - H$ and $error = \begin{pmatrix} x_1 & x_2 \\ y_1 & y_2 \end{pmatrix}.\boldsymbol{k}.\boldsymbol{error}$ is

$$\begin{pmatrix} (x_1 - x_2)\left(1 + \frac{0.333x_1y_1}{(x_1^2+y_1^2)^{(2/3)}}\right) + \left(\frac{0.333y_1^2}{(x_1^2+y_1^2)^{(2/3)}} + 0.5(x_1^2 + y_1^2)^{(1/3)}\right)(y_1 - y_2) \\ -1.04993(x_1^2)^{\frac{1}{3}}(x_1 - x_2) + 1(y_1 - y_2) \end{pmatrix}. \quad (16)$$

Finally, slave systems are

$$\frac{dx_2}{du} = -\frac{3}{4}x_2 + 0.5y_2(x_2^2 + y_2^2)^{\frac{1}{3}} + (x_1 - x_2)\left(1 + \frac{0.333x_1y_1}{(x_1^2+y_1^2)^{(2/3)}}\right) + \left(\frac{0.333y_1^2}{(x_1^2+y_1^2)^{(2/3)}} + 0.5(x_1^2 + y_1^2)^{(1/3)}\right)(y_1 - y_2), \quad (17a)$$

$$\frac{dy_2}{du} = \frac{3}{4}y_2 - 0.5x_2(x_2^2 + y_2^2)^{\frac{1}{3}} + 0.5A\,Cos(wu) - 0.5\gamma y_2 - 1.04993(x_1^2)^{\frac{1}{3}}(x_1 - x_2) + 1(y_1 - y_2). \quad (17b)$$

4. NUMERICAL RESULTS

In this section, we investigate the simulation results for synchronization of the master and slave Gursey systems using the fourth-order Runge Kutta algorithm. The sets of differential equations related to the master and slave systems are solved with step size 0.1 , length 1000, $A = 0.71$, $\omega = 1.04898$ and $\gamma = 0.316$. The initial values of the master and slave systems are taken as$(x_1(0); y_1(0)) = (0.2; 0.1)$, $(x_2(0); y_2(0)) = (1.6; 2.2)$, respectively. The bifurcation diagram is given in Figure 1. Gursey system shows regular and chaotic dynamics depending on the amplitude of driven force. The system exhibits regular dynamics until $A = 0.6$. After this value of A, system exhibits chaotic dynamics. There is only one stable fix points for less than $A = 0.4$. After that point there is periodic dumpling until $A = 0.6$. $A = 0.6$ is threshold point for transition regular to chaotic behavior. In order to prove chaotic dynamics of Gursey system we calculate Lyapunov Characteristic Exponents (LCEs) [25,26]. LCEs are $\lambda_1 = 0.0846347$, $\lambda_2 = -0.242635$, $\lambda_3 = 0$. In Figure 2, we show evolution of LCEs depending on u. In addition, for regular case, one LCE is 0 and all the other LCEs are less than zero (negative). There is one LCE, which is bigger than zero shows us chaotic dynamics of Gursey system. We start controlling at $u = 100$. After that point system exhibits synchronization.

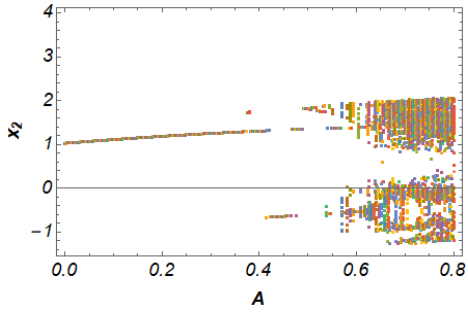

Figure 1 Bifurcation diagram for Gursey system.

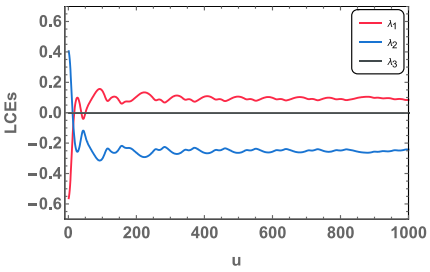

Figure 2 LCEs for chaotic Gursey system.

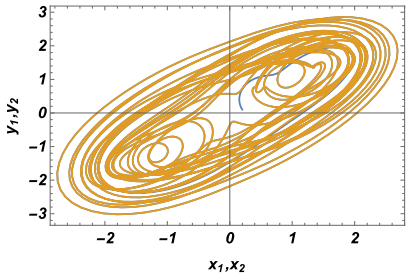

(a)

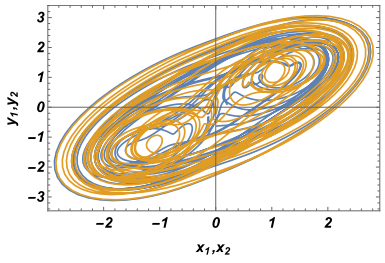

(b)

Figure 3 Synchronized and Unsynchronized Phase Space

The synchronized and unsynchronized phase space diagrams are given in Figure 3. Also Figure 4 and 5 show the dynamics of synchronized master and slave systems in the range 100 to 200. Control activated at $u = 100$. Before this value of u, systems are unsynchronized.

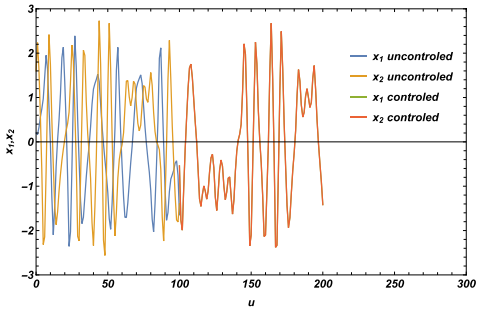

(a)

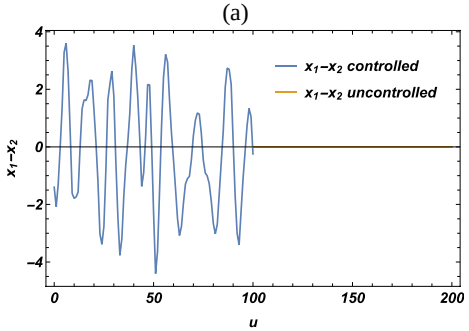

(b)

Figure 4 (a) Evolution graph (b) error graph, control function activated at $u = 100$, for x_1 and x_2

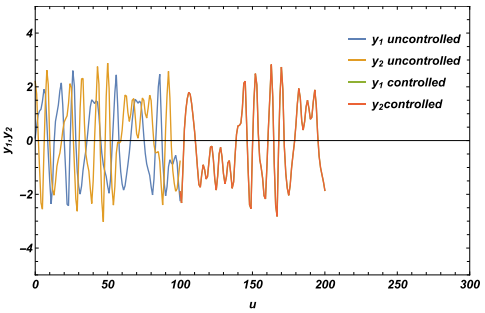

(a)

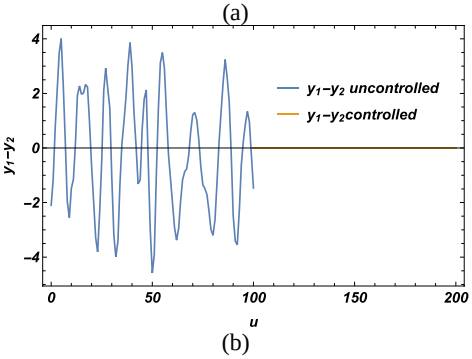

(b)

Figure 5 (a) Evolution graph (b) error graph, control function activated at $u = 100$, for y_1 and y_2

5. CONCLUSION AND DISCUSSION

In this paper, the validity of OPCL synchronization method is investigated for 4D fermionic Gursey model. The model exhibits chaotic dynamics depending on system parameters given in numerical results. In master-slave synchronization process, the selected slave and master systems are identical. Once the control function added to the slave system is activated, master and slave systems' orbits converge each other. The signals produced by control function stabilize the error between master and slave systems. The error signals go rapidly to the zero when control input function is activated at u=100 (Fig. 4 and Fig. 5). Two identical master and slave Gursey systems achieve the synchronization for different initial conditions. In Fig. 3 (a) Phase space and Fig. 4-5 (a) evolution graphs show synchronized dynamics after activated control signals.

Funding

The author (s) has no received any financial support for the research, authorship or publication of this study.

The Declaration of Conflict of Interest/ Common Interest

"No conflict of interest or common interest has been declared by the authors".

Authors' Contribution

The first author contributed 60%, the second author 40%.

The Declaration of Ethics Committee Approval

This study does not require ethics committee permission or any special permission.

The Declaration of Research and Publication Ethics

The authors of the paper declare that they comply with the scientific, ethical and quotation rules of SAUJS in all processes of the paper and that they do not make any falsification on the data collected. In addition, they declare that Sakarya University Journal of Science and its editorial board have no responsibility for any ethical violations that may be encountered, and that this study has not been evaluated in any academic publication environment other than Sakarya University Journal of Science.

REFERENCES

[1] F. Gursey, "On a conform-invariant wave equation," II Nuvovo Cimento, vol. 3, no. 5, pp. 998-1006, 1956.

[2] F. Kortel, "On some solutions of Gursey's conformal-invariant spinor wave eqution," II Nuovo Cimento, vol. 4, no. 2 pp. 210-215, 1956.

[3] C. Rebbi, G. Solliani, "Solitons and particles." 1st edition, World Scientific, USA, pp. 792-811, 1984.

[4] M. Soler, "Classical, Stable, Nonlinear Spinor Field with Positive Rest Energy," Physical Review D, vol. 1, no.10, pp. 2766–2769, 1970.

[5] S. Sağaltıcı, "Gürsey Solitonlarının Düzensiz Dinamik Yapılarının İncelenmesi," M.S. thesis, Istanbul University, Departmrnt of Physics, Istanbul, Turkey, 2004.

[6] S. Strogatz, "Nonlinear Dynamics and Chaos: With application to physics, biology, chemistry and engineering.", 2nd edition, CRC Press , USA, pp. 423-448, 2018.

[7] F. Aydogmus, E. Tosyalı, "Common Behaviors of Spinor-Type Instantons in 2D Thirring and 4D Gursey Fermionic Models," vol. 2014, no.148375, pp. 0-11, 2014.

[8] F. Aydogmus, "Chaos in a 4D dissipative nonlinear fermionic model," International Journal of Modern Physics C, vol. 26, no. 7, pp. 1550083, 2015.

[9] E. Tosyali, F. Aydogmus, "Soliton Solutions of Gursey Model With Bichromatic Force," *AIP Conference Preceeding Third International Conference Of Mathematical Sciences* (ICMS 2019) pp. 56–59, 2019.

[10] L. M. Pecora, T. L. Caroll, "Synchronization in chaotic systems," Physical Review Letters, vol. 64, no. 8, pp. 821–824, 1990.

[11] M. T. Yassen, "Chaos Synchronization Between Two Different Chaotic Systems Using Control", Chaos, Solitons and Fractals, vol. 23, no. 1, pp. 31-140, 2004.

[12] A. Ucar, K. E. Lonngren, E. Bai, "Synchronization of the unified chaotic systems via active control", Chaos Solitons and Fractals, vol. 27, no. 5, pp. 1292-1297, 2006.

[13] S. Oancea, F. Grosu, A. Lazar, I. Grosu, "Master–slave synchronization of Lorenz systems using a single controller", Chaos, Solitons & Fractals, vol. 41, no. 5, pp. 2575-2580, 2009.

[14] B. A. Idowu, U. E. Vincent, "Synchronization and Stabilization of Chaotic Dynamics in a Quasi-1D Bose-Einstein Condensate", Journal of Chaos, vol. 2013, no.-, pp. 723581, 2013.

[15] M. E., Yalcin, J. A. K. Suykens, J. P. L. Wandewalle, "Synchronization of Chaotic Lur'e Systems", Cellular Neural Networks Multi-Scroll Chaos and Synchronization, 1st edition, World Scientific Series on Nonlinear Science, Series A., USA, pp. 105-154, 2013.

[16] Q. Yang, "Stabilization and synchronization of Bose–Einstein condensate systems by single input linear controllers", Complexity, vol. 141, no. -, pp. 66-71, 2017.

[17] K. Ding, "Master-Slave Synchronization of Chaotic Φ6 Duffing Oscillators by Linear State Error Feedback Control", Complexity, vol. 2019, no. 3637902, pp. 1-10, 2019.

[18] E. Tosyali, F. Aydogmus, "Master-slave synchronization of Bose-Einstein condensate in 1D tilted bichromatical optical lattice," Condensed Matter Physics, vol. 23, no. 1, pp. 13001, 2020.

[19] E. A. Jackson, I. Grosu, "An open-plus-cloosed-loop (OPCL) control of complex dynamic systems" Physica D, vol. 85, pp. 1-9, 1995.

[20] H. Du, "Adaptive Open-Plus-Closed-Loop Control Method of Modified Function Projective Synchronization In Complex Networks" International Journal of Modern Physics C, vol. 22, pp. 1393-1407, 2011.

[21] E. A. Jackson, I. Grosu, "An open-plus-cloosed-loop Approach to Synchronization of Chaotic and Hyperchaotic Maps" International Journal of Bifurcation and Chaos , vol. 12, pp. 1219-1225, 2002.

[22] W. Heisenberg, "Zur Quantentheorie nichtrenormierbarer Wellen-gleichungen," Zeitschrift für Natuerforschung A, vol. 9, no. 84 pp. 292-303, 1954.

[23] C. W. Wu, L. O. Chua, "A simple way to synchronize chaotic systems with applications to secure communication systems," International Journal of Bifurcation and Chaos, vol. 3, no. 6 pp. 1619-1627, 1993.

[24] I. Grosu, "Robust Synchronization," Physical Review E, vol. 56, no. 3 pp. 3709-3712, 1997.

[25] M. Sandri, "Numerical Calculation of Lyapunov exponents," The Mathematica Journal, vol. 6, no. 3 pp. 78-84, 1996.

[26] J. P. Singh, B. K. Roy, "The nature of Lyapunov exponent is (+,+,-,-). Is it a hyperchaotic system?," Chaos Soliton & Fractals, vol. 92, no. - pp. 73-85, 2016.

SAKARYA ÜNİVERSİTESİ
FEN BİLİMLERİ ENSTİTÜSÜ DERGİSİ

Sakarya University Journal of Science
SAUJS

ISSN 1301-4048 | e-ISSN 2147-835X | Period Bimonthly | Founded: 1997 | Publisher Sakarya University | http://www.saujs.sakarya.edu.tr/

Title: An Investigation of the Correlation of Antibacterial Activity of Thyme (Thymus vulgaris L.) with its Nutrient Elements

Authors: Muazzez GÜRGAN ESER, Sevinç ADİLOĞLU

Recieved: 2022-04-29 00:00:00

Accepted: 2022-06-28 00:00:00

Article Type: Research Article

Volume: 26
Issue: 4
Month: August
Year: 2022
Pages: 820-828

How to cite
Muazzez GÜRGAN ESER, Sevinç ADİLOĞLU; (2022), An Investigation of the Correlation of Antibacterial Activity of Thyme (Thymus vulgaris L.) with its Nutrient Elements. Sakarya University Journal of Science, 26(4), 820-828, DOI: 10.16984/saufenbilder.1111059
Access link
http://www.saujs.sakarya.edu.tr/en/pub/issue/72361/1111059

Sakarya University Journal of Science 26(4), 820-828, 2022

An Investigation of the Correlation of Antibacterial Activity of Thyme (*Thymus vulgaris* L.) with its Nutrient Elements

Muazzez GÜRGAN ESER*[1], Sevinç ADİLOĞLU[1]

Abstract

The present study aimed to examine the correlation of plant nutrient elements with the antibacterial activity of methanol extract of *Thymus vulgaris* L. grown on soil from the experimental field without application of fertilizers or pesticides on two Gram-positive and two Gram-negative bacteria. The extract of thyme was obtained by maceration of aerial parts of the plant using methanol as the solvent. The contents of macro (P, K, Ca, and Mg) and micro (Fe, Cu, Zn, Mn, and B) nutrients were detected by ICP-OES. The results showed that the macro nutrients were compatible with herbaceous perennial plants, while Fe, Mn and B micro nutrients were high. The methanol extract was significantly effective on inhibiting *P. aeruginosa*, *S. aureus* and *E. faecalis*, while did not inhibit *E. coli*. The correlation of K and Mg was significantly positive with the growth inhibition of *P. aeruginosa* suggesting that higher K and Mg contents of the plant would result in higher antibacterial activity against P. aeruginosa, most probably up to a point. On the other hand, significant positive correlation of B was found with the inhibition of both Gram-positive bacteria. In addition, the positive correlation of Ca with the growth inhibition of *S. aureus* was highly significant. The importance of nutrient contents in medicinal aromatic plants such as thyme was shown with this study. The results therefore imply the conscious and sustainable agriculture of medicinal aromatic plants is crucial for the antibacterial activity of thyme.

Keywords: *Thymus vulgaris* L., antibacterial activity, macro and micro nutrient elements, correlation

1. INTRODUCTION

Around one third of the flora in Turkey consists of medicinal aromatic plants [1]. Among them the third largest plant family with 550 species is the *Lamiacaea* family [2]. *Thymus vulgaris* L, known as thyme, is a flowering plant species of this family. Although this particular species is not naturally found in the flora of Turkey, it has been cultivated intensively in Turkey, so that Turkey is the leading country for thyme production and export. Thyme production in Turkey is increasing year by year, with an average quinquennial

* Corresponding author: mgurgan@nku.edu.tr
[1] Tekirdağ Namık Kemal University
E-mail: sadiloglu@hotmail.com
ORCID: https://orcid.org/0000-0002-2966-1510, https://orcid.org/0000-0002-0062-0491

production of around 19 thousand ton/year [3]. There was a light decrease in 2021 compared to the previous year most probably due to decrease in demand in the market as a result of the pandemics.

The plant has a high drought tolerant and it can be cultivated in almost all soil types [4]. Thyme has a wide range of area of utilization. Pharmaceutical industry takes advantage of this medicinal aromatic plant in many applications due to its antimicrobial, uretic, blood glucose regulator, anti-inflammatory aspects. It is also a source for cosmetics such as soaps, detergents, creams, lotions, tooth pastes and mouth washes [5]. Thyme extracts have even been studied for its anti-anxiety effects through oral applications in rats [6]. Recently, thyme has been the focus of interest in agricultural applications. Thyme extract was tried on tomato wilt causing bacteria and promising results were obtained in order to use this herbal extract for field applications [7]. Similarly, thyme extract was shown to be utilized for crop protection of zucchini an alternative to chemical pesticides. The field trials revealed that thyme extract could be used as phyto-stimulant and plant strengthening hence increased crop yield [8].

The active phytochemicals in the essential oil of *Thymus vulgaris* L. are responsible for the medicinal aspects. The essential oil amount in *Thymus vulgaris* L. is 1.09-2.67%, which increases under drought as opposed to the crop yield [5]. The main components of the essential oil are thymol (40-70%), p-cymene, γ-terpinene, carvacrol, β-caryophyllene and α-terpinene, as the most abundant thymol is responsible for the characteristic smell of the plant [9].

Organic and clean agriculture is crucial for sustainable production of thyme, which is a very economically important plant for Turkey [5]. Moreover, all around the world, this plant matters as a medicinal aromatic plant, especially due to practical use in daily life for its antimicrobial activity. The nutrient contents of the agricultural crops depend on the agricultural implementations [10, 11]. The macro and micro nutrient elements are vital for growth, development and metabolic reaction of plants. The secondary metabolites are also dependent on the nutrient element contents. The nutrient change may considerably affect the antimicrobial activities of medicinal aromatic plants [12]. To the best of our knowledge, there is lack of information on the correlation of nutrient content and microbial inhibitory effect of *Thymus vulgaris* L. In order to sustain more conscious cultivation of plants with high medicinal and economical importance, information on medicinal aspects of such plants and their cultivation should be gathered and integrated. That is why, we have investigated the correlation of antibacterial activity of aerial parts of thyme with its nutrient elements in this study.

2. MATERIALS AND METHODS

The plant material used in this study was *Thymus vulgaris* L. grown under controlled lab conditions. The seeds purchased from a local seed supplier were germinated in peat (Klasmann Deilmann, Potground H). The specifications of the peat were provided elsewhere [13]. The seedlings were transferred to a 5L pot filled with soil acquired from the trial fields of Faculty of Agriculture, Namık Kemal University. Three seedlings were planted in the pot. The soil characteristics were as follows: The pH of the soil was 6.45, the content of available P_2O_5 was 36.2 mg/kg and exchangeable K_2O 225.18 mg/kg. Moreover, the organic matter concentration was 1.91% [12, 14]. No fertilizers and pesticides were used during the experiment. The plants were regularly watered and harvested after two months of period before the plants started to flower, the aerial parts were sequentially air dried and kept at 65 °C for 48 h in drying oven. The dried plant material was grinded and used to analyze the elemental content and the herbal extraction. The elemental content analyses were carried out in Namık Kemal University Central Lab (NABILTEM) on the dried plant material using ICP-OES (Inductively coupled plasma atomic emission spectroscopy).

In order to obtain herbal extraction, maceration was carried out with methanol as the solvent at room temperature. Grinded aerial parts of thyme were mixed with methanol (99.9%) (Sigma Aldrich) as 1:20 w/v. The mixture was kept at

room temperature for 3 days, filtered through filter paper, and the solvent was evaporated. The residual material after evaporation was dissolved in dimethyl sulfoxide DSMO (Thermo Fisher) and used for antibacterial activity test, as DMSO is known to have no antibacterial activity on the tested bacteria.

Agar well diffusion method was adopted to investigate the antibacterial activity of herbal extracts of *Thymus vulgaris* L. Mueller Hinton agar plates were prepared by autoclaving the agar medium at 121 ℃ for 20 minutes. All the equipment were also sterilized with autoclaving and the experiments were carried out under aseptic conditions. Two Gram positive bacteria (*Staphylococcus aureus* ATCC 29213 and *Enterococcus faecalis* ATCC 29212) and two Gram negative bacteria (*Escherichia coli* ATCC 25922 and *Pseudomonas aeruginosa* ATCC27853) were tested for the antibacterial activity of the thyme in this study. They were first grown on Columbia blood agar containing 5% sheep blood (Biomerieux). Next, for each bacterium, bacterial solution of 0.5 McFarland was prepared using sterile saline solution. The bacterial solutions were inoculated on the surface of Mueller Hinton agar plates (Himedia) with the help of sterile swab. Wells of 6 mm diameter were formed using sterile pipette tips and 50 µL of thyme extract was added to the wells. The plates were kept at 37 ℃ for 24 hours, after which the clearance around the wells were measured in mm and compared with the inhibition zone of 10 µg Gentamicin sulfate (Sigma Aldrich), as a positive control. The experiment was conducted with three replicates.

The basic statistics of the data were calculated using Minitab 13® and analyzed with Pearson Correlation.

3. RESULTS AND DISCUSSION

We studied the correlation of some nutrient elements of aerial parts of lab-grown thyme (*Thymus vulgaris* L.) with the antibacterial activity of its methanol extract on 4 different bacteria. The aboveground parts of the plant were dried as a whole and grinded to be used for macro and micro nutrient element determination and to obtain herbal extraction. The amounts of some of the macro and micro nutrient elements determined in thyme used in this study are given in Table 1.

Whole plants were dried and grinded properly, and some micro and macro nutrient elemental contents were determined with ICP-OES. The amounts of the micro and macro elements determined in basil plants used in this study is given in Table 1.

Table 1
Some macro and micro nutrient elements of *Thymus vulgaris* L.

	Nutrient Elements	**Amount**	**Limit values** (Mills and Jones 1996)**.**
Macro nutrient elements	P (%)	0.323 ± 0.003	0.25-0.29
	K (%)	2.515 ± 0.021	2.17-3.15
	Ca (%)	1.482 ± 0.306	0.50-1.25
	Mg (%)	0.414 ± 0.0872	0.29-0.40
Micro nutrient elements	Fe (mg kg^{-1})	585.00 ± 6.80	85-118
	Cu (mg kg^{-1})	1.27 ± 0.0153	6-9
	Zn (mg kg^{-1})	23.80 ± 0.377	68-99
	Mn (mg kg^{-1})	117.73 ± 2.15	38-98

B (mg kg^{-1})	34.63± 0.240	17-28

elements for the plants [18]The higher Mn and B levels in plant can be explained by this situation.

Table 2
Correlation between macro and micro nutrient elements of *Thymus vulgaris* L.

	P	**K**	**Ca**	**Mg**	**Fe**	**Cu**	**Zn**	**Mn**	**B**
P	1								
K	.992*	1							
Ca	.971	.934	1						
Mg	.978	.996*	.900	1					
Fe	1.00**	.990*	.975	.975	1				
Cu	.984	.954	.998**	.925	.986	1			
Zn	.910	.954	.785	.977	.904	.821	1		
Mn	1.00**	.995*	.965	.983	.999**	.979	.920	1	
B	.881	.816	.968	.763	.888	.952	.606	.870	1

The macro nutrient elements of the thyme grown in lab conditions on the soil obtained from the experimental fields of the university were very closed to the expected values given by Mills and Jones [15]. However, the situation for micro nutrient elements differs. While Cu is lower than the expected, iron is very high than the limit values. Iron is a very abundant element found in the earth crust, but not available for plants in alkaline and neutral soils [16]. The soil in Thrace Region of Turkey, where the university resides, is, however, usually acidic soil [17]. The soil in this study was also slightly acidic with pH 6.4 [14]. The acidity in soil increases the plant availability of the micro nutrient elements mentioned in this study.

Moreover, the concentrations of micro nutrient elements affect the availability of other nutrient

Moreover, a higher B level might be expectable since Turkey has the greatest reserves for boron, high boron concentrations in soil might be expected all around soil in Turkey [19]. The significant positive correlations of Fe and Mn, which are highly abundant in thyme in this study, with the other macro and micro elements can also be explained by this phenomenon (Table 2).

The methanol extract of thyme obtained by maceration was tested on two Gram-negative and two Gram-positive bacteria with agar well diffusion method (Figure 1). The cell wall differences between Gram-positive and Gram-negative bacteria may result in varying reactions of bacteria to different agents [20]. The results of this study were given in Table 3. When compared with the activity of a standard antibiotic

(Gentamicin), the extracts were most effective on the Gram- positive *E. faecalis* and the Gram-negative *P. aeruginosa*.

Figure 1 Examples from antibacterial activity testing agar

Table 3
Antibacterial effect of *Thymus vulgaris* L. on different bacterial strains

Bacterium	Inhibition zone (mm)	Zone of Gentamicin	Inhibition degree
S. aureus	11.67±1.53	23	++
E. faecalis	12.67±0.58	19	+++
P. aeruginosa	11.34±1.53	16	+++
E. coli	6.0 ± 0.00	18	+

++++ Excellent activity (100% inhibition), +++ Good activity (60-70% inhibition), ++ Significant activity (30-50% inhibition), + Negligible activity (10-20% inhibition), - no activity (<10% inhibition), Gentamicin: standard antibiotic

As a generalized result, a higher antibacterial activity of thyme extract on Gram-positive bacteria might be mentioned. The activity of the herbal extract on *E. coli* was negligible in this study. The two-layered cell wall of Gram-negative bacteria are usually responsible more resistance against antibacterial agents [21, 22]. However, a study on antibacterial activities of different plant extracts showed that E. coli was susceptible to herbal extracts [23]. Our previous results with another medicinal aromatic plant basil revealed a higher antibacterial activity against Gram-positive bacteria [12, 13]. Other studies also showed that thyme extract was highly effective on a Gram-positive bacterium *Clavibacter michiganensis* subsp. *michiganensis* which was the factor causing tomato wilt disease [7].

Methanol was found to be the one of the two best solvents among 7 other solvents for herbal extraction of thyme [24]. In the mentioned study, the researchers investigated the antibacterial activity of extracts with different solvents on a Gram-positive bacterium *Bacillus subtilis* and suggested to use either methanol or water + Tween 20 to obtain herbal extract. Methanol extraction was also chosen for basil and shown to degrade cell wall of bacteria, therefore can act better on Gram-positive bacteria whose cell wall consist of only peptidoglycan layer [25].

Table 4
Pearson's correlation coefficients between the antimicrobial activity and macro and micro nutrient elements of *Thymus vulgaris* L.

	P	K	Ca	Mg	Fe	Cu	Zn	Mn	B
S. aureus	.984	.954	.998**	.925	.986	1.000	.821	.979	0.99**
E. faecalis	.871	.804	.963	.749	.878	.945	.589	.859	1.00**
P. aeruginosa	.980	.997**	.904	1.000***	.997	.929	.974	.984	.769
E. coli	-	-	-	-	-	-	-	-	-

* = P < 0.1; ** = P < 0.05; ***= P < 0.01

The correlations of plant macro and micro nutrient elements with the antibacterial activity of the methanol extract were given in Table 4. The values used for antibacterial activity are inhibition zone diameters. Therefore, the higher the inhibition zone, the stronger the antibacterial effect of the extract. The antibacterial activity on *E. coli* was negligible, therefore, the correlation was alike. The significant positive correlation of Ca and B on Gram-positive bacteria are remarkable. The cell wall of these bacteria has high affinity for Ca and Mg, which destabilize the cell wall and thus kill the bacteria [26, 27]. Therefore, the plants grown in soils with similar

characteristics to the one used in this study might be suggested for higher antibacterial activity against especially *S. aureus*, which is very crucial by being a member of normal flora of human, but gained importance due to the methicillin resistance, which resulted in spreading of nosocomial infections [28]. Besides Ca, B correlation with antibacterial activity was very significantly positive. It is known that boron compounds damage bacteria cells by harming the enzymes in protein synthesis and therefore they are considered to be antibiotics and disinfectants [29, 30]. Boron compounds are increasingly used in detergents and disinfectants in Turkey as being the largest boron reserve of the world.

The highly significant positive correlation of Mg and K with inhibition of only *P. aeruginosa* growth is also remarkable. Studies showed that when Mg was limited in the growth environment, the bacterium showed a tendency to form a biofilm, and therefore persist in the environment, and also exerted its virulence and became pathogenic to the organism [31, 32]. Therefore, the plant extract being rich in Mg can be considered better for its antibacterial activity against this bacterium, which is and opportunistic human pathogen [33]. The molecular basis of the effect of extracellular K concentration on growth inhibition of *P. aeruginosa* was shown by Lindestam Arlehamn et al. (2010) [34]. Therefore, in order to fight with *P. aeruginosa* and *S. aureus* with thyme extracts, it would be better for the plant be rich in especially Ca, K, Mg, and B.

4. CONCLUSION

The present study aimed to examine the correlation of plant nutrient elements with the antibacterial activity of methanol extract of *Thymus vulgaris* L. grown on soil from the experimental field without application of fertilizers or pesticides. The plant was sufficient in terms of macro elements, while some micro elements such as Fe, Mn and B. The herbal extract was successful in inhibiting the growth of two Gram-positive and one Gram-negative bacteria, which are opportunistic human pathogens. The results revealed that the macro and micro nutrient elements were of importance for antibacterial activity of the herbal extract obtained from the aerial parts. Although, the extract of thyme was successful in inhibiting the growth of *S. aureus*, *E. faecalis* and *P. aeruginosa*, the correlation analysis of the nutrient elements showed which elements are more crucial in the fight with each bacterium. The results also suggested that higher K and Mg contents of the plant would result in higher antibacterial activity against *P. aeruginosa*, most probably up to a point. Similarly, Ca and B contents are important to fight against Gram-positive bacteria. Further studies might be carried out focusing on the maximum levels of macro and micro nutrients, especially resulting from fertilizer and pesticide use, in relation to the biological activities required for use of such medicinal plants in traditional medicine and pharmaceutical industry.

Funding

The authors have not received any financial support for the research, authorship or publication of this study.

The Declaration of Conflict of Interest/ Common Interest

No conflict of interest or common interest has been declared by the authors.

Authors' Contribution

MG: Data collection, statistical analyses, Literature research, Manuscript Preparation

SA: Data collection, Manuscript Preparation

The Declaration of Ethics Committee Approval

This study does not require ethics committee permission or any special permission.

The Declaration of Research and Publication Ethics

The authors of the paper declare that they comply with the scientific, ethical and quotation rules of

SAUJS in all processes of the paper and that they do not make any falsification on the data collected. In addition, they declare that Sakarya University Journal of Science and its editorial board have no responsibility for any ethical violations that may be encountered, and that this study has not been evaluated in any academic publication environment other than Sakarya University Journal of Science.

REFERENCES

[1] A. Tan, "Plant Genetic Resources and Conservation in Turkey ," Anadolu, vol. 20, no. 1, pp. 7–25, 2010.

[2] M. Dönmez, M. Kargıoğlu, M. Temel, "Stachys palustris L.'in Morfolojik, Anatomik ve Ekolojik Özellikleri" Afyon Kocatepe University Journal of Sciences and Engineering, vol. 11, pp. 1-9, 2011.

[3] TUIK, "Turkish Statistical Institute," 2022. https://biruni.tuik.gov.tr/medas/?kn=92&lo (accessed Apr. 03, 2022).

[4] M. Ashrafi, M. Reza, A. Moqadam, P. Moradi, F. Shekari, E. Mohsenifard, "Identification of Drought Tolerant and Sensitive Species of Thyme through Some Physiological Criteria," International Journal of Horticultural Science and Technology, vol. 5, no. 1, pp. 53–63, 2018.

[5] Ç. Bozdemir, "Türkiye'de Yetişen Kekik Türleri, Ekonomik Önemi ve Kullanım Alanları," Yüzüncü Yıl Üniversitesi Journal of Agricultural Sciences, vol. 29, no. 3, pp. 583–594, 2019.

[6] A. Komaki, F. Hoseini, S. Shahidi, N. Baharlouei, "Study of the effect of extract of Thymus vulgaris on anxiety in male rats," Journal of Traditional and Complementary Medicine, vol. 6, no. 3, pp. 257–261, Jul. 2016.

[7] S. Belgüzar, M. Yılar, Y. Yanar, İ. Kadıoğlu, G. Doğar. "Antibacterial activities of Thymus vulgaris L.(Thyme) extract and essential oil againt Clavibacter michiganensis subsp. michiganensis." Turkish Journal of Weed Science vol. 19, no. 2 pp. 20-27, 2016.

[8] C. Beni, L. Casorri, E. Masciarelli, B. Ficociello, O. Masetti, U. Neri, R. Aromolo, S. Rinaldi, P. Papetti, A. Cichelli. "Characterization of thyme and tansy extracts used as basic substances in zucchini crop protection." Journal of Agricultural Studies vol. 8, pp. 95-110, 2020.

[9] B. Galambosi, C. Rey, J. F. Vouillamoz, "Suitability of Swiss herb cultivars under Finnish climatic conditions," Acta Horticulturae, vol. 860, pp. 173–180, 2010.

[10] F. López-Granados, M. Jurado-Expósito, S. Atenciano, A. García-Ferrer, M. Sánchez De La Orden, L. García-Torres, "Spatial variability of agricultural soil parameters in southern Spain," Plant and Soil, vol. 246, no. 1, pp. 97–105, 2002.

[11] T. Rütting, H. Aronsson, S. Delin, "Efficient use of nitrogen in agriculture," Nutrient Cycling in Agroecosystems vol. 110, no. 1, pp. 1–5, 2018.

[12] M. Gürgan, S. Adiloğlu, "Increasing concentrations of iron fertilizer affect antibacterial activity of basil (Ocimum basilicum L.)," Industrial Crops and Products, vol. 170, p. 113768, 2021.

[13] M. Gürgan Eser, S. Adiloğlu, "The correlation of some nutrient elements and antibacterial activity of the basil (Ocimum basilicum)," Tekirdağ Ziraat Fakültesi Dergisi, vol. 17, no. 3, pp. 381–391, 2020.

[14] S. Adiloğlu, "Relation of chelated iron (EDDHA-Fe) applications with iron

accumulation and some plant nutrient elements in basil (Ocimum basilicum L.)," Polish Journal of Environmental Studies, vol. 30 no. 4, pp. 1-9, 2021.

[15] Mills H. A., Jones J. B. Jr, *Plant Analysis Handbook II: A practical sampling, preparation, analysis, and interpretation guide*. MicroMacro Publishing, 1996.

[16] M. L. Guerinot, Yi Ying, "Iron: Nutritious, noxious, and not readily available," Plant Physiology, vol. 104, no. 3, pp. 815–820, 1994.

[17] A. Adiloglu, S. Adiloglu, "The investigation of some available trace element contents of acid soils in Turkey," Archives of Agronomy and Soil Science, vol. 49, no. 2, pp. 179–185, 2003.

[18] B. Kacar, V. Katkat, Bitki Besleme (Plant Nutrition), vol. 1. Bursa: U. Ü. Güçlendirme Vakfı, 1998.

[19] C. Helvacı, "Borate deposits: An overview and future forecast with regard to mineral deposits," Journal of Boron, vol. 2, no. 2, pp. 59–70, 2017.

[20] A. Mai-Prochnow, M. Clauson, J. Hong, A. B. Murphy, "Gram positive and Gram negative bacteria differ in their sensitivity to cold plasma," Scientific Reports, vol. 6, no. 1, pp. 1–11, 2016.

[21] G. M. S. Soares, L. C. Figueiredo, M. Faveri, S. C. Cortelli, P. M. Duarte, M. Feres, "Mechanisms of action of systemic antibiotics used in periodontal treatment and mechanisms of bacterial resistance to these drugs," Journal of Applied Oral Science, vol. 20, no. 3., pp. 295–305, 2012.

[22] H. I. Zgurskaya, C. A. López, S. Gnanakaran, "Permeability barrier of Gram-negative cell envelopes and approaches to bypass it," ACS Infectious Diseases, vol. 1, no. 11, pp. 512–522, 2016.

[23] Z. Nalbantbaşi, A. Gölcü, "Kahramanmaraş Yöresine Ait Şifalı Bitkilerin Antimikrobiyal Aktiviteleri Antimicrobial Activities Of Medical Plants That Belong to Kahramanmaras Region," 2009.

[24] M. Benli, N. Yiğit, "Ülkemizde Yaygın Kullanımı Olan Kekik (Thymus vulgaris) Bitkisinin Antimikrobiyal Aktivitesi," Orlab On-Line Mikrobiyoloji Dergisi, vol. 3, no. 8, pp. 1–8, 2005.

[25] I. Kaya, N. Yigit, M. Benli, "Antimicrobial activity of various extracts of *Ocimum basilicum* l. and observation of the inhibition effect on bacterial cells by use of scanning electron microscopy," African Journal of Traditional, Complementary and Alternative Medicines, vol. 5, no. 4, p. 363, 2008.

[26] K. J. Thomas, C. V. Rice, "Revised model of calcium and magnesium binding to the bacterial cell wall," BioMetals, vol. 27, no. 6, pp. 1361–1370, 2014.

[27] Y. Xie, L. Yang, "Calcium and magnesium ions are membrane-active against stationary-phase Staphylococcus aureus with high specificity," Scientific Reports, vol. 6, no. 20628, pp. 1–8, Feb. 2016.

[28] B. Poorabbas *J. Mardaneh, Z. Rezaei, M. Kalani, G. Pouladfar, M. H. Alami, J. Soltani, A. Shamsi-Zadeh, S. Abdoli-Oskooi, M. J. Saffar, A. Alborzi* "Nosocomial Infections: Multicenter surveillance of antimicrobial resistance profile of Staphylococcus aureus and Gram negative rods isolated from blood and other sterile body fluids in Iran" Iranian journal of microbiology, vol. 7, no. 3, pp. 127–35, 2015.

[29] Z. Sayin, U. S. Ucan, A. Sakmanoglu, "Antibacterial and antibiofilm effects of boron on different bacteria," Biological Trace Element Research, vol. 173, no. 1, pp. 241–246, 2016.

[30] V. Hernandez, T. Crépin, A. Palencia, S. Cusack, T. Akama, S.J. Baker, W. Bu, L. Feng, Y.R. Freund, L. Liu, M. Meewan "Discovery of a novel class of boron-based antibacterials with activity against gram-negative bacteria," Antimicrobial Agents and Chemotherapy, vol. 57, no. 3, pp. 1394–1403, 2013.

[31] H. Mulcahy, S. Lewenza, "Magnesium Limitation Is an Environmental Trigger of the Pseudomonas aeruginosa Biofilm Lifestyle," PLOS ONE, vol. 6, no. 8, p. e23307, 2011.

[32] T. Guina, M. Wu, S.I. Miller, S.O. Purvine, E.C. Yi, J. Eng, D.R. Goodlett, R. Aebersold, R.K. Ernst, K.A Lee, "Proteomic analysis of Pseudomonas aeruginosa grown under magnesium limitation" J Am Soc Mass Spectrom, vol. 14, no. 7, pp. 742–751, 2003.

[33] W. Wu, Y. Jin, F. Bai, S. Jin, "Pseudomonas aeruginosa," in Molecular Medical Microbiology, Elsevier, 2015, pp. 753–767.

[34] C. S. Lindestam Arlehamn, V. Pétrilli, O. Gross, J. Tschopp, T. J. Evans, "The role of potassium in inflammasome activation by bacteria," Journal of Biological Chemistry, vol. 285, no. 14, pp. 10508–10518, 2010.

SAKARYA ÜNİVERSİTESİ
FEN BİLİMLERİ ENSTİTÜSÜ DERGİSİ

Sakarya University Journal of Science
SAUJS

ISSN 1301-4048 | e-ISSN 2147-835X | Period Bimonthly | Founded: 1997 | Publisher Sakarya University | http://www.saujs.sakarya.edu.tr/

Title: Investigation of Lateral and Vertical Dynamic Responses of a Full Car Model Exposed to Sine Road Input

Authors: Mustafa EROĞLU

Recieved: 2022-05-23 00:00:00

Accepted: 2022-06-28 00:00:00

Article Type: Research Article

Volume: 26
Issue: 4
Month: August
Year: 2022
Pages: 829-841

How to cite
Mustafa EROĞLU; (2022), Investigation of Lateral and Vertical Dynamic Responses of a Full Car Model Exposed to Sine Road Input. Sakarya University Journal of Science, 26(4), 829-841, DOI: 10.16984/saufenbilder.1120433
Access link
http://www.saujs.sakarya.edu.tr/en/pub/issue/72361/1120433

Sakarya University Journal of Science 26(4), 829-841, 2022

Investigation of Lateral and Vertical Dynamic Responses of a Full Car Model Exposed to Sine Road Input

Mustafa EROĞLU*[1]

Abstract

In this study, the full car model, which is exposed to a sinusoidal road input, has been examined to ensure the driving safety of the vehicles and the comfort of the passengers. In this context, the full car, including lateral and vertical movements, is modeled with fourteen degrees of freedom. The second-order equations of motion of the modeled vehicle were obtained using the Lagrangian method and reduced to first-order equations of motion using the state-space form. Then, these equations of motion were solved precisely in the time domain using the Euler method in the Matlab environment. To examine the lateral movements and the rotations of the vehicle in the pitch and roll axis, a sine wave with a wavelength of 5 m and an amplitude of 0,1 m was applied to the wheels of the vehicle. In the analysis, the right front wheel is exposed to a sinusoidal road input at t=0 s, while the left front wheel is exposed to a sinusoidal road input after the vehicle moves 2,5 m. Thus, both the pitch and roll motion of the vehicle will be examined in detail. In the study, four different vehicle masses 500 kg, 1000 kg, 2000 kg, and 3000 kg were taken into consideration and the effect of different vehicle masses on passenger and vehicle dynamic behaviors was investigated. In addition, the situation of passing vehicles at variable speeds from the given disruptive road input has also been examined. The maximum dynamic responses of the passenger and the vehicle were examined when the vehicle speed changed from 3 m/s to 50 m/s by 0,1 m/s. In the study, it has been observed that the vehicle mass and certain vehicle speed have effects on the vertical and lateral displacements and accelerations of the passenger and the vehicle.

Keywords: Full car model, passive suspension system, ride holding, passenger comfort

1. INTRODUCTION

Vehicle suspension systems are mechanical systems positioned between the wheels and the vehicle body to minimize the vertical vibrations of vehicles exposed to disruptive road inputs. The performance of the suspension systems is important in terms of vehicle driving dynamics and the comfort of the passengers carried. The main purpose of suspension systems consisting of spring, damping elements, and connection equipment is to ensure the driving safety of the vehicle and the comfort of the passengers.

* Corresponding author: mustafaeroglu@sakarya.edu.tr
[1] Sakarya University
ORCID: https://orcid.org/0000-0002-1429-7656

It is expected that both driving safety and passenger comfort will give the highest performance in vehicles. However, it is very difficult for both of them to give maximum performance in passive suspension systems. Because driving safety and passenger comfort are parameters that affect each other. Traditionally, passive suspension systems used in many vehicles have only spring and damping elements, and their coefficients are fixed but cannot be changed. In passive suspensions, there are semi-active and active suspensions that allow for external control. Within the scope of simulation and analysis of suspension systems, Agarkakli et al. performed the passive and active suspension analysis of the quarter car model exposed to different road inputs [1]. Again, using the quarter car model, Nagarkar et al. made optimization and control in Matlab/Simulink environment with PID and LQR controller [2].

Yildirim and Esen examined the dynamic behavior in the vertical direction only by using a full vehicle model, taking into account different road inputs and different vehicle speeds [3]. The most used controller as an active controller in vehicle suspension systems is usually fuzzy logic. Yagiz et al. studied the active suspension control of a five-degree-of-freedom car model using fuzzy logic [4]. Salem and Aly proposed an active suspension system to ensure the driving comfort of the quarter car, which was modeled as two degrees of freedom using a fuzzy logic controller [5]. Fuzzy logic controllers and PID type controllers are used as a hybrid. In this context, Singh and Aggarwal controlled the passenger seat vibrations of the semi-active quarter car model using hybrid fuzzy logic and the PID approach [6]. Again, the same author reduced the vibrations of a three-degree-of-freedom quarter-car by using fuzzy logic and a self-adaptive fuzzy logic controller modeled as a hybrid [7]. Swethamarai and Lakshmi designed a hybrid fuzzy logic and PID controller in the active quarter car model to minimize the vibrations affecting the driver [8].

Eroğlu et al. investigated the dynamic responses of the car using a fuzzy logic controller with PID in the car-bridge interaction model using a quarter car [9]. In some studies, bridges where high-speed trains pass have been modeled as Euler-Bernoulli beams and analyzed [10].

In the literature, it has been seen that vehicle models are generally modeled as quarter models for convenience. In some studies, controllers such as H∞, and LQR have been preferred to minimize the vibrations affecting the vehicle and passenger by using the quarter vehicle model [11-13]. In some studies, the dynamic behavior of bridges modeled as beams without using active controllers has been investigated using a tuned mass damper [14].

In most of the studies given above, car models are generally considered quarter or half models. In addition, almost all studies have examined the dynamic behavior of vehicles only in the vertical direction. In this study, the vehicle model can be modeled as having fourteen degrees of freedom and can be examined in dynamic responses in the lateral direction. With the full vehicle model, dynamic displacements and acceleration values affecting the passenger were examined according to the mass of the vehicle and the speed of the vehicle.

2. FULL CAR MODEL

In this section, the definitions of the full car model exposed to sinus road input will be made. When both lateral and vertical movements of the full car model examined in this study are examined, the full car model is modeled as fourteen degrees of freedom. Fourteen independent degrees of freedom are shown in Figure 1. In addition, a full car model and a passenger seat are also included in the model. Thus, lateral and vertical dynamic behaviors affecting both the passenger and the vehicle can be examined. When the parameters in Figure 1 are examined, the mass of the passenger is represented by md, the mass of the vehicle is represented by mc and the mass of the wheels is represented by mw. Icx and Icy represent the mass moments of inertia about the roll and pitch axis, respectively. The k_{dz}, c_{dz}, k_{dz} and k_{dy} parameters represent the vertical and lateral

suspension coefficients between the passenger seat and the vehicle, respectively. While k_{w1z}, k_{w2z}, k_{w3z} and k_{w4z} represent the stiffness coefficients in the vertical direction between the vehicle and the wheel, k_{w1y}, k_{w2y}, k_{w3y} and k_{w4y} represent the lateral stiffness coefficients. Similarly, c_{w1z}, c_{w2z}, c_{w3z}, and c_{w4z} represent the damping coefficient in the vertical direction, while c_{w1y}, c_{w2y}, c_{w3y}, and c_{w4y} represent the damping coefficient in the lateral direction. The parameters k_{r1}, k_{r2}, k_{r3}, and k_{r4} represent the stiffness coefficient of the tire. r_{dz} and rdy describe the vertical and lateral displacement of the passenger, respectively, while r_{cz} and rcy describe the vertical and lateral displacements of the vehicle. While r_{w1z}, r_{w2z}, r_{w3z}, and r_{w4z} describe the movement of the wheels in the vertical direction, r_{w1y}, r_{w2y}, r_{w3y} and r_{w4y} describe their movement in the lateral direction. In addition, the roll and pitch movements of the vehicle are represented by Θ_{cx} and Θ_{cy}. r_1, r_2, r_3, and r_4 represent the sinusoidal effect coming from the road to the wheels. Distances a and b define the length of the vehicle's center of mass to the front and rear wheels, respectively, while distances c and d define the distance to the right and left wheels. The lengths e and f define the distances from the passenger seat to the center of mass of the vehicle. The values of all given parameters are shown in Table 1.

To examine the dynamic responses of the full car model, it is necessary to obtain the equations of motion for each degree of freedom. In this study, the Lagrangian method was used to obtain the equations of motion. The kinetic energy, potential energy, and damping function of the full car model are given in Equations (1-3).

Using equation (1-3), the Lagrangian expression can be written as follows. The generalized coordinates of the full car model are taken as in Equation 5.

$$E_k = \frac{1}{2}\begin{bmatrix} m_d\dot{r}_{dz}^2 + m_d\dot{r}_{dy}^2 + m_c\dot{r}_{cz}^2 + m_c\dot{r}_{cy}^2 + I_{cx}\dot{\theta}_{cx}^2 + I_{cy}\dot{\theta}_{cy}^2 + m_w\dot{r}_{w1z}^2 + m_w\dot{r}_{w2z}^2 \\ +m_w\dot{r}_{w3z}^2 + m_w\dot{r}_{w4z}^2 + m_w\dot{r}_{w1y}^2 + m_w\dot{r}_{w2y}^2 + m_w\dot{r}_{w3y}^2 + m_w\dot{r}_{w4y}^2 \end{bmatrix} \quad (1)$$

$$E_p = \frac{1}{2}\begin{bmatrix} k_{dz}\left[r_{dz} - r_{cz} + \theta_{cy}e - \theta_{cx}f\right]^2 + k_{dy}\left[r_{dy} - r_{cy} + \theta_{cx}h\right]^2 \\ +k_{w1z}\left[r_{cz} - r_{w1z} - \theta_{cy}a - \theta_{cx}c\right]^2 + k_{w2z}\left[r_{cz} - r_{w2z} - \theta_{cy}a + \theta_{cx}d\right]^2 \\ +k_{w3z}\left[r_{cz} - r_{w3z} + \theta_{cy}b - \theta_{cx}c\right]^2 + k_{w4z}\left[r_{cz} - r_{w4z} + \theta_{cy}b + \theta_{cx}d\right]^2 \\ +k_{w1y}\left[r_{cy} - r_{w1y}\right]^2 + k_{w2y}\left[r_{cy} - r_{w2y}\right]^2 + k_{w3y}\left[r_{cy} - r_{w3y}\right]^2 \\ +k_{w4y}\left[r_{cy} - r_{w4y}\right]^2 + k_{r1}\left[r_{w1z} - r_1\right]^2 + k_{r2}\left[r_{w2z} - r_2\right]^2 \\ +k_{r3}\left[r_{w3z} - r_3\right]^2 + k_{r4}\left[r_{w4z} - r_4\right]^2 \end{bmatrix} \quad (2)$$

$$D = \frac{1}{2}\begin{bmatrix} c_{dz}\left[\dot{r}_{dz} - \dot{r}_{cz} + \dot{\theta}_{cy}e - \dot{\theta}_{cx}f\right]^2 + c_{dy}\left[\dot{r}_{dy} - \dot{r}_{cy} + \dot{\theta}_{cx}h\right]^2 \\ +c_{w1z}\left[\dot{r}_{cz} - \dot{r}_{w1z} - \dot{\theta}_{cy}a - \dot{\theta}_{cx}c\right]^2 + c_{w2z}\left[\dot{r}_{cz} - \dot{r}_{w2z} - \dot{\theta}_{cy}a + \dot{\theta}_{cx}d\right]^2 \\ +c_{w3z}\left[\dot{r}_{cz} - \dot{r}_{w3z} + \dot{\theta}_{cy}b - \dot{\theta}_{cx}c\right]^2 + c_{w4z}\left[\dot{r}_{cz} - \dot{r}_{w4z} + \dot{\theta}_{cy}b + \dot{\theta}_{cx}d\right]^2 \\ +c_{w1y}\left[\dot{r}_{cy} - \dot{r}_{w1y}\right]^2 + c_{w2y}\left[\dot{r}_{cy} - \dot{r}_{w2y}\right]^2 + c_{w3y}\left[\dot{r}_{cy} - \dot{r}_{w3y}\right]^2 \\ +c_{w4y}\left[\dot{r}_{cy} - \dot{r}_{w4y}\right]^2 \end{bmatrix} \quad (3)$$

$$\frac{\mathrm{d}}{\mathrm{d}t}\left(\frac{\partial L}{\partial \dot{\eta}_k(t)}\right) - \frac{\partial L}{\partial \eta_k(t)} + \frac{\partial D}{\partial \dot{\eta}_k(t)} = 0 \qquad k = 1, 2, 3 \ldots 14 \quad (4)$$

$$\boldsymbol{\eta}(t)=\left\{\begin{array}{cccccccc} r_{dz} & r_{dy} & r_{cz} & r_{cy} & \theta_{cy} & \theta_{cx} & r_{w1z} & r_{w2z} \\ r_{w3z} & r_{w4z} & r_{w1y} & r_{w2y} & r_{w3y} & r_{w4y} \end{array}\right\}^{T}, \tag{5}$$

Using the Lagrangian method, the fourteen equations of motion of the full car model are obtained as follows.

Vertical displacement of the passenger:

$$m_d\ddot{r}_{dz}+k_{dz}\left[r_{dz}-r_{cz}+\theta_{cy}e-\theta_{cx}f\right]+c_{dz}\left[\dot{r}_{dz}-\dot{r}_{cz}+\dot{\theta}_{cy}e-\dot{\theta}_{cx}f\right]=0 \tag{6}$$

Lateral displacement of the passenger:

$$m_d\ddot{r}_{dy}+k_{dy}\left[r_{dy}-r_{cy}+\theta_{cx}h\right]+c_{dy}\left[\dot{r}_{dy}-\dot{r}_{cy}+\dot{\theta}_{cx}h\right]=0 \tag{7}$$

Vertical displacement of the car body:

$$\begin{aligned} &m_c\ddot{r}_{cz}-k_{dz}\left[r_{dz}-r_{cz}+\theta_{cy}e-\theta_{cx}f\right]+k_{w1z}\left[r_{cz}-r_{w1z}-\theta_{cy}a-\theta_{cx}c\right] \\ &+k_{w2z}\left[r_{cz}-r_{w2z}-\theta_{cy}a+\theta_{cx}d\right]+k_{w3z}\left[r_{cz}-r_{w3z}+\theta_{cy}b-\theta_{cx}c\right] \\ &+k_{w4z}\left[r_{cz}-r_{w4z}+\theta_{cy}b+\theta_{cx}d\right]-c_{dz}\left[\dot{r}_{dz}-\dot{r}_{cz}+\dot{\theta}_{cy}e-\dot{\theta}_{cx}f\right] \\ &+c_{w1z}\left[\dot{r}_{cz}-\dot{r}_{w1z}-\dot{\theta}_{cy}a-\dot{\theta}_{cx}c\right]+c_{w2z}\left[\dot{r}_{cz}-\dot{r}_{w2z}-\dot{\theta}_{cy}a+\dot{\theta}_{cx}d\right] \\ &+c_{w3z}\left[\dot{r}_{cz}-\dot{r}_{w3z}+\dot{\theta}_{cy}b-\dot{\theta}_{cx}c\right]+c_{w4z}\left[\dot{r}_{cz}-\dot{r}_{w4z}+\dot{\theta}_{cy}b+\dot{\theta}_{cx}d\right]=0 \end{aligned} \tag{8}$$

Lateral displacement of the car body:

$$\begin{aligned} &m_c\ddot{r}_{cy}-k_{dy}\left[r_{dy}-r_{cy}+\theta_{cx}h\right]+k_{w1y}\left[r_{cy}-r_{w1y}\right]+k_{w2y}\left[r_{cy}-r_{w2y}\right] \\ &+k_{w3y}\left[r_{cy}-r_{w3y}\right]+k_{w4y}\left[r_{cy}-r_{w4y}\right]-c_{dy}\left[\dot{r}_{dy}-\dot{r}_{cy}+\dot{\theta}_{cx}h\right] \\ &+c_{w1y}\left[\dot{r}_{cy}-\dot{r}_{w1y}\right]+c_{w2y}\left[\dot{r}_{cy}-\dot{r}_{w2y}\right] \\ &+c_{w3y}\left[\dot{r}_{cy}-\dot{r}_{w3y}\right]+c_{w4y}\left[\dot{r}_{cy}-\dot{r}_{w4y}\right]=0 \end{aligned} \tag{9}$$

Pitch motion of the car body:

$$\begin{aligned} &I_{cy}\ddot{\theta}_{cy}+k_{dz}e\left[r_{dz}-r_{cz}+\theta_{cy}e-\theta_{cx}f\right]-k_{w1z}a\left[r_{cz}-r_{w1z}-\theta_{cy}a-\theta_{cx}c\right] \\ &-k_{w2z}a\left[r_{cz}-r_{w2z}-\theta_{cy}a+\theta_{cx}d\right]+k_{w3z}b\left[r_{cz}-r_{w3z}+\theta_{cy}b-\theta_{cx}c\right] \\ &+k_{w4z}b\left[r_{cz}-r_{w4z}+\theta_{cy}b+\theta_{cx}d\right]+c_{dz}e\left[\dot{r}_{dz}-\dot{r}_{cz}+\dot{\theta}_{cy}e-\dot{\theta}_{cx}f\right] \\ &-c_{w1z}a\left[\dot{r}_{cz}-\dot{r}_{w1z}-\dot{\theta}_{cy}a-\dot{\theta}_{cx}c\right]-c_{w2z}a\left[\dot{r}_{cz}-\dot{r}_{w2z}-\dot{\theta}_{cy}a+\dot{\theta}_{cx}d\right] \\ &+c_{w3z}b\left[\dot{r}_{cz}-\dot{r}_{w3z}+\dot{\theta}_{cy}b-\dot{\theta}_{cx}c\right]+c_{w4z}b\left[\dot{r}_{cz}-\dot{r}_{w4z}+\dot{\theta}_{cy}b+\dot{\theta}_{cx}d\right]=0 \end{aligned} \tag{10}$$

Roll motion of the car body:

$$
\begin{aligned}
&I_{cx}\ddot{\theta}_{cx} - k_{dz} f\left[r_{dz} - r_{cz} + \theta_{cy} e - \theta_{cx} f\right] - k_{w1z} c\left[r_{cz} - r_{w1z} - \theta_{cy} a - \theta_{cx} c\right] \\
&+k_{w2z} d\left[r_{cz} - r_{w2z} - \theta_{cy} a + \theta_{cx} d\right] - k_{w3z} c\left[r_{cz} - r_{w3z} + \theta_{cy} b - \theta_{cx} c\right] \\
&+k_{w4z} d\left[r_{cz} - r_{w4z} + \theta_{cy} b + \theta_{cx} d\right] - c_{dz} f\left[\dot{r}_{dz} - \dot{r}_{cz} + \dot{\theta}_{cy} e - \dot{\theta}_{cx} f\right] \\
&-c_{w1z} c\left[\dot{r}_{cz} - \dot{r}_{w1z} - \dot{\theta}_{cy} a - \dot{\theta}_{cx} c\right] + c_{w2z} d\left[\dot{r}_{cz} - \dot{r}_{w2z} - \dot{\theta}_{cy} a + \dot{\theta}_{cx} d\right] \\
&-c_{w3z} c\left[\dot{r}_{cz} - \dot{r}_{w3z} + \dot{\theta}_{cy} b - \dot{\theta}_{cx} c\right] + c_{w4z} d\left[\dot{r}_{cz} - \dot{r}_{w4z} + \dot{\theta}_{cy} b + \dot{\theta}_{cx} d\right] = 0
\end{aligned}
\tag{11}
$$

Vertical displacement of the right front wheel:

$$
\begin{aligned}
&m_w \ddot{r}_{w1z} - k_{w1z}\left[r_{cz} - r_{w1z} - \theta_{cy} a - \theta_{cx} c\right] \\
&+k_{r1}\left[r_{w1z} - r_1\right] - c_{w1z}\left[\dot{r}_{cz} - \dot{r}_{w1z} - \dot{\theta}_{cy} a - \dot{\theta}_{cx} c\right] = 0
\end{aligned}
\tag{12}
$$

Vertical displacement of the left front wheel:

$$
\begin{aligned}
&m_w \ddot{r}_{w2z} - k_{w2z}\left[r_{cz} - r_{w2z} - \theta_{cy} a + \theta_{cx} d\right] \\
&+k_{r2}\left[r_{w2z} - r_2\right] - c_{w2z}\left[\dot{r}_{cz} - \dot{r}_{w2z} - \dot{\theta}_{cy} a + \dot{\theta}_{cx} d\right] = 0
\end{aligned}
\tag{13}
$$

Vertical displacement of the rigth rear wheel:

$$
\begin{aligned}
&m_w \ddot{r}_{w3z} - k_{w3z}\left[r_{cz} - r_{w3z} + \theta_{cy} b - \theta_{cx} c\right] \\
&+k_{r3}\left[r_{w3z} - r_3\right] - c_{w3z}\left[\dot{r}_{cz} - \dot{r}_{w3z} + \dot{\theta}_{cy} b - \dot{\theta}_{cx} c\right] = 0
\end{aligned}
\tag{14}
$$

Vertical displacement of the left rear wheel:

$$
\begin{aligned}
&m_w \ddot{r}_{w4z} - k_{w4z}\left[r_{cz} - r_{w4z} + \theta_{cy} b + \theta_{cx} d\right] \\
&+k_{r4}\left[r_{w4z} - r_4\right] - c_{w4z}\left[\dot{r}_{cz} - \dot{r}_{w4z} + \dot{\theta}_{cy} b + \dot{\theta}_{cx} d\right] = 0
\end{aligned}
\tag{15}
$$

Lateral displacement of the rigt front wheel:

$$
m_w \ddot{r}_{w1y} - k_{w1y}\left[r_{cy} - r_{w1y}\right] - c_{w1y}\left[\dot{r}_{cy} - \dot{r}_{w1y}\right] = 0 \tag{16}
$$

Lateral displacement of the left front wheel:

$$
m_w \ddot{r}_{w2y} - k_{w2y}\left[r_{cy} - r_{w2y}\right] - c_{w2y}\left[\dot{r}_{cy} - \dot{r}_{w2y}\right] = 0 \tag{17}
$$

Lateral displacement of the rigt rear wheel:

$$
m_w \ddot{r}_{w3y} - k_{w3y}\left[r_{cy} - r_{w3y}\right] - c_{w3y}\left[\dot{r}_{cy} - \dot{r}_{w3y}\right] = 0 \tag{18}
$$

Lateral displacement of the left rear wheel:

$$
m_w \ddot{r}_{w4y} - k_{w4y}\left[r_{cy} - r_{w4y}\right] - c_{w4y}\left[\dot{r}_{cy} - \dot{r}_{w4y}\right] = 0 \tag{19}
$$

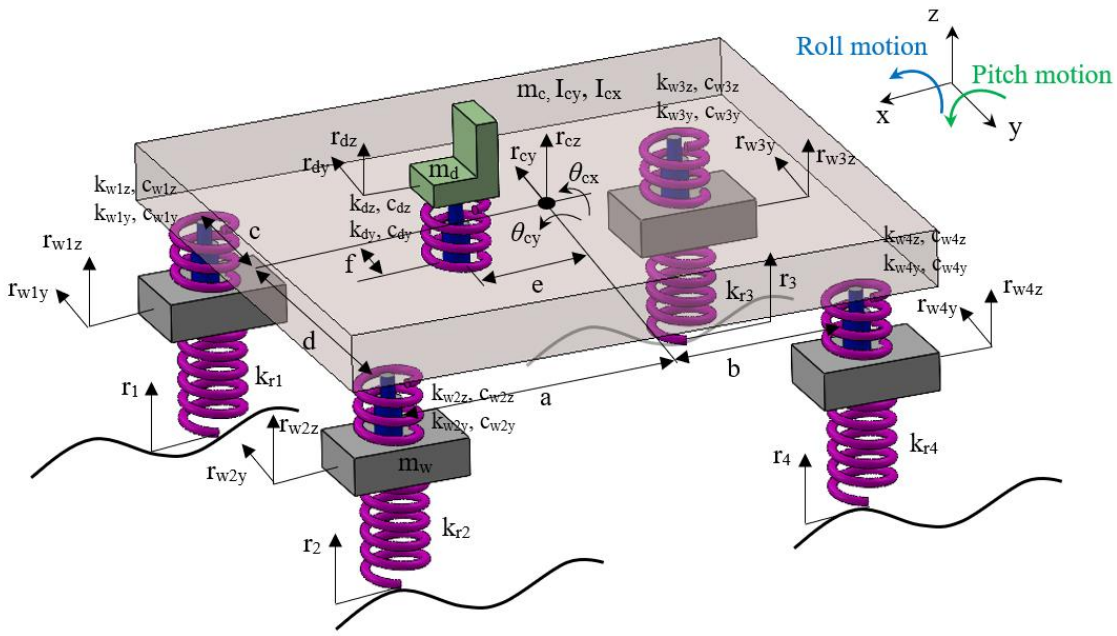

Figure 1 Full car model

The second-order equations of motion of the passengers, vehicles, and wheels in the vertical and lateral directions are given above. The obtained 14 differential equations are reduced to 28 first-order equations of motion by using state-space forms. Thus, when the sinusoidal road input is applied to the wheels of the full car, as in Figure 2, the dynamic responses of the vehicle and the passenger can be examined in the Matlab program environment by using the Euler method.

Table 1 Full car parameters

Full car model	
Driver mass (m_d)	100 kg
Car mass (m_c)	2000 kg
Wheel mass (m_w)	45 kg
Mass moment of inertia of car around pitch axis (Θ_{cy})	1500 kg.m^2
Mass moment of inertia of car around roll axis (Θ_{cx})	1680 kg.m^2
Primary suspension stiffness coefficient (k_{dz})	8000 N/m
Primary suspension stiffness coefficient (k_{dy})	14000 /m
Secondary suspension stiffness coefficient (k_{w1z}, k_{w2z}, k_{w3z}, k_{w4z})	25000 N/m
Secondary suspension stiffness coefficient (k_{w1y}, k_{w2y}, k_{w3y}, k_{w4y})	14000 N/m
Tyre stiffness coefficient (k_{r1}, k_{r2}, k_{r3}, k_{r4})	150000 N/m
Primary suspension damping coefficient (c_{dz})	600 Ns/m
Primary suspension damping coefficient (c_{dy})	1600 Ns/m
Secondary suspension damping coefficient (c_{w1z}, c_{w2z}, c_{w3z}, c_{w4z})	1000 Ns/m
Secondary suspension damping coefficient (c_{w1y}, c_{w2y}, c_{w3y}, c_{w4y})	1600 Ns/m
Distance between front wheels and center of the car (a)	1.4 m
Distance between rear wheels and center of the car (b)	1.7 m
Distance between right wheels and center of the car (c)	0,75 m[4]
Distance between left wheels and center of the car (d)	0.75 m
The vertical distance between driver and center of the car (e)	0.5 m
The lateral distance between driver and center of the car (f)	0.05 m

In this study, the sine input to the car wheels is given using the following formulas

Lateral displacement of the left rear wheel:

$$
\begin{aligned}
r_1 &= 0.1\sin\left(\pi\frac{vt}{\lambda}\right) && t \geq 0 \\
r_2 &= 0.1\sin\left(\pi\frac{v\left(t-\frac{\lambda}{2v}\right)}{\lambda}\right) && t \geq \frac{\lambda}{2v} \\
r_3 &= 0.1\sin\left(\pi\frac{v\left(t-\frac{a+b}{v}\right)}{\lambda}\right) && t \geq \frac{a+b}{v} \\
r_4 &= 0.1\sin\left(\pi\frac{v\left(t-\frac{a+b+0.5\lambda}{v}\right)}{\lambda}\right) && t \geq \frac{a+b+0.5\lambda}{v}
\end{aligned}
\tag{20}
$$

In Equation 19, the value represented by v represents the car speed and represents the wavelength.

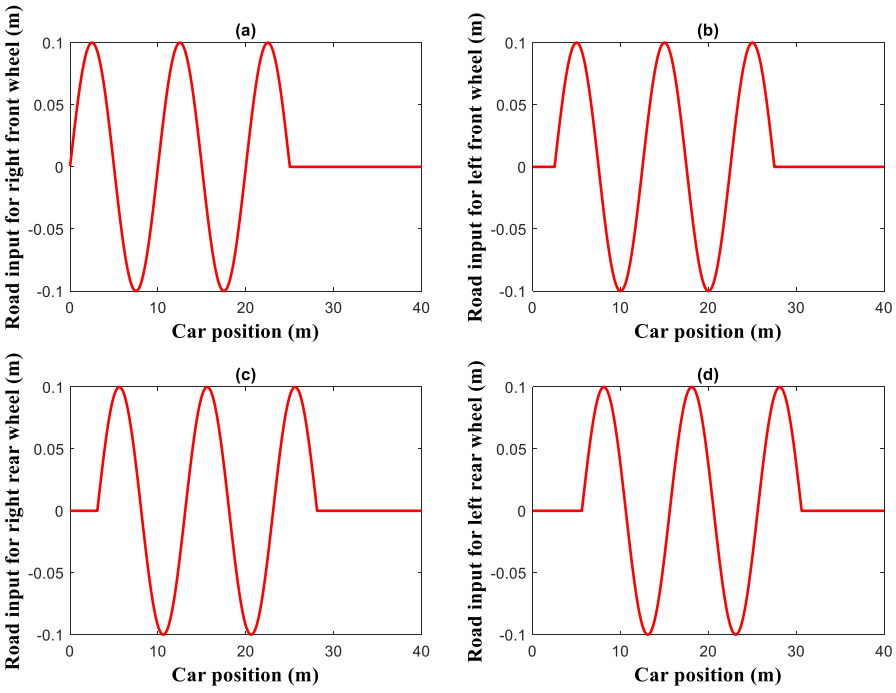

Figure 2 Road input in sine form

3. NUMERICAL SIMULATION

In this study, dynamic behaviors affecting both the vehicle and the passenger will be examined by using a sinusoidal road input. Two different situations were taken into consideration during the analysis. These; the effect of vehicle mass and variable vehicle speed. The road input with a wavelength of 5 m and an amplitude of 0.1 m given in Figure 2 is included in the wheels of the vehicle. When the figure is examined, the front wheels of the vehicle do not enter the disruptive input at the same time. First, the right front wheel is exposed to sinusoidal road input, while the left front wheel is exposed to disruptive road input after passing a distance of half the wavelength. Thus, the rotation of the vehicle around its axes will be examined.

In the analysis, the car speed was taken as a constant 20 m/s. The length of the road input with the sine function is accepted as 25 m. The total analysis time was taken as 6.25 s.

3.1. Effect of Car Mass

In this section, the dynamic responses of the vehicle and the passenger in the vertical and lateral directions will be examined if the vehicle mass is 500 kg, 1000 kg, 2000 kg, and 3000 kg.

In Figure 3 and Figure 4, the displacement and acceleration values of the passenger and the vehicle in the lateral and vertical directions are given. It can be seen from the graphs that while the vertical displacement of the passenger decrease as the vehicle mass increases, the lateral displacements almost do not change. However, with the increase in vehicle mass, it takes time to dampen the vertical displacements. For example, if the vehicle mass is 500 kg, the vertical displacements are damped when the vehicle travels approximately 60 m, while if the vehicle mass is 3000 kg, the vehicle must move more than 120 m for full damping.

When Figure 3c is examined, the vertical acceleration of the passenger increases to approximately 18 m/s^2 if the vehicle mass is 500 kg, while the maximum vertical acceleration of the passenger is approximately 6 m/s^2 if the vehicle mass is 3000 kg. In other words, with the increase in vehicle mass, the vertical acceleration value decreases 3 times.

When Figure 4 is examined, both the lateral and vertical dynamic responses of the vehicle decrease with the increase in vehicle mass. The vertical displacement graphs of the vehicle in Figure 4a are similar to those in Figure 3a. Similarly, according to the vertical acceleration graph of the vehicle, the acceleration of the vehicle decrease 3 times as the vehicle mass increases. In addition, the lateral dynamic responses of the vehicle in Figure 4 are also highly affected by the vehicle mass.

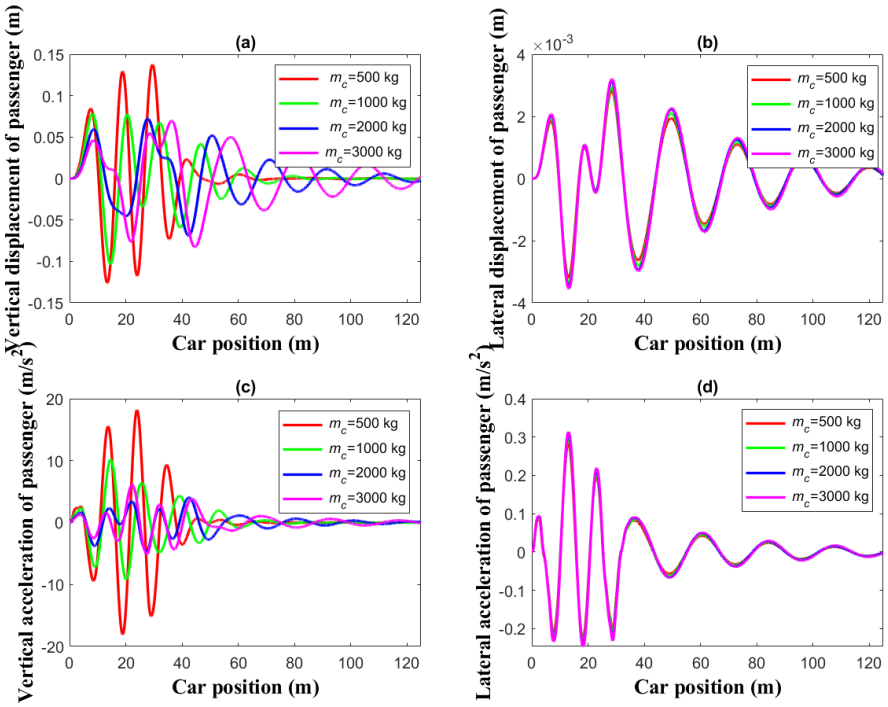

Figure 3 The effect of vehicle mass on the dynamic responses of the passenger in the lateral and vertical directions

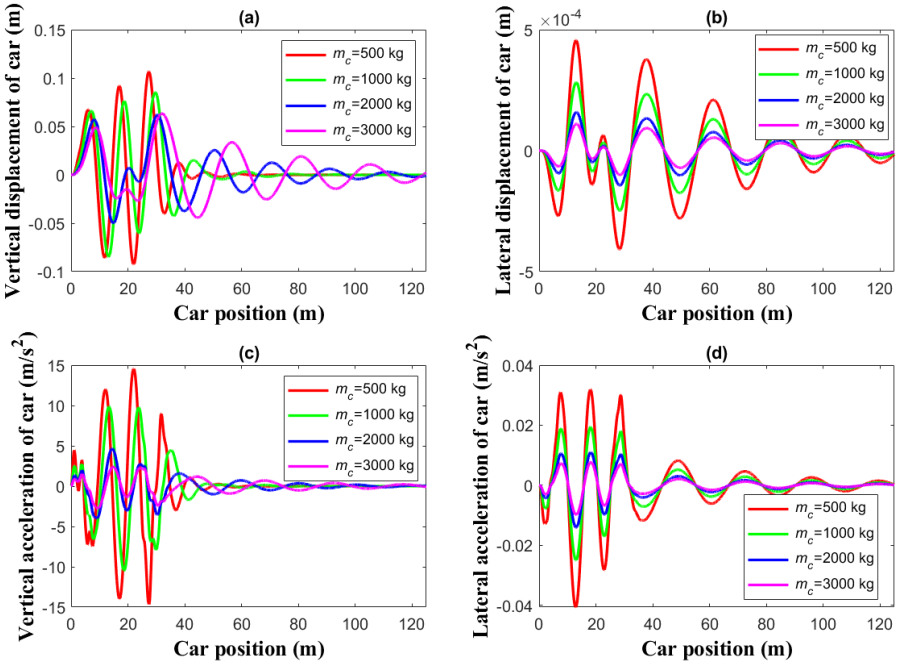

Figure 4 The effect of vehicle mass on the dynamic responses of the car in the lateral and vertical directions

3.2. Effect of Variable Car Velocity

In this section, the situation of the car passing over the sinus road profile at different speeds is examined. In Figure 5-7, when the vehicle changes from 3 m/s to 50 m/s in 0.1 m/s intervals, the maximum lateral and vertical displacements and acceleration values are examined.

When Figure 5 is examined, the maximum dynamic responses of the passenger in the vertical direction occur when the vehicle speed is about 10 m/s, while the maximum dynamic responses in the lateral direction occur when the vehicle speed is about 9 m/s. In all graphs, the maximum displacement and acceleration of the passenger decrease as the vehicle speed exceed 10 m/s. The lateral and vertical displacement and acceleration graphs of the vehicle in Figure 6 are quite similar to the ones in Figure 5. However, in Figure 6c, it is seen that the vertical acceleration value of the vehicle increases when the vehicle speed exceeds 27 m/s. In addition, the maximum vertical acceleration values affecting the passenger and the vehicle exceed the uncomfortable acceleration value that affects the human being. The uncomfortable acceleration value affecting the human is 0.49 m/s^2 according to the ISO 2631 standard [15].

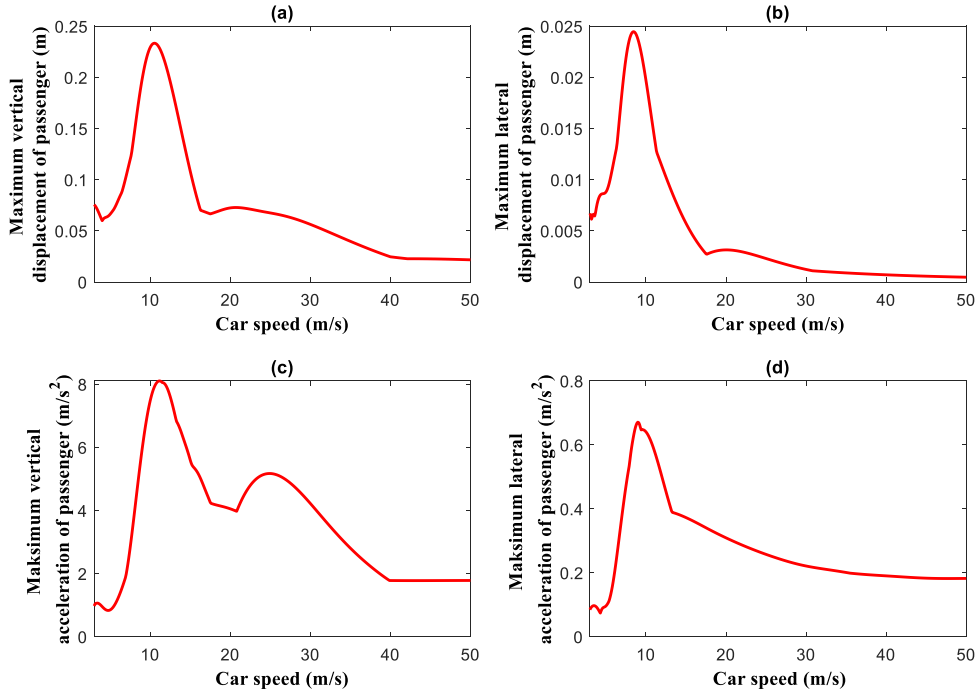

Figure 5 The effect of car speed on the maximum lateral and vertical dynamic responses of the passenger

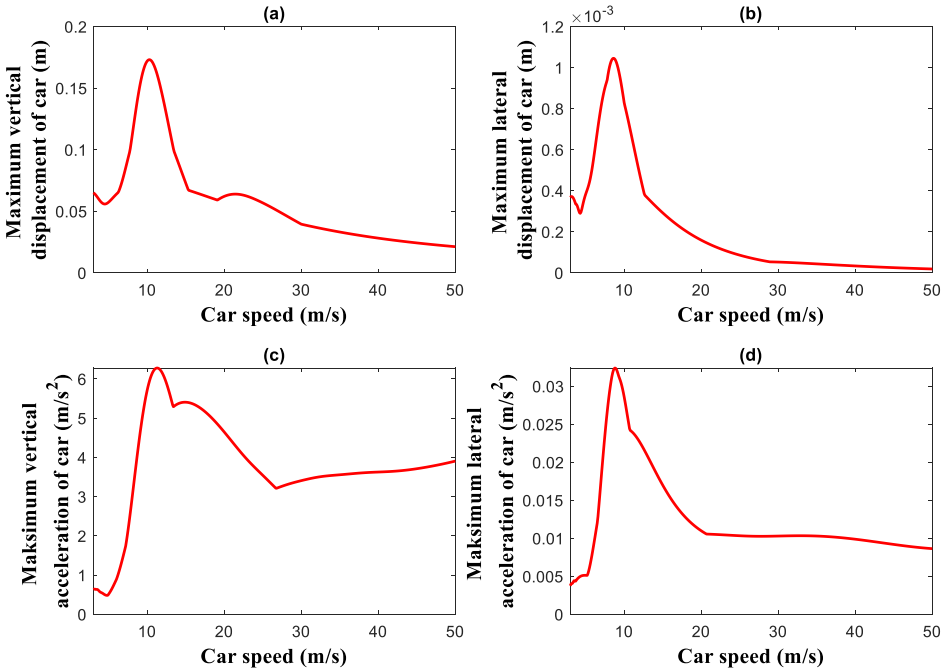

Figure 6 The effect of vehicle speed on the maximum lateral and vertical dynamic responses of the car

In Figure 7, the maximum pitch and roll movements are examined according to the speed of the car. While the roll response of the car increases until the car velocity is about 10 m/s, it is seen that the maximum roll motion decreases as the car velocity increase after this velocity. In Figures 7b and 7d, the car's maximum pitch motion occurred when the car velocity was 20 m/s.

4. CONCLUSION

In this study, lateral and vertical displacements and acceleration graphs of the full car model with fourteen degrees of freedom model with the passenger are given. In addition, the roll and pitch movements of the car were also examined. With the increase in the mass of the vehicle, the vertical displacements of the vehicle and the passenger decrease considerably, while the lateral displacement of the passenger almost does not change. However, the lateral displacement of the vehicle decreases as the mass increases. In addition, the vehicle's maximum dynamic response occurs when the car speed is approximately 10 m/s. Finaly, The effect of car mass and car speed on these dynamic responses has been examined with graphics, and as the car mass increases, the vertical displacement and acceleration values of the car decrease, while the damping of these values is delayed. At certain values of the car velocity, the car's maximum dynamic responses occur.

Acknowledgments
The authors would like to acknowledge the reviewers and editors of Sakarya University Journal of Science.

Funding
The author (s) has no received any financial support for the research, authorship or publication of this study.

The Declaration of Conflict of Interest/ Common Interest
No conflict of interest or common interest has been declared by the authors.

The Declaration of Ethics Committee Approval
This study does not require ethics committee permission or any special permission.

The Declaration of Research and Publication Ethics

The authors of the paper declare that they comply with the scientific, ethical and quotation rules of SAUJS in all processes of the paper and that they do not make any falsification on the data collected. In addition, they declare that Sakarya University Journal of Science and its editorial board have no responsibility for any ethical violations that may be encountered, and that this study has not been evaluated in any academic publication environment other than Sakarya University Journal of Science.

REFERENCES

[1] A. Agharkakli, G.S. Sabet, A. Barouz, "Simulation and Analysis of Passive and Active Suspension System Using Quarter Car Model for Different Road Profile" International Journal of Engineering Trends and Technology, vol. 3, pp. 636–644, 2012.

[2] M. Nagarkar, Y. Bhalerao, G.V. Patil, R.Z. Patil, "Multi-Objective Optimization of Nonlinear Quarter Car Suspension System - PID and LQR Control" Procedia Manufacturing, vol. 20, pp. 420–427, 2018.

[3] E. Yildirim, I. Esen, "Dynamic Behavior and Force Analysis of the Full Vehicle Model using Newmark Average Acceleration Method" Engineering, Technology & Applied Science Research, vol. 10, pp. 5330–5339, 2020.

[4] N. Yagiz, L.E. Sakman, R. Guclu, "Different control applications on a vehicle using fuzzy logic control" Sadhana - Academy Proceedings in Engineering Sciences, vol. 33, pp. 15–25, 2008.

[5] M.M.M. Salem, A.A. Aly, "Fuzzy Control of a Quarter-Car Suspension System" International Journal of Computer and Information Engineering, vol. 3, pp. 1276–1281, 2009.

[6] D. Singh, M.L. Aggarwal, "Passenger seat vibration control of a semi-active quarter car system with hybrid Fuzzy–PID approach" International Journal of Dynamics and Control, vol. 5, pp. 287–296, 2017.

[7] D. Singh, "Self-Tuning Fuzzy Control of Seat Vibrations of Active Quarter Car Model" International Journal of Computer and Systems Engineering, vol. 11, pp. 1127–1133, 2017.

[8] P. Swethamarai, P. Lakshmi, "Design and implementation of fuzzy-PID controller for an active quarter car driver model to minimize driver body acceleration" IEEE International Systems Conference (SysCon), pp. 1–6, 2019.

[9] M. Eroğlu, M.A. Koç, R. Kozan, İ. Esen, "Self-tuning fuzzy logic control of quarter car and bridge interaction model" Sakarya University Journal of Science, vol. 25, pp. 1197–1209, 2021.

[10] M.A. Koç, "Analytic Method for Vibration Analysis of Track Structure Induced by High-Speed Train" Sakarya University Journal of Science, vol. 25, pp. 146–155, 2021.

[11] C. Onat, S. Sivrioğlu, İ. Yüksek, "Bir Çeyrek Taşit Modeli İçin H∞ Kontrolcü Tasarimi" Mühendis ve Makine, pp. 40–46, 2005.

[12] M. Sever, H.S. Şendur, H. Yazıcı, M.S. Arslan, "Biodinamik sürücü modeli içeren bir taşıt süspansiyon sisteminin durum türevi geri beslemeli LQR ile aktif titreşim kontrolü" Gazi Üniversitesi Mühendislik-Mimarlık Fakültesi Dergisi, vol. 3, pp. 1573–1572, 2019.

[13] C. Belgütay, "H∞ Control and Mathematical Modeling of A Quarter- Car System via Non-Parametric Approach" Yıldız Technical University Graduate School of Natural and Applied Sciences, 2015.

[14] M.A. Koc, "Dynamic Response of an Euler-Bernoulli Beam Coupled with a Tuned Mass Damper under Moving Load Excitation" Sakarya University Journal of Science ISSN,

vol. 24, pp. 694–702, 2020.

[15] C. Mizrak, I. Esen, "Determining Effects of Wagon Mass and Vehicle Velocity on Vertical Vibrations of a Rail Vehicle Moving with a Constant Acceleration on a Bridge Using Experimental and Numerical Methods", Shock and Vibration, 2015.

SAKARYA ÜNİVERSİTESİ
FEN BİLİMLERİ ENSTİTÜSÜ DERGİSİ

Sakarya University Journal of Science
SAUJS

ISSN 1301-4048 | e-ISSN 2147-835X | Period Bimonthly | Founded: 1997 | Publisher Sakarya University | http://www.saujs.sakarya.edu.tr/

Title: A Numerical Study of a Pico Hydro Turbine

Authors: Ümit BEYAZGÜL, Ufuk DURMAZ, Orhan YALÇINKAYA, Mehmet Berkant ÖZEL, Ümit PEKPARLAK

Recieved: 2022-05-30 00:00:00

Accepted: 2022-07-04 00:00:00

Article Type: Research Article

Volume: 26
Issue: 4
Month: August
Year: 2022
Pages: 842-849

How to cite
Ümit BEYAZGÜL, Ufuk DURMAZ, Orhan YALÇINKAYA, Mehmet Berkant ÖZEL, Ümit PEKPARLAK; (2022), A Numerical Study of a Pico Hydro Turbine. Sakarya University Journal of Science, 26(4), 842-849, DOI: 10.16984/saufenbilder.1123442
Access link
http://www.saujs.sakarya.edu.tr/en/pub/issue/72361/1123442

Sakarya University Journal of Science 26(4), 842-849, 2022

A Numerical Study of a Pico Hydro Turbine

Ümit BEYAZGÜL[1], Ufuk DURMAZ*[1], Orhan YALÇINKAYA[1], Mehmet Berkant ÖZEL[1], Ümit PEKPARLAK[2]

Abstract

Pico hydro turbines are suitable for low head applications in power plants since their efficiency is more stable than other turbine types. In some situations, computational fluid dynamics (CFD) has also been utilized as well as experimental studies for the performance prediction of water turbines at a pico scale. Also, CFD methods are getting much closer to real conditions in terms of steady-state with moving references and transient domains with rotor movements. For this purpose, electricity production related to the flow in a PHT was investigated numerically. This study presents six degrees of freedom (6-DOF) and moving reference frame (MRF) methods to predict the maximum conditions of a pico scale two-dimensional turbine by comparing the torque and angular velocities on the runner based on the turbine output power of 1 W determined by an experimental study. Besides, the effect of the torque, angular velocity, tip speed ratio, and turbine body profile was investigated comprehensively. In this regard, MRF and 6-DOF methods were performed to validate and compare the numerical model with the experimental results. Also, the results obtained from 6-DOF and MRF methods were compared to experimental study. It is concluded that PHT is generating 0.3 W power under 6.47 rad/s angular velocity with 6-DOF method, however; this value corresponds to 31.4 rad/s angular velocity against 1 W with the MRF method. Also, the maximum velocity of the turbine was 6.1 m/s according to the simulation result. It is accepted that the turbine maximum velocity inlet was 0.53 m/s based on the experimental study. As a conclusion, numerical results for the pico hydro turbine were reasonable taking the experimental study into account. It is also concluded that there is a tip speed ratio of 2.36 with the MRF method and 0.48 with the 6-DOF method between water tangential velocity and runner velocity for the turbine model.

Keywords: Pico hydro turbine, moving reference frame, 6-DOF, turbine power output, tip speed ratio

* Corresponding author: udurmaz@sakarya.edu.tr
[1] Sakarya University
E-mail: umitbyzgl1@hotmail.com, orhanyalcinkaya@sakarya.edu.tr, mozel@sakarya.edu.tr
ORCID: https://orcid.org/0000-0001-5534-8117, https://orcid.org/0000-0002-1471-793X, https://orcid.org/0000-0003-2380-1727, https://orcid.org/0000-0002-2439-1494
[2] TBM Industry
E-mail: u.pekparlak@porte.com.tr
ORCID: https://orcid.org/0000-0002-5554-6989

1. INTRODUCTION

A pico hydro turbine (PHT) is an energy harvesting device that uses the energy of a water pressure drop. This energy is captured by the pico turbine and converted into electricity. The availability of a continuous energy source enables optimal pressure management that is continuously maintained at a lower value to reduce water leaks, improve network efficiency, and extend pipeline lifetime. PHTs are frequently used in water distribution pipelines. It is widely used for opening and closing valves, which regulate water flow rate [1, 2]. A previous study has conducted an experimental study to predict maximum water turbine performance.

Thakur et al. [3] evaluated the performance of the modified turbine using the CFD software. They compared it with some of the leading literature designs of the Savonius water turbine with a simple two-blade Savonius turbine. The ready-made design provided better performance than the selected Savonius turbine designs. To illustrate the increased performance of the Savonius turbine, several velocity vector plots were used utilizing the impinging jet duct design. Chichkhede et al. [4] examined the design parameters of the cross-flow turbine for different nozzle opening and water inlet angles. A full 3-dimensional steady-state flow simulation of the cross-flow turbine was performed considering the body, runner, and nozzle assembly. With the increasing inlet angle, the optimum blade angle value was observed to increase for the proposed geometry. Jiyun et al. [5] developed an inline vertical cross-flow turbine to collect the potential hydropower inside water supply pipes for providing power to the water monitoring systems. Besides, the effects of tip clearance and block shape on turbine performance were investigated. The proposed model turbine can supply enough power without influencing the regular water supply for any general water leakage monitoring system. Kim et al. [6] investigated the effect of blade thickness on the efficiency of a Francis turbine. The blockage effects were studied with numerical analysis at best yield and off-design conditions. Since the blockage ratio increased, the power and yield of the hydro turbine gradually decreased. Therefore, hydraulic performance characteristics should be considered a significant factor in designing the runner blades. As a result of their studies, they verified that the blockage effect considerably affects the design of Francis turbine models. Ji-Feng Wang et al. [7] estimated the flow characteristics from the water turbine with nozzle, wheel, and diffuser based on three-dimensional numerical flow analysis. They calculated and analyzed the extracted power and torque of a composite water turbine at different rotation speeds for a specific flow rate. They showed with the simulation results that the nozzle and diffuser could increase the pressure drop on the turbine and obtain more power from the available water energy. Acharya et al. [8] numerically conducted the characteristics and fluid flow in a cross-flow hydro turbine and optimized its performance by changing various geometric parameters. They determined a base model during the process, changing the nozzle's shape, the guide vane's angle, the number of runner blades, and simultaneously the design by making simulations separately. Oliy et al. [9] designed a suitable turbine using all turbine parameters to achieve a maximum efficiency cross-flow turbine and performed computational fluid dynamic simulation as an important tool for the turbine's performance. Ranjan et al. [10] aimed to increase the efficiency of a cross-flow hydro turbine with geometric modification by conducting numerical research of the cross-flow hydro turbine in Ansys Fluent using multiple physics finite volume solver. Makarim et al. [11] examined the effect of the blade depth ratio and the number of blades on the power coefficient of cross-flow water turbines. They carried it out in a 2-D method by using Ansys Fluent software. Prakoso et al. [12] compared the six-degree of freedom method by a using user-defined function (UDF) and the moving mesh method for the simulation of small-scale cross-flow turbines. They found that 6-DOF had a smaller deviation of about 6.8% from experimental results. Wang et al. [13] discussed the hydrodynamic performance of the vertical axis water turbine model both experimentally and numerically. In line with the current research, they proposed the 6-DOF method with CFD, which is suitable for performing analysis of rotor motion and

predicting hydraulic performance for a vertical axis water turbine.

In this study, a two-dimensional water turbine model was designed and simulated in the numerical study with computational fluid dynamics moving reference frame (MRF) and six-degree of freedom (6-DOF) methods. On the one hand, it obtained 31.4 rad/s angular velocity of the turbine under given 1 W with MRF method. On the other hand, it is determined that the turbine with the 6-DOF method generates almost the same power as in the experimental result. As a result of the study, the maximum turbine output power obtained from experimental data is in good agreement with the numerical simulation results.

2. METHODS

The two-dimensional geometry of the water turbine in this study was created in computer-aided design (CAD) software. PHT has a 13 mm inlet diameter, 32 mm inner diameter, and 40 mm outer diameter. Also, while the volumetric water flow rate at the inlet was 0.25 L/s, it was measured as 0.167 L/s at the outlet.

The boundary conditions of the mentioned geometry are illustrated in Figure 1. While the ratio between turbine inner diameter and outer diameter (D_o/D_i or R_o/R_i) was found to be 0.8. Also, the turbine blade inlet angle (β_1) and turbine blade outlet angle (β_2) was measured 48° and 118°, respectively.

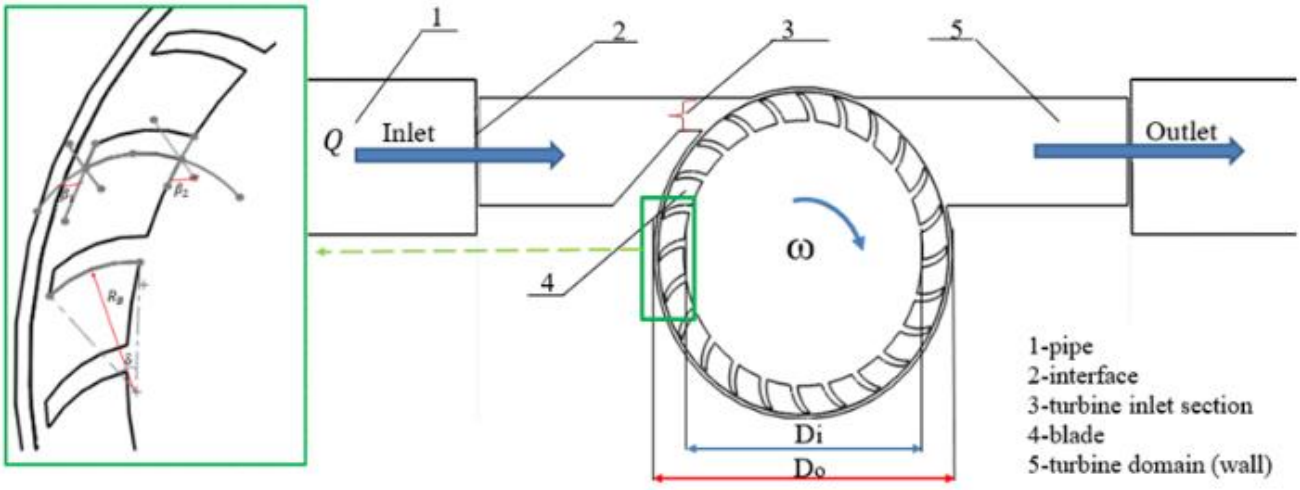

Figure 1 Schematic of geometry and boundary named selections

R_B represents the blade curve radius given relevance with β_1 in Eq. (1).

$$R_B = \frac{D_o^2 - D_i^2}{2R.cos(\beta_1)} \quad (1)$$

δ represents the blade curve angle, which is also given relevance with β_1 in Eq. (2).

$$tan\left(\frac{\delta}{2}\right) = \frac{cos(\beta_1)}{sin(\beta_1) + D_o/D_i} \quad (2)$$

Eq. (1) and Eq. (2) are simplified when the substituted value of blade inlet angle, it is obtained that R_B equals to $0.135D_o$, and δ corresponds to 37°.

To sum up, the main parameters as a result of equation sequences can be found in Table 1.

Table 1 PHT design parameters

Design Parameter	Value (mm)
Outlet velocity, V_{outlet}	0.53
Number of blades, z	24 pcs
Outer diameter, D_0	40

Inner diameter, D_i	32
Blade's length, L	3.15
Blade's width, B	1
The angle of attack, α	23°
Blade's inlet angle, β_1	48°
Blade's outlet angle, β_2	118°
Blade curve radius, R_B	5.38
Blade curve angle, δ	37°
Turbine discharge angle,λ	90°
Turbine inlet height, S_h	4

2.1. MRF and 6-DOF Simulation Setup

2-D steady domain was used to perform the analyses in this study. The simulation was run under steady CFD simulation with enabled gravitational acceleration, which was turned on in the y-axis direction, which corresponds to $g_y = -9.81\ \mathrm{m/s^2}$. The standard wall function k-ε turbulence modeling was employed in this simulation because this provides sufficient precision and has a high accuracy of backflow and rotation. Water-liquid was determined as the main phase. The velocity inlet is 0.53 m/s given from the experimental study. The turbulence intensity was 5%, and its turbulent viscosity ratio was 10 for the velocity inlet. In addition to the MRF simulation setup, a dynamic mesh setting with 6-DOF user-defined function was used in this study. The dynamic mesh option is turned on for the settings, and the 6-DOF properties name was written as one-DOF rotation with active mode. The moment of inertia in this study was given 0.005 kg.m^2 based on the mass properties simulation in computer-aided drawing software. The coupled pressure-velocity coupling discretization scheme was used for the calculations to obtain a robust and efficient single-phase implementation for steady-state flows, with superior performance compared to the segregated solution schemes. As for spatial discretization, the standard least-squares cell-based method was employed for gradient discretization and second order for pressure discretization as the default method in the simulation program. Other variable's discretization schemes were set as first-order upwind. The first-order discretization method is a promising and stable calculation process, yet, a finer mesh is supposed to obtain a good result. The autosave during calculation was turned on every five timesteps. The computations were run for a one-second simulation divided into 300 timesteps for MRF and 6-DOF methods.

2.2. *Procedure*

2-D model of original turbine components (runner blades, runner, domain, etc.) was modeled, and numeric analysis was carried out for the standard turbine model shown in Figure 2. Required parameters such as torque and angular velocity were acquired in both 6-DOF and MRF methods, and thus turbine efficiency was calculated between numerical and experimental results.

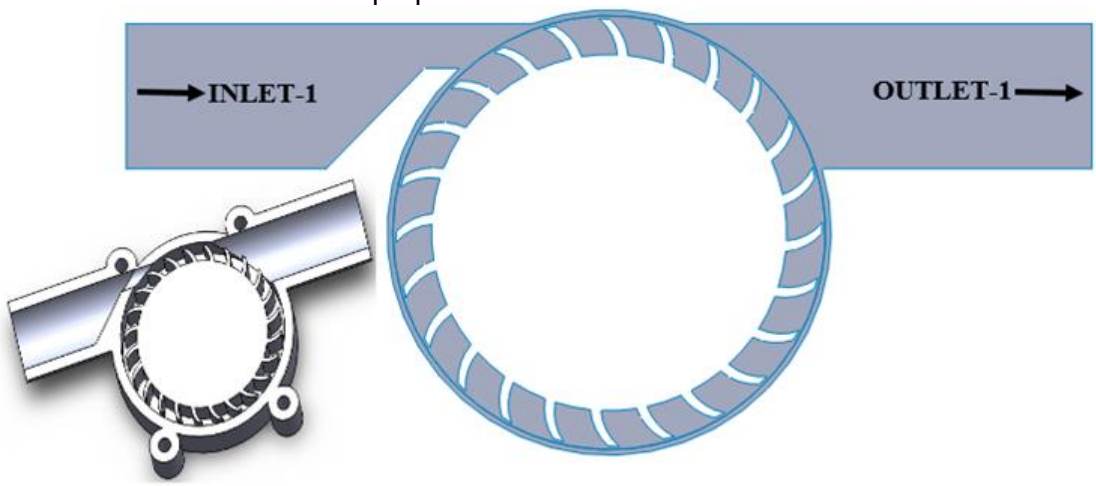

Figure 2 Original turbine body modification

The power output of PHT was determined using the basic water turbine equation between torque (T) and angular velocity (w) given in Eq. (3).

$$P_{out} = T.w \quad (3)$$

While P_{out} symbolizes the shaft power of the turbine, T is the torque at the shaft, and w is the angular velocity. Angular velocity coupled with torque will be directly calculated depending on the power in the named expressions section in CFD-Post simulation by using Eq. (8).

$$w = \frac{2.\pi.n}{60} \quad (4)$$

Where n is ascribed to the revolution per minute of the turbine.

In accordance with the analysis result, the tip speed ratio (TSR) is introduced along with the torque of blades, angular velocity, and the water velocity from the inlet to the outlet of the turbine that was recorded based on the volume flow rate in the experimental study. TSR means the ratio of the tangential velocity (V_t) of the turbine to the turbine runner velocity (V), and it can be calculated using Eq. (5), where r is the runner radius.

$$TSR = \frac{wr}{V} \quad (5)$$

3. RESULTS AND DISCUSSIONS

Original turbine MRF simulation was implemented to predict torque and angular velocity in a given power output defined by the experimental study. Firstly, to initiate the numerical study, it was given lower and upper angular velocity ranges to run the simulation automatically for the original turbine under the velocity of 0.53 m/s. It was found that angular velocity of 31.4 rad/s and the torque of 0.03 Nm were respectively determined to run the simulation under 1 W. The turbine was also run in the 6-DOF method, and 0.3 W was produced under the angular velocity of 6.47 rad/s with 0.05 Nm torque. Moreover, from simulation results, while the TSR value was obtained 2.36 in the MRF method, it was obtained 0.48 in the 6-DOF method.

Figure 3 shows the velocity contours in the internal flow field of the original model. It can be concluded that the water velocity has a uniform profile at the inlet, and the flow is distributed evenly. The velocity in the internal flow field is dominated directly by the runner shape. The water flow velocity field reaches the maximum velocities at the turbine outlet.

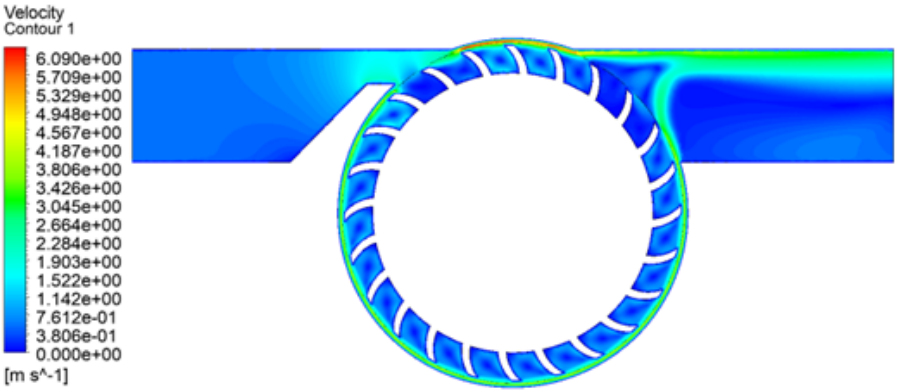

Figure 3 Velocity contour of original model

The maximum velocity of the original model is determined as 6.1 m/s. Figure 4 illustrates the pressure contours in the original model, where the turbine inlet pressure decreases along the runner passage, but the pressure at the turbine outlet is almost uniform.

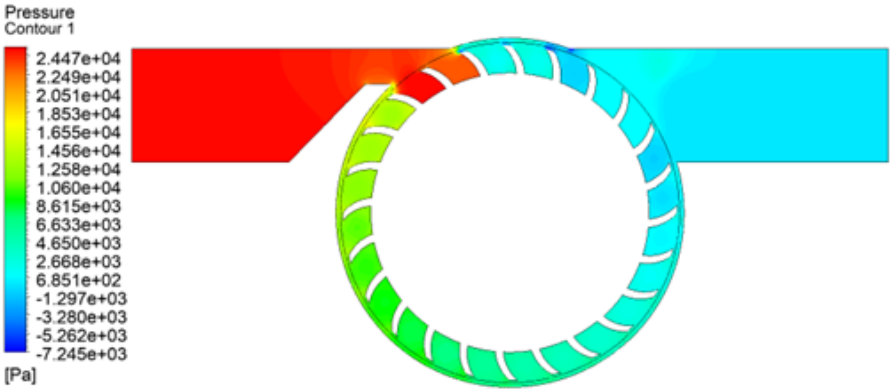

Figure 4 Pressure contour of original turbine model

The fluid pressure passing through the blades decreases rapidly. The maximum pressure of the original model was obtained 25 kPa.

Moreover, the mesh independency test was also executed using the steady-state method. The Richardson extrapolation method was used to obtain a suitable mesh for the assessment process in this study. Analysis results for four different mesh structures, Grid1, Grid2, Grid3, and, Grid4, were given in the table, and these structures consisted of 14175, 57764, 228176, and 904901 elements, respectively. The result of Richardson extrapolation is called Grid Convergence Index (GCI). The GCI refers to the error-index of the tested value from the extrapolated value in the extrapolation process. The number of the mesh was converted to a Normalised Grid Spacing (NGS): 1, 0.5, 0.25, and 0.125, respectively.

Table 2 Mesh independency test result

Grid	Number of elements	Torque (Nm)	NGS	GCI (%)
Grid1	14175	0.032858	1	-
Grid2	57764	0.034157	0.5	1.83%
Grid3	228176	0.03789	0.25	5.06%
Grid4	904901	0.041360	0.125	4.24%
	~	0.04786	0	-

Table 2 shows the mesh independency test result. Torque output value was variable in the mesh independency test, and since time is a one-dimensional unit, an equation for ratio modification was necessary for the Richardson extrapolation method. The acceptance criteria for a good simulation in terms of GCI index is below 2%. It can be concluded that Grid2 and below have the least torque error. Therefore, Grid2 or below is good enough to use for the simulation. As a result of the independency result, this study used 26191 mesh numbers with a skewness of 0.45.

4. CONCLUSION

This study provides a fundamental understanding of the pico water turbine, and this design and analysis methods are used to determine the turbine's performance significantly. The effect of the torque, angular velocity, TSR, and turbine body profile was investigated numerically on a pico hydro turbine in detail. As a result, numerical results show a good agreement with experimental data. When the MRF method was preferred, a deviation of about 2% from the experimental results was observed. In contrast, this rate reached nearly 30% with the 6-DOF method. According to the numerical results obtained, the MRF method for predicting water turbine performance at pico scale is more reasonable than the 6-DOF method. However, it could be taken advantage of calculating transient physics phenomena like torque and angular velocity rather than experimental devices. MRF or 6-DOF method results can be a preliminary reference the turbine model's performance can be captured effectively. Thus these methods shall be the right choice for water turbine simulations. In conclusion, there are three possible ways to optimize water turbine performance, firstly standard turbine inlet height (S_h) should be minimized, or recirculation or

vortex should be minimized. With this study, it is aimed to provide a better understanding of hydro turbines in terms of power performance.

NOMENCLATURE

α	Angle of attack [°]
β_1	Blade inlet angle [°]
β_2	Blade outlet angle [°]
δ	Blade curve angle [°]
λ	Turbine discharge angle [°]
w	Angular velocity [rad/s]
6-DOF	Six degrees of freedom [-]
B	Blade's width [mm]
CAD	Computer-aided design [-]
D_i	Inner diameter [mm]
D_o	Outer diameter [mm]
GCI	Grid Convergence Index [-]
L	Blade's length [mm]
n	Revolution per minute [rpm]
NGS	Normalized Grid Spacing [-]
PHT	Pico hydro turbine [-]
P_{out}	Shaft power [W]
R_B	Blade curve radius [°]
T	Torque [Nm]
TSR	Tip speed ratio [-]
S_h	Turbine inlet height [mm]
V	Runner velocity [m/s]
V_{outlet}	Velocity outlet [m/s]
V_t	Tangential velocity [m/s]
UDF	User-defined function [-]
MRF	Moving reference frame [-]
z	Number of blades [-]

REFERENCES

[1] B. R. Cobb, K. V. Sharp, "Impulse (Turgo and Pelton) turbine performance characteristics and their impact on pico-hydro installations," Renewable Energy, vol. 50, pp. 959–964, 2013.

[2] L. Alveyro, F. Jose, S. Aida, "Performance improvement of a 500-kW Francis turbine based on CFD," vol. 96, 2016.

[3] N. Thakur, A. Biswas, Y. Kumar, M. Basumatary, "CFD analysis of performance improvement of the Savonius water turbine by using an impinging jet duct design," Chinese Journal of Chemical Engineering., vol. 27, no. 4, pp. 794–801, 2019.

[4] S. Chichkhede, V. Verma, V. K. Gaba, S. Bhowmick, "A Simulation Based Study of Flow Velocities across Cross Flow Turbine at Different Nozzle Openings," Procedia Technology., vol. 25, pp. 974–981, 2016.

[5] D. Jiyun, S. Zhicheng, Y. Hongxing, "Performance enhancement of an inline cross-ow hydro turbine for power supply to water leakage monitoring system," Energy Procedia, vol. 145, pp. 363–367, 2018.

[6] S. J. Kim, Y. S. Choi, Y. Cho, J. W. Choi, J. H. Kim, "Effect of blade thickness on the hydraulic performance of a Francis hydro turbine model," Renewable. Energy, vol. 134, pp. 807–817, 2019.

[7] J. F. Wang, J. Piechna, N. Müller, "A novel design of composite water turbine using CFD," Journal of Hydrodynamics, vol. 24, no. 1, pp. 11–16, 2012.

[8] N. Acharya, C. G. Kim, B. Thapa, Y. H. Lee, "Numerical analysis and performance enhancement of a cross-flow hydro turbine," Renewable Energy, vol. 80, pp. 819–826, 2015.

[9] G. Birhanu Oliy, "Design and Computational Fluid Dynamic Simulation Study of High Efficiency Cross Flow Hydro-power Turbine," International Journal of Science, Technology and Society., vol. 5, no. 4, p. 120, 2017.

[10] R. K. Ranjan, N. Alom, J. Singh, B. K. Sarkar, "Performance investigations of cross flow hydro turbine with the variation of blade and nozzle entry arc angle," Energy Conversion and Management vol. 182, no. January, pp. 41–50, 2019.

[11] D. A. Makarim, D. D. D. P. Tjahjana, S. I. Cahyono, S. A. Mazlan, "Performance investigation of the crossflow water turbine by using CFD," AIP Conference Proceedings, vol. 2097, 2019.

[12] A. P. Prakoso, Warjito, A. I. Siswantara, Budiarso, D. Adanta, "Comparison between 6-DOF UDF and moving mesh approaches in CFD methods for predicting cross-flow pico-hydro turbine performance," CFD Letters., vol. 11, no. 6, pp. 86–96, 2019.

[13] X. Wang, X. Luo, B. Zhuang, W. Yu, H. Xu, "6-DOF numerical simulation of the vertical-axis water turbine," ASME-JSME-KSME 2011 Joint Fluids Engineering. Conferenes. AJK 2011, vol. 1, no. PARTS A, B, C, D, pp. 673–678, 2011.